Milliarcsecond Resolution Infrared Observations of the Recurrent Nova RS Ophiuchi and Low Mass Stellar Systems

by

Richard Keith Barry, Jr.

A dissertation submitted to The Johns Hopkins University in conformity with the requirements for the degree of Doctor of Philosophy.

Baltimore, Maryland

January, 2008

Abstract

We introduce the method of long-baseline stellar interferometry starting with the fundamental combination of electric fields. We describe beam combination techniques and how they are realized at the observatories used in the conduct of this research. We subsequently give a mathematical description of the *Keck Interferometer Nuller* and describe our pathfinder effort to produce the first science with this instrument. We present the results of a 2.5 year observing campaign using four different observatories; the *Spitzer Space Telescope*, the Infrared and Optical Telescope Array on Mt. Hopkins, Arizona, the Palomar Testbed Interferometer on Mt. Palomar, California, and the *Keck Interferometer* on Mauna Kea, Hawaii. We describe our observations of a broad array of low-mass binary stars and the recurrent nova RS Ophiuchi in outburst — a candidate Type Ia supernova progenitor. We present calculations that suggest a new paradigm for dust creation in recurrent novae. We explore this paradigm through analysis of line and continuum emission from near peak brightness to quiescence. We report radial velocity and astrometric model fitting on the low-mass M-dwarf binary Gliese 268. We derive masses of the constituent stars with 0.5% uncertainty.

Dissertation Advisors

- Dr. William C. Danchi
- Prof. Holland C. Ford

Dissertation Defense Committee

- Prof. Charles L. Bennett
- Dr. William C. Danchi
- Prof. Holland C. Ford
- Dr. Matthew A. Greenhouse
- Prof. Colin A. Norman

Acknowledgements

I am grateful to Dr. William C. Danchi, Senior Astrophysicist in the Exoplanets and Stellar Astrophysics Laboratory of NASA/GSFC for his direct patronage and to Holland C. Ford, Professor of Physics and Astronomy at The Johns Hopkins University and PI of the Hubble Space Telescope, Advanced Camera for Surveys for his guidance in my scientific research. I am further indebted to Dr. Damien Ségransen, Dr. Didier Queloz, and Brice-Oliver Demory of Observatoire de Genève, Switzerland for their advice and collaboration in reduction of IOTA and ELODIE data and fitting of binary orbits and to Dr. Guillermo Torres of the Harvard-Smithsonian Center for Astrophysics in Cambridge, MA for his patient tutelage regarding binary stars and stellar astrophysics. I am also grateful to Professor Augustin Skopal of the Astronomical Institute, Slovak Academy of Sciences for his help and collegial encouragement as I struggled to learn about the physics of continuum emission in novae. I would like to thank Dr. Wesley Traub, Chief Scientist of the Navigator Program at NASA's Jet Propulsion Laboratory and Project Scientist for the Terrestrial Planet Finder Coronagraph, who helped me to formulate my thesis and made it possible for me to obtain

the first science data from the Keck Interferometer Nuller. His general benevolence helped me survive some pretty rough spots, too.

I am grateful to Mr. Gerald L. Van Deusen, my high school biology teacher. His love of science and deep respect for nature had a very strong influence on me early in my life. I would also like to thank Dr. Marc Lacasse for his help with instrument engineering issues on Mt. Hopkins and Dr. Ben Lane of the Massachusetts Institute of Technology and Prof. John Monnier of the University of Michigan for their help and guidance in the analysis of early data on the nova RS Ophiuchi. I would like to thank Charles Bennett, Professor of Physics and Astronomy at The Johns Hopkins University and PI of the Microwave Anisotropy Probe, Dr. Matthew Greenhouse, deputy project scientist for the James Webb Space Telescope at NASA/GSFC and Dr. John C. Mather, PI of the Cosmic Background Explorer/FIRAS and senior project scientist for JWST for their early encouragement of my thoughts of going back to graduate school in astrophysics and to Dr. William R. Oegerle, Director of the Astrophysics Science Division, NASA/GSFC for our many productive talks.

I would like to thank the many scientists, engineers and technicians who designed, built and maintained the several observatories that I used to get the data I needed for this research. I have personally experienced many of these jobs and I know how terribly difficult it can be! With the greatest possible humility I would like to extend my very real gratitude to these colleagues - many of whom are unknown to me - for their countless hours of hard, quite often thankless, work.

I want to thank — no! to *praise*! — my family for their steadfast support. They were always there for me and helped me to face the many grim months I spent on the mountain struggling to obtain my thesis data. That was awfully hard for all of us, but we survived!

Lastly, and most importantly, I want to thank my kids;

Madeleine, whose love of life is a very real inspiration, and

Finnian, who tried to be good.

For Rebecca

Contents

Abstract **ii**

Acknowledgements **iv**

List of Tables **xi**

List of Figures **xii**

1 Introduction **1**

2 The Technique of Long-baseline Stellar Interferometry **11**
2.1 Young's Experiment 12
2.2 Beam Combination 14
2.2.1 A Mathematical Introduction 14
2.2.2 Visibility 20
2.2.3 Beam Combination Methods 23
2.2.4 Multiple Baselines and Closure Phase 26
2.3 Interferometric Observatories 28
2.3.1 The Infrared and Optical Telescope Array 28
2.3.2 The Palomar Testbed Interferometer 32
2.3.3 The Keck Interferometer Nuller 33
2.4 Mathematical Nulling Interferometry 38

3 The Recurrent Nova RS Ophiuchi **42**
3.1 Taxonomy RS Oph 43
3.2 Interferometric Observations of RS Oph
- Epoch 1 47
3.2.1 Observations 49
3.2.2 Analysis 52
3.2.3 Discussion 55

3.3 Interferometric Observations of RS Oph - Epoch 2 . . . 57
3.3.1 Observations . . . 58
3.3.2 Analysis . . . 60
3.3.3 Discussion . . . 64
3.4 On the Distance to RS Oph . . . 73
3.4.1 The Historical Record . . . 74
3.4.2 Epoch 2006 . . . 82
3.4.3 Outstanding Issues and a Distance Estimate . . . 88
3.4.4 Suggested Observations to Resolve the Distance Issue . . . 92
3.5 Conclusion . . . 93

4 Observations of RS Oph with the Keck Interferometer Nuller 96
4.1 The Keck Interferometer Nuller . . . 98
4.2 Observations . . . 101
4.3 Data and Analysis . . . 105
4.4 A New Physical Model of the Recurrent Nova . . . 123
4.4.1 Luminosity Evolution . . . 133
4.5 Supporting Evidence for the Proposed Dust Creation Paradigm . . . 140
4.5.1 *Spitzer* Observations . . . 141
4.5.2 Discussion of *Spitzer* Observations . . . 143

5 The Continuum of RS Oph 151
5.1 Symbiotic Stellar Systems . . . 152
5.2 The Continua of Symbiotic Stellar Systems . . . 157
5.2.1 Methodology for Analysis of Continua . . . 158
5.3 Analysis of the Continuum of RS Oph . . . 170
5.3.1 Fitting the SED . . . 172
5.3.2 On the Detection of Dust . . . 181
5.3.3 Implications for the KIN Outer Spatial Regime Data . . . 187
5.3.4 Evolution of the Spectral Energy Distribution . . . 189
5.3.5 Summary of the Continuum Analysis . . . 194

6 Stellar Masses from Spectroscopy and Interferometry 195
6.1 The Importance of Stellar Mass and Luminosity . . . 196
6.2 Scientifically Interesting Binary Stars . . . 199
6.3 The Astrometric Observing Program . . . 203
6.4 An Approach to Determination of Mass . . . 204
6.5 A Brief Review of Radial Velocity Orbits . . . 207
6.6 Measurement Error and Derived Stellar Parameters . . . 213

6.6.1 Line Blending 214
6.6.2 Starspots 215
6.7 The M-dwarf binary Gliese 268 217
6.7.1 Orbital solution 226
6.7.2 Model Testing 230
6.7.3 Conclusion 232

Bibliography **233**

Vita **253**

List of Tables

3.1 Epoch 1 interferometer observing log for RS Oph 49
3.2 Epoch 1 model fit parameters for RS Oph 53
3.3 Epoch 2 interferometer observing log for RS Oph 59
3.4 Epoch 2 elliptical gaussian model fits 61
3.5 Distance determinations for the recurrent nova RS Oph 87

4.1 KIN observing log for RS Oph 102
4.2 RS Oph model fitting results 107
4.3 Mid-infrared *Spitzer* line list: N-band 113
4.4 Continuum-normalized KIN emission source identification 114
4.5 Post-outburst evolution of the white dwarf star in RS Oph 134

6.1 Program stars 205
6.2 Orbital and binary elements of GL268 228
6.3 Physical parameters of the GL268 system and individual components 229

List of Figures

2.1 Thomas Young's experiment 13
2.2 Schematic representation of an interferometer 15
2.3 Corrugated interferometer acceptance pattern 18
2.4 Polychromatic fringe coherence 19
2.5 UV coverage of Keck Interferometer 20
2.6 Sample visibilities using the Keck Interferometer 21
2.7 Beam combination methods 23
2.8 Fiber beam combination 25
2.9 Closure phase 27
2.10 IOTA Observatory 29
2.11 IOTA baseline configuration 30
2.12 IOTA spatial frequency coverage 30
2.13 IOTA infrared optical beam train 31
2.14 PTI Observatory 33
2.15 PTI Observatory diagrammatic layout 34
2.16 PTI Observatory optical beam train 35
2.17 The Keck Interferometer Nuller 36
2.18 The KIN schematic layout 36
2.19 KIN interferometric chopping example 37

3.1 Epoch 1 IOTA visibilities for RS Oph 51
3.2 Epoch 1 IOTA closure phases for RS Oph 52
3.3 Epoch 2 χ^2 surfaces of 5 epochs of interferometric data 62
3.4 Epoch 2 Gaussian emission model size variation 63
3.5 Epoch 2 PTI measurements of NIR fluxes of RS Oph 67
3.6 Epoch 2 temporal variation of the mass of the NIR emission source . 69
3.7 Distances to RS Oph 90

4.1 Continuum models of RS Oph using KIN data 106
4.2 KIN data compared to *Spitzer* data 109

4.3 *Spitzer* data for three RS Oph epochs 111
4.4 KIN spectrum line matching 119
4.5 RS Oph 2006 lightcurve 121
4.6 Dust creation model 124
4.7 Model sublimation radius of dust 126
4.8 Model temporal variation of red giant star temperature 128
4.9 Spiral dust nebula model for RS Oph 129
4.10 Model temporal variation of V-band luminosity of RS Oph 132
4.11 *Spitzer* IRS spectra of silicates 141
4.12 *Spitzer* IRS spectra of silicates on 2006 Sep 9.8 142
4.13 *Spitzer* spectra on 2006 Sep 9.8 with 2MASS data 143
4.14 *Spitzer* spectra with linear continuum removed 145

5.1 Roche Lobe overflow - conceptual 153
5.2 Roche Lobe overflow critical equipotential 154
5.3 Stellar wind capture 155
5.4 Initial KIN continuum fit 174
5.5 KIN continuum with maximum HSS temperature 176
5.6 KIN continuum with best-fit HSS temperature 177
5.7 $H\alpha$ line profile on day 1.38 post-outburst 178
5.8 $H\alpha$ line profile on day 12.4 and 15.3 post-outburst 179
5.9 Asymmetric shock in early radio images 180
5.10 Hauschildt model of RS Oph RG 181
5.11 Model of RS Oph RG with dust fit to photometry 182
5.12 Model SED for KIN spectrum 183
5.13 Dust continuum model fit to *Spitzer* data 184
5.14 Model SED for KIN spectrum 185
5.15 Dust temperature 186
5.16 Continuum variation in RS Oph 190

6.1 Orbital elements 210
6.2 Velocity orbit of GL268 with ELODIE velocity points 220
6.3 IOTA observations of GL268 222
6.4 Physical orbit of GL268 226
6.5 Astrophysical model compared to measured GL268 data 230

Chapter 1

Introduction

The principle methods of astronomy are the measurement of the colors of light from distant objects and the imaging of those objects. We can draw inferences about their composition and motion through study of their color — a proxy for their temperature. We may probe the spatial distribution of their emitting material through imaging. Due to the immense distances and often intrinsic faintness of astronomical objects, the principle characteristic demanded of the scientific instrument used for the measurement of color is raw light-gathering power. For imaging, resolution. The more precise our knowledge about the spatial distribution of matter in and color of distant objects, the better we are able to postulate models of their underlying physics and test them against observation to determine the soundness of our understanding. In general terms, the larger the telescope aperture the greater its light grasp and ability to resolve spatial detail. Modern astronomy, however, is reaching the practi-

cal limits of a monotonic increase in pupil sizes of filled-aperture telescopes — both terrestrial and spaceborne. Clearly, new scientific techniques must be developed if we are to continue to advance our knowledge of the Universe beyond what we posses in the current epoch. The coherent interference of beams of light from a single source gathered by separated apertures (stellar interferometry) is one such tool. This thesis explores this technique as applied to the study of the recurrent nova, RS Ophiuchi (RS Oph), and the characterization of several low-mass stellar sources including the M dwarf binary, Gliese 268.

In Chapter 2 of this thesis, we introduce the basic theory of interferometry and develop it from first principles as illustrated by Young's double-slit experiment conducted at the dawn of the 19th century. We briefly discuss beam combination techniques used in interferometry in general and motivations leading to the development of new instruments in the current epoch. We present a mathematical approach to the fundamental combination of electromagnetic fields and a mathematical description of the interferometric techniques used in this thesis. In particular, we develop the mathematical description of a new nulling technique that exploits the destructive interference of light for the study of the faint environs of bright, distant astronomical sources. This nulling technique has been developed for the detection of Earth-like planets around nearby stars for NASA's flagship Terrestrial Planet Finder Mission and ESA's Darwin space mission.

Novae are important probes of stellar astrophysics. Several different types of

phenomena are taxonomized as novae — dwarf, classical, recurrent, and supernovae — with defining characteristics peculiar to each. Recurrent novae, in particular, are important for the study of stellar structure and evolution, as their repeating nature provides an ideal opportunity for the progressive adjustment of theoretical models toward agreement with new observations and discovery of underlying physical causes. Modern models of classical and recurrent novae suggest that these phenomena occur in symbiotic binary stellar systems. Symbiotic systems are thought to consist of a cool, post-main-sequence giant and a compact star in orbit about their common center of mass. The principal interaction between the stellar components, aside from their mutual gravitational attraction, is in the transfer of mass from the giant secondary star to the compact primary star. A great deal of energy is liberated in this process, and theory tells us that under certain conditions — when the primary component is a burned-out stellar core supported solely by electron degeneracy pressure and its mass exceeds a particular theoretical limit — it and the entire binary system will be completely destroyed in a colossal explosion called a Type-Ia Supernova. The primordial fireball that created the Universe approximately 13.7 billion years ago created only the very lightest elements. Supernovae are thought to be one of the principle engines of the nucleosynthesis of most of existing heavy elements including those condensed into rocky worlds such as our own. Theory suggests that recurrent novae may be progenitors of this type of supernova and, consequently, are of immense scientific interest. Most of the literature regarding novae phenomena is dominated by

the analysis of spectroscopic data alone, any spatial structure put forward as a basis of argument not being directly testable. Interferometric techniques, such as those described in this thesis, permit us to *directly* observe the distribution of matter in novae and have the potential to radically improve our theories about their underlying physics.

On the occasion of the 2006 outburst of the nova RS Oph an unprecedented array of astronomical instruments were used to observe this archetypical recurrent nova. In Chapter 3 we present the results of our spectroscopic and long-baseline interferometric campaign of observations of the nova RS Oph using four different observatories: The Infrared and Optical Telescope Array (IOTA), the Keck Interferometer, the Palomar Testbed Interferometer (PTI) and the Spitzer Space Telescope. Our experience suggests that many calculations and values derived from these measurements are quite sensitive to the distance to the emitting source. Historically, the distance to RS Oph has fallen in the range of 0.5 to >5 kpc with distances at the low end of this range derived during later epochs. In the final section of Chapter 3, we survey all of the pertinent literature prior to 2006 and review the various approaches taken to determine these distances. We report current analysis in the literature and discussions amongst colleagues with immediate involvement in both observation and theory in the current epoch. We also offer recommendations for further measurements and calculations to be undertaken to put bounds on the distance. In addition, we suggest that any future determination of distance be given as a range rather than as a specific number due

to its thoroughgoing effect on other calculations. Lastly, we report that for the 2006 epoch outburst of RS Oph, our derived distance is $d_{RS\ Oph} = 1.4^{+0.6}_{-0.2}$ kpc.

In Chapter 4 we report observations of RS Oph using the Keck Interferometer Nulling (KIN) Instrument, approximately 3.8 days after the most recent outburst that occurred on 2006 February 12. These observations and analyses represent the very first scientific results from the KIN instrument. In this instrument, light is gathered at the pupil of each of the Keck I and Keck II telescopes, the largest optical telescopes in the world, and is interferometrically combined in the mid-infrared. This new nulling technique is the sparse-aperture equivalent of the conventional coronagraphy used in filled-aperture telescopes. In this mode the stellar light itself is suppressed by a destructive fringe, effectively enhancing the contrast of the circumstellar material located near the star. By fitting the unique KIN data, we obtained the angular size of the mid-infrared continuum of 6.2, 4.0, or 5.4 milliarcseconds (mas) for a disk profile, gaussian profile (FWHM), and shell profile, respectively. The data show evidence of enhanced neutral atomic hydrogen emission and atomic metals, including silicon located in the inner spatial region near the white dwarf (WD) relative to the outer region. Nebular emission lines and evidence of hot silicate dust are located in the outer spatial region (centered at approximately 16.7 astronomical units [AU] from the WD) that are not found in the inner region. Our analysis suggests that the emissions were excited by the nova flash in the outer spatial region before the blast wave reached it. These identifications support the interpretation that the dust

appears to be present between outbursts. It is important to note that most models of the interaction between recurrent novae and the circumbinary medium in which they are embedded support the theory that dust — amorphous or crystalline aggregates of complex molecules — are created by the interaction of the blast wave initiated by a nova event with the stellar wind of the companion star. Data and calculations conducted in the context of this thesis suggest that this basic model may be incomplete or incorrect. We discuss the observations in terms of a new, unifying model of the system that includes an increase in density in the plane of the orbit of the two stars created by a spiral shock wave caused by the motion of the stars through the cool wind of the red giant star.

In Chapter 5 we outline the basic physics of symbiotic stellar systems and describe how this may manifest itself in the continuum emissions of such systems. Subsequently, we describe our current understanding of the components of the RS Oph recurrent nova system in quiescent and active states. We further detail observations we conducted to ascertain aspects of the RS Oph continuum and a methodology to disentangle the various continuum features such that they may be examined separately. Finally, we describe the interface of this process with the interferometric measurements conducted using the *Keck Interferometer Nuller* and high-spectral-resolution measurements using the *Spitzer Space Telescope* to determine what those measurements tell us about the astrophysics of the stellar system and, in the case of the KIN instrument, what the results tell us about this new technique.

Binary stellar systems are also quite important for the advancement of scientific theories of stellar evolution. Historically, the measurement of radial velocities through the Doppler Effect in multiple stellar systems has proven invaluable for obtaining information needed for these theoretical models. Specifically, the dynamical behavior of binary systems of stars are apt to a relatively simple physical central force model using opposite tangential velocities that can be measured spectroscopically. These particular systems of stars constitute astrophysical laboratories that allow the determination of critical stellar parameters such as the absolute mass of the components. In some favorable cases, stars in multiple systems may eclipse one another. This simple geometry allows us to derive precise information about the stellar radii of the components — a very sensitive diagnostic for evolution. Intrinsic luminosities may also be deduced, which, when combined with the masses and radii, provide important constraints to test our knowledge of stellar evolution. When the orbits are not edge-on, the unknown projection factor — the inclination angle between the plane of the orbit and the tangent plane of the sky — prevents us from determining the absolute mass directly unless the projection factor can be determined in some other way. Even so, masses are then sensitive to how accurately that angle is measured. Certain classes of stars for which few eclipsing cases are known suffer a penalty in accuracy with errors that can sometimes exceed 10% or 20% in the mass. This means that models for such stars are poorly constrained by observations. Recent advances in stellar long-baseline interferometry allow the possibility of extremely precise astro-

metric measurements of the motion of binaries in the tangent plane of the sky. In particular, the inclination angle can be determined to high precision. When taken together with radial velocity observations, these orthogonal observables may be integrated into a global least-squares orbital solution that allows for the determination of stellar characteristics with uncertainties small enough to be useful for testing models. These observations, as compared with theoretical models, are essential to improving our knowledge of the physics of stars.

As part of this thesis research, we pursued an intensive astronomical observing campaign using the IOTA instrument that employed 3, 0.5 m telescopes on 10 – 38 m baselines at the F. L. Whipple Observatory on Mt. Hopkins, Arizona. We utilized the observational methods outlined in Chapter 2 to obtain high-angular resolution astrometric data of the nova and several low-mass binary stellar systems using this experimental long-baseline near-infrared stellar interferometer. IOTA was one of only three facilities worldwide that were capable of obtaining the closure phase of a source brightness distribution. This interferometric observable, which requires a minimum of three telescopes (hence three baselines) and is mathematically independent of instrumental and atmospheric phase, was essential in obtaining measurements of a caliber that made this research possible. In the course of work culminating in this thesis, we obtained valuable experience working with the experiment and have secured many high-quality measurements of thesis objects as part of this vigorously active observing campaign. These observations were some of the last conducted using this facility, as

it was decommissioned and disassembled shortly after completion of our campaign.

In Chapter 6 we report scientific results from the first of these low-mass objects. In this chapter, we review interferometric and radial velocity observations of the M-dwarf binary GL268 and calculations leading to masses of the constituent stars with uncertainties of 0.5%. The total mass of the GL268 system is $0.4182 \pm 0.0020 M_{\odot}$ (0.5%). The masses of the constituent stellar components are $0.2259 \pm 0.0011 M_{\odot}$ for component A and $0.1923 \pm 0.0009 M_{\odot}$ for component B. The system parallax is determined by these observations to be $0.1594 \pm .0039$ arcsec (2.4%) in agreement with Hipparcos. The absolute H-band magnitude of the component stars are 7.65 ± 0.08 and 8.19 ± 0.08 for GL268A and B, respectively. These masses are amongst the most precise ever measured for visual binaries of any luminosity class or spectral type.

We begin with a hypothesis; we can understand the Universe.

Owing to our ancient ancestry as a species, we are hobbled by our limited physical senses – senses evolved for our survival on this one small planet, in this one brief epoch in time. Yet we are emboldened by our will to know! A direct expression of this is found in our determination to build ever more complex – often fragile – tools with which to explore. This is an important and exciting time to be in astronomy. At the beginning of the 21^{st} century, new technologies are opening a vast discovery space for human exploration. This thesis offers the briefest sketch of one such tool and some new measurements we have conducted with it. The study of the natural history of the Universe is perhaps our species greatest endeavor. Our will to know is part of us. It is precisely what makes us human.

Chapter 2

The Technique of Long-baseline Stellar Interferometry

In this chapter we will provide an heuristic description of interferometry by means of a brief review of Thomas Young's experiment. We will then extrapolate this, following a derivation by Lawson (2000), to the mathematical description of a standard long-baseline stellar interferometer in which we will show, using standard nomenclature (Jackson 1998), how the electric fields of the stellar light impinging on the separated apertures of the interferometer are combined. Subsequently, we will describe beam-combination techniques and the utility of multiple-baseline instruments including how the interferometric observable, closure phase, is constructed. We will later use these mathematical formulae in Chapters 3 and 6 for our discussion of interferometric observations of the nova RS Oph (Barry et al. 2008a; Barry and Danchi

2008; Monnier et al. 2006; Lane et al. 2007), the M-dwarf binary, GL268 (Barry et al. 2008), and several other low-mass binaries assayed in our observing campaign. Following this, we will provide a succinct description of the IOTA, PTI and KIN instruments and explain how these techniques are utilized, offering a brief outline of the configuration of each facility as an illustration of the techniques discussed, with in-depth details deferred to the observation sections of the appropriate chapter.

Finally, we will show the derivation of a concise mathematical description of the KIN instrument. We utilized this particular analytical approach, described in Kuchner and Barry (2008), in a suite of software tools we developed in the context of this research to process model source brightness distributions for comparison with measurements we made of the nova RS Oph. These data represent our pathfinder effort to obtain the *very* first scientific results with this instrument and are further described in Chapters 4 and 5 and in Barry et al. (2008).

2.1 Young's Experiment

Long-baseline stellar interferometry may be understood in its simplest form through careful scrutiny of Young's double-slit experiment. This is an idealized model of a two-aperture interferometer in which the slits are analogs of separated telescopes used for gathering light. Young (1803) described an experiment in which he interposed a screen with two narrow slits between a point-like light source and a second, distant viewing screen. (See Figure 2.1.) On the second screen, Young saw a set of bands of

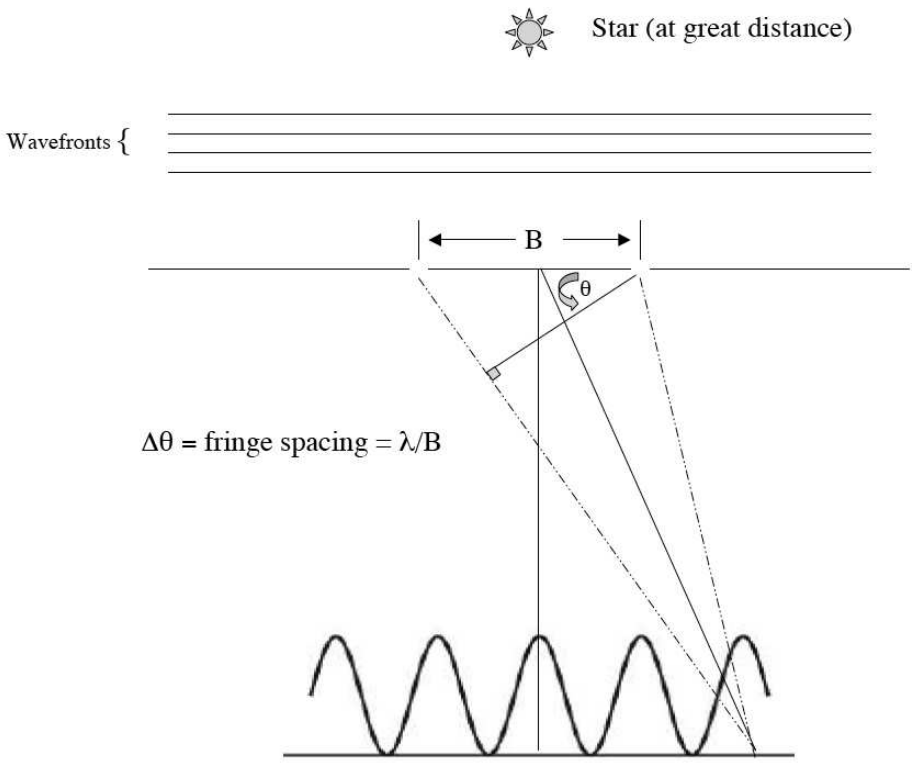

Figure 2.1 Depiction of the experiment described by Thomas Young in 1803 which illustrates the fundamental concepts of stellar long-baseline interferometry. The diagram shows the relationship between the baseline, b, and fringe spacing.

which the center one was white and the outer ones of varying color. He further described this in terms of the wave motion of light as proposed by Christiaan Huygens a century earlier and named them interference fringes. Subsequently, he used this phenomenon to determine, for the first time, the approximate wavelengths of light of differing color.

We may immediately write down the *geometric* condition for constructive interference from Figure 2.1 as

$$Fringe\ spacing = \frac{\lambda}{b}\ (rad) \tag{2.1}$$

in which b is the baseline - the distance between slits - and λ is the wavelength of light. The fringes per unit angle or fringe frequency is given as the inverse

$$Fringe\ frequency = \frac{b}{\lambda}\ (rad^{-1}). \tag{2.2}$$

These interrelationships between wavelength and baseline length are fundamental and we will come back to them to tie modern interferometers into this historic experiment.

2.2 Beam Combination

2.2.1 A Mathematical Introduction

The heuristic discussion in Section 2.1 may be put on a firmer footing through a mathematical description of a modern interferometer. Figure 2.2 depicts such an observatory. In this figure, we show two astronomical telescopes, aperture 1 and 2, separated by a baseline vector of length B. The vector $\boldsymbol{\sigma}$ describes the position of the stellar source we observe while the vectors $\mathbf{x_1}$ and $\mathbf{x_2}$ locate the telescope apertures in three-space with the baseline vector given by $\mathbf{B} = \mathbf{x_2} - \mathbf{x_2}$. For simplicity we consider monochromatic light emitted by a source at infinite distance. Consequently,

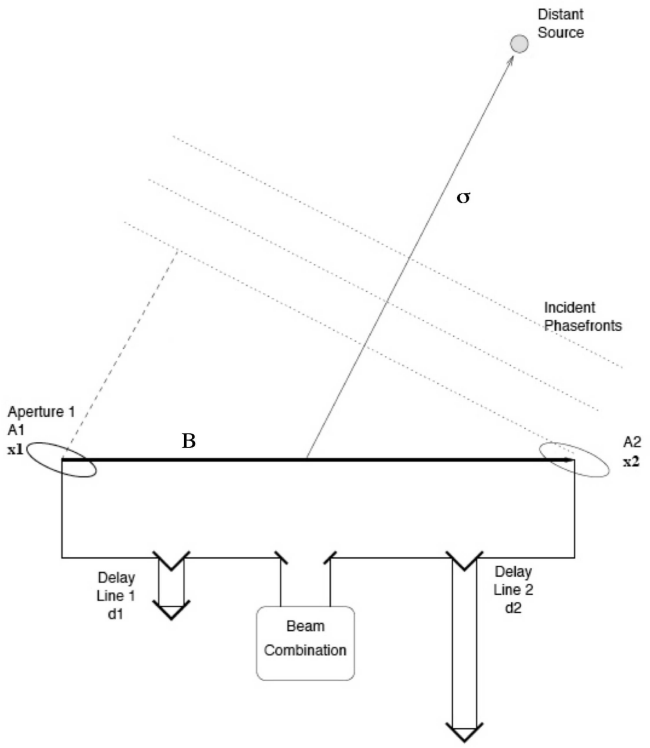

Figure 2.2 This is a depiction of a long-baseline interferometer in which the light from a distant object are gathered by two telescopes and combined at the detector. Adapted and modified from Lawson (2000).

the wavefronts are coplanar when they reach the observatory.

The plane-parallel monochromatic field, traveling radially in the direction $\mathbf{k}/k = -\boldsymbol{\sigma}/\sigma = -\hat{\boldsymbol{\sigma}}$ from the stellar object and impinging on the observatory is described as

$$\zeta = Ae^{i(\mathbf{k}\cdot\mathbf{x}-\omega t)} \tag{2.3}$$

in which ω is the frequency and $k = 2\pi/\lambda$ is the magnitude of the wavenumber $\mathbf{k}$. The phase of the monochromatic wavefronts at the two apertures are described as

$$\zeta_1 \;\propto\; e^{-i(k\hat{\boldsymbol{\sigma}}\cdot\mathbf{x_1}-\omega t)} \tag{2.4}$$

$$\zeta_2 \;\propto\; e^{-i(k\hat{\boldsymbol{\sigma}}\cdot\mathbf{x_2}-\omega t)} = e^{-i(k\hat{\boldsymbol{\sigma}}\cdot\mathbf{x_1}-k\hat{\boldsymbol{\sigma}}\cdot\mathbf{B}-\omega t)}. \tag{2.5}$$

Recalling that $\mathbf{B} = \mathbf{x_2} - \mathbf{x_1}$, absorbing the common phase term $e^{-ik\hat{\boldsymbol{\sigma}}\cdot\mathbf{x_1}}$ into a normalization, and accounting for the additional phase imparted by the instrument delay distances, d_1 and d_2 we obtain

$$\zeta_1 \;\propto\; e^{i(kd_1-\omega t)} \tag{2.6}$$

$$\zeta_2 \;\propto\; e^{i(kd_2-\omega t-k\hat{\boldsymbol{\sigma}}\cdot\mathbf{B})}. \tag{2.7}$$

Here we note that the term, $e^{-k\hat{\boldsymbol{\sigma}}\cdot\mathbf{B}}$ represents the phase delay that is a consequence of the viewing geometry. (This is referred to as the geometric delay.) In interferometry we seek to null out this added phase by changing the instrument delay distances, d_1 and d_2 so that the pathlengths are equalized.

Directly combining these fields at the square-law detector with $\zeta_{net} = \zeta_1 + \zeta_2$ yields the time-averaged power at wavelength λ as

$$P_\lambda \propto \zeta^*_{net}\zeta_{net} = \tfrac{1}{2}(1 + \sin k(\hat{\boldsymbol{\sigma}}\cdot\mathbf{B} + \phi)) \tag{2.8}$$

in which ζ^*_{net} is the complex conjugate and $\phi = d_1 - d_2$ is the total, instrumental geometric path delay.

Of particular interest in these equations are first that the time-averaged detected power varies sinusoidally with total delay, $D = \hat{\boldsymbol{\sigma}} \cdot \mathbf{B} + \phi$. Because $\hat{\boldsymbol{\sigma}}$ also describes any angle relative to the observatory, this function may be interpreted as the simplified interferometric observatory's transmission function - a corrugated acceptance pattern on the sky (Figure 2.3). This fringe pattern has adjacent crests separated by an angular distance, $\sigma = \lambda / B$. Thus we see the immediate connection to Young's double-slit experiment (Eqn. 2.1). Furthermore, from Equation 2.8 it is immediately obvious how time-averaged power varies with wavelength. This relationship is precisely what Young observed and used empirically to conduct his seminal work on the measurement of the wavelengths of different colors of light.

Equation 2.8 describes what we would measure if the light emitted by the source was monochromatic and with the additional simplification that we did not include the effect of the individual collecting apertures at A_1 and A_2 — the single-telescope beam patterns. While a single telescope beam pattern is well described by a Bessel function of the first kind, we here assume that the individual beam patterns are effectively unity which is valid for most very small sources. The addition of an explicit mathematical description will only serve to render the principal discussion obscure.

The illustration of the interferometer using monochromatic light is allowable because photons in the optical/infrared (OIR) wavelength regime do not interact and

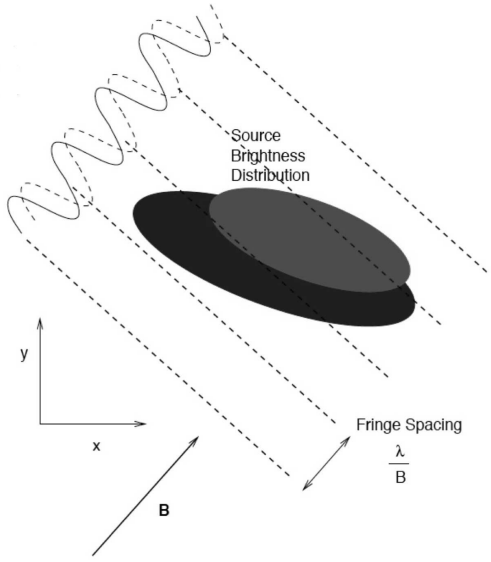

Figure 2.3 This is a depiction of a long-baseline interferometer corrugated acceptance pattern on the sky. The baseline vector **B** is also shown on the diagram to indicate that the corrugations are perpendicular to the baseline vector direction. Adopted and modified from Lawson (2000).

so we are free to posit chromatic decomposition. However, when working with real instruments and real astronomical objects, the emitted light and the instrument transmission will always have a finite bandwidth. In particular, most filters used in astronomical instruments are deliberately designed to have a bandpass that is well-described as a top-hat function with constant throughput, η, for wavelengths, $\lambda_0 \pm \Delta\lambda/2$. (For terrestrial work in the infrared regime, these ranges are specifically chosen to match the atmospheric pass-bands of water.) We derive the result by summing all wavelengths over some given passband as

$$P = \tfrac{1}{2} A(\hat{\boldsymbol{\sigma}}) F(\hat{\boldsymbol{\sigma}}) \eta \int_{\lambda_0+\Delta\lambda/2}^{\lambda_0-\Delta\lambda/2} P_\lambda \tag{2.9}$$

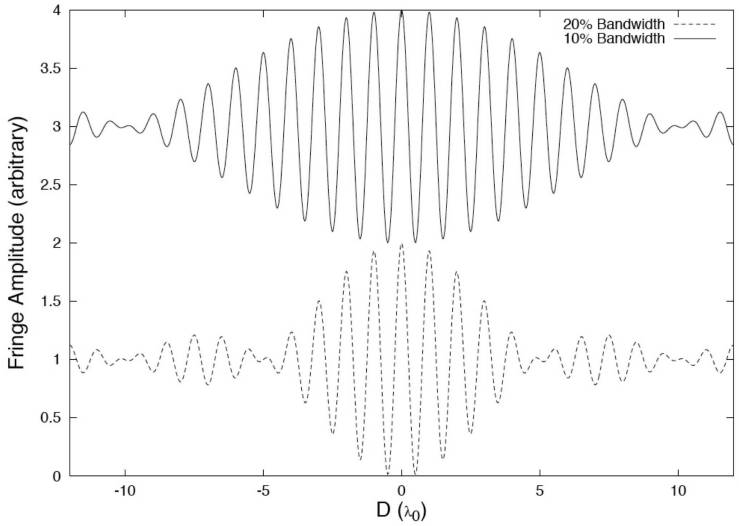

Figure 2.4 This is a depiction of the unrectified fringes modulated by a sinc function in the space of total delay, D, for two different bandwidth chromatic filters. Adapted from Lawson (2000).

assuming that the source power, $F(\hat{\boldsymbol{\sigma}})$, which may vary spatially, is approximately constant over the bandpass range. Here we give the single-aperture telescope transmission as $A(\hat{\boldsymbol{\sigma}})$ and the bandwidth, $\Delta\lambda$. The result of the integration is

$$P = \tfrac{1}{2}A(\hat{\boldsymbol{\sigma}})F(\hat{\boldsymbol{\sigma}})\eta\Delta\lambda\left[1 + \frac{\sin(\pi\Delta\lambda/\lambda_0^2 B)}{\pi\Delta\lambda/\lambda_0^2 B}\sin k_0 B\right] \tag{2.10}$$

in which k_0 is the wavenumber of the central wavelength, λ_0. We immediately recognize the expression multiplying the $\sin k_0 D$ as a sinc function. This function, which modulates the sine wave in Equation 2.8, has a characteristic scale - a coherence length - given as $\Lambda_{coh} = \lambda_0^2/\Delta\lambda$. The resulting product of the two sinusoidal functions is depicted in Figure 2.4.

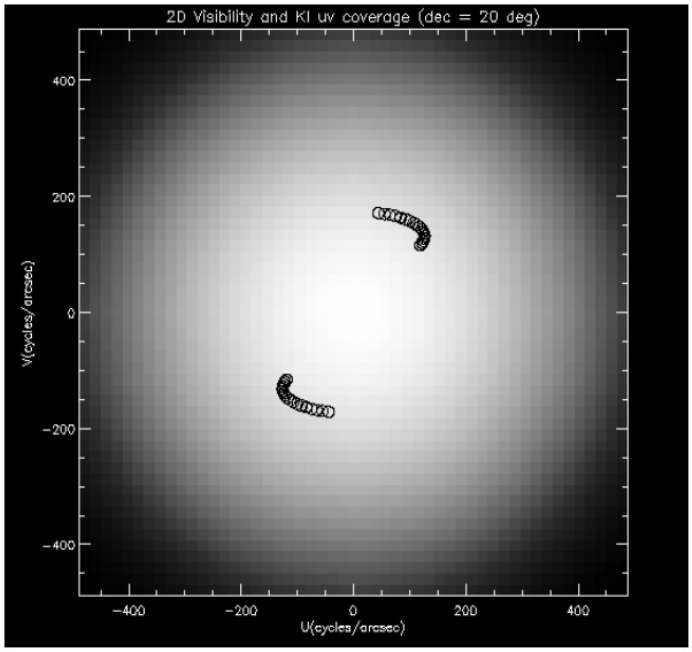

Figure 2.5 This is a depiction a simulated astronomical object represented by a 2D grayscale Gaussian source brightness distribution. Overplotted (dark circles) we show a locus of individual spatial frequencies measured by the interferometer. Adapted from http://msc.caltech.edu/software/KISupport/v2tutorial.html.

2.2.2 Visibility

The exact, quantitative relationship between the visibility, an interferometric observable, and the astronomical source structure is established by the *van Cittert-Zernike theorem* (Born and Wolf 1999). This theorem states that, given a source that has an intensity distribution on the sky $I(\boldsymbol{\sigma})$ in which $\boldsymbol{\sigma}$ is a two-dimentional sky coordinate, as in Figure 2.2, then the complex degree of coherence sampled by an interferometer of baseline, $\mathbf{B}$ will be

$$\nu = \frac{\int I(\boldsymbol{\sigma}) e^{-ik\mathbf{B}\cdot\boldsymbol{\sigma}} d\sigma}{\int I(\boldsymbol{\sigma}) d\sigma} \tag{2.11}$$

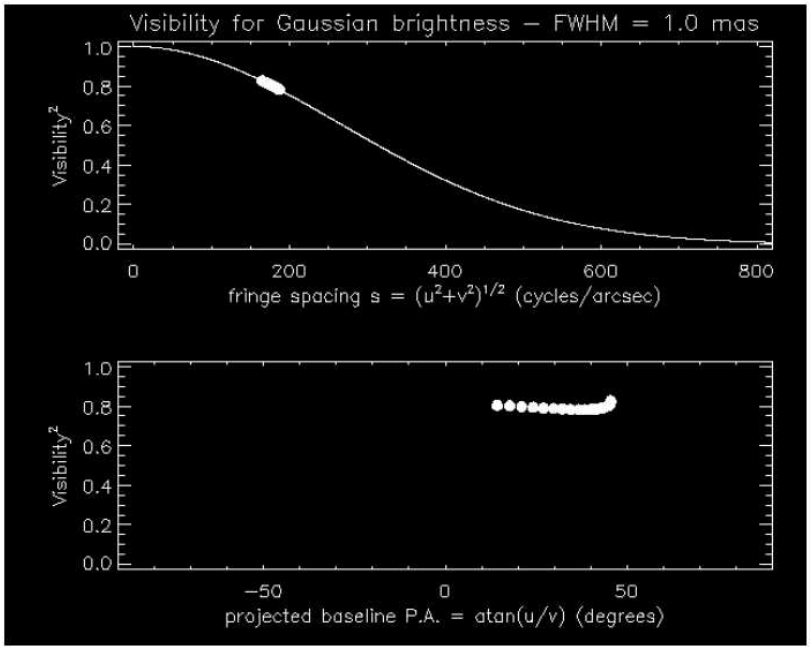

Figure 2.6 This is the visibility amplitude (V^2) curve for the object in Figure 2.5. The samples that the Keck Interferometer would take with a single 85m baseline are given as bright circles on the smooth visibility curve. The visibility amplitude is given as a function of both fringe spacing and projected baseline. Adapted from http://msc.caltech.edu/software/KISupport/v2tutorial.html.

in which k is the wavenumber. The visibility, or degree of partial coherence, is defined as the modulus of this while the phase is the argument. The visibility is usually given in interferometry as the squared modulus due to the use of power-linear detectors. Taking the dot product and expanding the term

$$e^{-ik\mathbf{B}\cdot\boldsymbol{\sigma}} = e^{-ik(\sigma_x B_x + \sigma_y B_y)} \tag{2.12}$$

Allows us to further define, as is conventional in interferometry, the *spatial frequencies*, u and v. These are given explicitly as

$$u \equiv \frac{B_x}{\lambda}, \quad v \equiv \frac{B_y}{\lambda}. \tag{2.13}$$

We illustrate the utility of this with a descriptive example adapted from tutorials on the Keck Interferometer website. Assuming that we are working with a single-baseline, standard OIR interferometer, the fundamental observable is the visibility amplitude. The instrument measures, with each observation, discrete spatial frequency components of the underlying spatial frequency spectrum of the object (c.f. Eqn. 2.11). The particular spatial frequencies sampled are functions of the wavelength and the length and direction of the projected baseline, and the location and spatial extent of the source brightness distribution as is evident from Equations 2.11 and 2.13.

Experimentally, the simple OIR interferometer just described measures individual components of the visibility function, individual (u, v) points, by forming fringes at the detector. Figure 2.5 depicts such samples being taken of a synthetic Gaussian source brightness distribution. Here we can see how the projected baseline length and direction both change with time as the Earth rotates. The contrast and phase of these fringes gives the amplitude and phase of the visibility function. These individual observations may then be plotted against fringe spacing or projected baseline as shown in Figure 2.6.

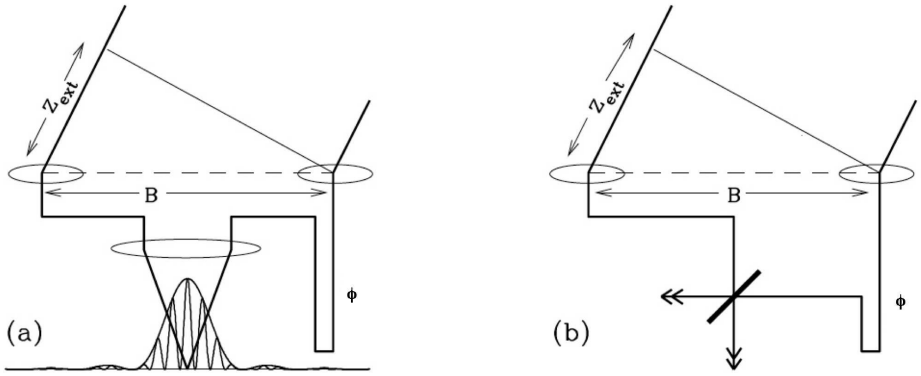

Figure 2.7 This is a depiction the two principal beam combination methods. Figure (a) gives a representation of Fizeau or image-plane combination. Figure (b) gives a schematic of Michelson or pupil-plane combination. Here $Z_{ext} = \hat{\boldsymbol{\sigma}} \cdot \mathbf{B}$ and $\phi = d_1 - d_2$ is the total instrumental delay. Adapted and modified from Lawson (2000).

2.2.3 Beam Combination Methods

In Sections 2.1 and 2.2 we presented a very basic approach to interferometry in which the beams were combined (interfered) at a screen or image-plane. This is depicted in Figure 2.7(a). This is called *Fizeau beam combination* after Fizeau who originally suggested the use of a double-aperture mask for the determination of stellar diameters (Lawson 1999). When the instrumental delay, ϕ, is adjusted such that it just matches the external delay (here $Z_{ext} = \boldsymbol{\sigma} \cdot \mathbf{B}$), the peak intensity of the constructive fringe pattern will be centered in the sinc function envelope. If ϕ is moved away from this point, the maximum in the fringe pattern will move within the envelope, which stays stationary. If we increase the bandwidth of the filter, the width of the sinc function envelope will decrease as expected (Eqn. 2.10).

We now introduce a second method in which the beams from the apertures are

combined at a pupil as shown in Figure 2.7(b). This method was given the eponym *Michelson beam combination* after Michelson's original interferometer built in 1893 which he used to prove that the speed of light is independent of the speed of the observer. This method superposes collimated beams typically within a half-silvered mirror (beam-splitter). The two output beams, which are out of phase by $\pi/2$ radians, are each focused on a single-pixel detector. The delay line is then scanned to map the variation of amplitude of the complex visibility (the intensity at the two outputs) as a function of relative delay. The effect of this combination technique is that the additional phase shift due to the half-silvered mirror changes the $+\sin k_0 B$ in Equation 2.10 to a $\pm\cos$ term. This has implications that we will revisit later in Section 2.4.

A third type of combination utilizes single-mode optical fibers to select the plane wave part of the wavefront and to interferometrically combine the wavefronts. Fibers filter the incoming wavefronts, which may be corrugated by the atmosphere or intervening imperfect optics, by rejecting wavelengths longer than the cutoff wavelength for the fiber. The cutoff wavelength is a simple function of core radius and cladding index (Harrington and Katzir 1989). Fiber combiners are formed by juxtaposing fibers such that their cores run parallel to one another with about one core diameter thickness of cladding material between them as shown in Figure 2.8. The principal mode excitation of each of these waveguides may then mix from one core to the other over this short distance thereby achieving the desired combination. Later versions of fiber

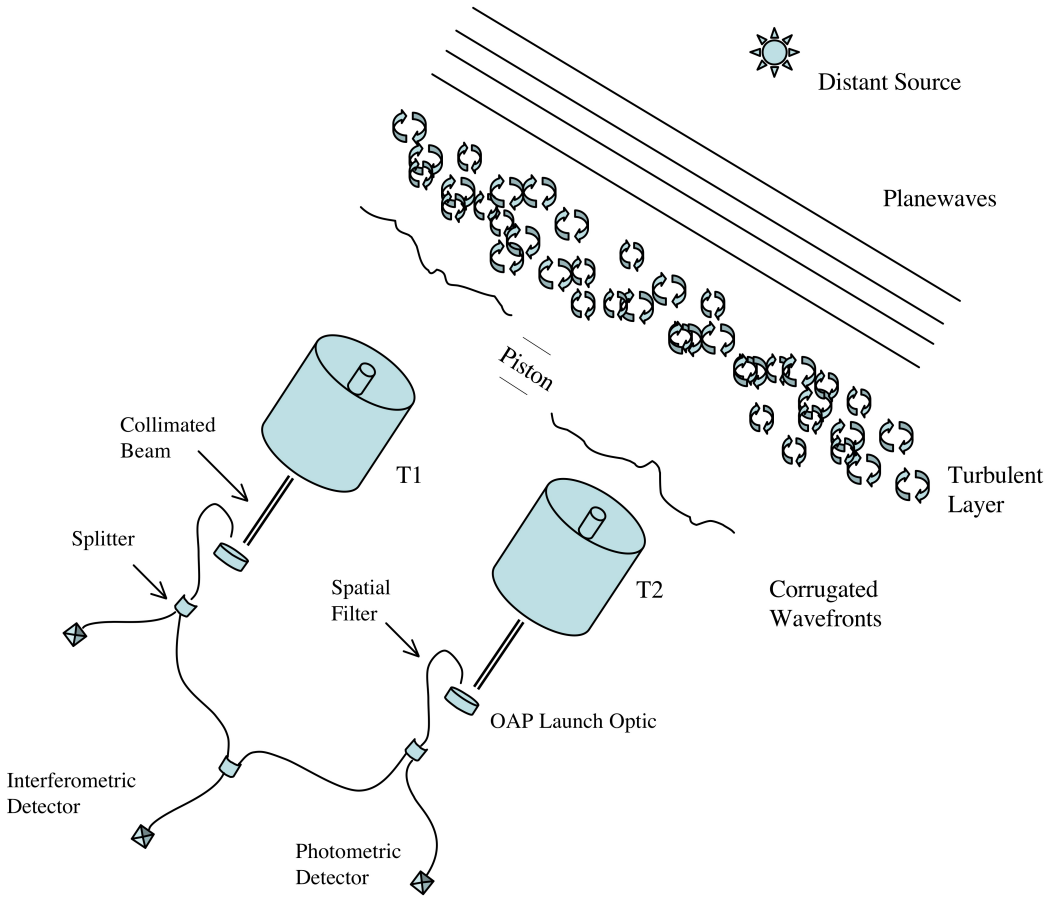

Figure 2.8 This is a simplified depiction of the combination and cleaning of stellar wavefronts corrugated by atmospheric turbulence and telescope optics. Geometric delay is not depicted but implied.

combiners accomplished this using integrated optics on which the light paths were directly etched on a substrate to better control parallelism and core-to-core distances. This fiber combiner method is usually categorized as a pupil-plane or Michelson-type combination although it does not occur at a specific plane but rather along a short distance of fiber while the fields mix. The particular advantage of this method is that when only the plane-wave component of incoming light is used in the combination process, the measured uncertainty in visibility becomes typically a full order of magnitude less than for the classical beam-splitter combiner, from a few percent with pupil or image plane combiners to $\sim 0.5\%$ (Coude Du Foresto 1998).

2.2.4 Multiple Baselines and Closure Phase

Most modern optical/IR interferometers have 3 or more telescopes, hence multiple baselines. Additional baselines increase the efficiency of observing because they allow the observer to sample several spatial frequencies simultaneously. In the case of observatories with three or more baselines, an interferometric observable called closure phase (CP) may also be constructed. The CP effectively allows the removal of phase errors induced by interaction of the light from the source with the time-varying index of the atmosphere. It can also facilitate the removal of instrument phase errors (e.g. from station-based position errors in spaceborne interferometers that rely on formation flying). To illustrate how this observable is formed, Figure 2.9 shows a simplified interferometric observatory with three apertures. Over one aperture is a

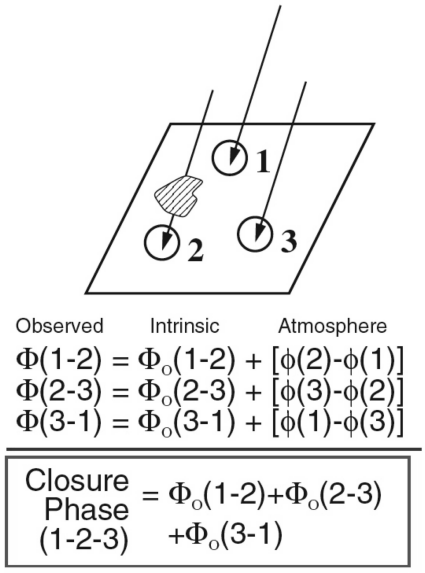

Figure 2.9 This is a depiction of how closure phase is formed. Closure phase is the interferometric observable, possible for observatories with three or more baselines, that is constructed by the summation of the phases from each baseline. The resulting term is insensitive to atmospheric phase as shown. Adapted and modified from Monnier (2003).

pocket of atmospheric gas which has a different index of refraction than that over the other two apertures. As a result, the phase of the light from the stellar source that passes through the pocket is advanced or retarded in the effected baselines relative to the other single baseline. This would normally manifest itself as an additional time-varying phase in those baselines. The CP is constructed by summing the phases of the light from each of three baselines as shown. The resulting sum cancels the atmospheric (and telescope-based) phase terms.

2.3 Interferometric Observatories

Here we give a very brief sketch of each of the interferometric observatories used during the course of thesis observations - IOTA, PTI and the KIN. We subsequently describe how the techniques outlined above are implemented at each observatory. Particulars about observations with each facility will be given in the observations sections of the appropriate chapter.

2.3.1 The Infrared and Optical Telescope Array

We conducted a large number of thesis observations at the experimental, PI-class IOTA facility at the F. L. Whipple Observatory on Mt. Hopkins near Tucson, Arizona (Traub et al. 2003). The instrument is an interferometer array of three telescope that are movable along L-shaped southeast and northeast arms, providing several different

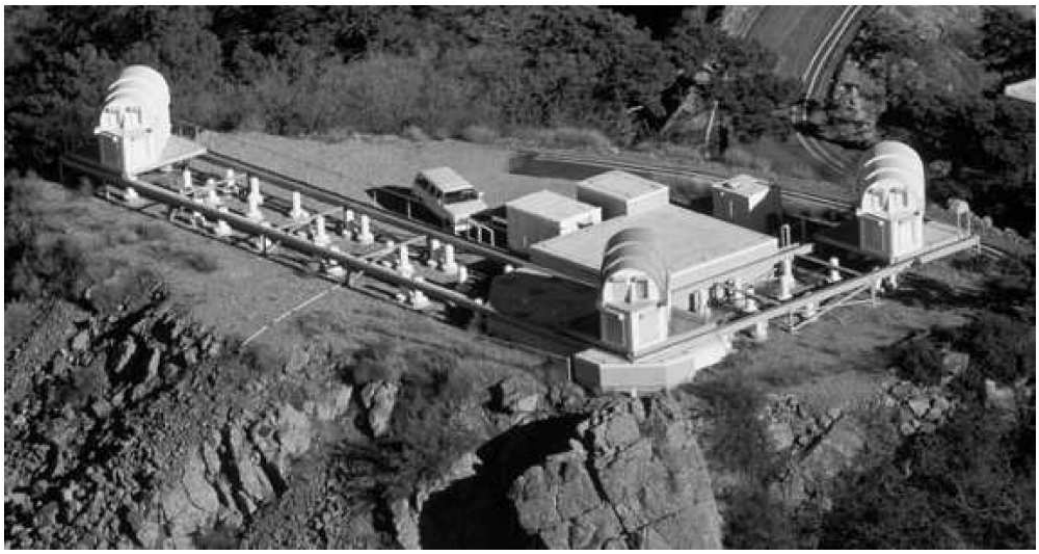

Figure 2.10 This is a photograph of the Infrared Optical Telescope Array facility at the F. L. Whipple Observatory on Mt. Hopkins in Tucson, Arizona. Adapted from Traub et al. (2003).

array configurations and having baselines from 5 to 38 m in length. See Figures 2.10, 2.11 and 2.12.

Light from each 0.45 m telescope is focused into a single-mode fiber, and the beams from the three fibers are first split then combined in pairs using integrated optics to form six fringes (Berger et al. 2003) as seen in Figure 2.13. Fringes are tracked and scanned by piezo scanners (Pedretti et al. 2004) in the delay lines and are then detected with a PICNIC camera. The instrument is capable of measuring three visibilities and one CP simultaneously over a wavelength range $\lambda = 1.5 - 2.4$ μm although we conducted all thesis observations in H-band ($\lambda_0 = 1.65$ μm, $\Delta\lambda = 0.3$ μm). This detection scheme allowed observations of stars of up to 8th magnitude in H band for precise measurements of visibilities and closure phases. All procedures

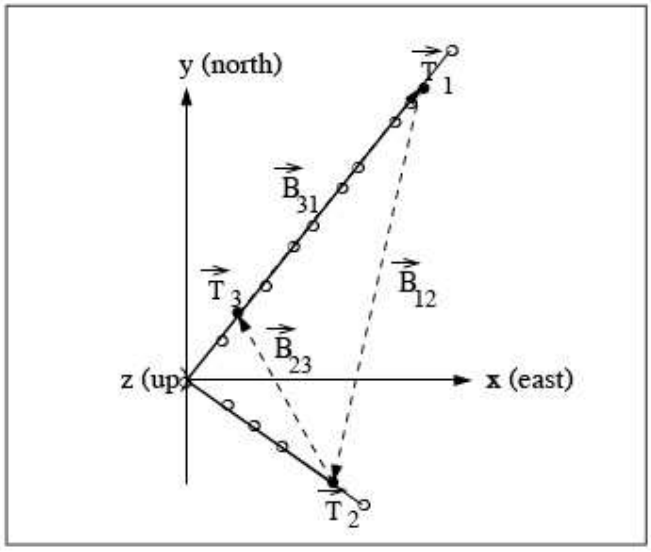

Figure 2.11 This is a depiction of the L-shaped baseline configuration of the IOTA observatory. Note that the individual telescopes may be moved along the baselines to provide changing baseline lengths and angles. Adapted and modified from Monnier (2003).

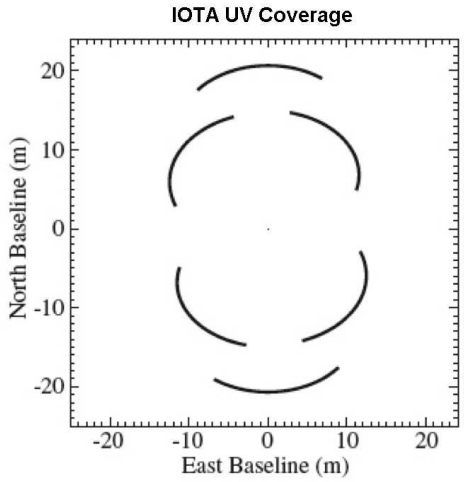

Figure 2.12 This is a depiction of the spatial frequency coverage of the IOTA instrument during the course of a typical observation. The curved lines are loci of individual *uv* points obtained by each of the three baselines. The lines are curved because the baselines change their orientation with respect to the fixed celestial sphere as the Earth rotates about its axis. Adapted and modified from Monnier (2003).

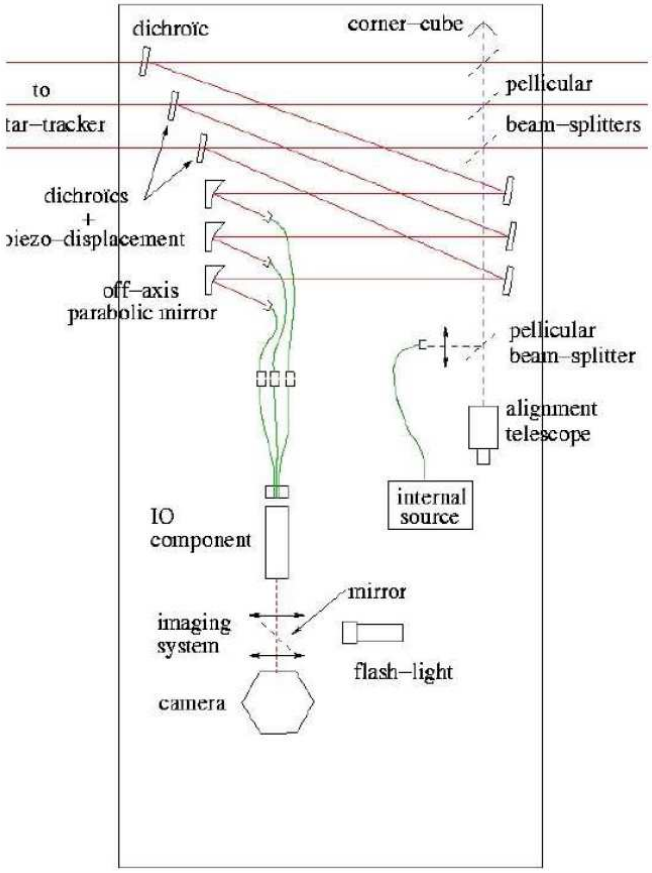

Figure 2.13 This is a schematic depiction of one of three optical tables utilized in the IOTA instrument. This is the infrared table used to scan, focus, and combine the science beams from the three 0.45 m telescopes. Adapted and modified from Berger et al. (2003).

used in the observatory including opening, optical alignment, observing, and closing procedures, were written by the author in the course of thesis observations.

2.3.2 The Palomar Testbed Interferometer

We conducted several observations at the PTI observatory. The facility, a long-baseline infrared interferometer, is located at the site of Palomar Observatory on Mount Palomar in California (Figure 2.14). It was developed by the Jet Propulsion Laboratory for NASA as a technology testbed for the Keck Interferometer (Colavita et al. 1998), which we further discuss in Section 2.3.3. PTI has three baselines; NS, NW and SW of 110, 86, and 87m length, respectively, as shown in Figure 2.15. The facility was operated as a two-element interferometer, combining light from two of the three siderostats at a time over a wavelength range $\lambda = 1.5 - 2.4$ μm. Because of this, PTI was unable to provide closure phase as did IOTA.

At PTI, light is collected by 0.4 m telescopes; each of which forms an image of the field. This image is split into primary and secondary beams by a dual-star feed and is directed through beam pipes to the central building, where they are then directed into a common long delay line (Figure 2.16). The use of a common delay line provides identical delays for the two beams and laser metrology used for servo control. The beams are then combined using a beamsplitter at a pupil-plane (Colavita 1999).

Figure 2.14 This is a photograph the Palomar Testbed Interferometer facility at Palomar Observatory, California. This picture was taken from the catwalk of the 5 m Hale telescope looking northeast. Note that the driveway and adjacent road are painted white to minimize daytime heating. Adapted from Colavita et al. (1999).

2.3.3 The Keck Interferometer Nuller

We conducted the first science observations using the Keck Nuller Interferometer instrument at the W. M. Keck Observatory on Mauna Kea, Hawaii (Figure 2.17). The KIN has one principal 85 m baseline between the two 10 m telescopes, oriented 37.7° East of North. Because of the unavailability of a chopping secondary with the Keck adaptive optics system, the KIN uses interferometric modulation to remove the thermal background. To accomplish this, the KIN divides each of the Keck telescopes into two subapertures to produce four beams on the sky. The post-telescope beam trains propagate the four resultant subaperture beams independently to the beam combiners in the observatory basement. The result is a set of baselines of two different types: long, 85 m, baselines between the corresponding subapertures on the two

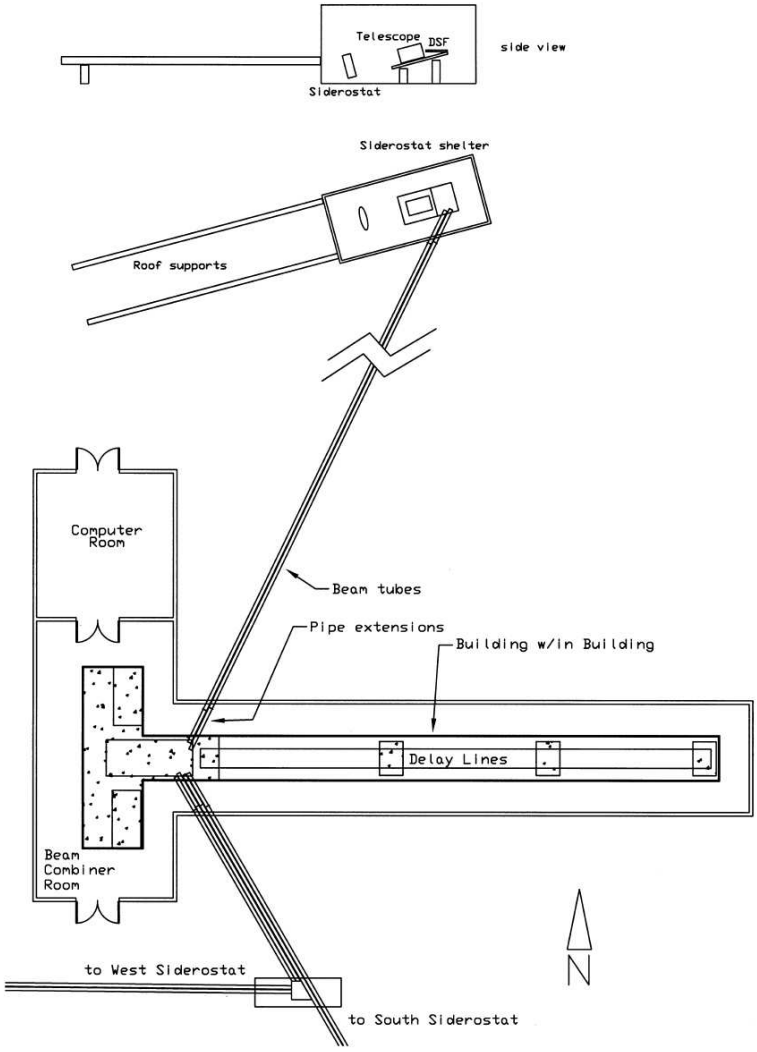

Figure 2.15 This is a schematic representation of the PTI building and overall layout. Adapted from Colavita et al. (1999).

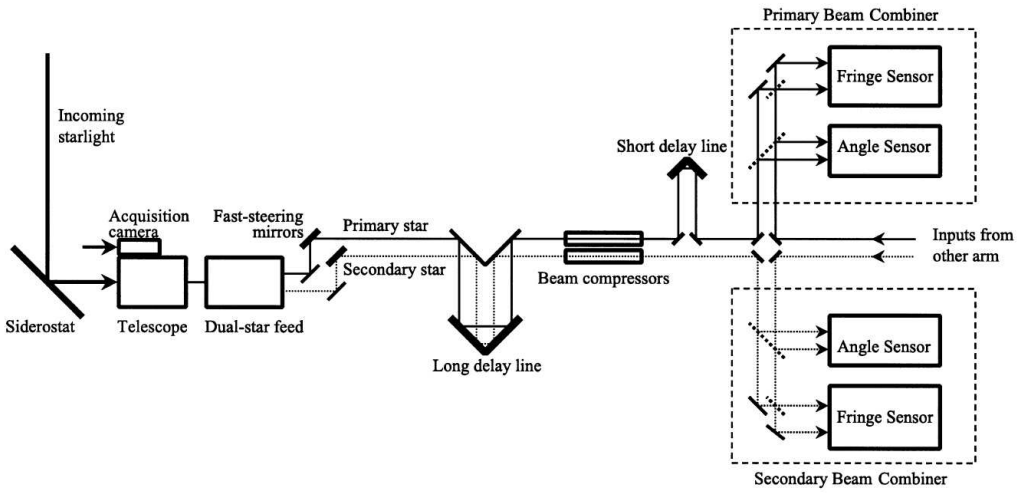

Figure 2.16 This is a schematic representation of the PTI optical beam train. Adapted from Colavita et al. (1999).

telescopes, and short, 5m, baselines between the two halves of each telescope as shown in Figure 2.18.

The stellar light from the two parallel long baselines are nulled by a pair of beam combiners, generating a destructive fringe pattern (to be derived in Section 2.4) for each subaperture pair. Then the outputs of the two nullers are fed into a pair of conventional scanning interferometric beam combiners which combine the nulled beams, creating a second fringe pattern with widely separated crests due to the relative shortness of the 5m baselines. This second fringe pattern is the standard fringe pattern for a single-baseline OIR interferometer as described in Section 2.2. After the beams are combined, they are spatially filtered by a pinhole.

Figure 2.19 is a representation of the KIN beam pattern on the sky. It displays a logarithmic contour plot of the brightness of a representative astronomical source

Figure 2.17 This is a photograph of the W. Keck Observatory on Mauna Kea, Hawaii. The Keck Interferometer and Keck Interferometer Nuller instruments combine the light from the two, 10 m apertures housed in the domed enclosures.

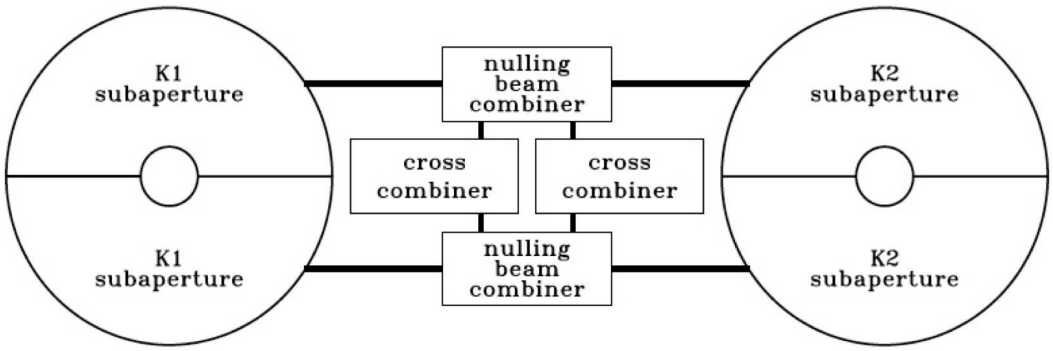

Figure 2.18 This is a schematic representation of the KIN showing the individual 10m apertures broken into two subapertures. The light is then sent directly to two nulling beam combiners and, subsequently, to cross combiners to affect interferometric chopping. Adapted from Kuchner and Barry (2008).

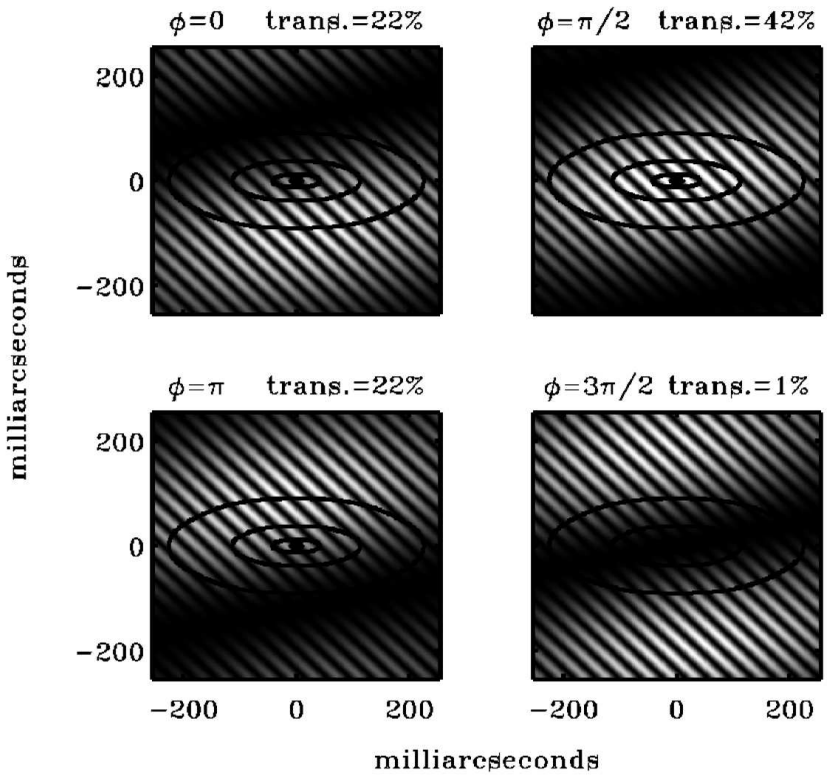

Figure 2.19 This is a computer-generated simulation of observations conducted using the KIN. The narrow dark lines running diagonally from top left to bottom right of each of the four figures is the interferometric corrugated instrument acceptance pattern of the long 85m baseline. The broad dark bands running in the opposite direction are those of the 5m cross combiner used for interferometric chopping to remove the IR background. Adapted from Kuchner and Barry (2008).

(in this case, a model exozodiacal dust cloud) and the product of the fringe patterns, together with the single-aperture power pattern, at four different values of short baseline delay. This is represented at 11.5 μm which is at the center of the N-band 10 - 13 μm atmospheric transmission window. The thin stripes are the fringes due to the long interferometric baseline and the broad bands are the fringes due to short, 5m, cross-combiner baselines. We have also indicated on this figure the percentage of the total flux from the modeled source transmitted by the combined fringe and individual telescope beam pattern. When the cross fringe phase is $\pi/2$, the transmission is maximum — 43%. But when the cross fringe phase is $3\pi/2$, 99% of the light from the centrally concentrated cloud is rejected. By chopping in this manner, the strong, variable IR background from the sky and telescope is removed.

2.4 Mathematical Nulling Interferometry

We now continue the mathematical introduction we began in Section 2.2 by providing an analytical description of the KIN instrument. We developed and utilized this particular mathematical approach, pioneered by Serabyn and Kuchner (unpublished) and described in Kuchner and Barry (2008), in a suite of software tools we developed to process model source brightness distributions for comparison with measurements made with the KIN of the nova RS Oph.

From Eqn. 2.8 in Section 2.2 we may describe the time-averaged power received by the KIN long baseline as

$$P_n(\boldsymbol{\sigma}) = \tfrac{1}{2}(1 - \cos(k\mathbf{B} \cdot \boldsymbol{\sigma})) \tag{2.14}$$

in which a negative sign is taken prior to the cosine because of the additional phase shift caused by the beam combiner when we use the destructive beam. The second fringe pattern from the shorter baselines is

$$P_{cross}(\boldsymbol{\sigma}) = \tfrac{1}{2}(1 \pm \sin(k\mathbf{B} \cdot \boldsymbol{\sigma} + \phi)) \tag{2.15}$$

in which the additional phase term, ϕ, is added because this fringe is not locked on the star but is scanned across the sky to modulate the signal so that the thermal background can be removed later. Thus, Eqn. 2.15 is the interferometric chopping term. After the beams are combined and spatially filtered by a pinhole the resulting interferometer total response is formulated as

$$R_{KIN}(u, v) = \int d\Omega \; F(\hat{\boldsymbol{\sigma}}) A(\hat{\boldsymbol{\sigma}}) P_n(\boldsymbol{\sigma}) P_{cross}(\boldsymbol{\sigma}, \phi) \tag{2.16}$$

in which $F(\hat{\boldsymbol{\sigma}})$ is the source brightness distribution, $A(\hat{\boldsymbol{\sigma}})$ is the single-telescope beam, $P_{cross}(\boldsymbol{\sigma})$, and $P_n(\boldsymbol{\sigma})$ are as described in Equations 2.14 and 2.15.

Expanding each of Eqns. 2.14 and 2.15 using de Moivre's theorem yields

$$P_n(\boldsymbol{\sigma}, \phi) = \frac{1}{2} - \left(\frac{1}{4} e^{-2\pi i \mathbf{B} \cdot \boldsymbol{\sigma}} + \frac{1}{4} e^{2\pi i \mathbf{B} \cdot \boldsymbol{\sigma}} \right), \tag{2.17}$$

and, identifying $\mathbf{B}'$ with the short baseline vector,

$$P_{cross}(\boldsymbol{\sigma},\phi) = \frac{1}{2} \pm \left(\frac{i}{4} e^{-2\pi i \mathbf{B}'\cdot\boldsymbol{\sigma} - i\phi} - \frac{i}{4} e^{2\pi i \mathbf{B}'\cdot\boldsymbol{\sigma} + i\phi} \right). \tag{2.18}$$

Taking the product of Eqns. 2.17 and 2.18 and expanding yields

$$P_n(\boldsymbol{\sigma})P_{cross}(\boldsymbol{\sigma},\phi) = \begin{array}{lll} \pm\frac{i}{16} e^{2\pi i((\mathbf{B}+\mathbf{B}')\cdot\boldsymbol{\sigma})} e^{i\phi} & -\frac{1}{8} e^{2\pi i \mathbf{B}\cdot\boldsymbol{\sigma}} & \mp\frac{i}{16} e^{2\pi i((\mathbf{B}-\mathbf{B}')\cdot\boldsymbol{\sigma})} e^{-i\phi} \\ \mp\frac{i}{8} e^{2\pi i \mathbf{B}'\cdot\boldsymbol{\sigma}} e^{i\phi} & +\frac{1}{4} & \pm\frac{i}{8} e^{-2\pi i \mathbf{B}'\cdot\boldsymbol{\sigma}} e^{-i\phi} \\ \pm\frac{i}{16} e^{-2\pi i((\mathbf{B}-\mathbf{B}')\cdot\boldsymbol{\sigma})} e^{i\phi} & -\frac{1}{8} e^{-2\pi i \mathbf{B}\cdot\boldsymbol{\sigma}} & \mp\frac{i}{16} e^{-2\pi i((\mathbf{B}+\mathbf{B}')\cdot\boldsymbol{\sigma})} e^{-i\phi}. \end{array} \tag{2.19}$$

Noting that the complex visibility may be expressed as

$$\nu = \int d\Omega \; F(\hat{\boldsymbol{\sigma}}) A(\hat{\boldsymbol{\sigma}}) e^{-ik\mathbf{B}\cdot\boldsymbol{\sigma}} \tag{2.20}$$

the response of the KIN may be reformulated by inserting Eqn. 2.19 into Eqn. 2.16, and, using Eqn. 2.20, gives

$$R_{\mathrm{KIN}}(\mathbf{B},\mathbf{B}',\phi) = \begin{array}{l} -\frac{1}{8}\nu(-\mathbf{B}) + \mathbf{\frac{1}{4}}\nu(\mathbf{0}) - \mathbf{\frac{1}{8}}\nu(\mathbf{B}) \\ \left(\pm\frac{i}{16}\nu(-\mathbf{B}-\mathbf{B}') \mp \mathbf{\frac{i}{8}}\nu(-\mathbf{B}') \pm \mathbf{\frac{i}{16}}\nu(\mathbf{B}-\mathbf{B}') \right)\mathbf{e^{i\phi}} \\ \left(\mp\frac{i}{16}\nu(-\mathbf{B}+\mathbf{B}') \pm \mathbf{\frac{i}{8}}\nu(\mathbf{B}') \mp \mathbf{\frac{i}{16}}\nu(\mathbf{B}+\mathbf{B}') \right)\mathbf{e^{-i\phi}}. \end{array} \tag{2.21}$$

Here we note that a real, astronomical source brightness distribution is positive

definite and that the Fourier transform of a positive definite pattern is Hermitian. As a result, $\nu(\mathbf{B})$ is the complex conjugate of $\nu(-\mathbf{B})$. Using this fact, we may simplify Equation 2.21 to

$$R_{\mathrm{KIN}}(\mathbf{B},\mathbf{B}^{'},\phi) = \tfrac{1}{2}[\hat{\mathbf{N}}(\mathbf{B},\mathbf{0}) \pm \mathbf{Im}\{\hat{\mathbf{N}}(\mathbf{B},\mathbf{B}^{'})\mathbf{e}^{-\mathbf{i}\phi}\}]. \tag{2.22}$$

In this equation, we identify $\hat{\mathbf{N}}(\mathbf{B},\mathbf{B}^{'})$ as the Keck Nuller Response Phasor defined as

$$\hat{\mathbf{N}}(\mathbf{B},\mathbf{B}^{'}) \equiv -\frac{\mathbf{1}}{\mathbf{4}}\nu(\mathbf{B}^{'}+\mathbf{B}) + \frac{\mathbf{1}}{\mathbf{2}}\nu(\mathbf{B}^{'}) - \frac{\mathbf{1}}{\mathbf{4}}\nu(\mathbf{B}^{'}-\mathbf{B}). \tag{2.23}$$

This equation is not the final answer as the interferometer response still has a large offset due to the thermal background. We deliberately allowed for modulation of the signal by varying ϕ in Eqn. 2.17 and, given the known scanning rate, we can detect the modulated part of the response in the presence of the background as

$$r_{\mathrm{mod}}(\mathbf{B},\mathbf{B}^{'},\phi) = \pm\frac{\mathbf{1}}{\mathbf{2}}\mathbf{Im}\Big\{\hat{\mathbf{N}}(\mathbf{B},\mathbf{B}^{'})\mathbf{e}^{-\mathbf{i}\phi}\Big\}. \tag{2.24}$$

The amplitude of the modulated part of the response is the *primary observable*. We used this particular formulation in subsequent analysis of the RS Ophiuchi data.

Chapter 3

The Recurrent Nova RS Ophiuchi

In this chapter we will introduce novae in general and show where the recurrent nova RS Oph fits into this taxonomy. Subsequently, we describe interferometric observations of the nova from shortly after peak visual brightness until 110 days later. We then give an interpretation of these data broken into two epochs: days 4 - 65 and days 40 - 110. Preliminary interpretations of the data for these two periods are somewhat different although each has merit. It is nonetheless interesting to see how they evolved as we accumulated data and were able to form a more coherent picture. While working with these data, we found that the distance to RS Oph was not well determined and that this was important to the interpretation of the data.

Motivated by these difficulties, in Section 3.4 we briefly review what is known about the distance to this object and derive a new distance estimate. In Section 3.4.1, we survey all of the literature prior to 2006 for the purpose of putting modern

calculations into historical perspective. This also provides a valuable way to show which early astronomical techniques are effective in light of current knowledge and which need to be modified or re-calibrated. In the Section 3.4.2, we report discussion of this issue in the literature and between workers with immediate involvement in observation and theory in the current epoch. In the Section 3.4.3 we discuss outstanding issues that affect our measurement of the distance and give our distance estimate for the current epoch. In the last section we make recommendations for further measurements and calculations to be undertaken to improve the precision of distance estimates.

3.1 Taxonomy RS Oph

Classical novae (CN) are categorized as cataclysmic variable stars that have had only one *observed* outburst - an occurrence typified by a Johnson V-band brightening of between six and nineteen magnitudes. These eruptions are well-modeled as a thermonuclear runaway (TNR) of hydrogen-rich material on the surface of a white dwarf (WD) primary star that, importantly, remains intact after the event. Current theory indicates that CN can be modeled as binary systems in which a lower-mass companion — the secondary — is in a long-period orbit about a WD primary such that the rate of mass transfer giving rise to the observed eruption is very low ($\ll 0.05 \times 10^{-7} M_{\odot}$, Hachisu and Kato (2001)). Recurrent novae (RN) are an important subclass of CN, which have been observed to have more than one eruption. Like

CN, RN events are well-represented as surface thermonuclear runaway (TNR) on WD primary stars in a binary system, but are thought to have much higher mass transfer rates commensurate with their greater eruption frequency. Theory tells us that this high mass transfer rate may be the result of Roche Lobe overflow or to a high wind capture rate by the WD (Warner 1995). Dwarf novae (DN) are distinct from either of these broad classes in that their eruptions, while high in frequency, are well-modeled as a sudden release of potential energy from a large clump of material as it is transfered from secondary — possibly through an accretion disk — of the primary (Warner 1976).

CN and RN produce a few specific elemental isotopes by the entrainment of metal-enriched surface layers of the WD primary during unbound TNR outer-shell fusion reactions (Warner 1995). In contrast, type Ia supernovae produce a large fraction of the elements heavier than helium in the Universe through fusion reactions leading to the complete destruction of their WD primary. Theoretical models indicate that RN could be a type of progenitor system for supernovae (Hachisu and Kato 2001). Importantly, these theories are predicated on two critical factors: 1.) the system primary must have a compact core supported solely by electron degeneracy pressure and 2.) there must be some mechanism to allow the WD mass to increase monotonically towards the Chandrasekhar limit past which equilibrium is lost and the object collapses. RS Oph is believed to be a member of this subclass of RN and we are very fortunate to have it as a nearby laboratory to advance our understanding of the

astrophysics of compact objects.

RS Oph has undergone six recorded outbursts of irregular interval in 1898 (Fleming and Pickering 1904), 1933 (Adams and Joy 1933), 1958 (Wallerstein 1958), 1967 (Barbon et al. 1969), 1985 (Morrison 1985) and now 2006. Two possible outbursts occurred in 1907 (Schaefer 2004) and 1945 (Oppenheimer and Mattei 1993). All outbursts have very similar light curves. This system is a single-line binary, cataclysmic variable with red giant secondary characterized as a K5.7 $\pm$ 0.4 I-II (Kenyon and Fernandez-Castro 1987) to a K7 III (Mürset and Schmid 1999) and a white dwarf primary in a 455.72 $\pm$ 0.83 day orbit about their common center of mass as measured using single-line radial velocity techniques (Fekel et al. 2000). Oppenheimer and Mattei studied all outbursts and found that rate of post-peak diminution of the brightness of RS Oph averaged 0.09 magnitudes/day for the first 43 days after outburst. A 2-magnitude drop would then require on average 22 days, establishing RS Oph as a fast nova based on the classification system of Payne-Gaposchkin (1957).

The most recent outburst of the nova RS Oph was discovered at an estimated V-band magnitude of 4.5 by H. Narumi of Ehime, Japan on 2006 February 12.829 UT Narumi et al. (2006). This is 0.4 magnitudes brighter than its historical average AAVSO V-band magnitude so it is reasonable to take Feb 12.829 (JD 2453779.329) as day zero. The speed of this outburst is characterized by its t_2 and t_3 times - the amount of time it takes for its brightness to drop by 2 and 3 V-band magnitudes - of 4.75 and 10.19 days, respectively.

There has been substantial disagreement concerning the distance to the RS Oph system in the literature, with a surprisingly broad range, from as close as 0.4 kpc (Hachisu and Kato 2001) to as far as 5.8 kpc (Pottasch 1967). As late as 2001, Hachisu and Kato quite thoroughly and persuasively argued for the nearer distance while analysis of X-ray data from the Rossi X-ray Timing Explorer confirmed a distance of 1.6 kpc (Sokoloski et al. 2006). This distance determination is of great importance as it effects interpretation of astrometric data (cf. Monnier et al. (2006)). Derivations of distance using reddening calculations in the nova's last epoch (Hjellming et al. (1986) & Snijders et al. (1985)) and, using envelope expansion parallaxes from new radio observations from the current epoch (Rupen et al. 2006) establish a distance at in the middle of this range. The distance to RS Oph is discussed in Barry et al. (2008) and, from this, we adopt a distance of $1.4^{+0.6}_{-0.2}$ kpc for purposes of astrometric calculations.

3.2 Interferometric Observations of RS Oph - Epoch 1

Most astronomers are familiar with classical novae, exploding stars in which an accreting white dwarf (WD) in an interacting binary system accumulates enough material for it to become unstable to hydrogen burning. The expanding blast wave from one such event, Nova Aql 2005, was recently observed with infrared (IR) interferometry (Lane et al. 2005), and the geometric distance was estimated based on velocities from spectral line observations. This result is consistent with the optically thick fireball model, which has been successfully used for nearly 20 years to explain the time evolution of the spectral energy distribution (SED) of classical novae (Gehrz 1988).

The special nature of RS Oph is thought to stem from two causes. First, the WD is likely extremely close to the Chandrasekhar limit, since the amount of hydrogen needed to trigger an outburst decreases dramatically as the WD mass increases. Indeed, detailed models indicate the WD mass is within 1% of exploding as a Type Ia supernova (Hachisu and Kato 2001). Second, the mass-losing companion for RS Oph is a red giant (RG) with a wind, providing material that accretes onto the WD and that the exploding blast wave interacts with. Bode and Kahn (1985) have produced the most successful model for recurrent novae, drawing a clear analogy to extragalactic supernovae and explaining the radio and X-ray light curves in this context.

Evans et al. (1988) were the first to study in detail the infrared (IR) time evolu-

tion of a recurrent nova. They monitored the 1-3.5 μm flux density of RS Oph for about 3 years after the 1985 eruption. They found that the flux density variation had a characteristic (2 mag) decay timescale of about 30 days and compared their observations to the predictions of the Bode and Kahn (1985) model. They concluded that their observations were consistent with emission from hot, postshock gas; this model would predict that the IR source should be seen linearly expanding at a rate of about $\sim$1 mas per day at a distance of 1.6 kpc. This distance estimate is based on the expanding size of the radio emission observed in 1985 by Hjellming et al. (1986) and Taylor et al. (1989), assuming association with the forward shock (new radio data reconfirm the 1985 observations; Rupen et al. (2006); Sokoloski et al. (2006); O'Brien et al. (2006)).

Challenging this interpretation, Hachisu and Kato (2001) recently produced a comprehensive model for recurrent novae meant to explain a wide range of the known nova properties, with a specific prediction for the origin of the near-infrared (NIR) continuum that is very different from Evans et al. (1988). Following onset of the thermonuclear runaway of the hydrogen shell around the WD, the shell expands to approximately 200 $R_{\odot}$ size, in effect turning the WD back into a red giant. The shell stably burns hydrogen for a few weeks, gradually shrinking back to the size of white dwarf with nearly constant luminosity. According to this model, hot postshock gas plays no role in forming the IR continuum. Furthermore, Hachisu and Kato (2001) prefer a much closer distance of 600 pc, implying a binary separation of 2.9 mas,

Table 3.1. Epoch 1 interferometer observing log for RS Oph

Days Since 2006 Feb 12	Date (UT)	Interferometer (Configuration)	Wavelength (μm)
4	2006 Feb 16	IOTA (A20B15C00)[a]	1.65
4	2006 Feb 16	Keck[a]	2.18
11	2006 Feb 23	IOTA (A20B15C00)	1.65
14	2006 Feb 26	IOTA (A20B15C10)	1.65
19	2006 Mar 03	IOTA (A20B15C10)	1.65
20	2006 Mar 04	IOTA (A20B15C10)	1.65
22	2006 Mar 06	IOTA (A20B15C10)	1.65
25	2006 Mar 09	IOTA (A20B15C10)	1.65
29	2006 Mar 13	IOTA (A20B15C10)	1.65
49	2006 Apr 02	PTI (NW)[a]	2.2
59	2006 Apr 12	IOTA (A20B15C10)	1.65
60	2006 Apr 13	IOTA (A20B15C10)	1.65
63	2006 Apr 16	PTI (NW)	2.2
65	2006 Apr 18	PTI (NW)	2.2

[a]We used the following calibrators for observations of RS Oph at IOTA : HD152601 (1.6 ± 0.4 mas), HD164064 (1.6 ± 0.5 mas), χUMa (3.24±0.04 mas; (Bordé et al. 2002)), ρ Boo (3.72±0.12 mas; (van Belle et al. 1999)), HD 143033 ($1.9 \pm 1.5 mas$), HD 156826 ($0.6 \pm 0.2 mas$), HD 157262 (1.5 ± 0.5). For our observation with the Keck Interferometer on 2006 Feb 16 we used the following calibrators: χUMa , ρ Boo. For our observations with PTI we used: HD 164064 and HD 161868 ($0.7 \pm 0.1 mas$).

easily detectable with current interferometers. In this research, we report first size measurements for RS Oph in the NIR using long-baseline interferometry. Our results are surprising, as they seem to contradict the expanding fireball model in which an expanding pseudo-photosphere would be expected to puff out well beyond the WD, raising doubts about the established distance to RS Oph, and motivating a new model for the NIR emission.

3.2.1 Observations

In this section we report on data from three different interferometers. A summary of our observations can be found in Table 3.1. We briefly introduce each data set.

Most of our data were obtained with the Infrared-Optical Telescope Array (Traub et al. 2003), an observatory discussed in Chapter 2, which has baselines between 5 and 38 m. The IONIC3 combiner (Berger et al. 2003) was used to measure three visibilities (V^2) and one closure phase (CP) simultaneously in the broadband H-band filter ($\lambda_0 = 1.65\mu$m, $\Delta\lambda = 0.3\mu$m). Data analysis procedures have been documented in recent papers (Monnier et al. 2004, 2006). For the data here, we have adopted a calibration error $\Delta V^2 = 0.05$ (relative error) on baselines AB and AC and $\Delta V^2 = 0.10$ for baseline BC.

The Keck Interferometer (KI) was used to observe RS Oph on a single night four (4) days after the burst (UT 2006 February 16) with a baseline of $\sim$ 85 m. Facility and instrument descriptions can be found in recent KI publications (Colavita and Wizinowich 2003, 2000). The K-band ($\lambda_0 = 2.18$ μm, $\Delta\lambda = 0.3$ μm) data reported here were the by-product of a nulling observation (being prepared for a separate publication), and the calibration sequence is somewhat modified from the standard procedures; in particular, only one ratio measurement was made per integration.

Lastly, the Palomar Testbed Interferometer (PTI) observed RS Oph on three nights in 2006 April using the K-band detection system ($\lambda_0 = 2.20$ μm, $\Delta\lambda = 0.4$ μm) with a $\sim$ 85 m baseline (oriented in a northeast direction). Detailed instrument and data analysis descriptions for PTI can be found in the literature Colavita et al. (1999). Because of the faintness of the source in April, coherent integration was used for analysis, and a large calibration error of $\Delta V^2 = 0.10$ (absolute, not relative) was

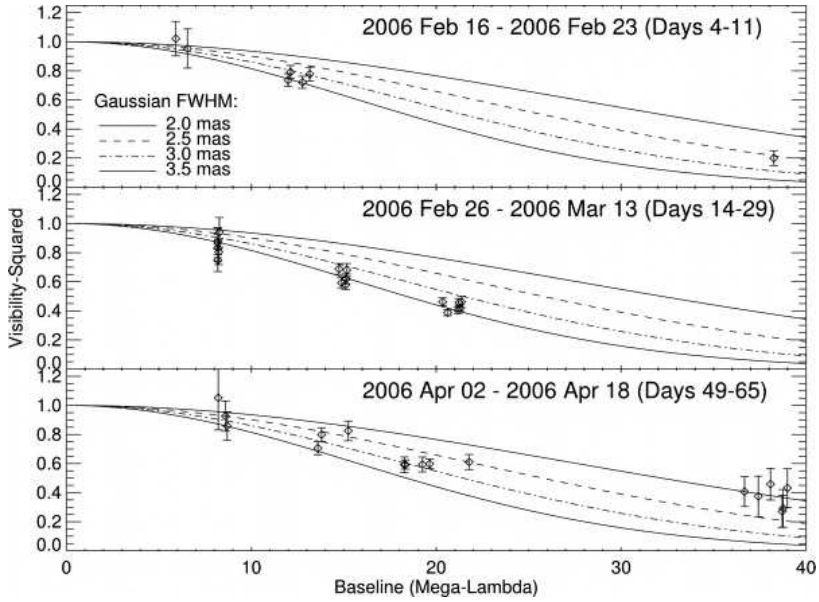

Figure 3.1 (u, v)-averaged visibility data for RS Oph split into three different time periods. The x-axis shows the spatial frequency (projected baseline in units of wavelength), while the y-axis shows the visibility-squared. Four curves representing Gaussian profiles are also included to show the characteristic size and to allow intercomparison of data in the different panels. For reference, all data shortward of 25 Mλ derive from IOTA, while longer baseline data come from KI (epoch I) and PTI (epoch III). Adapted from Monnier et al. (2006)

added in quadrature with the internal error for model fitting.

We have split the data into three epochs - from 2006 February 16 to 23 (days 4 – 11), from February 26 to March 13 (days 14 – 29), and from April 2 to April 18 (days 49 – 65). The (u, v)-averaged visibility data for each epoch are presented in Figure 3.1, along with some Gaussian profiles for comparison. The IOTA closure phase results are shown in Figure 2, also split into the three epochs. All V^2 and closure phase data are available from the authors; all data products are stored in the FITS-based, optical interferometry data exchange format (OI-FITS), described in Pauls et al. (2005).

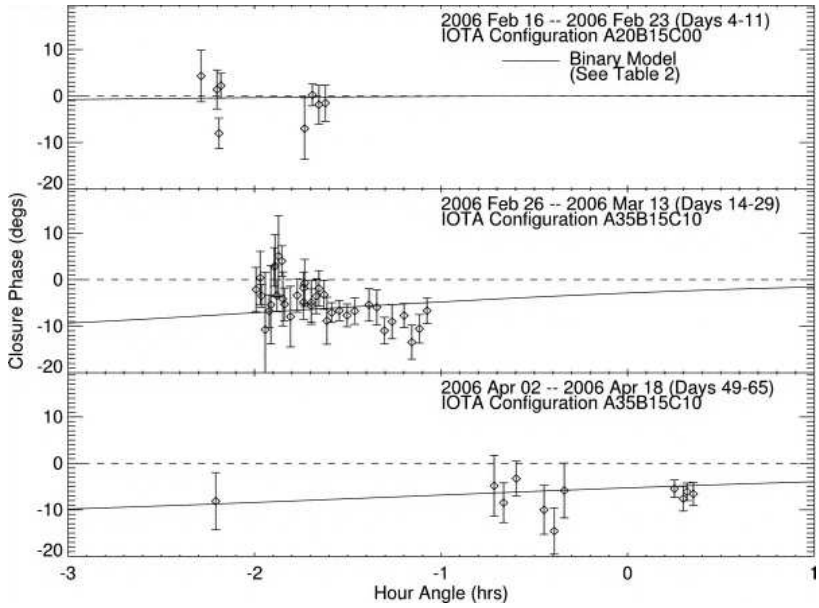

Figure 3.2 IOTA closure phase data for RS Oph split into three different time periods. The x-axis shows the hour angle, while the y-axis shows the observed closure phase. The solid line shows the expected closure phase for the binary model parameters found in Table 3.4. The dashed line shows the expected closure phase signal for the symmetric Gaussian model. Note that the binary model is a poor fit for the data. Adapted from Monnier et al. (2006)

3.2.2 Analysis

Inspection of Figure 3.1 reveals that the visibility curve for RS Oph changes very little between day 4 and 65 (since the outburst). This is surprising since the H-band brightness decreased by a factor of 110 during this time. This result is discordant with the prediction of Evans et al. (1988), who interpreted the IR light curve in terms of the time evolution of optically thick postshock gas with temperature 10^5 K moving at the speed of the contact discontinuity, 1400 km s^{-1}, following the earlier fireball model of Bode and Kahn (1985). This model predictes the IR emission will be expanding at a rate of $\sim$1.0 mas day^{-1} (assuming a distance of 1.6 kpc), an interpretation that

Table 3.2. Epoch 1 model fit parameters for RS Oph

Model Parameter	2006 Feb 16-23 (Days 4 - 11)	2006 Feb 26 - Mar 13 (Days 14 - 29)	2006 Apr 02 - 18 (Days 49 - 65)
Gaussian Profile (fit to 1.65 μm data)			
FWHM (mas)	3.3 ± 0.09	3.47 ± 0.03	2.87 ± 0.07
Reduced χ^2 V^2	0.6	1.3	1.1
Reduced χ^2 CP	1.3	3.6	5.4
Gaussian Profile (fit to 2.2 μm data)			
FWHM (mas)	2.56 ± 0.24	N/A	2.00 ± 0.09
Reduced χ^2 V^2	0[a]	N/A	1.0
Reduced χ^2 CP	N/A	N/A	N/A
Binary Model[b](fit to both 1.6 & 2.2 μm data)			
Separation (mas)	3.13 ± 0.12	3.23 ± 0.13	3.48 ± 0.23
P. A. (deg east of north)	36 ± 10[c]	45 ± 5	27 ± 5
Brightness Ratio[d]	0.42 ± 0.06	0.40 ± 0.06	0.21 ± 0.03
Reduced χ^2 V^2	0.6	1.7	1.2
Reduced χ^2 CP	1.1	1.3	0.5

[a]Only one *Keck* data point available for fitting.

[b]Brightness ratio assumed the same for H and K bands. Individual components have adopted UD diameters of 0.5 mas. Here we consider only those solutions with separations ¡ 10 mas.

[c]180° ambiguity, since closure phase data are indistinguishable from zero for this epoch.

[d]Fainter component with respect to brighter component.

is now ruled out.

Before introducing alternative models in Section 3.2.3, we discuss some model fitting to the interferometry data. Here we only consider two simple models - a circularly symmetric Gaussian, and a binary star model. For all fits and calculation of reduced χ^2 we have used the original data points.

First, we fit a circularly symmetric Gaussian to each epoch of data, for each wavelength. Table 3.2 displays the best-fitting FWHM and the reduced χ^2 for both the V^2 and CP (the model CP is always zero for a Gaussian profile). The Gaussian

model is a reasonable fit for the IOTA visibility alone but clearly cannot fit the nonzero closure phase seen in March and April. Also, Figure 1 shows that no good fit was possible when combining IOTA data with Keck and PTI data, indicating that this model is too simplistic to explain the full range of baselines and/or the wavelength dependence. Sizes derived from the longer baseline K-band data are systematically smaller than those derived from shorter baseline H-band data (IOTA).

Hachisu and Kato (2001) showed that the novas IR light curve might be due primarily to a rapid increase in brightness of the WD as it returns briefly to a red giant phase. Motivated by this work, we realized that the IR emission might be due to the underlying RS Oph binary itself, and this might explain the general puzzling features of our data: nonexpanding emission size, the inadequacies of the Gaussian fit, and the nonzero closure phase.

In order to test this idea, we fitted binary models to the data for each of the three time periods, treating the brightness ratio as independent of wavelength in order to fit the H- and K-band data together. The IOTA, KI, and PTI complement each other in Fourier coverage, and an exhaustive grid search of separations less than 10 mas found unique binary star solutions.

Table 3.2 contains the best-fit binary models for the three time periods, including the reduced χ^2(V^2, CP). All three epochs χ^2 are reasonably fit by a similar binary model. The only parameter that changed significantly between the epochs was the brightness ratio. The closure phase predictions for the binary models are plotted along

with the closure phase data in Figure 3.2. We note that our (u, v)-plane is missing coverage in the northwest direction, and thus elongated structure in this direction would be observed foreshortened.

3.2.3 Discussion

Because the expanding fireball model in Section 3.2.2 fails to explain the nearly static size scale of the IR emission, we now seek suitable alternative emission mechanisms for the time-variable IR emission from the recurrent nova RS Oph. We utilized the alternative TNR model of Hachisu and Kato (2001) and found that our three-interferometer combined data set can be explained by a simple binary model with separation of ∼3.2 mas, P.A. 30° east of north, and a brightness ratio varying from 2.5 : 1 to 5 : 1.

Binary Interpretation of Data

On the basis of single-line radial velocity data, Fekel et al. (2000) found the RS Oph binary orbit was roughly circular with a period of 455.72 ± 0.83 days and mass function $f = 0.221 \pm 0.038\ M_{\odot}$. (The mass function for a binary is defined as $f(m) = (m_2)^3 \sin^3 i/(m_1 + m_2)^2$ in which m_1 and m_2 are the masses of the primary and secondary and i is the inclination angle with respect to the tangent plane of the sky.) Red Giant (RG) stars in symbiotic systems such as RS Oph typically have masses of 1 – 3 $M_{\odot}$ (Dobrzycka and Kenyon 1994), and we expect recurrent novae to

contain a near Chandrasekhar mass WD ($\sim$1.4 $M_{\odot}$); these facts combined with the known mass function rule out RG masses greater than $2M_{\odot}$. Assuming the RS Oph system mass to be $2.4 - 3.4M_{\odot}$, we find the component separation to be $1.55 - 1.74$ AU, or (unprojected) $2.59 - 2.90$ mas at the 600 pc distance preferred by Hachisu and Kato (2001) - only slightly smaller than our observed separation of 3.2 mas.

The binary model fits (Table 3.2) show evidence for a change in the brightness ratio over time. While the Hachisu and Kato (2001) theory predicts a time-changing brightness ratio, it is beyond the scope of this chapter to test the compatibility with the observed IR light curves due to complications from the role of the irradiated RG photosphere and the presence of a post-outburst WD accretion disk.

Circumbinary Reservoir of Hot Gas

The distance estimate of 540 pc noted in the last section contrasts with other estimates more commonly adopted in the literature. The most significant constraints on distance are set by radio observations of the previous and current outburst (Hjellming et al. 1986; Taylor et al. 1989; Rupen et al. 2006; O'Brien et al. 2006). By assuming that observed radio proper motions (on the sky) can be ascribed to the fast-moving ejecta or forward shock, workers consistently derive a distance of $\sim$1600 pc. Similarly, large distances were found considering interstellar UV absorption lines (Snijders 1987a) and HI absorption measurements (Hjellming et al. 1986).

Given the strength of the evidence, we now consider the implications of the 1600

pc distance. This distance would rule out the binary interpretation of the near-IR interferometry data laid out in Section 3.2.3, given existing constraints. Instead, we hypothesize that the IR emission arises from a quasi-stationary hot gas reservoir that contributes a combination of emission lines and free-free/bound-free emission in the NIR bands. The observed FWHM of $\sim$3 mas is $\sim$5 AU at 1600 pc, about 3 times the expected RS Oph binary separation. This size is reasonable for a circumbinary disk or reservoir of hot gas, perhaps kept ionized by the outward moving blast wave or soft X-ray luminosity from the WD itself following outburst. This gas reservoir might be analogous to the fallback disk inferred to form after some supernovae (e.g., Wang et al. 2006).

Clearly, the hypothesized gas reservoir must be elongated and somewhat off-center with respect to the central source in order to fit the combined IOTA, KI, and PTI interferometry data, especially the nonzero closure phases.

3.3 Interferometric Observations of RS Oph - Epoch 2

In Section 3.2 we used long-baseline interferometry to resolve the emission from the outburst. Our evidence suggested that the IR emission is consistent with a source that is larger than the binary system. Here we report on observations of the RS Oph system using PTI, an observatory discussed in Chapter 2, on 15 nights following the

2006 outburst. We are able to resolve the emission on milliarcsecond (mas) scales and can place limits on the emission mechanism, including the possibility that the emission is from the binary components. The angular resolution provided by this long-baseline (85 – 110 m), near-infrared (1.2 – 2.2 μm) interferometer is approximately 4 mas. A complete description of the instrument can be found in Colavita et al. (1999).

3.3.1 Observations

We observed RS Oph on 15 nights between 2006 March 24 and June 13 (covering the period from 40 to 121 days after the outburst). Data from three of these nights have been previously discussed in Section 3.2, together with data from the Infrared Optical Telescope Array (IOTA; Traub et al. 2000) and the Keck Interferometer (Colavita et al. 2003) also described in Chapter 2. We include all of these observations in subsequent model fits to help constrain models of this source. In addition to the data obtained after the 2006 outburst, we present data from an observation of the RS Oph system taken on 2003 May 22, i.e., before the outburst.

For these observations PTI operated using one interferometric baseline at a time. On the 2003 night (during quiescence) and eight of the 2006 nights, RS Oph was observed using the northwest baseline, the remaining observations were done using the southwest baseline. The observing wavelength was 2.2 μm (K band; note that the IOTA data were obtained in the H band, $\lambda = 1.6$ μm, which may complicate inter-comparisons of the data sets). Observations on the first eight nights were done using

Table 3.3. Epoch 2 interferometer observing log for RS Oph

Days Since 2006 Feb 12	Date	u^a (meters)	v^a (meters)	V^2	σ
- 997[b]	2003 May 22	83.2191	20.7015	0.970	0.242
40	2006 Mar 24	83.1262	22.8196	0.126	0.050
49	2006 Apr 2	83.2183	21.2903	0.337	0.077
63	2006 Apr 16	81.0884	20.1695	0.411	0.031
65	2006 Apr 18	81.5573	19.8387	0.300	0.050
76	2006 Apr 29	80.9573	19.6682	0.459	0.029
77	2006 Apr 30	81.1711	19.9687	0.448	0.029
78	2006 May 1	49.2736	58.0854	0.366	0.058
79	2006 May 2	49.3282	58.0682	0.389	0.026
101	2006 May 24	80.2290	19.2295	0.493	0.144
102	2006 May 25	47.8541	57.7800	0.424	0.072
107	2006 May 30	46.9012	57.6591	0.556	0.074
108	2006 May 31	80.9950	19.4490	0.458	0.051
110	2006 Jun 2	45.7106	57.4739	0.485	0.094
120	2006 Jun 12	51.3773	58.3395	0.735	0.454
121	2006 Jun 13	82.8230	20.4248	0.892	0.078

[a]Projected baseline coordinates in meters.

[b]Data taken between outburst epochs.

a fringe-tracking integration time of 20 ms, but as the source faded the integration time had to be increased to 50 ms. We performed model fits to the incoherently averaged V^2data output and verified that they gave consistent answers (but with larger uncertainties).

Each nightly observation with PTI consisted of one or more 130 s integrations during which the normalized fringe visibility of the science target was measured. These visibilities were calibrated by dividing them by the point-source response of the instrument, determined by interleaving observations of a calibration source: HD 161868 (A0 V, $m_V = 3.75, \theta = 0.69 \pm 0.1$ mas). The angular diameter of the calibration source was determined by fitting a blackbody to archival broadband photometry. For further details of the data-reduction process, see Colavita (1999) and Boden et

al. (2000). The calibrated data, averaged by night, were listed in Table 3.3; although given as averages, the fits to the models were done using the individual data points.

The normalized fringe visibility obtained from an interferometer is related to the intensity distribution on the sky via the van Cittert-Zerneke theorem (Chapter 2). For simple parametric models, such as uniform disks, Gaussians, or binary sources, we use the procedure outlined in Eisner et al. (2003) to generate models that can be fitted to the observations. We perform least-squares fits of these models to the observed fringe visibilities.

It is important to note that the IOTA data in Section 3.2 indicate a nonzero closure phase; this implies that the emission is not point symmetric. However, the amplitude of the signal ($\sim 10^{\circ}$) also indicates that the degree of asymmetry is not very large on scales resolved by that interferometer at the time of the observations. PTI, when operated a single-baseline interferometer, is not able to measure closure phases and therefore any model fits will have a 180°ambiguity in position angle. We consider intrinsically asymmetric models (e.g., binaries), as well as symmetric ones - in the latter case recognizing that the model can only provide an approximation of the true intensity distribution.

3.3.2 Analysis

We find that the data can be reasonably fitted by a simple elliptical Gaussian model (Table 3.4); the χ^2_r (reduced) is further improved when the parameters are

Table 3.4. Epoch 2 elliptical gaussian model fits

Model Parameters	All PTI	Epoch 1 (day 4-11)	Epoch 2 (day 14 - 29)	Epoch 3 (day 49-65)	Epoch 4 (day 76-80)	Epoch 5 (day 101-121)
Major Axis (mas)	2.6 ± 0.9	3.2 ± 0.1	5.88 ± 0.4	2.7 ± 0.2	2.1 ± 0.23	2.0 ± 0.8
Minor Axis (mas)	1.7 ± 0.7	1.9 ± 1.3	3.4 ± 0.1	1.5 ± 0.02	2.0 ± 0.1	1.0 ± 0.4
PA (E of N)	11 ± 14	29 ± 14	127 ± 2	10 ± 42	149 ± 85	-25 ± 17
χ^2_r	1.9	1.4	2.4	4.4	1.1	1.5
Number of Points	90	22	108	52	36	33

allowed to vary slowly in time. Given that all the PTI data from any given night are limited to a single baseline, it is not possible to constrain complex models such as elliptical Gaussians on a night-by-night basis. We therefore group the available data into sets of several nights, comprising observations using multiple baselines, and fit the data for size, aspect ratio, and position angle of the long axis. Results are shown in Table 3.4 and Figure 3.3. The χ^2 surface indicates that the emission morphology first expanded in size, with a position angle (P.A.) of 120° subsequently, the orientation changes to $\sim 0°$, and the source begins contracting. The apparent angular diameter of the major axis reaches 5 mas at maximum extent, but contracts to 2 mas by day 100. It should be emphasized that these observations trace the emission and not the material itself; as discussed in Section 3.3.3, the apparent contraction does not necessarily require infall of material.

We explore the changing angular size of the emission by constraining the aspect ratio to the best overall value (major/minor =1.4) and position angle (PA $\sim 0°$) of the models and fitting for the size of the corresponding elliptical Gaussian on a night-by-night basis. The results are shown in Figure 3.3.

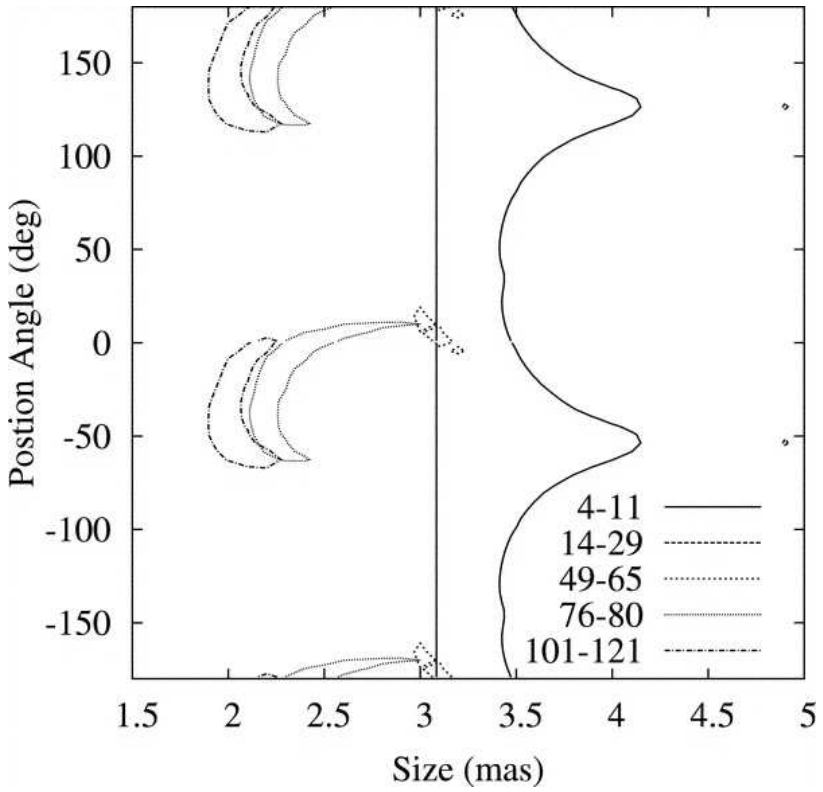

Figure 3.3 Plot of the χ^2 surface of fits to five epochs of data on RS Oph, assuming an elliptical Gaussian intensity distribution. The surface is a function of the size of the major axis and position angle (degrees east of north) of the ellipse. The minor axis of the fit was allowed to vary to minimize the χ^2 and the best-fit value is given in Table 3.4. The contours represent the $1-\sigma$ uncertainty level, and the key indicates which contour corresponds to which epoch. Adapted from Lane et al. (2007)

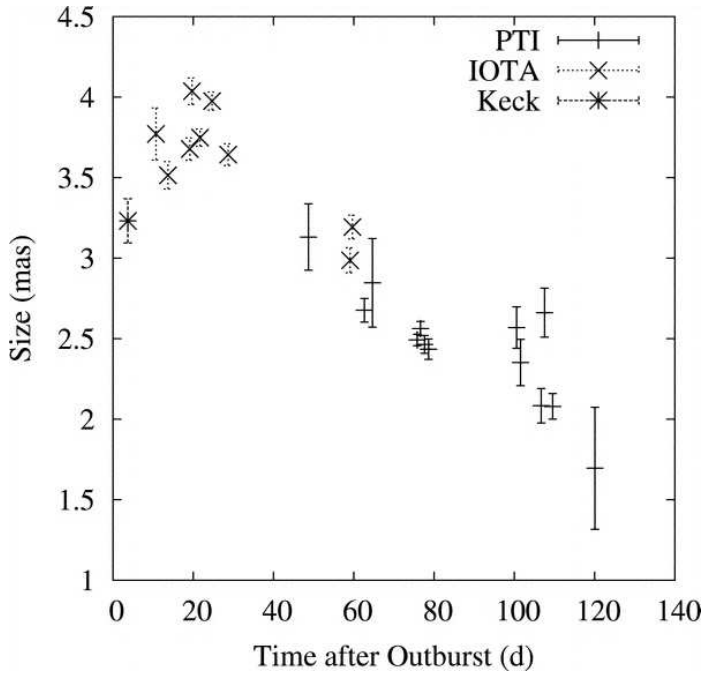

Figure 3.4 Best-fit night-by-night angular diameter of the major-axis of Gaussian emission model, with the orientation and position angle constrained to the overall best-fit values explained in the text. Adapted from Lane et al. (2007)

It is also possible to fit the data from each epoch using a two-component model (indeed, there is a degeneracy between a partially resolved two-component model and an elongated disk). In Section 3.2 we found that early-epoch RS Oph data were possibly consistent with a pair of components separated by ∼3 mas. However, if one is in fact observing a binary, then the two-component model should obey a Keplerian constraint. Hence, we fit a Keplerian binary model constrained to the orbital period (P = 460 days), eccentricity (0), and epoch (T_0 = 2450154.1 JD) determined by radial velocity observation (Fekel et al. 2000). We search for the best-fit semimajor axis, inclination, longitude of ascending node, and component intensity ratio. We find no acceptable fit with a semimajor axis smaller than 2.3 mas, corresponding to ∼3.7 AU. Thus, we conclude that we cannot be seeing the binary itself.

The observation in 2003 is comparatively limited in that it comprises only two 130 s integrations on one night, using a single baseline. The resulting (u, v) plane coverage is so limited as to preclude meaningful fits to anything but the simplest uniform disk model. However, the data are consistent with a single essentially unresolved source with an angular diameter of $\theta_{UD} = 0.7 \pm 0.5$ mas (the large error bar comes from the fact that $\theta_{UD} \ll \lambda/B$).

3.3.3 Discussion

The interferometric observations from IOTA and PTI directly constrain certain aspects of the near-IR emission. First, the shortest baseline data (from IOTA, base-

line length ∼10.5 m) taken on days 4-11 indicate a fringe contrast near unity (V ∼ 0.99; see Figure 3.1 in Section 3.2. This places an upper limit on the amount of emission that can be coming from a source larger than the interferometric field of view ($\lambda^2/B\Delta\lambda \sim 0.08$" for IOTA). That upper limit is ∼0.7%. Second, the long-baseline observations indicate that the source is in fact resolved; for the longest baselines $V^2 \sim 0.4$, indicating a size on the order of $\sim \lambda/B \sim 3$ mas. For reference, if the blast wave from the nova expanded at ∼3500 km s^{-1} (Sokoloski et al. 2006), implying an angular diameter of 5 mas by day 4, and an expansion rate of ∼1.2 mas day^{-1} assuming peak brightness on 2006 Feb 12.83 as the origin of time.

Let us now consider the source of the observed extended near-IR emission. Given the measured angular size scale of 3 mas, the physical scale is 2 AU, slightly larger than the expected orbital separation of 1 AU (Fekel et al. 2000). One possible source of extended near-IR emission is blackbody radiation from optically thin dust surrounding the RS Oph system. We point out that if there were dust, it is hard to explain the apparent contraction of the emission source; if the dust is evaporating it would likely evaporate from the inner regions first yielding an expanding ring morphology. The dust emission could be masked by other, stronger sources, however.

Another possible source of the extended near-IR emission is the postoutburst wind emanating from the nova. It is expected that after the initial explosion, shell material on the WD will undergo hydrogen burning for weeks to months; the energy thus liberated will cause most of the shell material to leave the WD in a strong

stellar wind (Kato & Hachisu 1994). Radio observations of the ejecta indicate an asymmetric morphology with a jet-like feature at a position angle near 90° this is reasonably consistent with the initial elongation seen in our data (PA ∼120), which may represent the base of that jet (O'Brien et al. 2006). In this scenario the initial elongation would represent faster moving material leaving along the polar axis of the system; subsequent, slower material would be concentrated along the system orbital plane. It is important to remember that even if the emission region appears to shrink, it does not necessarily imply that the material is falling in; what we are seeing is the effective photospheric diameter, which is a function of the optical depth of the material. If the mass-loss rate from the WD drops, then the apparent photospheric radius would be expected to shrink even as the material continues flowing outward.

A post-nova wind would be expected to radiate free-free, bound-free, and line emission (Rybicki & Lightman 1979; Pearson et al. 2005), and proper treatment would require a full photoionization model. However, a simplified treatment using only the free-free emission should be adequate for initial mass estimates. In this context we note that PTI is equipped with a low-resolution spectrometer that disperses light in the K band across five channels, providing both photometry and fringe visibilities in each channel. A close inspection of the spectrally resolved data reveals no significant change in fringe visibility nor any significant excess emission in the channels thatwould contain known strong emission lines (e.g. Br γ, 2.166 μm); the level of photometric uncertainty is ∼5%. This does not exclude line emission, but

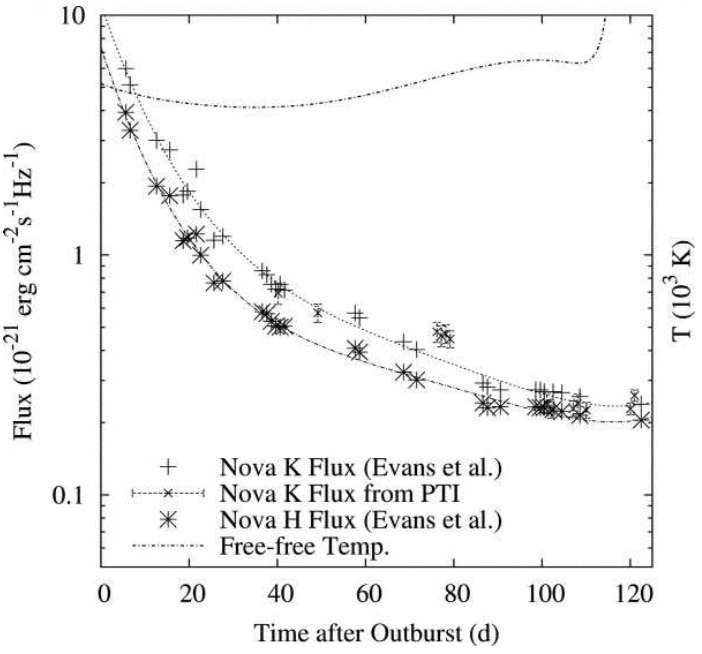

Figure 3.5 Near-IR fluxes from the nova source as measured by PTI and from Evans et al. (1988), together with the derived color temperature assuming free-free emission. We have fit Low-order polynomials, described as dotted curves, to the photometry for use in interpolation. Adapted from Lane et al. (2007)

indicates that the total flux seen by PTI is dominated by continuum emission. This is consistent with previously measured equivalent widths in the Br γ line (Callus et al. 1986). It is also consistent with H- and K-band IR spectra by Evans et al. (2007), which indicate that the line/ continuum ratio is in the range 10%-30% in the period from 11 to 55 days after the eruption (with the ratio decreasing over time).

We use previously published IR photometry (Evans et al. 1988) and reddening estimates of $E(B-V) = 0.73$ from Snijders et al. (1985) obtained during the 1985 outburst to constrain the emission model, justified by the fact that we find that the 1985 light curve is consistent with the 2006 K-band light curve as measured by PTI. In addition to the postulated wind emission source, there is another source of IR radiation: the M giant companion. We are therefore left with only the M giant companion; we attribute all of the near-IR emission at the minimum intensity point in the light curve to it. (Note that a much more thorough analysis of the continuum radiation in Chapter 5 discusses sources of IR emission in detail. While the M giant star does emit in the IR there are other important sources of emission.)

After subtracting the flux from the companion, we derive the H- and K-band intensities of the nova source. The H/K flux ratio thus derived can be used to determine the emission temperature for the thermal bremsstrahlung process ($f(H)/f(k) \sim \exp[h(\nu_H - \nu_k)/kT]$ neglecting variations in the Gaunt factors); this yields a temperature in the range of $\sim 10^4$ K (Figure 3.5. Note that for an apparent angular diameter of $\sim$3 mas, in order to match the angular size, brightness, and color temperature, the

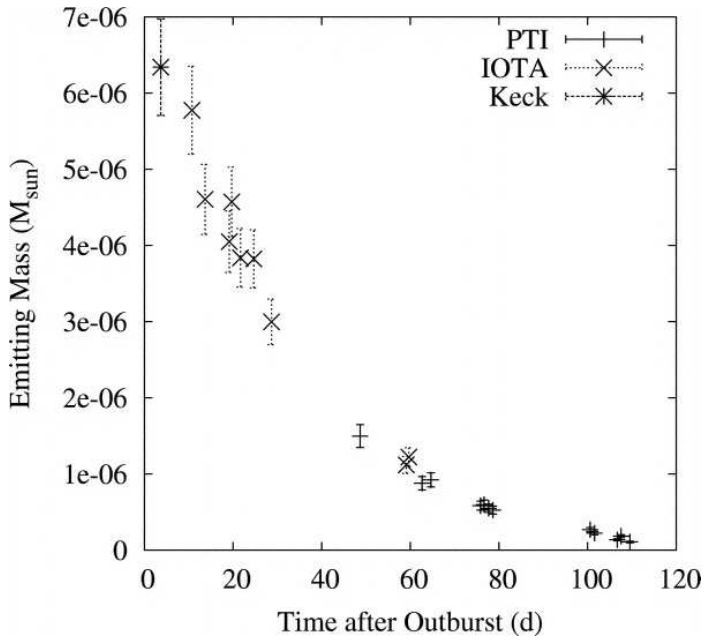

Figure 3.6 Mass of the near-IR emission source as a function of time, assuming thermal free-free emission. The emission measure was determined from the 1985 light curve, while the angular diameter measurements allow us to solve for n_e^2 and total mass separately, assuming a uniform electron density distribution (see text). Adapted from Lane et al. (2007)

source must be optically thin (Ney and Hatfield 1980).

For thermal bremsstrahlung, the emitted intensity is proportional to $\int n_e^2 dV$, i.e., the emission measure. Using the interferometrically determined sizes, we can find the total volume, V, and hence infer the electron density and total emitting mass as a function of time, assuming that the electron density is uniform throughout the emitting volume. Results are shown in Figure 3.6. In determining the volume, we assume the emitting region to be an ellipsoid of revolution with dimensions equal to the major and minor axes of the best-fit Gaussian model.

$$M_{ej} = \frac{T_{ej} m v_{exp}}{R} \tag{3.1}$$

where T_{ej} is the duration of mass ejection (60 days; Hachisu et al. 2006), m is the amount of mass in the emitting region at any given time, v_{exp} is the expansion velocity, and R is the size of the emitting region. Hence, the total amount of mass ejected postoutburst is $\sim 6 \times 10^{-5} (T_e j/60 \text{ days})(V_{exp}/100 \text{ km s}^{-1} M_\odot)$.

Such a large ejected mass is consistent with the shell mass determined by Bohigas et al. (1989) but is larger that the predicted value from models by Yaron et al. (2005) ($10^{-6} - 10^{-7} M_\odot$), and larger than estimates based on X-ray observations from the 1985 outburst (OBrien et al. 1992). We note that the mass estimate of a few $\times 10^{-7} M_\odot$ by Sokoloski et al. (2006) is based on the X-ray properties of the shock in the period immediately after the outburst and would not be sensitive to mass ejected many days after optical maximum, as seen here. Nevertheless, this is comparatively large amount of mass, roughly equal to the amount of mass lost from the red giant in the inter-outburst period; this would cast doubt on the notion that the nova is a net gainer of mass.

One can however propose other mechanisms to explain the presence of a few $\times 10^{-6} M_\odot$ of emitting material around the nova binary system if this material is considered to be quasistationary. Two sources of material are readily available in the system: the accretion disk and the red giant. The first scenario would be that the observed material comes from the accretion disk surrounding the WD (the disk

is thought to be disrupted by the nova); if this material is heated by the passing shock wave and enough momentum is imparted to move it outside of the binary, it might be possible to match the observed morphology, i.e., the elongation with PA $\sim$0 would then be aligned with the orbital plane (inferred by OBrien et al. [2006] to be perpendicular to the jet direction). If we are indeed seeing gas emission by material from a disrupted disk, then these measurements represent a measurement of the mass of that disk. If we assume that the material is quasi-stationary then the inferred disk mass is $1 - 6 \times 10^{-6} M_{\odot}$.

The second possibility is that the blast wave from the nova impacts the red giant with sufficient momentum to strip off a portion of the companion atmosphere. Such scenarios have been studied in the context of supernovae (Marietta et al. 2000; Wheeler et al. 1976), and it has been shown that considerable mass stripping will occur. However, the greatly reduced energy available in novae limits the magnitude of this effect. Assuming a blast wave velocity of 3000 km s^{-1} and mass of $5 \times 10^{-7} M_{\odot}$ (Sokoloski et al. 2006), an RG radius of $\sim$30 $R_{\odot}$ and mass of $\sim 0.7 M_{\odot}$ and an orbital separation of $\sim$320 $R_{\odot}$(Hachisu & Kato 2006) and using equations (8) and (9) from Wheeler et al. (1976), we find that their parameter $\Psi \sim 5 \times 10^{-8}$ (Ψ is essentially the ratio of the momentum of the portion of the blast wave that impacts the companion to the momentum required to move the companion at its own escape velocity). Wheeler et al. (1976) find that the fraction of mass stripped from the companion is $\propto \Psi^3$; hence, we conclude that the amount of mass stripped from the RG is negligible.

In summary, we found that the near-IR emission is on the scale of a few mas, corresponding to ∼2 AU at the 1.6 kpc distance. This is factor of ∼50 smaller that the size of the radio emission source at this time, but is also larger than the separation of the WD and RG stars. The emission is also not spherically symmetric. Initially, the source appeared to expand and was elongated with a major-axis position angle of $\sim 120^{\circ}$ subsequently, the source appeared to contract and the orientation angle changed to $\sim 0^{\circ}$. We explored possible sources of this emission and attribute it to free-free emission emanating from the strong wind leaving the WD. We derived an upper limit to the mass in the emitting region to be a few $\times 10^{-6} M_{\odot}$ and used it to infer the total amount of mass lost by the WD during the days immediately following the outburst to be $\sim 6 \times 10^{-5}$ $(T_{ej}/60 \text{ days})(V_{exp}/100 \text{ km s}^{-1})$ $M_{\odot}$.

3.4 On the Distance to RS Oph

During the 2006 outburst of the nova RS Oph, observations were conducted over much of the currently accessible electromagnetic spectrum including the X-ray (Sokoloski et al. 2006; Bode et al. 2006), visible light, infrared (Monnier et al. 2006; Chesneau et al. 2007a; Das et al. 2006; Barry and Danchi 2008), and radio (Anupama and Kantharia 2006; O'Brien et al. 2006). For the first time, new interferometric observations were conducted in the infrared at such observatories as The Very Large Telescope Interferometer (Chesneau et al.) and the Keck Interferometer (Barry et al. 2008). The breakthrough technologies utilized by these observatories hold the potential to facilitate the development and testing of scientific theories that predict the spatial distribution of matter within complex systems such as RS Oph. All of these measurements are, to some degree, sensitive to the distance to the object.

To assess the true nature of this object, the absolute values of photometric magnitude, emission line and continuum intensity, and plateau luminosity must be measured to augment existing observations. Note that the interpretation of imaging and interferometric methods are sensitive to the assumed distance (Monnier et al. 2006; Connelley and Sandage 1958). How does the rate of decline of intensity post-outburst relate to absolute magnitude? How do we assess the density of absorbing material in the vicinity of the object and in the intervening space? Where is dust created in the system? What is the density of the ejecta and the rate of mass transfer from the red giant (RG)? Is the mass transfer mechanism RG stellar wind capture or Roche

Lobe overflow? Without an accurate estimate of the distance, our answers to these questions may be imprecise and could effect our understanding of the physics of the source. The distance to RS Oph is a critical parameter.

From the earliest observations of this object by Jump-Cannon and Pickering (Pickering 1905) to current efforts by such workers as Sokoloski et al. (2006) and Evans et al. (2006), RS Oph has been of intense interest to the astrophysics community. For the 2006 outburst of RS Oph, an unprecedented array of astronomical observatories were brought to bear on this archetypical recurrent nova (RN). This is due in part to the object's historical record of repetitions, its value as a probe of the physics of extremely dense matter, and the science of accreting white dwarfs. It is also due in large measure to the theory and growing body of evidence indicating that RS Oph may be a supernova Ia progenitor. The system's proximity to the solar system makes observations easier than for other such objects and an accurate distance estimate is beneficial for the derivation of the greatest benefit from this object as a laboratory for stellar astrophysics.

3.4.1 The Historical Record

RS Oph has undergone six recorded nova outbursts of irregular interval in 1898 (Fleming and Pickering 1904), 1933 (Adams and Joy 1933), 1958 (Wallerstein 1958), 1967 (Barbon et al. 1969), 1985 (Morrison 1985) and now 2006 (Narumi et al. 2006). The very earliest calculation of a distance to this important object was undertaken

by Payne-Gaposchkin (1957) after the discovery the previous year (Arp 1956)of a relationship between maximum absolute magnitude and rate of decline (MMRD) through analysis of observations of 30 novae in M31 over a period of two years. Using Arp's relation Payne-Gaposhkin calculated an absolute magnitude from the measured for RS Oph given its fast ($t_3 = 10$) rate of decline and, using the distance modulus relation, derived a distance of 1.7 kpc. She also included in her calculation a correction for obscuration using a factor deduced by Joy (1939) in which he determined that all distances for objects within a layer of $\pm$500 pc from the Galactic plane should be increased by a factor of 0.85/kpc through observations of 156 Galactic Cepheid variable stars, determination of their absolute magnitudes from the well-established Cepheid period-luminosity relationship, and comparison with apparent magnitude.

One year later, Connelley and Sandage (1958) derived a peak outburst absolute magnitude for RS Oph of -8.7, again using the Arp MMRD relationship, after observing the the object using the 100-inch telescope on Mt. Wilson and the then-new "photoelectric detectors" filtered in Johnson V-band. Surprisingly, Connelley and Sandage did not report a distance to the object although they had all the necessary information to calculate it. This was not accomplished until fully a decade later when Pottasch (1967) used a new method attributed to McLaughlin (1960) to check Arp's MMRD relationship. Using a light-curve obtained by Eskioglŭ (1963) resulted in a t_3 time of 16 days and a corresponding absolute magnitude at maximum light for RS Oph of $M_v(abs) = -8.5$ in good agreement with Connelley and Sandage. Splitting

the difference and using a value $M_v(abs) = -8.6$ together with the V-band apparent magnitude $M_v(app) = 5.15$ measured by Eskioglŭ they then used this distance modulus to obtain the result 5.8 kpc which should have been 5.6 kpc using the values they reported. We note that Pottasch did not deredden the values obtained through the MMRD expression and that this particular t_3 time is much larger than others found subsequently. As a result, this distance is the largest of record.

There were no estimates of the distance to RS Oph for eight years until, after the 1985 outburst of the RN, Cassatella et al. (1985) discussed the issue fairly thoroughly and introduced two new methods to set bounds on the distance. As a basis, Cassatella et al. applied the MMRD relation, based on a new calibration by Cohen (1985), to data from the 1933 and 1958 epochs to obtain the distances of 2.08 and 2.4 kpc, respectively. Cassatella et al. also introduced the method of calculating the distance modulus at quiescence. Fitting a spectral type to the optical and NIR spectral energy distribution and noting the TiO bands in the NIR spectrum allowed the identification of the RG as an M0 III star. Using a V-band absolute magnitude for the RG star of -0.7 (Mikami and Heck 1982) and using the quiescent V-band apparent magnitude of 12.1 as measured by Wallerstein (1963) resulted in a distance of 1.3 kpc. Of particular importance in Cassatella et al. was their inclusion of the effects of interstellar dust absorption from the Carina arm of the Galaxy. They noted that if the object was greater than 2.0 kpc away, the observations would show an interstellar absorption spectrum shifted by 20 km s^{-1} due to cool gas in the arm. This feature was not

detected, indicating that the distance measured using the magnitude/rate of decline mechanism was an upper limit.

One year later, Hjellming et al. (1986) reported the first observed radio source associated with a recurrent nova event and observations of HI absorption measurements towards RS Oph. Measurements along two lines of sight allowed comparison of the absorption spectra between RS Oph and a neighboring object. The density of the neutral hydrogen along each line of sight was estimated by use of the fact that the relative occupation probability of neutral hydrogen's two spin states, parallel and antiparallel, is temperature dependent when the medium is in thermal equilibrium. Assuming the spin temperature of $T_s = 100$ K and using the relation $N_H/T_s = 1.59$ $cm^{-2}K^{-1}kpc^{-1}$, as derived by Dickey et al. (1983), yielded an absorption distance of 1.7 kpc in agreement with the lower range of Cassatella et al. Importantly, Hjellming et al. did not see the $+15 \rightarrow +20$ km s^{-1} absorption spectrum associated with the Carina arm of the Galaxy in the data from RS Oph while they did detect it for a neighboring object, again confirming the result of Cassatella et al.

In the same year Livio et al. (1986) introduced the idea that if the secondary's Roche Lobe (RL) was overfilled, the distance to the object would have to be greatly increased to account for the resulting increased bolometric magnitude. Using binary component identifications atypical for cataclysmic variables (CV), Livio et al. adopted masses $M_g = 3M_\odot$ and $M_s = 2M_\odot$, by assuming RS Oph to be phenomenologically similarity to T CrB. Here both the 'primary', M_g, and the 'secondary', M_s were

assumed to be giants of M2 and M0 spectral class, respectively, although Livio et al. did leave open the possibility that the 'secondary' could be a white dwarf (WD). They also adopted an orbital period of 230 days, and, as a result, calculated a component separation of 270 $R_{\odot}$ and an effective radius of the RL of 112 $R_{\odot}$, which resulted in a distance of 3.1 kpc. While these calculations are internally consistent, they are based on component masses and a period which we now know to be incorrect. The approach of Livio et al. does seem prescient, however, in light of the Hachisu and Kato (2001) reborn RG model, to be described below, in which the WD regains a large, red pseudo-photosphere — is essentially 'reborn' as an RG — for a short period after a surface thermonuclear runaway (TNR) event.

A year later, Evans (1987) identified the RS Oph RG spectroscopically as an M0III and, from that, inferred an intrinsic infrared brightness. Evans then examined IUE spectra of both RS Oph and another object, Y Oph, a cepheid along the same line of sight. From these, Evans noted that the reddening, $E(B-V) = 0.73$, was similar in each and inferred that the bulk of it was due to interstellar reddening rather than reddening local to RS Oph. Using the interstellar extinction law of Savage and Mathis (1979), Evans reported a distance of 1.3 kpc.

In the same publication, Snijders (1987b) confirmed the upper limit of 2.0 kpc (Cassatella et al. 1985) by failing to detect any velocity shift in the line spectrum in the IUE data from day 42.8, 55.8, 72.7 of 1987 outburst due to the Carina arm. Snijders (1987a) utilized a new method to determine the distance based on theoretical work

of Starrfield et al. (1985). In this paper the authors calculated that if the outburst is caused by a TNR event then there should be a plateau in the bolometric magnitude curve shortly after peak optical brightness, and that this should be just short of the Eddington luminosity limit for the WD. Snijders (1987a) did observe a plateau in the RS Oph bolometric magnitude curve between days 8 and 35. Assuming that the observed plateau flux was all of the light emitted during the Eddington phase and that this represented 99% of the Eddington limit emission for a WD of $1.38 M_{\odot}$, Snijders (1987a) found a distance of 1.37 kpc. Following the interstellar extinction law of Seaton (1978, 1979), and adopting an interstellar reddening of $E(B-V) = 0.73 \pm 0.1$ Snijders then determined the distance to be 1.6 kpc. Snijders further indicates that this distance calculation is very sensitive to the adopted value of interstellar reddening, with an error of only $\Delta E(B-V) = \pm 0.1$ yielding a distance error of 30 - 40%. We note that Snijders (1987b) calculated an extinction of $E(B-V) = 0.73 \pm 0.06$ - a significant reduction in uncertainty.

The end of the century saw the advancement of many new methods for the determination of distance beginning with that of Sekiguchi et al. (1990). Previously Feast and Glass (1990) noted that there are M stars, thought to be members of the Galaxy's thick disk, that have colors similar to those in the Galactic Bulge (wherein a metallically gradient has a strong effect on color). Sekiguchi et al. found that assuming that RS Oph is a reddened Bulge-M star fitted the quiescent data better than identifying it as normal M giant. They calculated a distance of 1.0 kpc using

the Johnson K-band distance modulus and using work on M-giant colors by Frogel and Whitford (1987) that assumed a quiescent $K_{mag} = 6.4$, interstellar reddening of $E(B-V) = 0.73$ and a spectral type of M1 III. Three years later, Harrison et al. (1993), working with a new K-band spectrum of RS Oph in quiescence, found that it was not possible to reconcile the measured color with the colors of M0III - M2III by application of reddening alone. They noted that the Johnson-K spectrum lacks any CO absorption features typical of these stellar classes and suggested that either RS Oph is not a normal M0/M2 giant or that there is emission from some other source effecting the IR luminosity observed. They further noted that the quiescent continuum of RS Oph is very much like that of T CrB in which the continuum is thought to originate in the photosphere of the secondary. Harrison et al. went on to propose that weak CO *emission* is occurring in the system and so is veiling the expected CO absorption while not having any effect on the shape of the continuum. In their estimate, Harrison et al. assumed that all K-band luminosity is from the RG and that it is of M0III spectral class, yielding a distance of 1.29 kpc. We note that the following year, Scott et al. (1994) found that there was evidence that the depth of the 2 μm CO bands change significantly over time. As a result, the distance found by Harrison et al. may have been based on incomplete information.

Just prior to the current epoch, Hachisu and Kato (2000, 2001) discussed the distance issue in the context of the TNR reborn RG model mentioned previously, advancing several different methods which produced a very close distance of ~ 0.6 kpc.

In the first of these papers Hachisu and Kato (2000) conducted extensive modeling of the UV flux from RS Oph and determined this came from the accretion disk. Their model gave a luminosity that, when dereddened, yielded a distance of 0.6 kpc. The authors interpreted ultraviolet observations by Mason et al. (1987) as evidence of accretion and calculated a distance of 0.45 kpc assuming dereddening. In the second paper, Hachisu and Kato (2001) further developed these models and derived following results: 1) that there is an accretion disk about the WD and it reappears within a few days after maximum light, 2) that the UV light curve depends on the existence of the disk but only weakly on the disk parameters, 3) the UV light comes mostly from the inner part of the accretion disk, 4) that the RG does not contribute to the UV flux as it's irradiated side reaches a temperature of only 4000 K. Hachisu and Kato subsequently calculated absorption for a range of distances and found that 0.57 kpc yields absorption consistent with color excess of $E(B-V) = 0.73$ after Snijders (1987a). In support of this distance, Hachisu and Kato showed that if we assume that distance is 1.6 kpc, the radio measurements conducted at the VLBI on day 77 (Taylor et al. 1989) would require an *average* expansion speed of 4000 km s^{-1}. They also noted that the ejecta would be decelerated by collision with circumbinary matter (CBM) formed by the RG wind during quiescence arguing for an even shorter distance. Hachisu and Kato then appeal to a "shock breakout" model in which the signature of the shock breaking out of the outer edge of the RG wind would be detectable as a sudden fall-off of soft X-ray emission (Mason et al. 1987; Itoh and Hachisu 1990).

Here the outer edge of the CBM formed by the RG wind, with an upper velocity limit of 20 km s^{-1}, as calculated by Gorbatskii (1972), would have a radius that does not exceed $R_{cbm} = 1 \times 10^{15}$cm, with the RG wind that would have existed previously to this having been swept away by the 1967 outburst. Hachisu and Kato also showed that the observed rapid decrease in soft X-ray emission 60 days after peak V-band brightness suggests a distance of 0.65 kpc in support of the shorter distance. A third supporting line of reasoning offered by Hachisu and Kato was used to explain the super-soft X-rays detected 251 days post-outburst as accretion luminosity rather than hydrogen shell burning. Using a blackbody temperature of $T_{bb} = 3.5 \times 10^5$ K, $R_{WD} = 0.003 R_\odot$ calculated from $M_{WD} = 1.377 M_\odot$, and comparing this result with that measured by Mason et al. (1987) yields a distance of 0.4 kpc. Lastly, Hachisu and Kato compared the H_β measurement on day 201 to that predicted by assuming an emitting radius of $R_{WD} = 0.003 R_\odot$ again, yielding 0.6 kpc.

3.4.2 Epoch 2006

The 2006 outburst of the nova RS Oph has brought a great deal of new interest in and work on the problem of the distance to this important object. Between this outburst and the previous one in 1985, new technologies have evolved allowing the creation of new kinds of observatories. The entire field of optical and infrared stellar interferometry, for example, has blossomed in this short period of time. The field of X-ray astronomy has vastly improved capabilities, with new observatories, such as

the *Rossi X-ray Timing Explorer* (*RXTE*), *Chandra*, and *XMM Newton*, which were built and launched into orbit within the past two decades. Likewise, the study of the interaction of cosmic rays with blast waves has advanced in this same time period and it may bear strongly on our determination of distance. In this section, we will give an account of the relevant measurements made during this outburst epoch, outline new theoretical predictions and calculations based on new observations, and describe the concept of how cosmic rays effect blast waves and how this may effect our distance estimates.

In the current outburst epoch of RS Oph, the first estimate of a distance to the object is in the work of Sokoloski et al. (2006) who performed a first-ever direct measurement of a nova blast wave deceleration by comparing it to the radio image size to make a determination. The method proceeded by assuming that the X-rays originate in the shock as the rapidly expanding ejecta plows into the circumbinary gas. The X-ray gas temperatures have been measured starting a few days after peak V-band brightness, which can be converted to the ejecta velocity ($v \propto T^{1/2}$, where T is temperature). Since the temperature varies as a power law function of time, t, to be $\propto t^{-2/3}$. the velocity of the shock, v, was determined to vary as $v \propto t^{-1/3}$. Relying on the determination of the initial shock speed of 3500 km s^{-1} from the optical emission lines, this new result allowed the calculation of blast wave radius as a function of time. Lastly, the calculated blast wave radius was compared to radio measurements of angular size conducted very early after peak brightness to confirm a distance of 1.6

kpc.

Rupen and Sokoloski (2008) advances a refinement of these calculations based on a new comparison of the angular size observed by the VLBI with the radius inferred from optical and X-ray observations. The authors assume a constant initial ejecta velocity and estimate velocity thereafter by measurements of X-ray temperature from observations by the *RXTE*, as did Sokoloski et al., then incorporate new X-ray data from the *Swift* spacecraft for later times. They subsequently fitted these velocity profiles with two independent power laws and compare the calculated sizes to the angular sizes measured by the VLTI. Importantly, the authors caution that if the radio ring is due to a two-dimensional structure, its inclination angle, i, strongly affects this calculation with derived distances increased by a multiplicative factor of $(\cos i)^{-1}$ from 6% at $i = 20\,\mathrm{deg}$ to a factor of 3 for $i = 70\,\mathrm{deg}$ but then estimate this effect should be no greater than 10% due to the observed circularity of the ring. Dominant error terms in these calculations are the uncertainty in inclination angle in the time of the explosion relative to peak V-band brightness and in the systematic uncertainty in the relation between the calculated and measured angular size. The authors then give the final calculated distance of 1.44 ± 0.23 kpc.

A second distance estimate is found in the work of Hachisu and Barry (2008) in which they describe how a new determination of a cool red giant wind velocity by Iijima (2008) corrects the findings in Hachisu and Kato (2001). Specifically, Iijima reported the velocity of the cool red giant wind of -36 km s^{-1}, which defines the

outermost edge of the circumstellar matter as 36 km s^{-1} × 21 years = 2.4×10^{15}cm. He also reported the shock breakout time of about 90-100 days. Combining these two yields a mean shock velocity of 3000 km s^{-1} along the line of sight until the shock breakout. This new finding effectively doubles the distance estimate of Hachisu and Kato (2001) to about 1.2 kpc as they had assumed a cool red giant stellar wind velocity of less than 20 km s^{-1}.

As a rough check on the distance to this object, Barry and Danchi (2008) compared the outburst of RS Oph to that of V1187 Sco noting that the absolute scale brightness is quite similar for these two objects. Lynch et al. (2006) gave a distance of 5.3 +/- 0.5 kpc for V1187 Sco with an extinction of $A_V = 4.3$ magnitudes. Barry and Danchi went on to note that if the nova RS Oph has the same absolute V-band magnitude at peak brightness as V1187 Sco and is located at 1.6 kpc it should have a peak visual magnitude in the range 4.6 to 5. The average V-band magnitude at discovery (IAUC 8671) was approximately 4.6 in good agreement again confirming this distance.

Also calculated in Barry and Danchi (2008) is a range of distances based on a determination of the absolute peak V-band magnitude of the object using a newly calibrated MMRD. For the 2006 epoch, the decline rates, assuming a day zero of JD 2453779.329 Narumi et al. (2006) with a peak observed V-band magnitude of 4.5, $t_2 = 4.75$ days and $t_3 = 10.19$ days using AAVSO data. If we restrict ourselves to the use of the t_3 time as a more settled figure, and apply the MMRD expression $M_{V_{t_3}} = (-11.99 \pm 0.56) + (2.54 \pm 0.35) * \log(t_3)$ attributed to Downes and Duerbeck (2000) we

obtain a range of peak absolute magnitudes for this outburst of $M_{V_{t3}} = -9.43 \pm 0.91$. We de-redden our peak V-band observed magnitude $M_v = 4.5$ (Narumi et al. 2006) using the reddening coefficient $E(B-V) = 0.73 \pm 0.06$ (Snijders 1987a) and and apply $R_v = 3.1$ for Galactic sources (Cardelli et al. 1989) to obtain, through the expression $A_v = R_v * E(B-V)$, a range of extinctions $A_v = 2.263 \pm 0.186$. Applying the distance modulus equation yields a range of distances of $D_{RSOph} = 2.44 \pm 1.14$ kpc. To this broad range we apply an additional constraint. As first noted by Cassatella et al. (1985), the distance to RS Oph cannot exceed approximately 2.0 kpc because it's spectrum does not contain evidence of absorption by material in the Carina arm of the Galaxy. Presence of this feature, as evidenced by the relative $+15 \rightarrow +20$ km s^{-1} velocity of the Carina arm, is completely lacking in spectra obtained by Cassatella et al. (1985). This finding was convincingly confirmed by Hjellming et al. (1986) who searched for the $+15 \rightarrow +20$ km s^{-1} for two objects along the same sight-line. In this work, Hjellming et al. did not detect the Galactic signature for RS Oph while they did detect it for the neighboring object. The Galactic upper constraint and the MMRD lower constraint (1.23 kpc) calculated above yields a range of distances to the nova RS Oph of 1.65 ± 0.35 kpc. We note that there is some theoretical evidence that the use of the MMRD expression as derived for CN may not be directly applicable to RN, however, historical values found using this method, while sensitive to calibration, do give distances that are within reason.

All historical and current distance estimates are recorded in Table 3.4.2. Distances

Table 3.5. Distance determinations for the recurrent nova RS Oph

Distance (Kpc)	Date	Method	Reference
1.7	1957	MMRD[a], $t_3 = 10$, Arp (1956)	Payne-Gaposchkin
5.8	1967	MMRD, $t_3 = 16$, McLaughlin (1960)	Pottasch (1967)
2.08[b]	1985	MMRD, $t_2 = 3$, Cohen (1985)	Cassatella et al.
2.4 [b]	1985	MMRD, $t_2 = 7$, Cohen (1985)	Cassatella et al.
1.3	1985	QED, M0 III[c]	Cassatella et al.
≤ 2.0[d]	1985	AGS[e]	Cassatella et al.
1.7	1986	H_β absorption	Hjellming et al.
3.1	1986	RLO[f] QED, M0III + M2 III	Livio et al.
1.3	1987	QED,M0 III	Evans
≤ 2.0	1987	AGS	Snijders (1987a)
1.6	1987	EED, $1.39 M_\odot$[g]	Snijders (1987a)
1.44	1987	EED, $1.39 M_\odot$	Snijders (1987a)
1.0	1990	QED, Bulge - M1 III	Sekiguchi et al. (1990)
1.29	1993	QED, M0 III	Harrison et al. (1993)
0.6	2000	Model UV ALED[h]	Hachisu and Kato (2000)
0.45	2000	UV ALED	Hachisu and Kato (2000)
0.57	2001	Model UV ALED	Hachisu and Kato (2001)
0.65	2001	SBT[i]	Hachisu and Kato (2001)
0.4	2001	Model SS X-ray ALED	Hachisu and Kato (2001)
0.6	2001	H_β absorption	Hachisu and Kato (2001)
1.6	2006	parallax & direct deceleration measurement	Sokoloski et al. (2006)
1.44 ± 0.23	2007	parallax & direct deceleration measurement	Rupen and Sokoloski (2008)
1.2	2007	SBT	Hachisu and Barry (2008)
1.65 ± 0.35	2007	MMRD + AGS, $t_3 = 10.19$	Barry and Danchi (2008)
3.1 ± 0.5	2008	RLO QED, M0 III	Barry and Danchi (2008)
$1.4^{+0.6}_{-0.2}$	2008	Aggregate, Epoch 2006 canonical distance	Barry et al. (2008)

[a]Maximum Magnitude Rate of Decline listed with the decline time and reference for the particular MMRD formulation used.

[b]MMRD applied to data from two outburst epochs: 1933 & 1958, respectively.

[c]Quiescent Extinction Distance estimate when RG light dominates system luminosity, given with identification of secondary.

[d]Imposition of outer distance limit.

[e]Absence of Galactic Signature - outer distance limit due to non-detection of $^+20$ kms^{-1} signature of Carina arm of the Galaxy.

[f]Extinction distance estimate assuming secondary Roche Lobe overfill.

[g]Eddington Extinction Distance estimate based on luminosity of Chandrasekhar-mass WD at Eddington limit.

[h]Accretion Luminosity Extinction Distance estimate when post-outburst light is dominated by AD luminosity.

[i]Shock Breakout Timing

are given together with the date of determination, the method used, and a reference. In the case of MMRD calculations, the reference for the particular calibrated expression is also given in the method column together with the decline rate for the epoch examined. A comparison of the distance determinations grouped according to method is given graphically in Figure 3.7. Note that the result of Pottasch (1967) of 5.8 Kpc has been removed as an outlier as no dereddening was used.

3.4.3 Outstanding Issues and a Distance Estimate

In this section we discuss outstanding issues that affect our distance estimate to this important object and outline observations that may be conducted to improve the precision of the estimates. The first issue is that the linear size of the RG appears quite large, $R_{\rm g} \sin i = 105 \pm 13\,R_{\odot}$, as inferred from its rotation velocity measured by Zamanov et al. (2007) and assuming the giant's rotation is synchronized with the orbital period. This implies that the RG may fill its Roche Lobe. If this is the case, the distance must be sufficiently large to account for the observed flux level in quiescence. Assuming that the RL is filled, and using the binary parameters from Brandi (2008), we estimate $R_{\rm g} = 106 \pm 15\,R_{\odot}$, implying a distance of 3.1 ± 0.5 kpc. We note that if the RG is at a distance of about 1.5 kpc these measurements indicate that the RG radius is a factor of 2 smaller than the RL radius, which also means that its measured rotational velocity is at least a factor of 2 higher than the synchronized value. If the RG does *not* fill its tidal lobe, and the $d \cong 1.5$ kpc is approximately

correct, we have another outstanding issue: Why is the evolutionary status and the mass transfer mode of RS Oph so significantly different from those of T CrB? It is especially meaningful that RS Oph is more active during quiescence and has much shorter recurrence time between TNR nova outbursts than T CrB. While it is possible that RG wind capture is the primary mass transfer mechanism, it is easier to ensure the required high mass transfer/accretion rate if the RG is filling or close to filling its tidal lobe.

A second issue is the effect of cosmic ray braking. After a nova event, the blast wave expands away radially from the WD primary. A large magnetic field of stellar origin is expected to pre-exist in the RG wind and to be frozen in to that wind (Baring 2004). Any turbulent motions in the RG wind and magnetic interactions between trapped particles and plasma waves will further amplify the magnetic field (Lucek and Bell 2000). Charged particles interact to first order, through the mediation of the magnetic field, with the *entire* shock front, which has a significant mass and is traveling radially at approximately 3500 km s^{-1}. As a result, the charged particle gets an enormous energy boost. This effect is significantly greater for particles moving against the blast wave, resulting in a slowing of the front (Decourchelle et al. 2000). Low energy seed particles will eventually gain enough energy to escape the shock front and will have depleted its kinetic and thermal energy. (This could also strongly effect shape of the shock early after its departure from the surface of the primary.) These interactions may sap the energy from the post-shock plasma causing a rapid

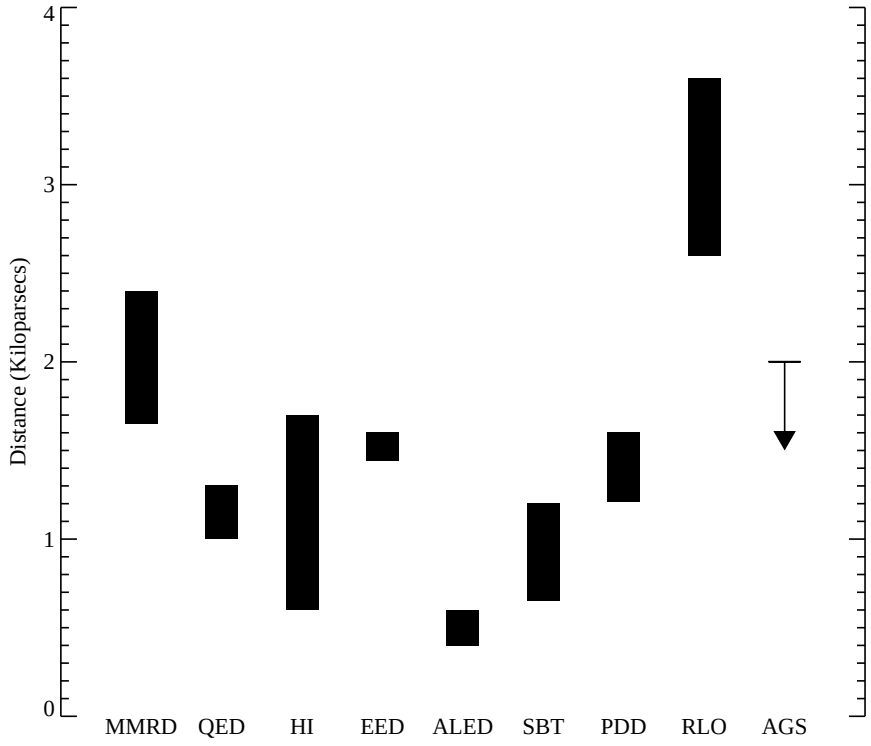

Figure 3.7 The different distance determination for the recurrent nova RS Oph grouped according to method. Methods are: MMRD - Maximum Magnitude Rate of Decline, QED - Quiescent Extinction Distance, HI - hydrogen beta extinction, EED - Eddington Extinction Distance, ALED - Accretion Luminosity Extinction Distance, SBT - Shock Breakout Timing, PDD - Parallax and Direct Deceleration measurement, RLO - Roche Lobe Overflow quiescent extinction distance, AGS - Absence of Galactic Signature (an outer limit). Note that the 5.8 Kpc MMRD finding by Pottasch (1967) has been removed as indicated in the text.

decrease in its temperature. This temperature is used to infer the velocity of the shock and the resulting calculated radius is compared to radio angular size to obtain a distance (cf. Sokoloski et al.). An expansion parallax derived by these methods would then underestimate the distance to the object. There is a strong possibility that acceleration of cosmic rays is occurring in the RS Oph system (Tatischeff and Hernanz 2007) so this effect could have a significant impact on distance estimates.

Recently, Brandi (2008) derived spectroscopic orbits for both components of the RS Oph system based on the radial velocities of the M giant absorption lines and the broad emission wings of Hα. They have also constrained the orbit inclination, $i \geq 49 \pm 3$ degrees, using the estimated hot component mass, $M_{\rm h} \sin^3 i = 0.59\,{\rm M}_\odot$, assuming that the white dwarf mass cannot exceed the Chandrasekhar limit. (Due to a lack of appropriate UV observations, we cannot establish whether or not the WD is spinning - and thus theoretically allowed to exceed the mass limit as theorized by Yoon and Langer (2004). It is not clear, however, exactly how the inclination angle of the orbit is related to that of the radio ring observed by O'Brien et al. (2006). If the radio ring is really 2-dimensional, then the obvious explanation is that it's preferentially bright in the orbital plane. But, if this was the case, the low inclination of the ring requires the orbital inclination to be low, which is excluded by Brandi. If, on the other hand, the radio ring is a limb-brightened sphere, as Rupen and Sokoloski (2008) suggests, then it should look circular whatever the orbital inclination may be and Brandi does not constrain the result. In any case, it is evident from the results of

Rupen and Sokoloski that approaches that rely on geometric parallax will be sensitive to the origin of the radio ring and that this needs to be further measured, modeled and constrained.

Note that each of the effects outlined above would lead to an underestimate of distance. Given this, the very sophisticated calculation of Sokoloski et al. & Rupen and Sokoloski should be taken as a lower limit to the distance to RS Oph, while the upper limit is set by the absence of the Galactic signature. This upper constraint is somewhat soft as it is unknown how deep within the Carina arm the object would have to be imbedded to begin to show a measurable 20 km s^{-1} feature. Further analysis through modeling of the density profile of the Galactic arm is warranted. The calculation in Barry and Danchi (2008) using the very latest, calibrated MMRD equation gives a number closer to the historical 1.6 kpc. Given these constraints and observations, a conservative estimate of the distance to RS Oph is $d_{RSOph} = 1.4^{+0.6}_{-0.2}$.

3.4.4 Suggested Observations to Resolve the Distance Issue

One way to improve the precision of the distance estimates is to use interferometric measurements of the dust environment. Barry and Danchi (2008) propose an improved physical model of RS Oph, in which spiral shock waves associated with the motion of the two stars through the cool wind from the red giant create density enhancements within the plane of their orbital motion. Interferometric measurements of this phenomenon, if the spiral does reform as hypothesized, taken together with

new radial velocity measurements by Brandi and the revised spectroscopic orbit calculated therein could be used to resolve the $\cos i$ ambiguity. New radio geometric parallax measurements could also be undertaken in the even that, in quiescence, the ring can still be detected.

We recommend that a renewed effort be made to measure the ellipsoidal variation of the RG star using near infrared photometry over several orbital cycles. This will tell us the size of the RG relative to its Roche Lobe. At the same time, high resolution spectra should be obtained at several orbital phases. An independent confirmation of the rotation velocity as measured by Zamanov et al. (2007) would be worthwhile and would provide another estimate of the absolute size of the RG star, since it may be co-rotating with the orbit. Similarly, spectroscopic observations should be undertaken similar to those of Hjellming et al. (1986) to check for the absence of the Galactic signature and modeling should be conducted to determine the density profile of the Galactic arm.

3.5 Conclusion

Following the recent outburst of the recurrent nova RS Oph on 2006 February 12, using our Epoch 1 observations, outlined in Section 3.2 Table 3.2, we measured its near-infrared size using the IOTA, Keck, and PTI Interferometers. The characteristic size of $\sim$3 mas changed little over the first 60 days of the outburst leading us to suggest that currently popular models whereby the near-infrared emission arises from

hot gas in the expanding shock may be incorrect. We also found the emission to be significantly asymmetric, evidenced by nonzero closure phases detected by IOTA. We discovered that the physical interpretation of these data depends strongly on the adopted distance to RS Oph. For Epoch 1, we suggested that our data could be interpreted as the first direct detection of the underlying RS Oph binary, lending support to the recent reborn red giant models of Hachisu and Kato (2001). However, this result hinges on an RS Oph distance of $\sim$ 540 pc, in strong disagreement with the widely adopted distance of $\sim$1.6 kpc. At the larger distance, our observations imply instead the existence of a nonexpanding, dense, and ionized circumbinary gaseous disk or reservoir responsible for the bulk of the near-infrared emission. Long-baseline infrared interferometry is uniquely suited to distinguish between these models and to ultimately determine the distance, binary orbit, and component masses for RS Oph, one of the closest known (candidate) Type 1a supernova progenitor systems.

We report a second set of observations observations in Section 3.3, of the recurrent nova RS Oph using long-baseline near-IR interferometry. We are able to resolve emission from the nova for several weeks after the 2006 February outburst. The near-IR source initially expands to a size of $\sim$ 5 mas. However, beginning around day 10, the IR source appears to begin to shrink, reaching $\sim$ 2 mas by day 100. We combine our measured angular diameters with previously available interferometric and photometric data to derive an emission measure for the source, and hence are able to determine the mass-loss rate of the nova in the days following the outburst. In

Section 3.4 we reviewed the entirety of the literature on the topic of the distance to RS Oph and have placed our recent calculations in their historical context. We have also undertaken to identify the unknowns that bear on this calculation and give our most conservative estimate of this important value. We conclude by observing that the historical record has large systematic uncertainties depending on the astronomical techniques used for distance estimation that can lead to results that are quite inaccurate if those techniques are not well calibrated. Given this, we recommend that any estimate of astronomical distance should *always* be reported with an associated uncertainty interval because of the effect of this important measure on many calculations. Finally, we report that for the 2006 epoch outburst of the recurrent nova RS Oph, our best estimate of the distance is $d_{RSOph} = 1.4^{+0.6}_{-0.2}$ Kpc.

Chapter 4

Observations of RS Oph with the Keck Interferometer Nuller

We report in Sections 4.1 to 4.4 of this chapter new observations of the nova RS Oph using the *Keck Interferometer Nuller* (KIN), approximately 3.8 days following the most recent outburst that occurred on 2006 February 12. These observations represent the first scientific results from the the KIN which operates in N-band from 8 to 12.5 μm in a nulling mode. The nulling technique is the sparse aperture equivalent of the conventional corongraphic technique used in filled aperture telescopes. In this mode the stellar light itself is suppressed by a destructive fringe, effectively enhancing the contrast of the circumstellar material located near the star. By fitting the unique KIN inner and outer spatial regime data, we have obtained an angular size of the mid-infrared continuum of 6.2, 4.0, or 5.4 mas for a disk profile, gaussian profile

(FWHM), and shell profile respectively. The data show evidence of enhanced neutral atomic hydrogen emission and atomic metals including silicon located in the inner spatial regime near the white dwarf (WD) relative to the outer regime. There are also nebular emission lines and evidence of hot silicate dust in the outer spatial region, centered at approximately 2.5×10^{14} cm (16.7 AU) from the WD, that are not found in the inner regime. Our evidence suggests that these features were excited by the nova flash in the outer spatial regime before the blast wave reached these regions. These identifications support a model in which the dust appears to be present between outbursts and is not created during the outburst event. We further discuss the present results in terms of a unifying model of the system that includes an increase in density in the plane of the orbit of the two stars created by a spiral shock wave caused by the motion of the stars through the cool wind of the red giant star. These data show the power and potential of the nulling technique which has been developed for the detection of Earth-like planets around nearby stars for the NASA flagship Terrestrial Planet Finder mission and the ESA Darwin mission.

Subsequently, in Section 4.5, we present further *Spitzer Space Telescope* observations of the recurrent nova RS Oph, obtained over the period $208 - 430$ days after the 2006 eruption. The later *Spitzer* IRS data show that the line emission and free-free continuum emission reported earlier is declining, revealing evidence for the presence of silicate emission features at 9.7 and 18 μm. We conclude that the silicate dust survives the hard radiation impulse and shock blast wave from the eruption. The existence

of the dust may have significant implications for understanding the propagation of shocks through the red giant wind and likely wind geometry.

4.1 The Keck Interferometer Nuller

The KIN is designed to address the high-resolution, high-contrast problem of detecting faint emission due, for example, to an optically-thin dust envelope, at small angular distances from a bright central star. Its operation differs in several ways from the more common fringe scanning optical interferometer. The fundamental measurement quantity is the *null leakage*, N, which is defined as the ratio of the fringe intensity at the null (i.e., the destructive phase) to the intensity at the peak (the constructive phase). N is related to the classical interferometer visibility $V = (I_{max} - I_{min})/(I_{max} + I_{min})$, the modulus of the complex visibility $\hat{V}$, by a simple formula:

$$N = \frac{1 - V}{1 + V} \tag{4.1}$$

Because the instrument operates in the mid-infrared N band centered near 10 μm, the light seen by the detector includes a strong and variable contribution due to thermal emission of the interferometer and telescope optics, and to the terrestrial atmosphere. It is therefore necessary to modulate the coherent astrophysical light at a frequency above the background fluctuations, and to use a lock-in amplifier to

detect it. Rather than the traditional approach of chopping the secondary mirror, the starlight modulation is done interferometrically. This requires a more complicated optical train. Each telescope aperture is split into a pair of equal-sized subapertures. The baselines associated with the split telescope pupils are short ($\sim$ 5 m) compared to the baselines joining the telescopes ($\sim$ 85 m). The Nuller beam combiner sums the fields in these four subapertures after applying an adjustable phase delay to each. The fringe phases are chosen such that the two long baselines share one common phase (π or 0, i.e., destructive or constructive) and the two short baselines share another common phase. One can therefore think of the KIN as having only two baselines, one short and one long.

The short baseline produces fringes spaced at $\lambda/B'_\lambda \sim 400$ mas, which is similar to the size of the primary beam and is assumed to be large compared to the extent of the target object. Modulating its phase therefore modulates the transmitted flux of the entire astronomical source, and the amplitude of this modulated signal is proportional to the flux that passes the fringe produced by the long baseline. The advantage of this approach is the replacement of large tilting secondary mirrors by small flats which need only move a few microns in piston and can therefore operate at high frequency. The moving flats induce no beam-walk and therefore do not modulate the thermal background.

The measurement of the long-baseline fringe phases is interleaved with the measurements of the peak and null intensities. The switching between these various

configurations happens very rapidly, in a cycle that runs at 5 or 2.5 Hz. The long-baseline fringe phases are measured using either of two methods, which are discussed in detail in Kuchner and Barry (2008). Briefly, the first method involves sweeping the delay on each long baseline by a wavelength (hence the phase of the central wavelength) while the other long baseline is shuttered off, and measuring the phase of the resulting sinusoidal intensity variation. The second method involves setting one long baseline to zero (constructive) phase and the other to π (destructive) phase. It can be shown that in this configuration the transmitted flux has a component proportional to the error in the phase of the nulled baseline.

This overall system design permits the visibility to be measured with precision. The errors in most quantities, including the long-baseline fringe phases and amplitudes, polarization, and wavefront, contribute only second-order and higher terms to the null leakage. Square-law biases are mostly eliminated because the detection of both the peak and null fringes is coherent and linear. Finally, the comparatively long observing wavelength, compared to the more common 2.2 μm or shorter for most other interferometric systems, makes the KIN intrinsically less sensitive to pathlength errors.

The mathematical foundation for the function of the KIN is thoroughly described in Chapter 2 and Kuchner and Barry (2008). These are given for completeness and because these data represent the first scientific result from this instrument.

Before discussing our observations in detail, we briefly discuss the physical im-

plementation of the nulling interferometry principles discussed above. As mentioned above, the long baseline comes from the separation of the two 10-m *Keck* telescopes, themselves, (B_λ) while the pupils of the two telescopes are split in half creating two approximately elliptically shaped pupils separated by 5 m, thus providing a short baseline, B'_λ. The pupils of the long baselines are combined in a modified Mach-Zehnder beamsplitter arrangement (Colavita et al. 2006), which is optimized for maximum symmetry between the two input pupils and this provides the "achromatic" null output. However, unlike a conventional beamsplitting interferometer, where there are two output beams for two input beams, in this configuration there are four output beams for the two input beams, i.e., two null outputs and two bright outputs. The modified Mach-Zehnder configuration used here leaves the two other inputs to the beamsplitter system receiving room temperature blackbody radiation. The two null outputs from the two modified Mach-Zehnder interferometers are next combined in a conventional beamsplitter, called the cross-combiner, thus producing 4 output beams (two null and two bright) that are sent to a mid-infrared, low-resolution spectrometer system — the KALI camera. It is the intensity of the two null output beams that are actual physical measurement of the KIN system.

4.2 Observations

We observed the nova about an hour angle of -2.0 on the *Keck Interferometer* in nulling mode on 2005 Feb 16 with a total of three observations between day 3.831 and

Table 4.1. KIN observing log for RS Oph

Object	Type	Time (UT)	U (m)	V (m)	Airmass
Chi UMa	cal	15: 07: 07	23.85	80.61	1.38
Chi UMa	cal	15: 15: 39	21.92	81.25	1.41
RS Oph	trg	15: 50: 15	54.57	64.75	1.46
RS Oph	trg	16: 03: 46	55.35	64.37	1.39
RS Oph	trg	16: 12: 35	55.75	64.12	1.35
Rho Boo	cal	16: 34: 24	39.63	75.14	1.08

3.846 post-outburst bracketed with observations of two calibrators stars, ρ Boo and χ UMa. We obtained data in N-band from 8 to 12.5 μm through both ports of the KALI spectrograph with the gating of data for long baseline phase delay and group delay turned on. The Infrared Astronomical Satellite (IRAS) Low Resolution Spectrometer (LRS) spectra for the calibrator stars were flux-scaled according to the broadband IRAS 12 μm fluxes. We observed the calibrators ρ Boo and χ UMa and used them for flux calibration and to remove telluric features. A journal of observations is presented in Table 4.1.

Our data analysis involves removing biases and coherently demodulating the short-baseline fringe with the long-baseline fringe tuned to alternate between constructive and destructive phases, combining the results of many measurements to improve the sensitivity, and estimating the part of the null leakage signal that is associated with the finite angular size of the central star. Comparison of the results of null measurements on science target and calibrator stars permits the instrumental leakage — the system null leakage — to be removed and the off-axis light to be measured.

Sources of noise in the measurements made by this instrument have been well described elsewhere (Koresko et al. 2006), however, we think it is important to outline them here for completeness. The null leakage and intensity spectra include contributions from the astrophysical size of the object, phase and amplitude imbalances, wavefront error, beamtrain vibration, pupil polarization rotation, and pupil overlap mismatch. There are also biases, mostly eliminated by use of sky frames, in the calculated fringe quadratures, caused mainly by thermal background modulation due to residual movement of the mirrors used to shutter the combiner inputs for the long baselines. Another source of error is the KALI spectrometer channel bandpass, which is large enough to produce a significant mismatch at some wavelengths between the center wavelength and the short-baseline stroke OPD. This effect, termed warping, distorts the quadratures and is corrected by a mathematical dewarping step accomplished during calibration. There is also the effect of the partial resolution of extended structure on the long baselines which will cause the flux to be undercounted by some amount depending on the spatial extent and distribution of the emitting region. Compared to the error bars this is a rather small effect for most normal stars, and is unlikely to have much influence on the actual spectrum, though, unless the emission lines are coming from a very extended shell approaching 25 mas in angular size. We do not expect this to be the case for nova RS Oph at day 3.8. Other sources of noise include the difference between the band center wavelength for the interferometer and that of the IRAS LRS calibrator, undercounting of stellar flux resulting

from glitches in the short-baseline phase tracking, and the chromaticity of the first maximum of the long-baseline fringe. None of these are significant factors. Firstly, the calibration is based on the IRAS LRS spectrum rather than broadband photometry. Secondly, short-baseline tracking glitches happens nearly as frequently on target observations as on calibrator observations so it should have minimal effect on overall calibrated flux. The effect of chromaticity should likewise be negligible because fringe detection is done on a per-spectral-channel basis. As a result, it is only affected by dispersion within the individual KALI spectral channels, which are about 0.3 μm in width. The last, and clearly the most important contributor to measurement noise would be the sky and instrument drifts between target and calibrator. These observations were exceedingly difficult and so were conducted over a long period making this a significant effect, which we assume can contribute as much as 10 percent to the measurement error.

The uncertainty in our measurements with the KIN, then, as indicated by the error bars in Figure 4.2, are primarily statistical. They come principally from fluctuations in null depth that we obtain when we measure the value many times. For example, one basic sequence lasts a few 100 msec (depending on mode) and in one observation data is collected for some number of minutes, so after bad data rejection (gating) there are N estimates of the null depth, and the errors reported are the RMS of the N estimates conservatively augmented by the contributers noted above. We also note that error terms are different for each spectral channel, since they are treated and

analyzed independently, and each spectral channel has a different amount of light. Large differences in error bars among nearby well illuminated channels, however, would have been flagged and those data appropriately gated.

4.3 Data and Analysis

Figure 4.1 shows two sets of $8 - 12.5$ μm spectra of RS Oph on day 3.8 post-outburst. The upper plot shows the outer spatial regime which is the dimensionless null leakage spectrum, i.e., the intensity of light remaining after destructive interference divided by the intensity spectrum, plotted against wavelength in microns. The lower plot is the intensity spectrum, which is light principally from the inner 25 mas centered on the source brightness distribution orthogonal to the *Keck* Interferometer baseline direction - 38 degrees East of North. The null leakage spectrum may be broadly described as a distribution that drops monotonically with increasing wavelength overlaid with wide, emission-like features. The intensity spectrum, with an average flux density of about 22 Jy over the instrument spectral range, may be similarly described but with a continuum that has a saddle shape with a distinct rise at each end. The underlying shape curves sharply upward for wavelengths shorter than approximately 9.7 μm and longer than 12.1 μm. Overlaid on each of these are traces representing simple models of source brightness distributions fit to the data, described below.

We developed a complete mathematical solution and software suite to model the

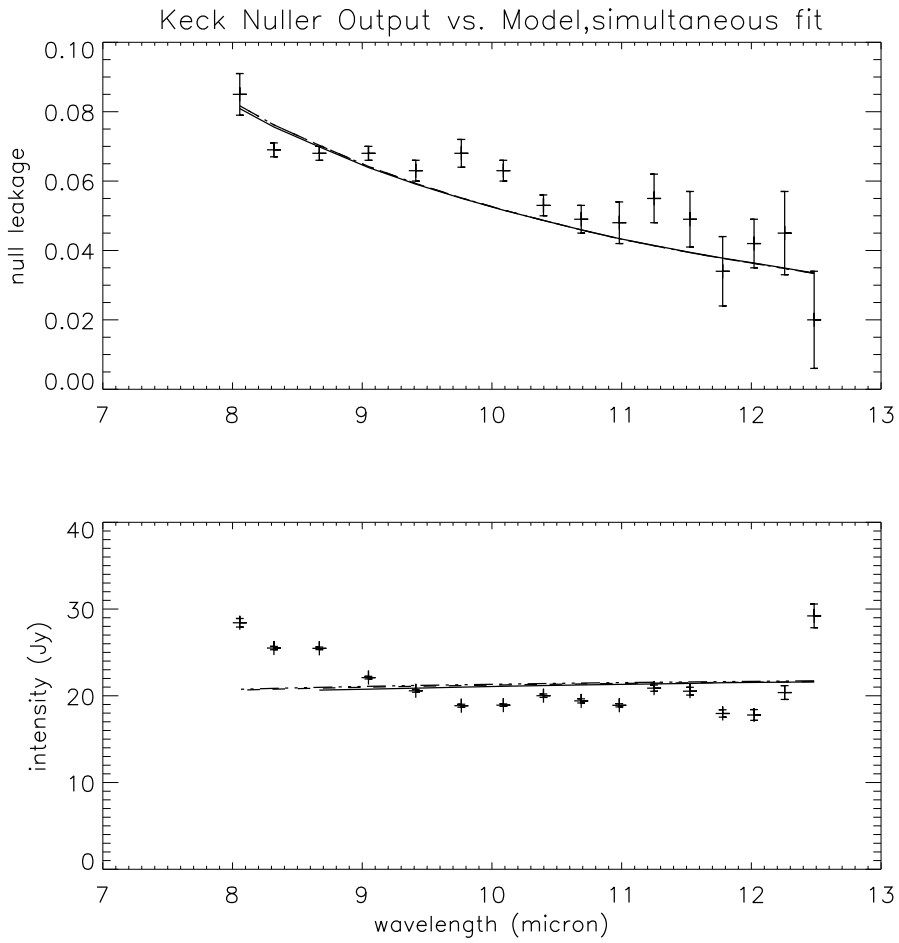

Figure 4.1 Plot of three best-fit continuum models against *Keck* Nuller data. All three models; disk, shell, and Gaussian, that minimized χ^2 simultaneously against the null leakage and intensity spectra, lie effectively on top of one another. The top trace gives the dimensionless null leakage or interferometric observable which is the null fringe output divided by the intensity spectrum. The lower trace is the constructive fringe output or intensity spectrum. As described in the text we have removed five data points from the original set for the purpose of fitting the continuum.

Table 4.2. RS Oph model fitting results

Source Model	Angular Size (mas) (N band)	Radiant Flux (Jy)	Major Size (mas) (K band)	Minor size[a](mas) (K band)
Uniform Disk	$6.2^{+0.2}_{-0.5}$	$22.4^{+3.9}_{-3.7}$	4.9 ± 0.4	3.0 ± 0.3
Uniform Gaussian[b]	$4.0^{+0.4}_{-0.4}$	$22.4^{+3.8}_{-3.7}$	3.1 ± 0.2	1.9 ± 0.3
Uniform Shell[c]	$5.4^{+0.5}_{-0.5}$	$22.4^{+3.8}_{-3.7}$	3.7 ± 0.3	1.9 ± 0.2

[a]Sizes for continuum values at 2.3 μm after Chesneau et al. (2007a).

[b]Full width at half maximum.

[c]Spherical shell with thickness 1.0 mas - optically thin.

observatory and source brightness distribution, and to conduct exhaustive grid search and Monte Carlo confidence interval analysis of solution spaces of these models. Using this suite we thoroughly explored three types of models for the source surface brightness distribution; Gaussian, disk, and shell. Limited (u, v) coverage permitted only rotationally-symmetric models with two parameters - size and flux. We used χ^2 minimization to obtain the best fit models for both the inner and outer spatial regimes simultaneously. Table 4.2 displays size measurements and flux values along with their respective $1 - \sigma$ confidence interval values.

The measurements made with the two KALI ports are somewhat independent - the data they produce are combined for purposes of fringe tracking, but not for data reduction. The system null and the final calibrated leakage are computed separately for the two ports. The apparent inconsistency detected between the ports is the result of optical alignment drifts at the time of the measurement. In particular, the last calibrator measurement showed a sudden change in the system null for Port 1, while for all the other calibrator measurements the system nulls were stable. We therefore

compared our source brightness distribution models against KALI port 2 data alone. For the best-fit models in Table 4.2 we used *Spitzer* spectra to identify and remove emission features centered at 8.7, 9.4, 10.4, 11.4, and 12.5 μm in the KIN Inner and 8.9, 9.8, and 11.4 μm in the KIN outer spatial regime. We removed the emission feature data because our intention was to model the continuum.

Figure 4.2 shows the inner and outer spatial regimes from the KIN data together with *Spitzer* data from day 63 (Evans et al. 2007). The absolute flux of these data are unscaled and given with a broken ordinate axis for clarity. In efforts to identify the sources of these emission features we took the high resolution *Spitzer* spectra and, using boxcar averaging, down-binned the data until it and the KIN data had the equivalent resolution. Close examination of this trace shows that it is similar in character to that of the KIN spectra. Importantly, the sum of the inner and outer spatial regime KIN spectra is nearly identical to the down-binned *Spitzer* spectrum with the exception that the absolute scale magnitude is, on day 3.8, about an order of magnitude greater than that of the *Spitzer* spectrum. This is as expected as the summed inner and outer spatial regime data should very nearly reproduce the transmission of a standard, single aperture instrument without occultation. Of particular interest in Figure 4.2 are the features between 9 and 11 μm. Here we note that the inner and outer KIN spatial regimes are subtly different from one another but, when summed (not shown), are similar to the down-binned *Spitzer* trace. It is also important to note that each of these low-flux features are better than one$-\sigma$ detections.

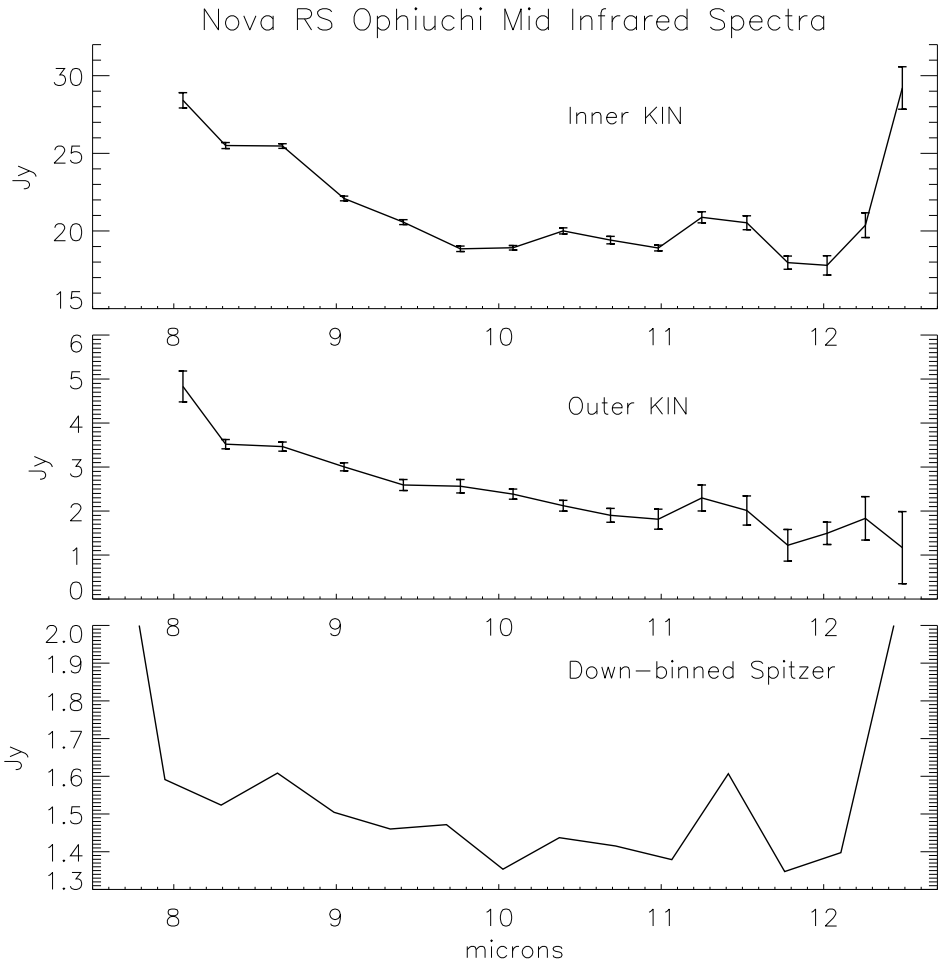

Figure 4.2 Plot of KIN spectra together with a *Spitzer* spectrum. Upper trace is the intensity spectrum or inner KIN spatial regime - light dominated by the inner 25 mas about the center of the source brightness distribution at mid band. The middle trace is the nulled fringe output which is the interferometric observable times the intensity spectrum. This is the outer spatial regime - light dominated by emission from material greater than about 12.5 mas (∼17 AU at 1.4 kpc) from the center of the source. The lower trace is *Spitzer* data (Evans et al. 2007) from day 63 boxcar averaged to yield approximately the same spectral resolution as the *Keck* Interferometer Nuller. None of the data were continuum normalized. Note especially the features between 9 and 11 μm and how the inner and outer spatial regime spectra are different from one another.

We discuss these features in greater detail below.

The frequency range sampled by the KALI spectrometer, 8 - 12.5 μm, covers many important discrete transitions such as molecular rotation-vibration, atomic fine structure, and electronic transitions of atoms, molecules, and ions. This range also samples several important transitions in solids such as silicates found in dust and polycyclic aromatic hydrocarbons (PAHs) formed by the juxtaposition of benzene rings. With the exception noted below, spectral features in the KIN data are clearly not resolved by the instrument and are often, in the associated *Spitzer* spectrum, Doppler broadened and blended. Also, because the *Spitzer* spectra were not taken contemporaneously with the KIN spectra and because of the transient nature of the RN, identification of KIN features with emitting species is somewhat problematical.

Figure 4.3 shows spectra taken using the *Spitzer* space telescope on days 63, 73 and 209 after peak V-band brightness. Here we see the monotonic decline in the continuum as time progresses. The average value of the continuum in these spectra are approximately 1.4, 1.1, and 0.25 Jy for the April 14, 26 and September 9 spectra, respectively. The first two spectra on April 14 and 16, 2006 show strong atomic line spectra with no obvious evidence of dust emission although we expect that thermal bremsstrahlung from the central source will overwhelm any other faint sources in these very low spatial resolution *Spitzer* spectra. In contrast, the spectrum taken on 2006 September 9 shows a distinct broad, blackbody-like feature spanning a range of wavelengths from 8.9 to 14.3 μm peaking at 10.1 μm. Additionally, there are several

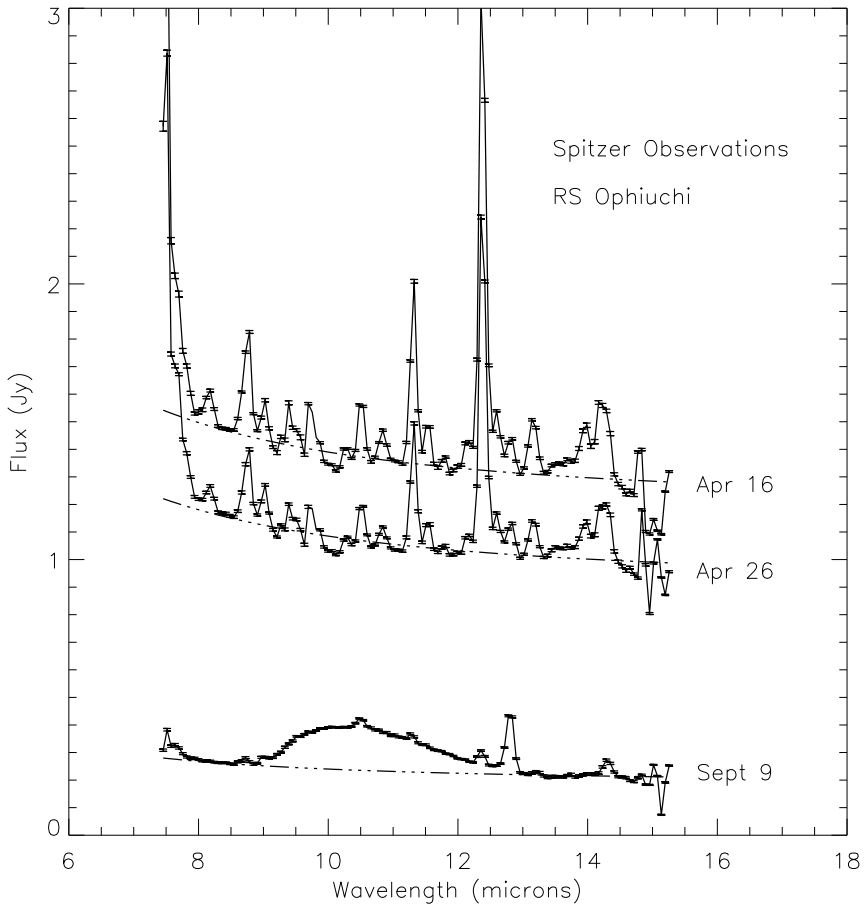

Figure 4.3 *Spitzer* space telescope spectra from days 63, 73 and 209. Here we see that the continuum drops rapidly as time advances with the spectral emission features almost identical on days 4/16 and 4/26. Data obtained on 9/9 is starkly different with a strong solid-state feature evident between 9 and 13 μm (Evans et al. 2007).

narrow emission features in this latter spectrum some of which appear to be similar to those evident in the earlier spectra. We proceed on the assumption that this is a solid-state continuum emission from a condensate in the vicinity of the nova.

Referring again to the KIN spectrum in Figure 4.2, continuum radiation is apparent in both inner and outer spatial regimes. In contrast, while the continuum was still clearly visible in J, H, I, K bands on February 24 and detectable on April 9 (Evans et al. 2008), it is readily apparent that it has substantially subsided by day 63 in Figure 4.2 and Figure 4.3. When we compare the spectra from RS Oph to those from V1187 Sco (Lynch et al. 2006) we note that the continuum given for V1187 Sco is non-Planckian showing an excess longwards of 9 μm and is strongly red as compared to a F5V Kurucz spectrum. Making a direct comparison of the V1187 Sco and RS Oph continua we find that the slope (the rate of change of the intensity as a function of λ) agrees to within 10%. While both free-bound and free-free transition processes lead to emission of continuum radiation, in the MIR spectral range thermal bremsstrahlung free-free emission dominates. We attribute the drop in continuum radiation evident in Figure 4.2 to the transition to line-emission cooling mechanisms. Also, by the time *Spitzer* data were taken, the object had become less dense and so the emission coefficient for thermal bremsstrahlung (proportional to number density of protons and electrons) had dropped considerably. The continuum emission is described in detail by Barry et al. (2008b) and Chapter 5.

Table 4.3. Mid-infrared *Spitzer* line list: N-band

Wavelength (μm)	ID	*Spitzer* 4/16 (Jy)	*Spitzer* 4/26 (Jy)	*Spitzer* 9/9 (Jy)
7.460	$Pf\alpha - HI$: $6-5$	detected[a]	detected	detected
7.652	$[NeVI]$	detected	detected	detected
8.180	FeI	0.009	0.007	–
8.760	HI: $10-7$	0.042	0.038	0.020[b]
8.985	$[VII]$, Si I, & Ca I]	–	–	0.010
9.017	FeI	0.015	0.021	–
9.288	CaI	0.004	0.004	–
9.407	SiI	0.014	0.013	–
9.529	CI	0.009	0.008	–
9.720	CII	0.018	0.017	–
9.852	CaI	0.007	0.008	–
10.285	MgI	0.007	0.006	–
10.492	HI: $12-8$	–	–	0.013
10.517	NeI	0.026	0.026	–
10.833	$CI]$	0.018	0.016	–
11.284	HI: $9-7$	–	–	0.007
11.318	HeI	0.060	0.053	–
11.535	$HeII$	0.016	0.013	–
12.168	HI: $36-11$	0.011	0.009	–
12.372	$Hu\alpha - HI$: $7-6$	0.158	0.150	0.037
12.557	SiI	0.040	0.036	–
12.803	$[NeII]$	–	–	0.159
12.824	HeI	0.009	0.015	–
13.128	$HeII$	0.009	0.011	–
13.188	HI: $18-10$	0.009	0.010	0.005

[a]Detected in *Spitzer* spectrum but not fit due to intrusion of band edge.

[b]Blended with neutral hydrogen lines at 8.721 and 8.665 μm

Table 4.4. Continuum-normalized KIN emission source identification

Center Wavelength (μm)	Spectroscopic Width (μm, FWZM)	Flux (Jy)	Attributed to
	KIN Inner Spatial Regime		
8.7	8.3 - 9.1[b]	0.06[b]	H I: 10-7, FeI, Ca I[c]
9.4	8.9 - 11.1	0.02	Ca I, Si I, C I, C II
10.4	9.9 - 11.1	0.04	Mg I, Ne I, C I]
11.4	11.1 - 11.8	0.07	He I, He II
12.5	12.1 - 12.6	0.15	Huα
	KIN Outer Spatial Regime		
8.9	8.3 - 9.5	0.14	H I: 10-7, [V II], Si I, Ca I][d]
9.8	9.0 - 10.7	0.24	Silicate Dust[e]
11.4	11.0 - 11.8	0.19	H I: 9 - 7, He I, He II

[a]Approximate FWZI continuum crossing points.

[b]Because *Keck* and *Spitzer* data were not taken simultaneously and because of the transient nature of the RN outburst it is not possible to determine particular flux numbers to the atomic lines attributed to the KIN feature. The flux listed should be considered the maximum, bounding flux for any one of the atomic species shown here.

[c]All atomic line emission in the KIN inner spatial regime is assumed to be emitted by a species at approximate cosmic abundance as for RN only a very moderate amount of nucleosynthesis is expected to occur.

[d]All atomic line emission in the KIN Outer spatial regime are assumed to be predominantly of nebular abundance with some contribution from uncondensed metals.

[e]Spectral feature is spectrally and partially spatially resolved. Silicate dust feature has more than seven spectral elements across it and emits relatively strongly at a distance centered approximately at 2.5×10^{14}cm from the WD. All flux is assumed to be attributable to emission by the dust.

Table 4.3 identifies all narrow features in Figure 4.3 where it is possible to do so. Identifications are restricted to the N-band as our purpose is to attempt to draw conclusions about features detected in the KIN spectra. Here we give the particular process and assumptions used in determining these atomic species. Table 4.3 was generated using line lists of atomic species assuming that all ionization stages of all elements were possible for the three *Spitzer* spectra. We further imposed the restriction that all elements were assumed to have standard cosmic abundances as set forth

in Grevesse (1984). After continuum normalization, we carefully fit each emission line with a Gaussian and, where necessary, de-blended using IRAF. We then obtained line wavelengths and fluxes and made a comparison to the line list we calculated previously. Where there was ambiguity due to the closeness of generated lines we identified the species with the greatest cosmic abundance as the source. If atomic species in the calculated line list had significantly similar abundances we compared transition probabilities and opted to report the species with the highest probability. In the unlikely event that the Einstein transition probabilities *and* the cosmic abundances were similar, we report whichever species had the lowest-lying starting energy state on the assumption that those species would have the greatest occupation numbers although the environment was doubtlessly not in thermal equilibrium. For the species recorded for the *Spitzer* data taken on September 9, 2006, an additional restriction was levied on the generated atomic line list in the event that two or more calculated species shared very similar emission line wavelength. In this case, based on the evidence of the solid-state feature in the spectrum, we assumed that the environment of RS Oph at that time had become substantially nebular in character. Here we assumed that metals would more likely have condensed onto dust grains in the vicinity of the nova and that allowed transitions of hydrogen and helium, magnetic dipole and electric quadrupole transitions of all other elements, and ground-state forbidden transitions would be the likely source of line emission (Cowie and Songaila 1986). Importantly, we still allowed the possibility of cosmic-abundance atomic line emission as we had

no way of knowing the particular depletion state in the vicinity of the nova a priori. Finally, we suppressed all hydrogen fine structure and auto-ionization states in this line identification list as the former would be irretrievably blended and the latter would provide no new information.

Table 4.4 gives our identification of particular emission sources with the continuum normalized spectral features in the KIN inner and outer spectra. In this table, we list the center wavelength of each of the broad features for easy identification. We then list a width for each feature where we identify the cutoff wavelength at the intersection of the the feature and the unity continuum line — the full-width zero intensity (FWZI) level of the feature. We list the flux contained in that feature through measurement of the total area under it and above the unity continuum level. Lastly, we identify particular atomic species found in the *Spitzer* spectrum with each KIN spectral feature. It is important to note that each KIN spectral feature listed in Table 4.4 is a minimum $1-\sigma$ detection. Because the *Spitzer* Space Telescope lacks the spatial resolution to discriminate the inner from the outer regions of the nova and the KIN lacks the spectral resolution to discriminate among atomic species we asserted that features in the KIN spectra would most reasonably be identified with *Spitzer* features we had already established as being represented in later spectra. In particular, we assumed in this association of *Spitzer* emission lines with KIN features that the KIN inner spatial regime, dominated by light originating in the close vicinity the WD, would be well-represented by a cosmic distribution of atomic elements. We

reasoned that any condensates within the blast radius of the nova would be sublimated away and dissociated into atoms and that the nucleosynthesis that occurred in the outer layers of the WD during TNR would only minimally impact abundances. We then keyed the KIN inner spatial regime spectral features to *Spitzer* spectral features in the 4/16 and 4/26 spectra. Similarly, the KIN outer spatial regime, light predominantly from a region approximately 2.5×10^{14} cm from the WD, is keyed to the *Spitzer* spectrum taken on 9/9 as we assumed that the abundances of atomic species in the latter, nebular *Spitzer* spectrum would reasonably be representative of the environment sensed by that KIN channel.

We note that, with analogy to other symbiotic novae (e.g. V1016 Cyg, RR Tel), prominent features at 10 and 18 μm such as are evident in our extended *Spitzer* spectrum have been fitted by crystalline silicate features (Sacuto et al. 2007; Schild et al. 2001; Eyres et al. 1998). Motivated by this and in support of our assumption that the *Spitzer* 9/9 data are indicative of a nebular environment and to assess whether or not dust can survive in the environment observed by the KIN, we calculated the temperature and emission SED of various species of dust at the range from the WD at which the KIN's outer spatial regime has maximum transmission. The center of the first constructive fringe, when the null fringe is located on top of the WD, at a wavelength of 9.8 μm and a projected baseline of 84 m, is approximately 24 mas from the WD. At a distance to the object of $1.4^{+0.6}_{-0.2}$ kpc (Barry et al. 2008) this corresponds to about 2.5×10^{14} cm or about 16.7 AU. On day 3.8 after maximum

V-band brightness the WD luminosity was approximately 2×10^{37} erg/sec. The theoretical heating rate of dust depends quadratically on the geometrical cross section of the grains and inversely as the square of the distance to the WD. The luminosity of the grains depends on the mass absorption characteristics of the particular type of dust and may be found by convolving a blackbody of a given temperature with the mass absorption coefficient per unit wavelength of the dust. The intersection of the locus of points of luminosity of the dust as a function of temperature and the heating rate for a given range from the WD yields the dust temperature. We tested models of particulate 0.1 μm and 0.0042 μm graphite, carbon, and silicate dust located in a field at a range of distances of from 2.5×10^{14} cm to 5.0×10^{14} cm from the WD and found that sublimation temperatures were not exceeded for the given WD luminosity. We further compared the resulting theoretical dust emission SED to that measured in the *Spitzer* 9/9 data. Using a very simple model of the continuum that included only the warm dust emission with nebular continuum we found that, to first order, silicate dust at about 200 K fit the data well and that the other types of dust appeared to be excluded by the data. Furthermore, we tested several temperatures of silicate dust and found that dust in a temperature range of 800 - 1000 K was consistent with the KIN outer spatial regime data.

Importantly, the dust feature in the *Spitzer* 9/9 spectrum falls across over seven spectroscopic elements in the KIN outer spatial channel opening the possibility that the dust is both spectrally resolved and spatially localized. A much more thorough

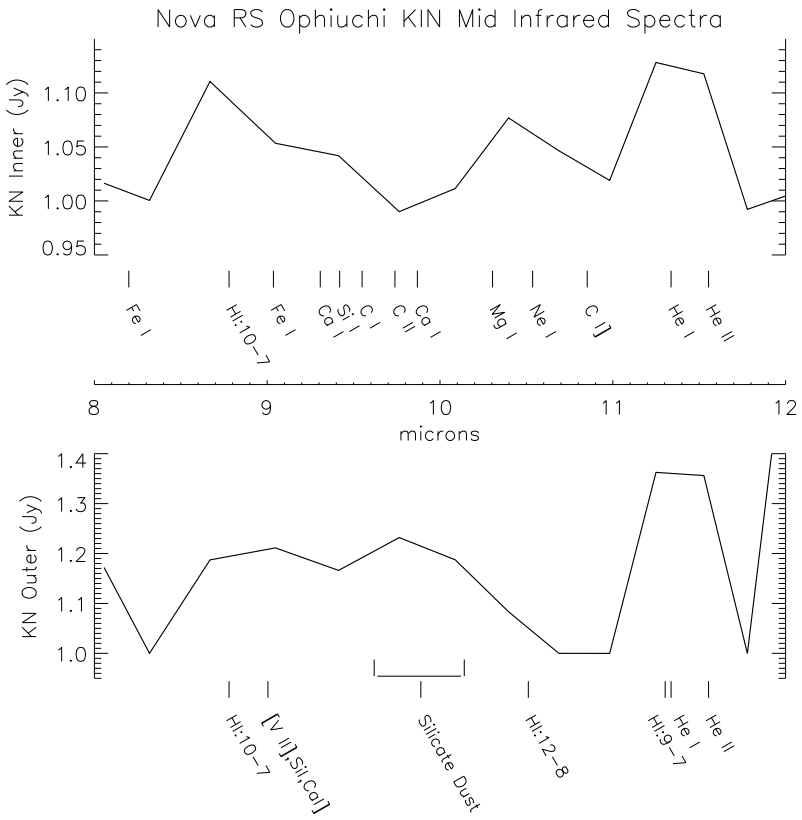

Figure 4.4 Continuum normalized KIN spectra 3.8 days after peak V-band brightness. Spectra are shown matched with lines identified in *Spitzer* spectra. The inner spatial regime line identification was matched to the cosmic abundances seen in the earlier *Spitzer* spectra while the outer spatial regime was biased towards the later spectrum on September 9, 2006 that included a solid state feature and were assumed to have primarily nebular abundances. Note that we removed error bars and truncated the spectrum at 12 microns to remove the very strong feature in the KIN Inner spatial regime identified with Huα for clarity. The rise at the longward end of the KIN Outer spectrum is an artifact of the polynomial continuum fit.

analysis of the continuum emission in these spectra have been carried out and will be reported in Barry et al. (2008b) and Chapter 5, however, it is likely that the solid state feature in the *Spitzer* 9/9 data may be attributed to silicate dust and that the theoretical temperatures of silicate dust at a range from the WD that would be sensed by the KIN outer spatial channel are below the sublimation temperature of this species.

Figure 4.4 shows the association of identified *Spitzer* atomic emission lines with the continuum-normalized KIN inner and outer regime spectral features. We note that the two spectra are markedly different. It is also important to emphasize that when the inner and outer spatial regimes are summed, the result closely follows the down-binned *Spitzer* spectra with the exception of the KIN outer spatial regime feature (lower plot) centered at 9.8 μm. Based on our assumptions of a primarily nebular environment in the vicinity of the outer spectrum, the atomic metals evident in the upper trace (KIN inner spatial regime) would be unlikely to contribute to this feature. In any case, the total power in these metal lines in the wavelength range of this feature (cf. Table 4.3), i.e., Ca I, Si I, C I, & C II, evident in the upper plot is 0.05 Jy while that in the broad feature centered at 9.8 μm in the lower plot is substantially more intense at 0.24 Jy. Our models suggest that the source of this feature may be hot silicate dust in the temperature range 800 - 1000 K.

It is very important to note that the result of deliberately obscuring the bright source centered on the WD by placing a destructive interferometric fringe over it

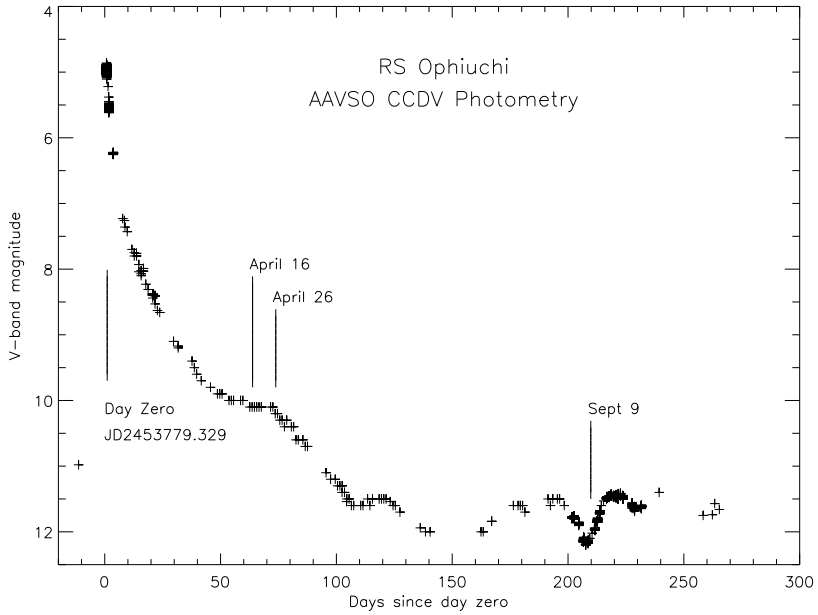

Figure 4.5 AAVSO photometry with $T_2 = 4.75$ days and $T_3 = 10.19$ days indicated. Note the end of the plateau phase on 4/26/06 - evidence of the hydrogen burning turnoff theorized by Hachisu et al. (2006). Note the evident strong, short-duration fluctuation of V-band brightness about 9/9/06. This may be evidence that dust orbited into the line of sight.

allows us to sense the faint emission originating in outlying areas and that these areas are well outside of the blast radius assuming an initial front velocity of 3500 km/s (O'Brien et al. 2006) and negligible deceleration. The radiation in this spatial channel originates primarily in material around the nova that has been illuminated and warmed by the nova flash and, as a result, must have been there *before* the nova event. This establishes that silicate dust, created in the vicinity of the RS Oph system some time previous to the 2006 epoch outburst, is detected by these measurements.

Figure 4.5 gives the AAVSO V-band photometry from the maximum to 300 days post-outburst. Centered at about September 4, 2006 (JD 2453983) is a strong depression in visual intensity. We have indicated on the lightcurve the dates that *Spitzer* spectra were taken (Evans et al. 2007). In particular, we note that the *Spitzer* data of 2006 September 9 shows the broad, rounded spectral features noted earlier as being associated with resonances in aggregates of molecules or dust grains. In classical novae, fluctuations in V-band emission have been shown to be closely related to rapid changes in mass loss from the primary and have also been shown to be contemporaneous with reprocessing of the light into infrared wavelengths. Taken together, these are evidence for a possible sudden obscuration of the light source by dust. As argued previously, the KIN measurements indicate the possibility that there is dust in the system that exists between nova events and it could be this dust that is evident in Figure 4.5.

4.4 A New Physical Model of the Recurrent Nova

One aspect of the RS Oph binary system that has been neglected in the current literature regarding the recent outburst is the effect of the motion of the two stars through the wind created by mass loss from the red giant star. Garcia (1986) suggested that there could be a possible ring of material of diameter less than 40 AU around the RS Oph binary system or possibly surrounding the red giant component, based on his measurements of an absorption feature in the core of the Fe II emission line profile at 5197 Å. The observations were performed in 1982 and 1983, several years before the 1985 nova outburst.

Subsequently, and motivated by somewhat different observations, Mastrodemos and Morris (1999) computed three-dimensional hydrodynamical models of morphologies of the envelopes of binaries with detached WD and RG/AGB components in general. Their purpose was to see if these models could reproduce some of the observed characteristics of axisymmetric or bipolar pre-planetary nebulae. Their study focused on a parameter space that encompassed outflow velocities from 10 to 26 $km\ s^{-1}$, circular orbits with binary separations from 3.6 to 50 AU, and binary companions having a mass range of 0.25 to 2 $M_{\odot}$. For binary separations of about 3.6 AU and mass ratios of 1.5, it was possible to generate a single spiral shock that winds 2-3 times around the binary before it dissipates at > 25 times the radius of the RG star. There is an density enhancement of about a factor of 100 over the normal density in the wind in the plane of the orbit of the two stars, and an under density or

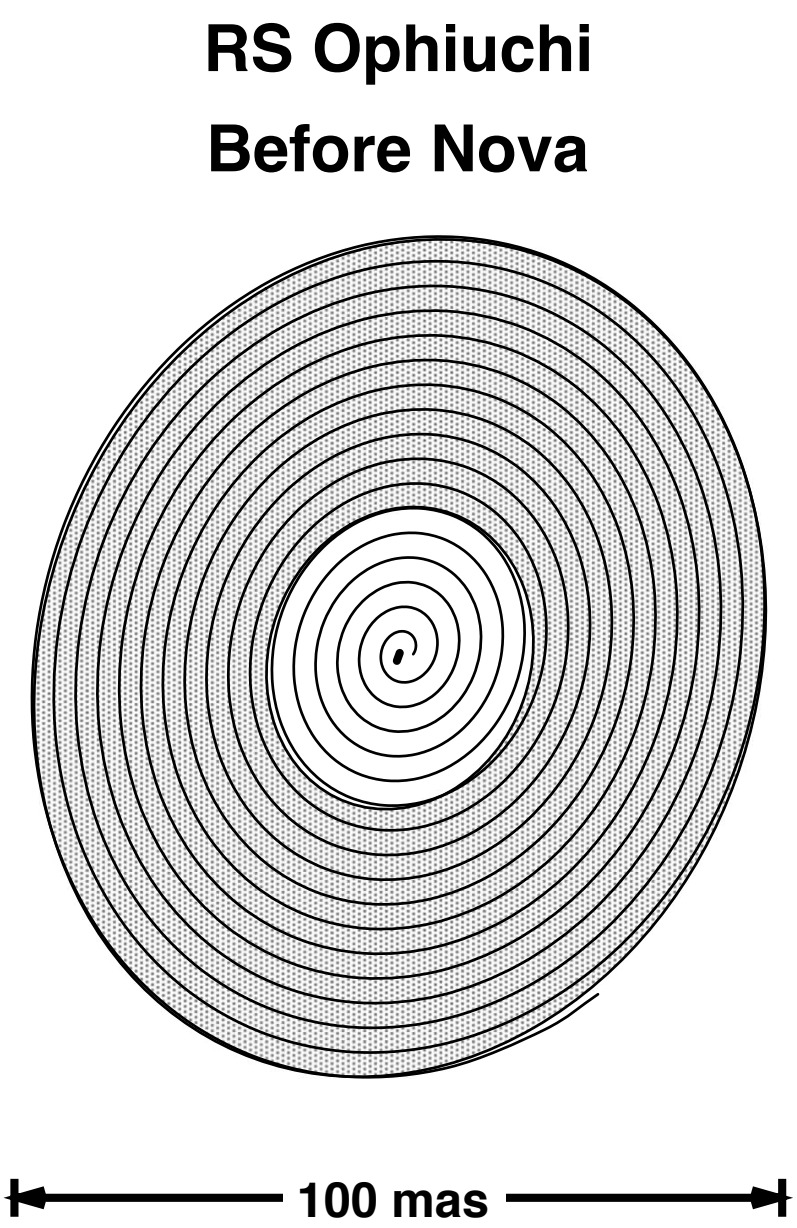

Figure 4.6 Proposed model of circumstellar material surrounding the binary RS Oph before the nova eruption. The interaction of the white dwarf and red giant star in the slow dense wind of the red giant star can create a spiral shock with an enhanced density in the plane of the orbit of the two stars. The overall size of the dense in-plane material is of the order of 100 mas if RS Oph is at a distance of 1600 pc and the wind speed is about 20 km/s.

evacuated region perpendicular to the plane of the orbit. Observational support for this model was fond recently by Mauron and Huggins (2006) who observed a spiral pattern around the AGB star AFGL 3068 which is consistent with the model of Mastrodemos and Morris. The underlying binary, a red giant and white dwarf, was discovered by Morris et al. (2006), who also determined the binary separation and hence approximate orbital period, which was consistent with expectations from the appearance of the spiral nebula pattern seen by Mauron and Huggins and the model.

Figure 4.6 shows the proposed geometry of the nebula in the plane of the orbit of the RS Oph system based on the parameters adopted from Dobrzycka and Kenyon (1994) for the system, including an orbital period of 460 days, and an inclination angle of about 33 degrees, for the epoch just prior to the nova outburst. The spiral shock model produces an archimedean spiral nebula, with the separation between adjacent windings of about 3.3 mas based on the period noted above and a wind speed from the red giant star of 20 km/s. Note that we expect there should be about 17 such rings created between outbursts, with the overall size of the nebula of the order of 100 mas.

In order to better understand the KIN observations and other high angular resolution observations, we have modeled the evolution of the circumstellar nebula following the outburst. For the purposes of this discussion, we adopt the model of Hachisu and Kato (2001), but with the simplifcation of a flat accretion disk geometry, i.e., not warped as in their paper. The details of our calculations are presented below.

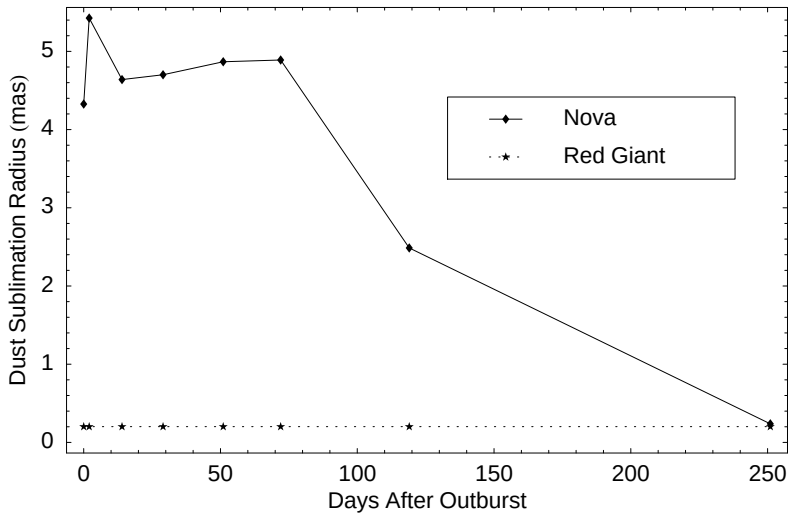

Figure 4.7 Sublimation radius of dust (mas) as a function of the number of days post-outburst for the Nova and for the red giant companion.

The results are of fundamental importance to the interpretation of the data, and we begin with the most immediate effect after the blast, which is the sublimation of dust within a zone where the temperature of a blackbody dust grain would be > 1500 K in equilibrium. Figure 4.7 (the derivation of which is described in Section 4.4.1) displays the evolution of the dust sublimation radius, which is roughly 4-5 mas until about day 70, after which it steadily declines to $<<$ 1 mas about 250 days after the outburst. This means that much or all of the dust within this zone has entered the gaseous phase, except for a small "sliver" of material in the shadow of the red giant star. This provides additional hot gas (rich with metals) that is subsequently affected by the blast wave passing through within the next few days.

As the two stars move relative to each other in their orbit about their common center of mass, the location of the shadow of the nova moves, and consequently

the material in the shadow that has not been affected by the blast wave from the nova will be sublimated during this luminous phase, creating hot gas in the vicinity within a few mas of the stars. This material may still have the type of repeating density structure that was initially present, and may be observable with high angular resolution instrumentation.

Whether or not this particular material is observable, depends in part on the density distribution as a function of latitude of the plane of the orbit of the two stars. If the material is uniformly distributed over 4π steradians, then the fraction of the total solid angle subtended by the red giant star as seen by the white dwarf star is approximately 0.13 – 0.29% for a RG star between 27 and 40 $R_\odot$ and a binary separation of 1.72 AU. However, the hydrodynamical studies of Mastrodemos and Morris show that the density falls of steeply as a function of latitude, and is as low as 1% of the mid-plane density by latitudes of about ± 40 degrees. This gives a scale height of about 9 degrees. Thus, the red giant star subtends a much bigger fraction of the solid angle up to this scale height, i.e., to as much as 1.9%.

Furthermore, studies of the supernova blast waves around red giant stars indicate that the blast wave diffracts around the RG star, with a hole in the debris of angular size $\sim$ 31-34 degrees, which did not depend strongly on whether the companion star was indeed a RG star or a main sequence or subgiant star (Marietta, Burrows, & Fryxell 2000). In this case the fraction of the sky subtended by this hole in the debris field is $\sim$ 10-13 %. If the material is concentrated in the mid-plane, the effect

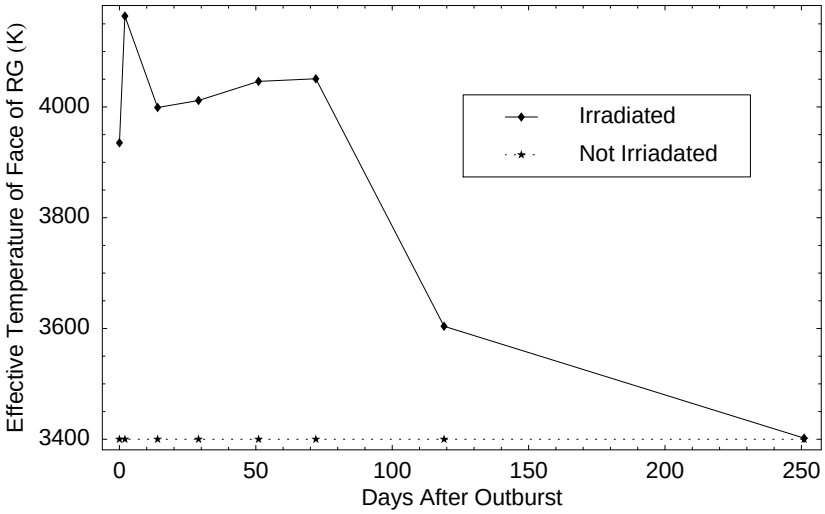

Figure 4.8 Temperature of red giant star for the surface that is facing the Nova as a function of the number of days post-outburst. Also plotted is the temperature of the non-irradiated side of the red giant. Modeled temperature rise is due to heating from irradiation by the nova and neglects any effect due to the passage of the forward shock.

is substantially bigger as noted in the previous paragraph. Thus there are several reasons to expect that material in the shadow of the RG star can have an observable effect.

Stripping of material from the red giant companion by the blast wave for supernova has been studied by Wheeler, Lecar, & McKee (1975) and by Lyne, Tuchman, & Wheeler (1992), however, Lane et al. (2007) showed that stripping of material for the RG star is negligible for the less energetic blasts from RS Oph.

Another effect, depicted in Figure 4.8 (with derivation given in Section 4.4.1) is the heating of the surface of the red giant star that faces the nova for times past the maximum in the visible light curve. Our calculations indicate that this side

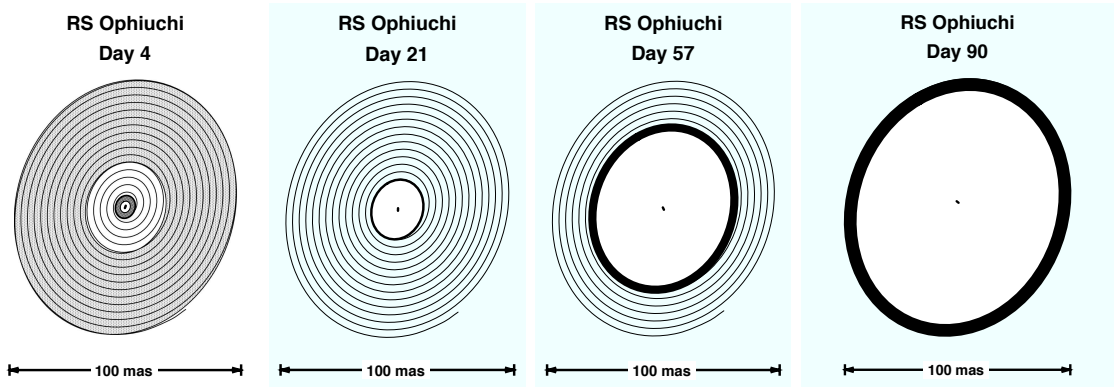

Figure 4.9 Spiral dust nebula model of RS Oph. (a) Top left panel displays the system geometry at 4 days post-outburst. A gray ring is drawn in the center of the figure to indicate the size of the shocked region at this epoch. The outer part of the spiral is overlayed with light gray to indicate that it is not known if the material stays in a coherent spiral past the first several turns. The diameter of the shocked region is about 5 mas assuming the blast wave travels at a velocity of $\sim$ 1800 km/s in the plane of the orbit. (b) Top right panel. The blast wave is now about 13 mas in diameter on day 21. (c) Bottom left panel. The blast wave is about 36 mas in diameter on day 57. (d) Bottom right panel. By day 90 the blast wave has traversed the entire spiral pattern.

of the red giant star increases from about 3400 K to as much as 4200 K within a few days past the outburst. The temperature steadily declines from day 70 until it reaches equilibrium with the other side around day 250. The surface of the RG star is initially heated by the shock from the blast wave (not included in our calculations), however, the continued heating during the high luminosity phase is important as it affects the interpretation of data from modern complex instrumentation such as stellar interferometers and adaptive optics systems, where various subsystems are controlled at wavelengths other than the measurement wavelength.

Figure 4.9 displays a schematic view of the system geometry from days 4 to 90

after the recent outburst. Assuming typical wind velocities of about 20 km/s for the red giant wind, there are roughly 17 rings separated by approximately 3.3 mas that form between RS Oph outbursts. The top left panel displays the system geometry at 4 days post-outburst. A gray ring is drawn in the center of the figure to indicate the size of the region affected by the blast at this epoch. In (a) the outer part of the spiral is overlaid with light gray to indicate that it is not known if the material stays in a coherent spiral past the first few turns. The diameter of the shocked region is about 8.8 mas assuming the blast wave travels at a velocity of $\leq$ 1800 km/s in the plane of the orbit, using the velocity measured by Chesneau et al. (2007a), at approximately the same epoch as our measurements. (We acknowledge that most out-of-plane blast-wave velocities noted in the literature are much higher than this.) In this figure we assume the blast wave moves at constant velocity as it traverses the spiral shock material. We show the extreme case in which the blast wave is 100% efficient in sweeping up material, thus creating a ring-like structure that propagates outward from the system. Note this figure is meant only to be illustrative and differs in detail from estimates of the position of the blast wave from observations, such as O'Brien et al. (2006) who obtained a value of the shock radius of 8.6 mas at day 13.8 by which time the blast wave had apparently slowed considerably. We obtain a value of 10.5 mas for the shock radius assuming a constant velocity of $\sim$ 1800 km/s from one day past the initiation of the TNR process, which is about 3 days before maximum light in V band (Starrfield et al. 1985). The value of 8.6 mas at day 13.8

is consistent with a somewhat lower mean velocity, of the order of 1400 km/s. It is beyond the scope of this paper to compute the evolution of the blast wave, however, this figure makes a connection with the previous observational evidence for a ring of material concentrated in the plane of the orbit as discussed by Garcia (1986) and with the recent observations of Chesneau et al. (2007a) who observe different velocities perpendicular to the plane of the orbit than in the plane of the orbit.

The evolution of the luminosity of the red giant and nova is also significant in aiding our understanding of the observations. Figure 4.10(a) displays computed V band light curves up to day 250 after the outburst including the effect of the irradiation of the accretion disk and the irradiation of the red giant star by the nova. Note this calculation overestimates the total luminosity of the nova during the period from about 10 days to about 50 days, and this is likely due to the simplified disk geometry that we have employed in our own calculations. Most importantly these light curves show that the V band luminosity is dominated by the nova for about the first 50-70 days, and after that the red giant star dominates the V band luminosity. This is significant as most telescopes track on V band light (including interferometers) and the tracking center then moves by a mas or so during the post-outburst evolution of the system. H band luminosity evolution is plotted in Fig. 4.10 (b), and is different than that of the V band evolution. At H band the nova dominates the luminosity only for the first 5 days or so, and after that the H band light curve is completely dominated by the red giant star. This means the phase center for fringe detection

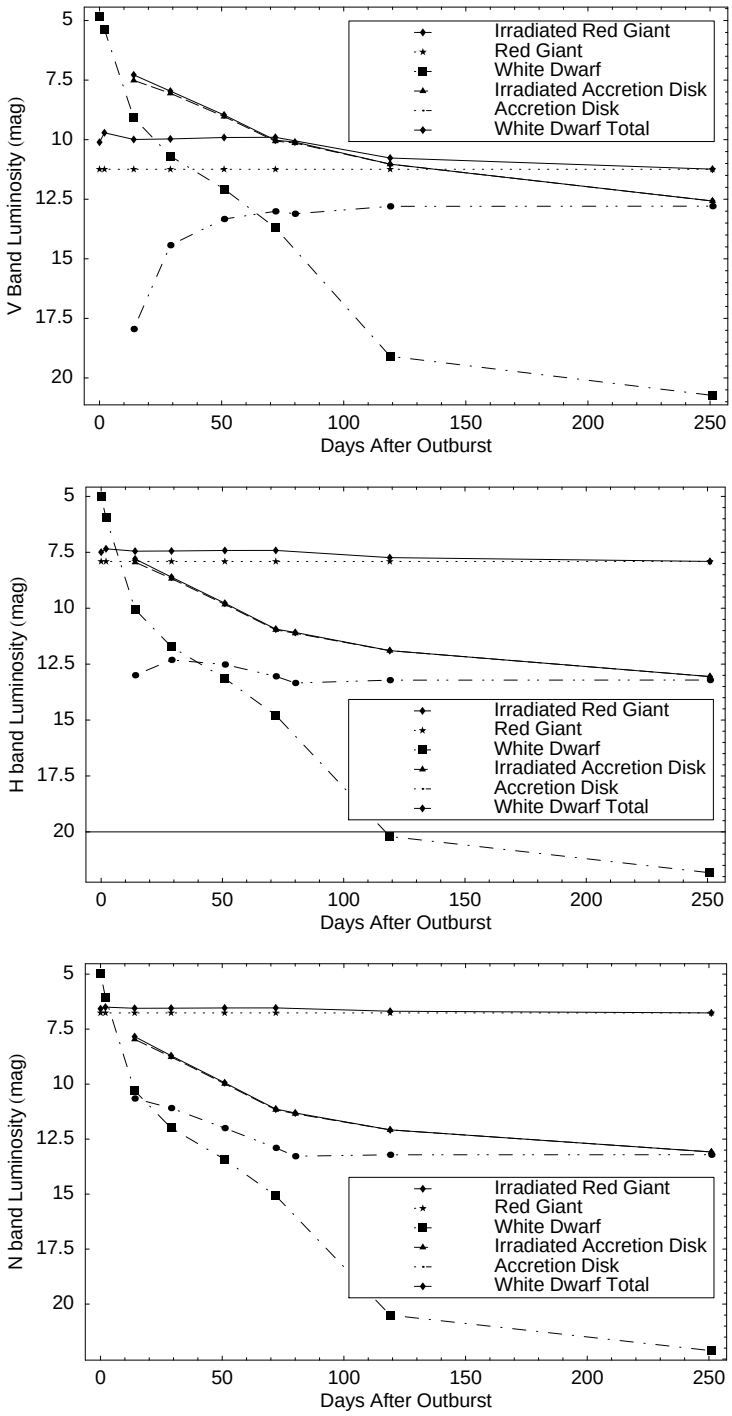

Figure 4.10 (a) V Band luminosity as a function of time for Nova and red giant components of binary system.(b) H band luminosity evolution. (c) N band luminosity evolution.

is offset from that of the tracking center from days 5 onward by a mas or so, as mentioned above. The N band luminosity, displayed in Fig. 4.10 (c), evolves like that of the H band, and the nova dominates the mid-infrared light only up to day 4. After that there is an offset between the tracking center and N band fringe center like that noted for the H band.

4.4.1 Luminosity Evolution

In this section we discuss the mathematical formulation used to derive the evolution of the luminosity of the white dwarf star starting at the maximum magnitude in V band. Our calculations are based on those presented in the paper by Hachisu and Kato (2001), who expanded on their discussion of their light-curve model presented in Hachisu and Kato (2001).

Our purpose is to evaluate the light curve not only at V band, but also at H, K, and N bands, which have been used by the AMBER, IOTA, KIN, and PTI interferometers to observe RS Oph after the 2006 outburst. Our discussion is in fact relevant to any modern instrument that has wavefront sensing and control, and also tracking, at wavelengths different than that of the observations of interest. For example, the IOTA interferometer performs its precison pointing at V band, but observations are made at H band. Similarly the KIN does precision pointing at V band, wavefront control of the two large apertures at H band, and the data are taken at N band. This difference in wavelengths is important because as the V band luminosity of the white

Table 4.5. Post-outburst evolution of the white dwarf star in RS Oph

Time[a] (days)	Radius ($R_\odot$)	Temperature (K)
0	45	12200
2	21	20000
14	1.6	67000
29	0.56	114000
51	0.23	181000
72	0.083	302000
119	0.0037	1020000
251	0.003	350000

Note. — Stellar parameters for the white dwarf star after the 2006 outburst of RS Oph based on Hachisu and Kato (2001)

[a]The origin of time for these parameters is the V band maximum light, which occurs about 3-4 days after the thermonuclear runaway process begins.

dwarf star decreases, the observed light from the binary is mainly from the red giant star, which gives a shift in the center of light. This shift can affect the calibration of these instruments as there is an offset, which will change over time as compared to a calibrator, which has all the same optical center at all times for all of these wavebands.

The evolution of the stellar parameters for the white dwarf are given in Table 4.5 (Hachisu and Kato 2001), while we assume the parameters for the red giant star remain constant with $R_{rg} = 40R_\odot$, and $T_{rg} = 3400$ K.

The blackbody flux density at a frequency, ν, for a star of temperature, T_*, radius, R_*, and distance, D is:

$$F_*(\nu) = 2\pi(R_*/D)^2(h\nu^3/c^2)/[exp(h\nu/kT_*) - 1], \tag{4.2}$$

where h, k, and c, are Planck's constant, the Boltzmann constant, and the speed of light, respectively.

The total luminosity is:

$$L_* = 4\pi\sigma {R_*}^2 {T_*}^4, \tag{4.3}$$

where σ is Stefan's constant.

Sublimation Radius

The temperature of a black grain in radiative equilibrium at a distance, r, from a star with luminosity, L_* is:

$$T_{grain} = \left(\frac{L_*}{16\pi\sigma r^2}\right)^{1/4} = \frac{T_*}{\sqrt{2}}\left(\frac{R_*}{r}\right)^{1/2}. \tag{4.4}$$

A simple rearrangement of the above equation yields a formula for the sublimation radiius, R_{sub}, assuming a sublimation temperature, T_{sub}:

$$R_{sub} = \left(\frac{L_*}{16\pi\sigma T_{sub}^4}\right)^{1/2} = \frac{R_*}{2}\left(\frac{T_*}{T_{sub}}\right)^2. \tag{4.5}$$

where T_{sub} is the sublimation temperature. For this paper we assume a sublimation temperature of 1500 K.

The evolution of the sublimation radius for the red giant star (dashed lines) and nova (solid lines) beginning at the maximum in V band is displayed in Fig. 4.7. Note

that the sublimation radius remains approximately constant at about 5 mas for the first 70 days, after which it gradually reduces to < 0.2 mas after about day 120.

Ilumination of the Red Giant Star

During the high luminosity phase of the outburst, the surface of the red giant star facing the nova is heated substantially. We calculate the effect of the nova luminosity on the red giant star using Eqn. (10) of Hachisu & Kato (2001), which is based on thermal equilibrium between the faces of the two stars, which we display here:

$$\sigma {T_{rgi}}^4 = \eta_{rg} \cos(\theta) L_{wd}/(4\pi r^2) + \sigma {T_{rg}}^4 \tag{4.6}$$

where T_{rgi} is the new effective temperature of the red giant star for facing side and where we include an extra term from the white dwarf luminosity, L_{wd}. There are two additional constants included in this new term, the first is η_{rg}, which is an effective emissitivity for the stellar surface, while the second, $\cos(\theta)$ is the average inclination angle of the surface. The term, r, is the distance between the two stars, and T_{rg} is the original temperature of the red giant star. Equation 4.6 was evaluated as a function of time, using the evolution of the white dwarf luminosity derived from Eqn. 4.3 and the values from Table 4.5. The result of our computation of this effect is displayed in Fig. 4.8, in which we use $r = 325 R_\odot$, $\cos(\theta) = 0.5$, $\eta_{rg} = 0.5$, and $T_{rg} = 3400$ K.

Accretion Luminosity

The computation of the evolution of the accretion luminosity is based on the treatment of Hachisu and Kato with the simplification of a flat accretion disk, instead of adding the complexity of a warped accretion disk that is used in their paper. These calculations are based on the well known Lynden-Bell and Pringle (1974) and Pringle (1981) equations for the luminosity of an accretion disk, where the accretion luminosity is based on a numerical integration of the flux from the accretion disk, assuming a temperature distribution across the disk. Normally the temperature of the accretion disk is determined solely by the accretion rate onto the disk for normal viscous heating of the disk. To this Hachisu and Kato added an additional term based on additional heating of the disk from the white dwarf star as it is in a high luminosity state and is contracting and heating during the constant high luminosity period after the outburst. The flux density of the disk at frequency, ν, is given by:

$$F_{disk}\left(\nu\right) = \frac{2\pi\cos(\theta_{inc})}{D^2}\int_{R_{in}}^{R_{out}} \rho B_{\nu}[T_{disk}(\rho)]d\rho \tag{4.7}$$

The conventional expression for the radial distribution of the temperature of the disk is:

$$T_{disk1}\left(\rho\right) = \left(\frac{3GM_{*}\dot{M}}{8\pi\sigma\rho^3}\left[1-\left(\frac{R_{*}}{\rho}\right)^{1/2}\right]\right)^{1/4} \tag{4.8}$$

where T_{disk1} is the temperature in the accretion disk (Pringle 1981) and D is the distance to the Earth. The quantity B_{ν} is the Planck function, M_{*} is the mass of the

white dwarf, R_* is its radius, $\dot{M}$ is the accretion rate onto the disk, ρ is the radial coordinate in the plane of the disk,θ_{inc} is the inclination angle with respect to the tangent plane of the sky, and σ and G are the Stefan-Boltzmann constant and the gravitational constant, respectively. The maximum temperature in the accretion disk occurs at a radius $R_{max} = 1.36\ R_*$, and is given by

$$T_{max} = 0.488 \left(\frac{3GM_*\dot{M}}{8\pi\sigma R_*^3} \right)^{1/4} \tag{4.9}$$

as discussed in Lynden-Bell and Pringle (1974), Pringle (1981), and Hartmann (1998). In this treatment we neglect the emission from the boundary layer, which occurs over a very small angular region around the surface of the white dwarf star and emits at a very high temperature, which would have a negligible contribution to the luminosity in the infrared region near 10 μm. The evolution of the luminosity of the accretion disk will be calculated using the formulation of Hachisu and Kato, which we will set up below.

Let us now formulate the evolution of the accretion disk luminosity by adjusting some of the parameters in the equation above as a function of time, in particular the outer radius of the accretion disk, R_{disk} is parametrized by a power law decrease from day 7 until day 79 using the following formulae:

$$R_{disk} = \alpha {R_1}^* \tag{4.10}$$

$$\alpha = \alpha_0 \left(\frac{\alpha_1}{\alpha_0} \right)^{(t-t_0)/72} \tag{4.11}$$

In these equations ${R_1}^*$ is the inner critical radius of the Roche lobe for the white dwarf (nova) component, which we assume is 138.6 $R_\odot$

The parameter α helps define the size of the accretion disk which varies between $\alpha_0 = 0.1$ and $\alpha_1 = 0.008$, and so the power law form of Eqn. 4.10 is to make an interpolation function. Hachisu and Kato include irradiation of the accretion disk as the WD luminosity changes between days 7 and 79, where the accretion disk temperature is given by:

$$\sigma[T_{disk}(\rho)]^4 = \eta_{disk} \cos(\theta_{inc}) \left(\frac{L_{wd}}{4\pi\rho^2} \right) + \left(\frac{3GM_*\dot{M}}{8\pi\rho^3} \left[1 - \left(\frac{R_*}{\rho} \right)^{1/2} \right] \right) \tag{4.12}$$

The second term of this equation is the traditional accretion luminosity term, while the first term includes the luminosity of the white dwarf. The parameter η_{disk} is an efficiency factor, and is assumed to be 0.5, and $\cos(\theta_{inc})$ is 0.1, based on the average inclination of the surface. They assume the outer radius of the accretion disk is at a temperature of 2000 K, and is not affected by radiation from the WD photosphere. For the remainder of the calculation we will compute α in discrete time intervals corresponding to what we have done before over the days that this effect matters.

The integral is numerically evaluated at the center wavelengths for V (0.55 μm),

H (1.65 μm), and N (10.5 μm) bands, using an inner radius given by the radius of the white dwarf star and the outer radius given by the equation for R_{disk}, for the time steps of Table 4.5 and the white dwarf parameters in that table. The results are plotted in Fig. 4.10. In this figure the quantities plotted include the the contributions of the red giant and white dwarf alone (stars and solid squares), the red giant including effects of irradiation by the white dwarf (diamonds), the accretion disk alone (solid circles and dash-dot-dot line), the irradiated accretion disk (triangles and dashed line), and the total for the white dwarf including the irradiated accretion disk (diamonds and solid line).

4.5 Supporting Evidence for the Proposed Dust Creation Paradigm

Observations of RS Oph obtained with *Spitzer* during the period from 2006 April 16 through 26 UT ($\simeq$ 67 days after outburst) were described by Evans et al. (2007). We present here further IR observations conducted as part of a long duration synoptic campaign, obtained later in the outburst with the *Spitzer* Infrared Spectrometer (IRS) (Houck et al. 2004).

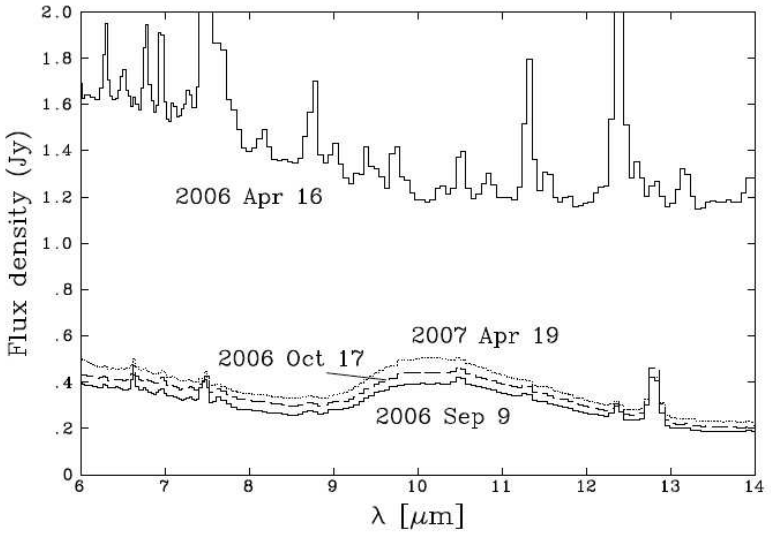

Figure 4.11 *Spitzer* IRS spectra of RS Oph from 2006 April 16 (hot gas dominant) to 2007 April 19 showing prominent silicate features. Adapted from Evans et al. (2008).

4.5.1 *Spitzer* Observations

We observed RS Oph with the *Spitzer* IRS as part of the Director's Discretionary Time program, Program Identification (PID) 270 on 2006 September 9.83 UT (day 208), 2006 October 10.4 UT (day 246) and 2007 April 19.5 UT (day 367.2). We performed all observations using all IRS modules and the blue peak-up on RS Oph. The spectroscopy consisted of 5 cycles of 14 second ramps in short-low mode, 5 cycles of 30 second ramps in both short-high and long-low modes, and 5 cycles of 60 second ramps in long-high mode. IRS basic calibrated data products (BCDs) were processed with versions 14.4.0 (2006 observations) and 16.1.0 (2007 observation) of the pipeline. The extracted spectra were not defringed. Full details of the data reduction process are given in Evans et al. (2007) and are not repeated here.

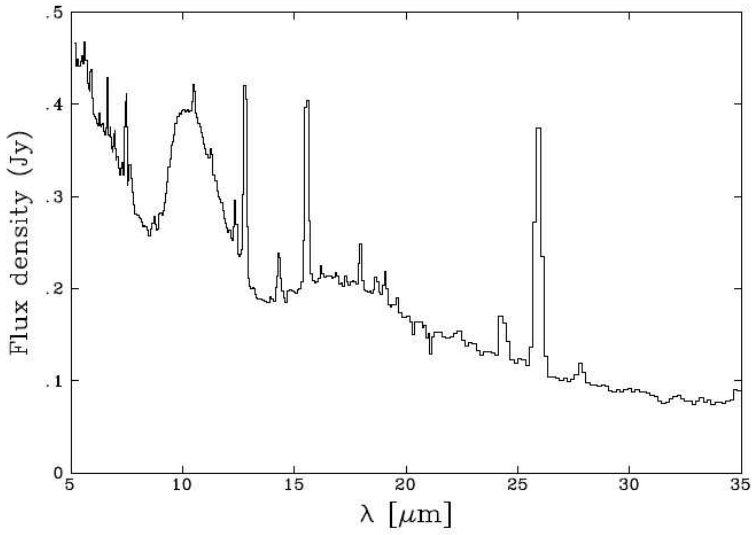

Figure 4.12 *Spitzer* low-resolution IRS spectra of RS Oph from 2006 September 9.8 showing prominent silicate features centered at 9.7 and 18 μm. Adapted from Evans et al. (2008).

Figure 4.11 shows, with the same flux density scale and over the wavelength range $6 - 14$ μm, the *Spitzer* spectrum from Evans et al. (2007), when free-free radiation and fine structure lines dominated the emission, along with the three new spectra reported here. In the period covered by these observations reported here there seems to have been little change in the level of the emission - the differences of approximately 10% are comparable with the uncertainty in the flux calibration. We conclude that, in 2006 April, emission from the hot gas dominated the dust emission but as the emission from the gas subsided, emission from dust was revealed. The low resolution *Spitzer* spectrum of 2006 Sept. 09.83 UT is shown in Figure 4.12, in which the silicate features at 9.7 and 18 μm are clearly visible.

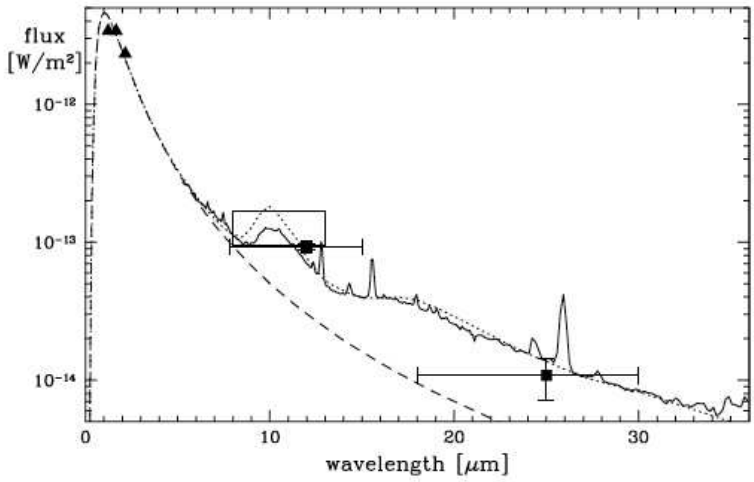

Figure 4.13 *Spitzer* IRS spectrum from 2006 September 9.8 UT, together with data from 2MASS, IRAS, and Geisel et al. (1970). Triangles: 2MASS; squares with error bars: IRAS; large open square: Geisel et al. (1970). The broken curve is a 3600 K blackbody, used as input into DUSTY; the dotted curve is the DUSTY fit. Adapted from Evans et al. (2008).

4.5.2 Discussion of *Spitzer* Observations

The formation of silicate dust requires an environment in which $O > C$ by number (Whittet 2003). Therefore on the assumption that the silicate dust we see in the *Spitzer* spectrum arises in the RG wind (see below), we conclude that the RG in the RS Oph system cannot be carbon-rich; this is consistent with the presence of TiO bands in the optical (Blair et al. 1983), and the presence of deep OI absorption combined with no carbon absorption in the X-ray range (Ness et al. 2007).

RS Oph is listed as a 12 μm source in the IRAS Point Source Catalog, with a flux density (not colour corrected) 0.42 Jy and upper limits in the other IRAS bands. To obtain a better estimate of the mid-IR flux densities, we retrieved the original scans from the IRAS database (Assendorp et al. 1995) and used the GIPSY software to

measure flux densities from traces through the position of the star. In this way the 12 μm value is refined to 0.37 ± 0.02 Jy, and a marginal detection, 0.09 ± 0.03Jy, is recovered at 25 μm; RS Oph was not detected at 60 or 100 μm, to uninterestingly large upper limits. These data, along with the 10 μm flux from Geisel et al. (1970), the 2MASS survey (Skrutskie et al. (2006) data obtained on 22 April 1999) and the *Spitzer* spectrum from 2006 September, are shown in Figure 4.13.

Given that the IRAS, 2MASS and Geisel et al. (1970) data were obtained between eruptions, we are confident that they represent the quiescent state of RS Oph. Moreover the fact that the *Spitzer* data are superficially consistent with the inter-outburst IR observations (see Figure 4.13), and that the dust was present at day 430, suggests that the dust seen by *Spitzer* is likely present between outbursts (note that Hodge et al. (2004) found no evidence of dust in ISO spectra of RS Oph, but their data only went as far as 9μm). We have made a preliminary fit using DUSTY (Ivezic and Elitzur 1997) with a 3600 K blackbody (to represent the RG during quiescence) as input radiation field. Using silicate optical constants from Ossenkopf et al. (1992), we find optical depth $\tau_V \simeq 0.1 \pm 10\%$, dust temperature at the inner edge of the dust shell $T_o \simeq 600K \pm 100K$ and dust shell inner radius of 1.5×10^{14} cm (10 AU). We derive a luminosity $L \simeq 440 L_\odot$, mass-loss rate $\dot{\mathrm{M}} \simeq 2.3 \times 10^{-8} M_\odot$ yr^{-1} (typical for these stellar parameters; van Loon et al. (2005)) for a dust to gas mass ratio of 0.005, and a terminal wind speed $v_\infty = 28.1$ km s^{-1}.

While we caution against taking these derived parameters too literally, the outer

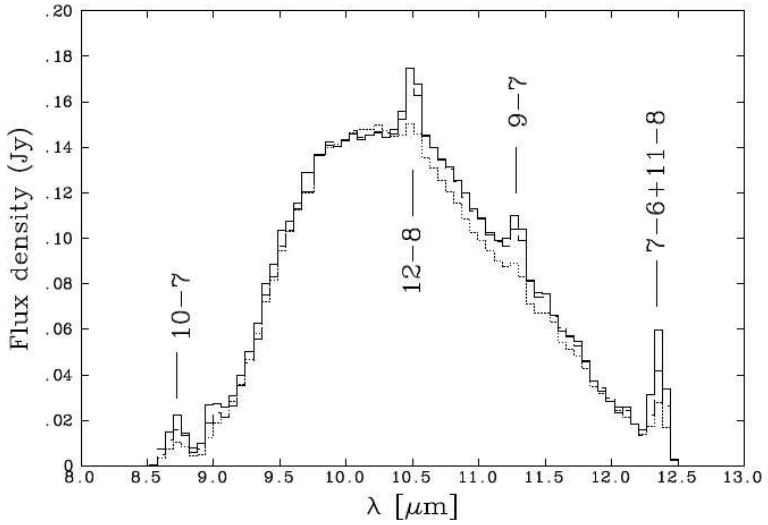

Figure 4.14 *Spitzer* IRS spectrum from 2006 - 2007. a linear continuum has been removed from the $8.5 - 12.5\mu$m region. Principal H recombination lines $(n - m)$ are identified. Spectra for 2006 September and October are essentially identical; note that the 9.7μm feature for 2007 April (dotted line) is noticeably narrower. Adapted from Evans et al. (2008).

edge of the wind (defined by $v_\infty \Delta t$, where Δt is the time between the 1985 and 2006 eruptions) is $\simeq 5.4 \times 10^{14}$cm (36 AU). The ejecta from the 2006 eruption, travelling at constant velocity, would have overtaken the outer edge of the wind even at the earliest of our observations (t = 208 days). However the shock, which is decelerating (Bode et al. 2006; Das et al. 2006; Evans et al. 2007) may not, as yet, have reached the wind edge. Taking $\tau_V \simeq 17.8$ (cf. Mathis (1998)) and silicate opacity from Ossenkopf et al. (1992), we deduce a dust mass of $4.1 \times 10^{-9} M_\odot$. Also, the inner radius of the dust shell is rather greater than the binary separation $\simeq 2.2 \times 10^{13}$ cm (1.47 AU), assuming that the mass of the RS Oph system is $\simeq 2M_\odot$).

We have determined the full-width at half-maximum (FWHM) of the 9.7 μm fea-

ture by drawing a linear continuum between 8.5 μm and 12.5 μm (see Figure 4.14, in which the fluxes at 10 μm have been normalized to the 2006 September value). We find that, on 2006 September 9 and October 17, the FWHM was 2.17 μm and 2.14 μm respectively, with no evidence for change; indeed it is difficult to distinguish the silicate features for these two epochs. By 2007 April 19, however, the FWHM was significantly smaller, 1.99 μm, perhaps because the dust had experienced some processing (resulting in a change in the dust optical properties) since 2006 September/October. The profile of the 9.7 μm feature in RS Oph broadly resembles those of the Type C silicate features of AGB stars in the classification of Speck et al. (2000). However the silicate feature in RS Oph may differ in detail from those of AGB stars for several reasons, such as lack of hot dust in RS Oph, or to grain size, shape, and composition differences. Differences may also arise because the dust in RS Oph is persistently exposed to ultra-violet (UV) radiation from the WD, as well as suffering frequent exposure to hot ionized gas (see below); the latter is known to anneal amorphous silicate (Carrez et al. 2002).

Dust formation in the winds of classical novae during eruption is well-documented (Gehrz 2008). Indeed our observations were obtained during an inflection in the visible light curve, where the V -band magnitude abruptly decreased by approximately 0.6 magnitudes, recovering shortly thereafter. In classical novae such inflections, accompanied by changes in the IR spectral energy distribution, are associated with dust condensation in the ejecta.

However, in RS Oph we are confident that dust did not form in the ejecta, for two reasons. First, the temperature of the shocked gas - approximately 10^6 K (Evans et al. 2007) - is not conducive to grain formation, which requires dense, relatively cool ($\simeq$ 2000 K) gas. Second, the strength of the 18 μm feature relative to that of the 9.7 μm feature indicates that the dust has been processed. In freshly-condensed silicate dust, the 18μm feature is expected to be weak by comparison with the 9.7μm feature (Nuth and Hecht 1990). Alternatively, the 18 μm/9.7 μm ratio for silicate features in these circumstellar environments could be solely dependent on dust temperature. We have already noted the apparent paucity of hot dust in RS Oph, so the 9.7 μm feature will be less strong. In fact our DUSTY fit (Figure 4.14) overestimates the 9.7 μm feature strength, even though the model satisfactorily fits the dust continuum as well as the 18 μm feature. We conclude that the silicate emission evident in the RS Oph *Spitzer* spectra is inconsistent with dust formation in the 2006 eruption.

Previous models of the evolution of the remnant of RS Oph following eruption, for example Bode and Kahn (1985) and O'Brien et al. (1992), have, for reasons of simplicity, assumed spherical symmetry. Accordingly the ejecta sweep into the RG wind, are shocked, and eventually reach the outer edge of the wind. In this scenario the entire RG wind is completely engulfed by the ejecta, and is replenished only after the eruption has subsided and the RG wind starts anew. As a result any dust condensing in the RG wind would also be engulfed by the shocked gas.

However the presence of warm silicate dust so soon after the 2006 eruption, and

its likely presence between eruptions, may imply that a substantial portion of the RG wind never sees the eruption at all. If we assume that the RG fills its Roche lobe (understanding that there is evidence to the contrary), its radius is $\simeq 0.7$ of the binary separation for a mass ratio (secondary/primary) $\simeq 0.4$. It therefore presents a solid angle ~ 0.3 steradians to the WD (i.e. it covers $\simeq 2.5$ % of the WD's sky).

When the RN eruption occurs on the surface of the WD it sweeps past the RG in ~ 1.5 days, potentially arriving at the nominal outer edge of the wind in a few tens of days. This is $\ll$ than the orbital period, so 2.5% of the wind is shielded by the RG and sees neither the eruption itself nor the expanding ejecta. However the situation is more complex than this in view of the radial-dependence of the wind density, and it is likely that the shocked gas will encroach into the shielded volume. Nevertheless our estimate of 2.5% for the fraction of shielded wind is likely of the right order: shielding of the wind by the RG is unlikely to account for the dust we see.

On the other hand, the density of circumstellar material in binaries is greatest in the binary plane (Spruit and Taam 2001; Gehrz et al. 2001), so the RG wind will not be spherically symmetric. Outflow, both of the wind and the 2006 ejecta, will be inhibited in the binary plane and indeed, anisotropies are suggested by HST (Bode et al. 2007) and radio (O'Brien et al. 2006) observations, and IR interferometry (Monnier et al. 2006). We expect a significant amount of dust to survive in the binary plane; such a dense medium would be consistent with the shock deceleration seen in the early Swift (Bode et al. 2006) and IR (Das et al. 2006) data.

The higher density material in the binary plane is effectively shielded and may not experience the eruption (which in any case may not have been spherically symmetric); this offers, in part, an explanation for the continued presence of silicate dust in the environment of RS Oph after eruption.

Much of the dust in the RG wind away from the binary plane would not survive the surge of UV radiation emitted at outburst. The temperature of grains at the inner edge of the dust shell would rise by a factor ($L_{Edd} = L^{1/5} \simeq 2.5$ when heated by UV radiation from a source at the Eddington limit, L_{Edd}, for a Chandrasekhar-mass WD. Thus grains at 600 K at quiescence would be heated to $\sim$ 1500 K, the nominal evaporation temperature (Speck et al. 2000) of silicate dust. Indeed, silicate grains would not survive the eruption out to distance $r_{evap} \simeq 2.2 \times 10^{14}$ cm (15 AU) from the WD in outburst. Furthermore, it is likely that a substantial amount of dust may have survived in denser regions swept-up in winds from previous outbursts.

Any dust beyond the evaporation distance would survive the UV blast, so we consider whether this dust would survive the passage of the shock. As discussed in Evans et al. (2007), the gas temperature implied by the IR fine structure and coronal lines likely ranges from 150,000 K to 900,000 K, with an electron density $\sim 2.2 \times 10^5$ cm^{-3} in the cooler region; the x-ray data indicate shock temperatures even higher than this (Bode et al. 2006). Dust grains in this environment will be sputtered as they are engulfed by the shock. Assuming that the sputtering threshold for silicate grains is $\sim$ 6 eV (Tielens et al. 1994), the time-scale for complete erosion of 0.1 μm silicate

grains in the environment implied by the IR data is $\propto Y^{-1}$ years, where the yield, Y which is the number of grain atoms ejected per incident ion is 10^{-3}(Tielens et al. 1994). As this erosive time-scale is $\gg \Delta t$ (the inter-outburst interval) any grains in the RG wind would survive passage of the shock, but might well be processed during the passage of the hot gas.

Our conclusion is that the *Spitzer* data are consistent with our N-band interferometric observations conducted on day 3.8, which independently detected the dust as discussed in Section 4.1 (Barry et al. 2008). In particular, the nearest constructive peak in the interferometer's outer acceptance pattern is at angular separation ∼12.4 mas from the center of the source brightness distribution, equivalent to $\sim 3 \times 10^{14}$ cm (20 AU) at a distance of 1.4 kpc. The initial shock velocity would need to have been 9000 kms^{-1} to reach this distance, travelling at constant velocity, far higher than observed (Evans et al. 2007; Bode et al. 2007). Therefore this emission line was not excited by passage of the shock front but by the UV flash from the TNR event. Thus this measurement is consistent with our conclusion that dust detected by *Spitzer* was not created by the collision of the ejecta with the RG wind or by subsequent condensation, but was more likely formed during quiescence.

Chapter 5

The Continuum of RS Oph

In this chapter we outline the basic physics of symbiotic stellar systems and describe how this may manifest itself in their continuum emission. Subsequently, we describe a methodology and mathematical approach to disentangle the various continuum features and show specifically how we extended this approach to model our mid-IR KIN data. We outline our current understanding of each the components of the RS Oph system in quiescent and active states and further detail observations we conducted to ascertain aspects of the RS Oph continuum. Subsequently, we describe how we apply this process to the high angular resolution interferometric measurements conducted using the KIN and high-spectral-resolution measurements using the *Spitzer* space telescope and determine what those measurements tell us about the astrophysics of the system. We outline how our analysis suggests the possible detection of dust and evidence for non-spherical mass ejection. Finally, we present a description

of the temporal evolution of the continuum from shortly after peak brightness to near quiescence.

5.1 Symbiotic Stellar Systems

Symbiotic systems are known to consist of a cool giant and a compact star in orbit about their common center of mass with a typical period of from one to three years. The principal interaction between the stellar components, aside from their mutual gravitational attraction, is in the mass loss from the RG secondary to the compact primary. Mass is transfered through the mediation of an accretion disk - a structure formed of diffuse material that is in orbit about the primary. (Throughout this discussion, the more compact stellar component is referred to as the primary, the cool giant as the secondary - this relation being independent of relative mass.) There is a great deal of energy liberated in this mass transfer process. How energy is released determines the phase the object is in: active or quiescent.

Two mechanisms for mass transfer from the RG secondary to the compact primary are stellar wind capture (SWC) and Roche Lobe overflow (RLO). The Roche Lobe is a region formed between two stars and bounded by a critical gravitational equipotential. Close to each stellar component is a potential surface which is roughly spherical and concentric with the star. The surface becomes ellipsoidal further from either component and is elongated along the axis that passes through the center of mass of each. There is a critical surface for which there is one point between the stellar bodies

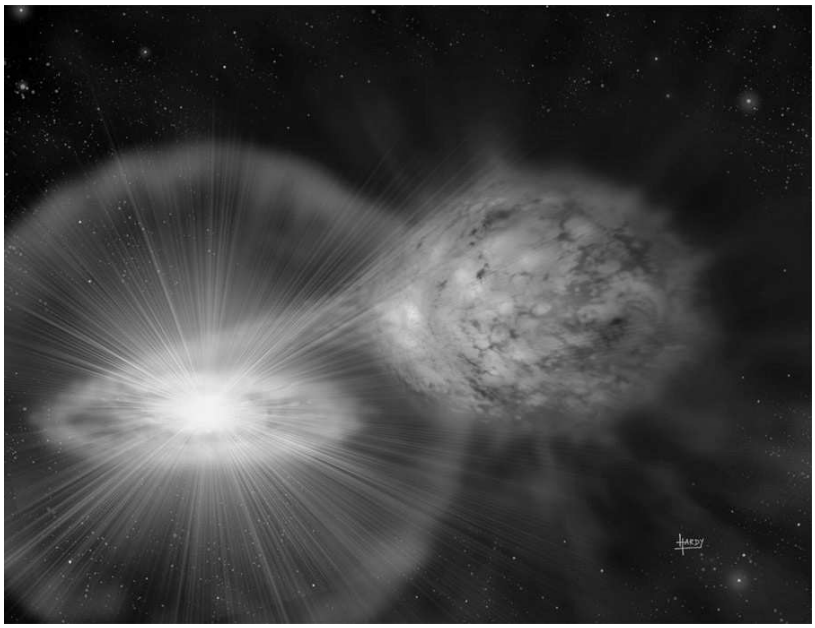

Figure 5.1 Conceptual depiction a symbiotic stellar system in Roche Lobe overflow. In the upper right is a tidally distorted RG. In the lower left is a compact star forming an accretion disk. Adapted and modified from conceptual artwork by D. A. Hardy.

that is in gravitational equilibrium. This point, termed the inner Lagrangian point, L1, defines the limiting size of the Roche Lobe. Its location is fixed by the relative mass of each star and the distance between them. This is represented graphically in Figures 5.1 and 5.2. Importantly, material within this region is acted on by a potential which is calculated in a frame of reference that co-rotates with the binary pair and is, therefor, non-inertial. As a result, there is a pseudo-potential, and an associated centrifugal force, that acts on material within this region. Roche Lobe overflow occurs when the diffuse outer envelope of the expanding stellar component fills and then overflows this critical equipotential. Hydrogen-rich matter from this outer envelope then falls through the inner Lagrangian point through the gradient of the centrifugal

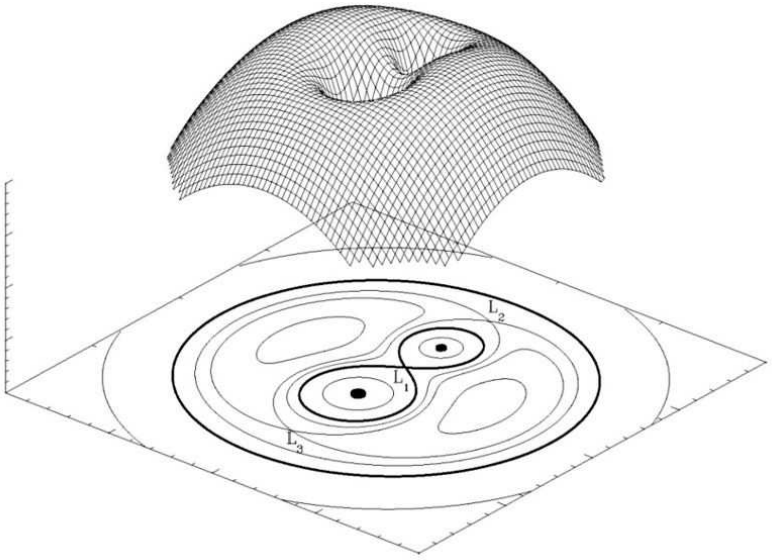

Figure 5.2 Depiction of the critical gravitational equipotential associated with Roche Lobe overflow and identification of the Lagrangian points referred to in the text. The ordinate is gravitational potential. The other two axis are spatial coordinates in the plane of the orbit. Adapted under GNU Free Documentation License (non-copyrighted image)

pseudo-potential. Theoretical work by Podsiadlowski and Mohamed (2007) describes the presence of significant stratification effects in the extended atmosphere of red giants such as the secondary in the RS Oph system. This suggests that, in the case of such stars, there is no single radius value - radius depending on the species of material causing the opacity. As a result, there is some indeterminacy as to precisely what material fills the Roche Lobe to produce its overflow.

In contrast, SWC is a mechanism in which the WD gravitationally captures some fraction of the massive wind emitted by the RG. Figure 5.3 shows a conceptual depiction. The rate of capture through this mechanism was first theorized by Bondi and Hoyle (1944) and later elaborated by Livio et al. (1986) for the particular case

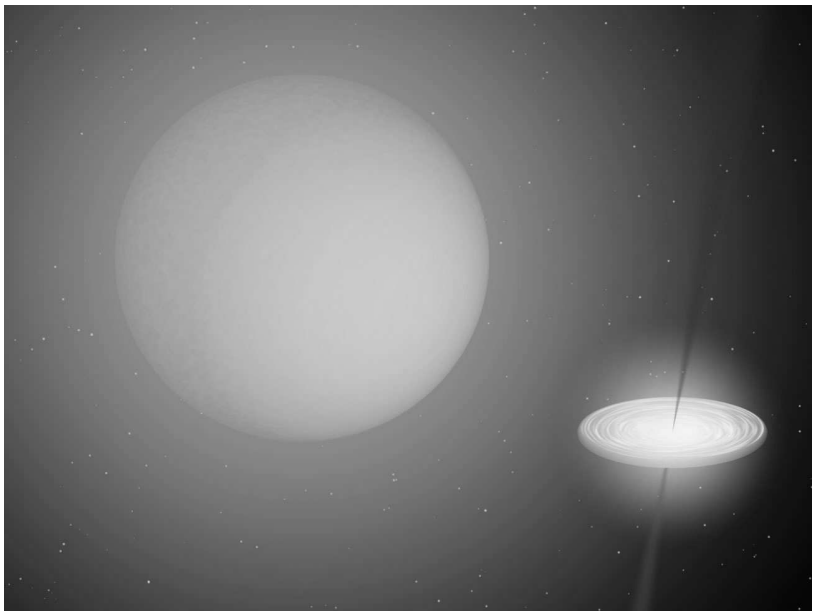

Figure 5.3 Conceptual depiction of a symbiotic stellar system in wind capture. This shows an RG with a compact star and accretion disk. The system is enveloped in a massive wind nebula from the RG. Adapted and modified from G. Wynn, unpublished

of RS Oph. In contrast to systems in RLO, systems in which component interaction is due to SWC should have little gravitational distortion of the RG. This may be observationally ascertained by detailed analysis of quiescent-period lightcurves (LC) in which the LC of RLO systems depart from that typically found in fully detached binary systems. This is manifested as a variation caused by one component of the binary system being tidally distorted by the other commonly called ellipsoidal variability. These variations cannot be caused by an undistorted RG nor by the slow wind from the giant filling the Roche Lobe rather than the tidally distorted star itself (Podsiadlowski and Mohamed 2007) because the wind must be optically thick in both visible and near-IR wavelength regimes.

An accretion disk forms when material from the diffuse, hydrogen rich outer layers

of the RG is captured by the compact star through one of these mechanisms. Because the stellar components are in orbit about one another and are likely to be in synchronous rotation under only a limited set of circumstances, the in-falling material must change energetics rapidly. In particular, when matter falls inwards it loses not only gravitational energy but also angular momentum. Since the total angular momentum of the disk must be conserved, the angular momentum loss of the mass falling into the center has to be compensated by an angular momentum gain of the mass far from the center - there must be some mechanism to transport angular momentum away from the center for matter to accrete. Because an accretion disk is expected to be in a state of laminar flow this excludes the possibility of a hydrodynamic mechanism for the angular momentum transport. Lynden-Bell and Pringle (1974) showed that if we assume that the disk has a weak magnetic field, instabilities in this field and, as a result, in the diffuse matter in the disk, would provide such a direct mechanism. Magnetic field instabilities in the disk, then, redistribute angular moment and, as a result, material in the disk spirals inward towards the compact star. As the material falls through the primary's potential well, gravitational energy is released, transformed into heat, and is emitted as electromagnetic radiation at the surface of the disk.

5.2 The Continua of Symbiotic Stellar Systems

The continua of symbiotic stellar systems can be quite complex but are nevertheless understandable when analyzed into their components. First in order of importance is to identify the principal source of luminosity. As alluded to previously, the accretion process generates a very hot, strong radiation. The frequency range of the radiation depends on the gravity gradient of the primary. Consequently, accretion disks surrounding young stars and protostars radiate in the infrared, while those around white dwarf stars radiate primarily in the ultraviolet, and those about neutron stars and black holes mostly in the X-ray portion of the spectrum. The amount of energy liberated depends on the phase of the accretion process. During quiescent phases the hot component - the accretion disk - releases its energy approximately at a constant rate and spectral distribution. The hot radiation ionizes a fraction of the electrically neutral wind from the giant, which gives rise to nebular emission comprising numerous lines of high excitation and ionization and a continuum. As a result the spectrum consists of three components of radiation: two stellar and one nebular. Measurements of the radiation evolved by this process in quiescence may be exploited to calculate a mass loss rate from the secondary. In contrast, during active phases the radiation associated with the hot component changes significantly in spectral distribution leading to a multi-magnitude brightening of the object in the visible band. A feature typical of active phases is a high-velocity mass outflow (distinct from the continuous mass outflow from the RG) as determined by measurement of

the Doppler shifting of the spectroscopic lines associated with the emitting material. This outflow can significantly disrupt the ionization structure of symbiotic nebulae, and, in some cases the nebular emission dominates the UV/optical spectrum and in others disappears entirely at the optical maximum.

5.2.1 Methodology for Analysis of Continua

The basic approach to disentangling the continuum emission is to proceed on the assumption that the combined continuum *is* the sum of the radiation from the several components in the system. The model spectral energy distribution (SED) is fitted to the observed SED, the the model SED is calculated by the superposition of fluxes from the cool giant star, the WD in thermonuclear runaway - modeled as a hot star - and a nebula including the effects of Rayleigh scattering processes. Historically, similar approaches have been taken in the pioneering work of Kenyon and Webbink (1984) in which the authors attempted to determine the fundamental parameters of a nova by modeling it's ultraviolet spectrum. Kenyon and Webbink elaborated a grid of synthetic spectra for a number of binary models and compared the calculated and observed ultraviolet continuum colors to make a determination of the type of binary source — massive secondary with WD accretor or a single hot star — together with an associated hot star temperature and accretion rate. Muerset et al. (1991) added a nebular continuum to this basic profile as a refinement of the model. The theoretical nebular continuum accounted for fractional rates of photons capable of

ionizing He^{+} and H and including a geometrical structure of the circumbinary He^{++} and H^{+} ionized zones. Skopal (2005) formalized this process and applied it to several different sources. We now describe the particular aspects of the mid-IR that must be incorporated into a model of the continuum to achieve a model of highest fidelity. Subsequently, we discuss the specific, mathematical formulation of this process.

Extension of the Analysis Method to the Mid Infrared

As noted above, the basic method of continuum analysis has been described in the literature previously. However, extension into the mid infrared is unique to the current effort and bears some description. In the mid-IR, the nebular continuum should include the effects of bound-free and thermal bremsstrahlung (free-free) emission components but the spectrum will be dominated by free-free emission (Osterbrock and Ferland 2006). As a result, the contribution from bound-free transitions is usually neglected in calculations. However, to obtain the highest degree of faithfulness to the underlying physics, we added *both* of these effects together with a third possible nebular contributor - warm dust emission. In this we assumed that the reactive component of the nebular environment consists of a very tenuous distribution of primarily H^{+} and He^{++} ions, free electrons, and dust. We further argue that most atomic metals have nucleated into dust (under the correct conditions of temperature and density) and would not be evident in the spectrum, although we cannot know this a priori.

The first component we incorporated in the calculation of the mid infrared nebular

continuum radiation is the contribution from free-bound transitions of H^+ and He^{++} ions. In particular, we included all species from HH7 - HH12 in hydrogen and He14 - He24 in helium. (HH7, for example, is the recombination 'edge' value representing the energy of an electron of arbitrary velocity recombining to the n = 7 principle quantum state of hydrogen.) To calculate the nebular continuum correctly, these frequencies are added to the H^+ and He^{++} series in this spectroscopic region. For each species, a contribution is made to the continuum for the noted wavelength and all shorter wavelengths as electrons of arbitrary speed can be captured by the particular H^+ and He^{++} ionic quantum level. These are thus 'edge' frequencies that are incorporated into the free-bound emission coefficient (cf. Equation 5.8 et seq. in the subsection below.).

The second component is the contribution from free-free emission. First, we calculated an appropriate Gaunt factor - a quantum correction for the interaction of one charge with the Coulomb field of the other charge when treated classically - for the N-band. Osterbrock and Ferland (2006) suggests adoption of a Gaunt factor in the range $1.0 \leq g_{ff} \leq 1.5$ for nebular conditions. Calculation of the photon energy in the mid N-band (10.5 μm) and comparison of this with the energy associated with a range of expected electron temperatures places all values within the "small-angle classical region" (Rybicki and Lightman 1986). Thus we adopt a value of $g_{ff} = 1.3$.

We model the effects of a generalized dust emission as a cool blackbody. This allows us to correct the model SED curvature without unduly burdening the fitting

process with complex calculations. Later, if dust emission is detected, high-fidelity models of different species of dust are used to improve the calculation. This process is further elaborated in section 5.3.2.

Mathematical Description of the Continuum Analysis

We began by giving a qualitative description of the process of continuum disentanglement. Here we give a mathematical description of the process we followed to produce the results in Section 5.3. This approach is based on Kenyon and Webbink (1984), Muerset et al. (1991) and Skopal (2005). We extend their analytical method to the N-band for use with the KIN spectra.

According to the model presented in the sections noted above, we can express the observed total continuum flux, $F(\lambda)$, as the superposition of a hot stellar component, $F_h(\lambda)$, a cool stellar component, $F_c(\lambda)$, a warm dust component, $F_d(\lambda)$, and a nebular component, $F_N(\lambda)$.

$$F(\lambda) = F_h(\lambda) + F_c(\lambda) + F_d(\lambda) + F_N(\lambda). \tag{5.1}$$

We approximate the hot stellar component, $F_h(\lambda)$, by a black-body, $B_\lambda(T_h)$, at a temperature, T_h. The flux from this black-body may be attenuated by Rayleigh scattering due to the presence of neutral hydrogen atoms in proximity to the WD. Thus the first term is described as

$$F_h(\lambda) = k_h \times \pi B_\lambda(T_h) \exp(-n_H \sigma_\lambda^R) \tag{5.2}$$

in which n_H is the column density of hydrogen atoms, $B_\lambda(T_h)$ is the integrated Plank function at temperature, T_h, and σ_λ^R is the Rayleigh scattering cross section of atomic hydrogen given by Nussbaumer and Vogel (1989) as

$$\sigma_\lambda^R = \sigma_e \left[\sum_j \frac{f_k}{(\frac{\lambda}{\lambda_k})^2 - 1} \right]^2 . \tag{5.3}$$

In this expression f_k, λ_k and σ_e are the oscillator strengths of the Lyman hydrogen lines, the associated wavelengths and the Thomson cross-section of an electron. (Recall that a photon is scattered, not absorbed, by a free electron through the process of Thomson scattering. The Thomson cross section has the same value for all wavelengths; $\sigma_e = 6.55 \times 10^{-25} cm^2$.)

The coefficient, k_h is a dimensionless scaling factor which may be expressed as

$$k_h = \frac{F_h(\lambda)}{\pi B_\lambda(T_h)} = \frac{L_h}{4\pi d^2 \sigma T_h^4} = \left(\frac{R_h}{d} \right)^2 = \theta_h^2 \tag{5.4}$$

in which R_h, L_h, T_h and θ_h are the characteristic radius, luminosity, temperature, and angular size of the region of space attributed to the hot stellar source and d is the distance from the observer to the object, 1.4 kpc (Barry et al. 2008).

The flux, $F_c(\lambda)$ in Equation 5.1 is due to the cool stellar source. We approximate the flux from the cool stellar source as a synthetic Hauschildt spectrum, $F_\lambda^{Hauschildt}$,

of a given effective temperature, T_{eff}. This temperature and a scaling factor similar to that of the hot stellar source, $k_c = \theta_c^2$, determine the flux received at the Earth's surface summed over all wavelengths (bolometric). This may be expressed as

$$F_c^{obs} = \int_\lambda F_\lambda^{Hauschildt}(T_{eff})d\lambda = k_c \int_\lambda \pi B_\lambda(T_{eff})d\lambda = k_c \sigma T_{eff}^4. \tag{5.5}$$

The term, $F_d(\lambda)$ in Equation 5.1 is treated in a similar way to the hot stellar source and also includes the effects of Raleigh scattering as

$$F_d(\lambda) = k_d \times \pi B_\lambda(T_d) \exp(-n_H \sigma_\lambda^R) \tag{5.6}$$

wherein n_H is the column density of hydrogen atoms and k_d is the dimentionless scaling variable that is constructed similarly to that of the hot stellar source in Equation 5.4.

The final term in Equation 5.1 is the contribution of the symbiotic nebular emission. As noted above, this term includes contributions from singly ionized hydrogen, doubly ionized helium for all processes of thermal bremsstrahlung and free-bound transitions for all wavelengths from ultraviolet to N-band infrared. The term is, therefore, expressed as

$$F_n(\lambda) = \frac{1}{4\pi d^2} \int \left(j_{\lambda,H}(T_e) N_{H^+} + j_{\lambda,He^+}(T_e) N_{He^{++}}\right) (N_{e^-}) dV. \tag{5.7}$$

In Equation 5.7, N_{H^+}, $N_{He^{++}}$, N_{e^-} are the number densities of ionized hydrogen,

ionized helium, and electrons, respectively. Each of the emission coefficients, $j_{\lambda,H}$ and j_{λ,He^+} is a function of the electron temperature, T_e. The emission coefficients are formed by the sum of two expressions for each of free-free and free-bound transitions. The first of these are given, after Osterbrock and Ferland (2006), as

$$j_\lambda^{ff} = \frac{1}{4\pi} N_+ N_{e^-} \frac{32 Z^2 e^4 h}{3 m^2 c^3} \left(\frac{\pi h^2 c}{\lambda 3 k T_e} \right)^{1/2} (g_{ff})\ e^{\frac{-hc}{\lambda k T_e}} \tag{5.8}$$

wherein g_{ff} is a Gaunt factor quantum correction to the classical Coulomb collision approximation, N_+ is the number density of any positive particle, Z is the atomic number, e is the charge of an electron, c is the speed of light, and h is Plank's constant. Similarly, the expression for free-bound transitions is given as

$$j_\lambda^{bf} = \frac{1}{4\pi} N_+ N_{e^-} \sum_{n=n_1}^{\infty} \sum_{L=0}^{n-1} u \sigma_{nL} \frac{hc}{\lambda} \tag{5.9}$$

for recombination of free electrons with velocity, u, to levels with principal quantum number $n \geq n_1$. In this expression σ_{nL} are the recombination cross sections given by the detailed balancing or microscopic reversibility Milne relations between capture and photo-ionization cross sections (Osterbrock and Ferland 2006).

We now briefly describe each component of the continuum separately to outline considerations specific to them. Subsequently, we apply this model to our data on the nova RS Oph in Section 5.3.

The Hot Stellar Continuum

We model the hot stellar source (HSS) continuum as a black-body radiation source at a temperature, T_h. This black-body simulates the emission of a very hot accretion disk when the object is in quiescence and the luminosity of the WD thermonuclear runaway event in the active phase. Given that the luminosity is an intrinsic characteristic of the emitter, in quiescence one could theoretically obtain the size of the accretion disk from the hot stellar emission by scaling the model flux to match the observed quantity. For example, in the particular case of the accretion disk of the symbiotic system Z Andromedae (Skopal and Wolf 2006; Skopal and Pribulla 2006) the disk was found to be approximately ten times larger than the WD. Assuming that this is a fairly typical size, directly observing the disk is precluded with current interferometers. In modeling the HSS, we consider that light emitted by this source may be attenuated by neutral atoms of hydrogen due to the Rayleigh scattering process. This is the scattering of light by particles much smaller than the wavelength of light under consideration. In particular, the size of a scatterer is defined by the ratio of its characteristic dimension, r, to that of the wavelength of the scattered beam. Rayleigh scattering is defined as scattering in the the parameter regime $x \ll 1$ in which the parameter x is given as $x = \frac{2\pi r}{\lambda}$. Importantly, the *amount* of light that is scattered by the Rayleigh process depends on the relative size of the particles to that of the wavelength of light under consideration.

The Cool Stellar Continuum

We also incorporate the flux contribution of the cool giant star in the model spectral energy distribution. To attain the very highest fidelity, cool giants may not be modeled as low-temperature black-bodies for a number of reasons. First, in order of importance is that low temperature, evolved stars typically have dust that condenses at 2 – 5 stellar radii. Also line blanketing effects, especially from the so-called iron curtain are quite significant in this regime. This effect, an absorption spectrum due mostly to Fe^{+} transitions, was first identified by Shore and Aufdenberg (1993) as the origin of anomalies in the emission-line fluxes found in differential absorption as the line-of-sight pathlength was changed in their observations. The absorption was determined to have originated in an intervening slab of cool gas. For our model, the veiling gas is representative of the neutral wind from the cool giant with the effect being greatest at inferior conjunction (Dumm et al. 1999). This line blanketing effect results in the complex profile of the observed continuum.

For the cool star continuum we have chosen to utilize models constructed by Hauschildt et al. (1999) and Allard et al. (1996) — hereafter refered to as Hauschildt models. These are recognized as the models of the very highest fidelity and include many of the effects anticipated to exist in the atmospheres of stars with temperatures $3000 \leq T_{eff} \leq 10,000$ K. In particular, both molecular and atomic lines are treated in the model by a computationally intensive direct-opacity sampling method in which relevant local thermal equilibrium (LTE) emission lines are dynamically selected at

the beginning of each iteration of every model, and the contribution of all such lines are summed to compute the total opacity. These opacities are then selected at arbitrary wavelength points of the constructed spectrum. This is important for our analysis as the line-forming regions in cool stars span a large range of pressure and temperature and, as a result, the line wings may form under quite different conditions than the line cores. Hauschildt models treat the variation of the line profile and the level excitation more accurately than any other model. Using parallel supercomputers, a line list of about 10×10^6 lines is down-selected from a master list of possible line emissions that consists of 47 million atomic and up to 350 million molecular lines by application of an emission threshold set by the localized bound-free absorption coefficient. In addition to Rayleigh scattering noted above, Thomson scattering is also accounted for. In the Thomson process, charged particles are the scatterers and the electric and magnetic components of the incident photon accelerate them. As a result of changes in the energy of the particles, they in turn, emit radiation. In the non-relativistic case - anticipated in the atmosphere of cool stars - the charged particles react to the electric field component of the impinging photons and will move in the direction of the oscillating field. The resulting electromagnetic dipole radiation will be emitted most strongly in a direction that is perpendicular to the motion of the particles in the incident field. Finally, Hauschildt et al. included the effects of dust condensation and line blanketing into the models and thoroughly tested them against observations and the earlier best-fidelity models of Kurucz (1992).

The Nebular Continuum

Another term to be considered in the model SED represents flux in the continuum emitted by the symbiotic nebula. The nebular radiation is transformed stellar radiation via ionization and recombination processes. To produce the observed amount of nebular emission requires a sufficient number of photons, produced by the ionizing stellar source, which are capable of ionizing the medium. The number of ionizing photons is given by the HSS temperature and its associated luminosity. For the purpose of these calculations we consider nebular contributions from hydrogen and doubly ionized helium generated by processes of free-bound transitions (recombination) and free-free transitions (thermal bremsstrahlung). For free-free processes in particular, in which radiation is due to the acceleration of a charge in the Coulomb field of another charge, we consider that in electron-ion bremsstrahlung the electrons will be the primary radiators since the acceleration experienced by each equally charged particle is inversely proportional to its mass. We also assume that both the singly ionized hydrogen (protons) and doubly ionized helium occupy the same volume such that the ions in the nebula are in the same pool of electrons. This greatly simplifies the expression of a relative number density of each of these species. Because the emission profile of singly ionized helium is very similar to that of hydrogen it makes it very difficult to identify any signature of the emission from He^+ in the observed spectrum. Also, He^+ is much less abundant than hydrogen in stellar atmospheres and circumstellar environments. Consequently, we neglect this contribution.

The nebular radiation is characterized by a uniform electron temperature, T_e, that is assumed constant throughout the nebula. In particular, the temperature of a distribution of particles in a plasma in which the velocities of the particles are in a Maxwell-Boltzman distribution is well defined as an electron temperature. This temperature can be several orders of magnitude higher than that of the ions or neutral hydrogen. One interesting feature of this is that during quiescence the electron temperature, which is directly related to flux of the ionizing radiation, can be exploited to find the mass-loss rate from the RG as all light from the WD accretion disk would be from material from the RG. Our analysis, however, is taken during the active period of the object under consideration.

The nebular emission is also characterized by the emission measure. The emission measure is defined as the integral of the number density of particles of a particular species along the sight-line and within a given solid angle. The HSS, the ionizing source, is pumping out energetic photons and the nebula emits at higher or lower luminosity depending on the emission measure - the number density of particles available to reprocess the HSS photons into nebular radiation. As a result, there is an interdependency among the emission measure, the ionizing flux, and the nebula electron temperature temperature. For example, there could be a very large number of ionizing photons but if there are only a limited number of particles being ionized, more nebular flux will not be produced even for larger and larger number of ionizing photons. To model a larger number of ionizing photons one can increase the temperature

or the luminosity or both parameters of the HSS. However, the process is limited by realistic quantities. There is a minimum temperature at which the ionizing source is just capable of giving rise the observed nebular emission. The HSS temperature must then be commensurate with the nebular electron temperature.

5.3 Analysis of the Continuum of RS Oph

We analyzed the composite spectrum of RS Oph beginning with an exploration of the various components that could contribute to the combined SED. From this we derived physical parameters of individual components of radiation and the HSS and RG including temperatures, radii and luminosities of the electron temperature and the emission measure of the nebula. The observed SED was reconstructed by adding the fluxes from the cool giant, hot stellar source (HSS), warm dust and nebula. Using data from several disparate sources including the KIN, we conducted this analysis over several temporal epochs from near outburst to late post-outburst.

In order to properly study the continuum associated with the nova we incorporated a very broad range of observations from the ultraviolet to the mid infrared. Data for the continuum between 0.12 and 3.4 μm are from the International Ultraviolet Explorer (IUE) spectra from the 1985 outburst, the optical U, B, V, R_C and I_C and infrared J, H, K, L photometric flux-points (Evans et al. 1988; Stickland 1988; Snijders 1987a). We took the B, V, R, I magnitudes from the CCD photometric light curves summarized by Variable Star Observers League in Japan (VSOLJ) mem-

bers (Barry, private communication). The used flux points were measured practically simultaneously with the KIN data in particular. Only the I_C magnitude was interpolated to the day 3.8. For the J, H, K, L points where we did not have the particular date we obtained them by linear and parabolic extrapolation to the desired date from published data (Evans et al. 1988). As described previously, we approximated the RG continuum by the photometric Johnson V-band, R_C, and I_C fluxes from the post-outburst minimum, J, H, K, L flux-points in quiescence. We used an archival ISO spectrum from 23/09/96 for determination of the region between 2.3 and 4.0 μm. We dereddened all flux observations with $E(B-V) = 0.73 \pm 0.1$ (Snijders 1987a) and scaled relevant parameters for a distance of 1.4 kpc (Barry et al. 2008).

In the mid infrared we utilized spectra from the KIN obtained on day 3.8 post-outburst. We acquired archive high-resolution spectra from the *Spitzer* space telescope as published by Evans et al. (2007) on 2006 Apr 16 (t = 62.51 days), 2006 Apr 26 (t = 72.54 days) and 2006 Sep 09 (t = 209.3). The Spitzer observations were performed using all IRS modules, with IRS blue ($13.3 - 18.6$ μm) peak-up on RS Oph. We chose to use IRS basic calibrated data products from the archive processed with version 14.0.0 of the IRS pipeline.

We obtained an SED of the RG continuum from an archive of Hauschildt models (Hauschildt et al. 1999). We selected the model by approximating the giant's continuum using the photometric Johnson V-band R_C and I_C fluxes from the post-outburst minimum J, H, K, L flux-points obtained during quiescence (Evans et al. 1988) and

the archival ISO spectrum from 23/09/96 determining the region between 2.3 and 4.0 μm. The fluxes, all with maximum 15% uncertainty, proscribed a Hauschildt model with $T_{eff} = 3800^{+200}_{-100}$ K. As observed above, the scaling factor for the RG is the angular size. The size $\theta_g = (8.5 - 9.6) \times 10^{-7}$ mas is related to the observed flux integrated over all wavelengths as $F_g^{Hauschildt} = \theta_g^2 \sigma T_{eff}^4 = (6.8 - 7.7) \times 10^{-9}$ erg cm^{-2} s^{-1}.

We now break out individual features of the RS Oph spectrum to show the methodology and to illustrate how the individual component spectra fit into the total spectrum. Following this section we will describe the implications of the continuum fitting to the KIN spectrum. Finally, we will describe the temporal evolution of the spectral energy distribution.

5.3.1 Fitting the SED

We describe our initial fits of the data on day 3.8 post-outburst using the combined KIN inner and outer spatial regime data. Functionally, this treats the KIN as a single, filled aperture instrument removing gross instrumental effects associated with nulling interferometry.

Figure 5.4 displays a series of continuum fits. In this figure, individual flux measurements are given as dark, black squares with the particular filter used noted along the ordinate. The Hauschildt, 3800 K RG model is the dotted trace at the bottom of the figure. The scaling of this, again, is governed by the quiescent behavior of the object and is sensitive to the adopted distance. We have scaled this for the RG model

chosen above and the distance as established in Barry et al. (2008).

We plot the model nebular flux as a dashed line. This is also made obvious by the discontinuities in the spectrum at $\lambda = 3650, 8200, 14590, 22795\mathring{A}$, etc., which are due to free-bound recombination of a free electron with a proton. For simplicity, we show only the hydrogen recombination spectrum for the data we analyse as it is sufficient for this zeroth-order fit to assume that the abundance of He^{++} ions is negligible. The particular curvature of this trace is determined by the species included in the model. The scaling of the trace is controlled by the emission measure adopted.

The HSS, which is the model for the WD TNR flux, is given as a thin, solid line and the combined model SED is the thick solid line. This is the sum of all of the model components. For this initial fit, we have deliberately neglected the effects of dust as that will be dealt with separately below, but for completeness we include in this graph the KIN outer and total spectra. The total spectrum is at issue although we include the outer spatial regime for later reference. We again note that the KIN total spectrum is dominated in scale and slope by light from the central HSS source.

The initial rough fit to the $BVR_CI_CJHK\&L$ flux points is reasonably good. The combined, model SED also passes through the center of the KIN total spectrum giving immediate confidence that the method has merit. However, we note immediately that the HSS temperature that is well-suited to the $BVR_CI_CJH\&K$ band flux points is much too low to yield the amount of the nebular emission (EM$\sim 1.2 \times 10^{62}$ cm^{-3}) we need an HSS blackbody radiating at about 50,000K and scaled - by effectively

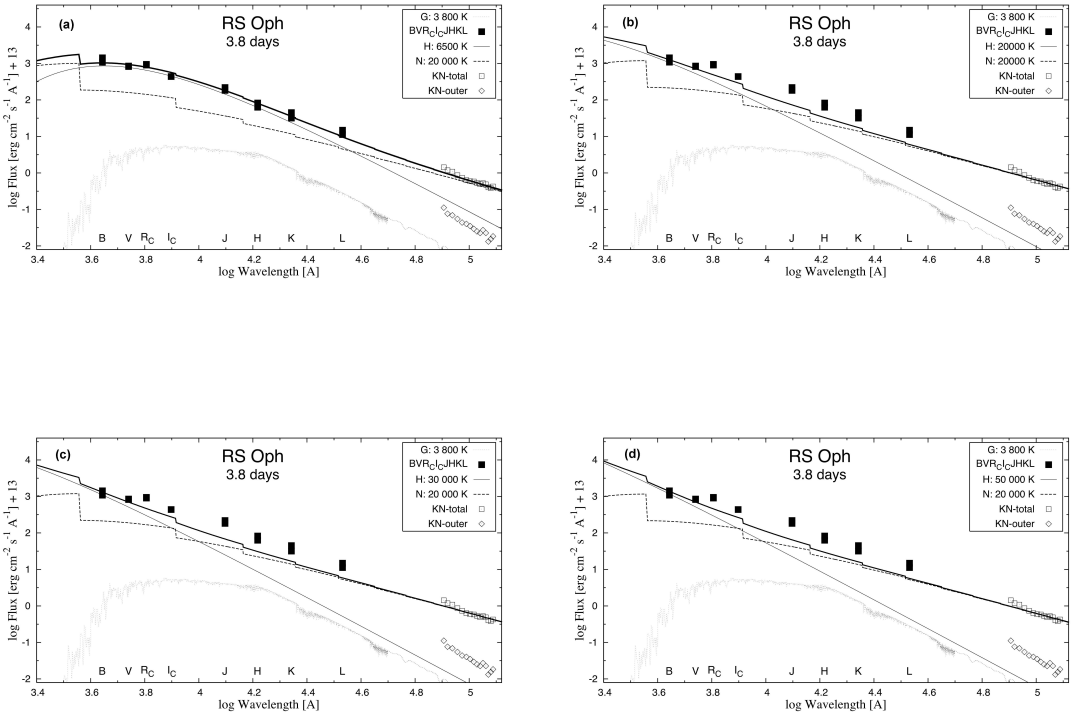

Figure 5.4 A series of model continuum SED fits to the Keck Interferometer data on day 3.8 post-outburst. In (a) we begin fitting with an HSS blackbody temperature of 6500K and a nebular electron temperature of 20,000 K. This fits the combined KIN data well but is not physical - this HSS temperature could not have given rise to the nebular temperature. In subsequent fits, we adjusted the HSS temperature upwards to show how the fit in B-L wavelength range is lost as we do so. We interpret this as an indication of non-spherical mass ejection.

changing the number of ionizing photons - to just fit the observations. (Note that the particular electron temperature is not important here. Also note that the volume emission coefficient for hydrogen runs from 2.56 to 1.0×10^{-13} erg cm^3 s^{-1} for electron temperatures of 1×10^4 to 3×10^4, respectively (Nussbaumer and Vogel 1987).) Again, the nebular radiation is transformed stellar radiation via ionization and recombination processes. To produce the observed amount of nebular emission we require a sufficient number of photons of the correct energy distribution, produced by the ionizing stellar source given by the HSS temperature and its luminosity, which are capable of ionizing the nebular medium.

In attempting to rectify this problem, we adjusted the temperature of the HSS slowly upward in Figure 5.4 from 20,000K to 50,000K - the temperature that is just capable of producing the nebular electron temperature. We noted that as we did this, the fit of the individual $BVR_CI_CJHK\&L$ dereddened fluxes progressively deteriorated.

Finally, we set the HSS temperature to $T_h = 120,000$K and assumed a dominant, 20,000K nebular flux in the N-band. This fit is reasonably good at optical and IR wavelengths. (See Figure 5.5.) However, the total KIN flux is a full factor of 3 less than that suggested by the model. While this is the very first scientific result from the instrument, engineering tests establish that the absolute flux calibration should be better than about 25% (C. Koresko, private correspondence, 2006). The implication of this is clear. We are forced to reject model SED's that have HSS temperatures

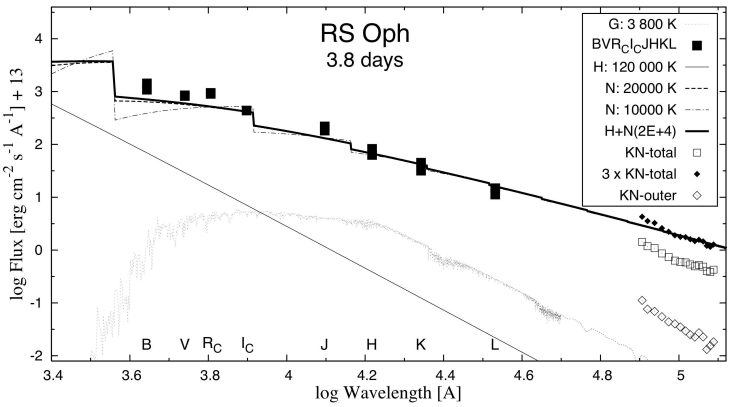

Figure 5.5 The Keck Interferometer Nuller Continuum Fit with maximum HSS temperature of 120,000K and a nebular continuum of 20,000K. Fit in the UV to NIR bands is poor.

approaching - and even exceeding - that required to produce the nebular continuum seen in the MIR. The approximate SED fit in Figure 5.4 and reproduced for clarity in Figure 5.6 is the best of the rough fits and suggests that the measured spectral energy distribution *as observed* includes an anomalously low hot stellar source temperature. This model then requires a different interpretation.

We hypothesize non-spherical mass ejection as the source of this apparent disagreement. For the outburst of RS Oph on day 3.8 we posit an obscuration of the hot central ionization source by a belt of absorbing material in the direction of the observer. This obscuration could be from the disk, as indicated during quiescence, or an P-Cyg type absorption in the rapidly out-flowing material ejected from the sur-

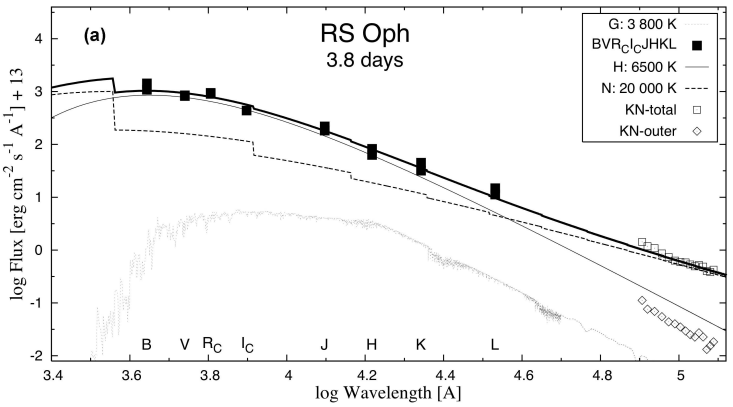

Figure 5.6 The RS Oph Continuum Fit with best-fit HSS temperature of 6500K and a nebular continuum of 20,000K. We hypothesize non-spherical mass ejection as a source of this temperature disagreement.

face of the WD. A similar situation is described for the case of the symbiotic object Z Andromedae by Skopal and Wolf (2006) and Skopal and Pribulla (2006).

Other evidence that indirectly supports this hypothesis may be found in Skopal et al. (2008), who modeled the $H\alpha$ line over the course of the 2006 outburst of RS Oph. The line profile, as shown in Figure 5.7, corresponds to a very fast acceleration of the wind particles and suggests that the broad triangular profile is due to kinematics of the photoionized and optically thin stellar wind from the WD. The authors further argue that the narrow central absorption and emission components may represent radiative transfer of the emission through an optically thick fraction of the wind in the immediate vicinity of the WD.

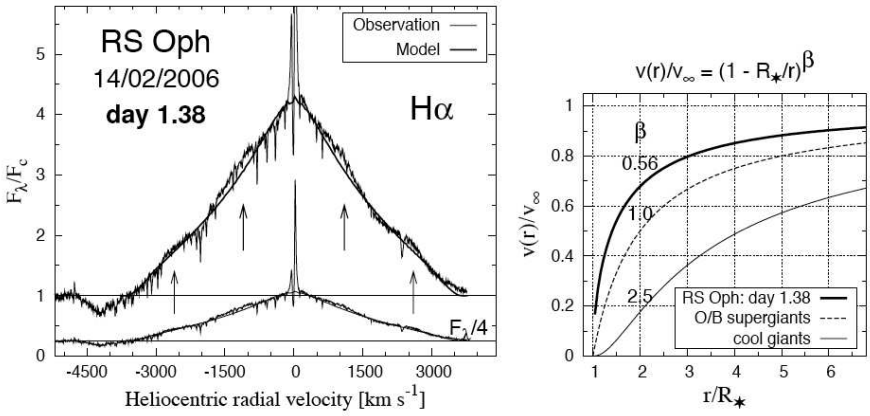

Figure 5.7 The initial $H\alpha$ line profile taken of the nova showing a very broad component, triangular in profile, which the authors state can be matched by a bipolar wind model with a very high acceleration of the particles. In the left panel, the arrows indicate emissions located at $\pm 2500 km\ s^{-1}$ and $\pm 1000 km\ s^{-1}$. The right panel shows the wind-law β factor for the nova as compared to O/B super-giants and cool giants - proof that the nova is in outburst. Reproduced from Skopal et al. (2008).

In the same paper, the authors present a measurement of the $H\alpha$ line profile from days 12.4 and 15.3 post-outburst reproduced here in Figure 5.8. In this, the data show broad shoulder features interpreted by Skopal et al. (2008) as evidence for bipolar, high-velocity jets located, symmetrically, at ± 2430 kms^{-1}. These satellite components were isolated from the total $H\alpha$ emission profile by fitting the central emission with symmetric Gaussian curves.

The findings of Skopal et al. in Figures 5.7 and 5.8 bracket our observations in time and support our interpretation of a non-spherical mass ejection very early in the nova outburst. The bipolar wind model with a very high acceleration of particles may be caused by a ring or disk of material that focuses the ejection. It is this disk material that we may detect in the KIN data.

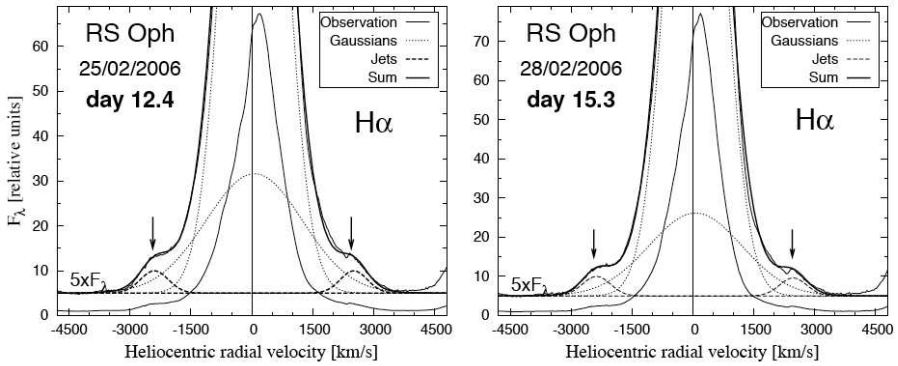

Figure 5.8 The $H\alpha$ line profile taken of the nova on days 12.4 and 15.3 post outburst showing very broad shoulder features (arrowed). These are attributed to high-velocity jets located at $\pm$2430 kms^{-1}. Reproduced from Skopal et al. (2008).

Other supporting evidence of a very early asymmetric mass ejection comes from O'Brien et al. (2006) in which their Figure 1, reproduced below as Figure 5.9, shows the very early expanding shock wave recorded at wavelengths of 6 cm and 18 cm using the VLBA observatory on day 13.8 and 28.7 post-outburst. These results are interpreted by the authors as evidence of bipolarity in the outburst which is the result of either a very early asymmetry in the mass ejection from the white dwarf, or a shaping of the shock wave caused by interaction with an equatorial enhancement in the red giant wind.

Our hypothesis of non-spherical mass ejection is well-supported by other findings that are nearly contemporaneous with our observations and we submit that our interpretation of the data in Figure 5.6 is directly substantiated by them. This result is further explored in Barry et al. (2008b).

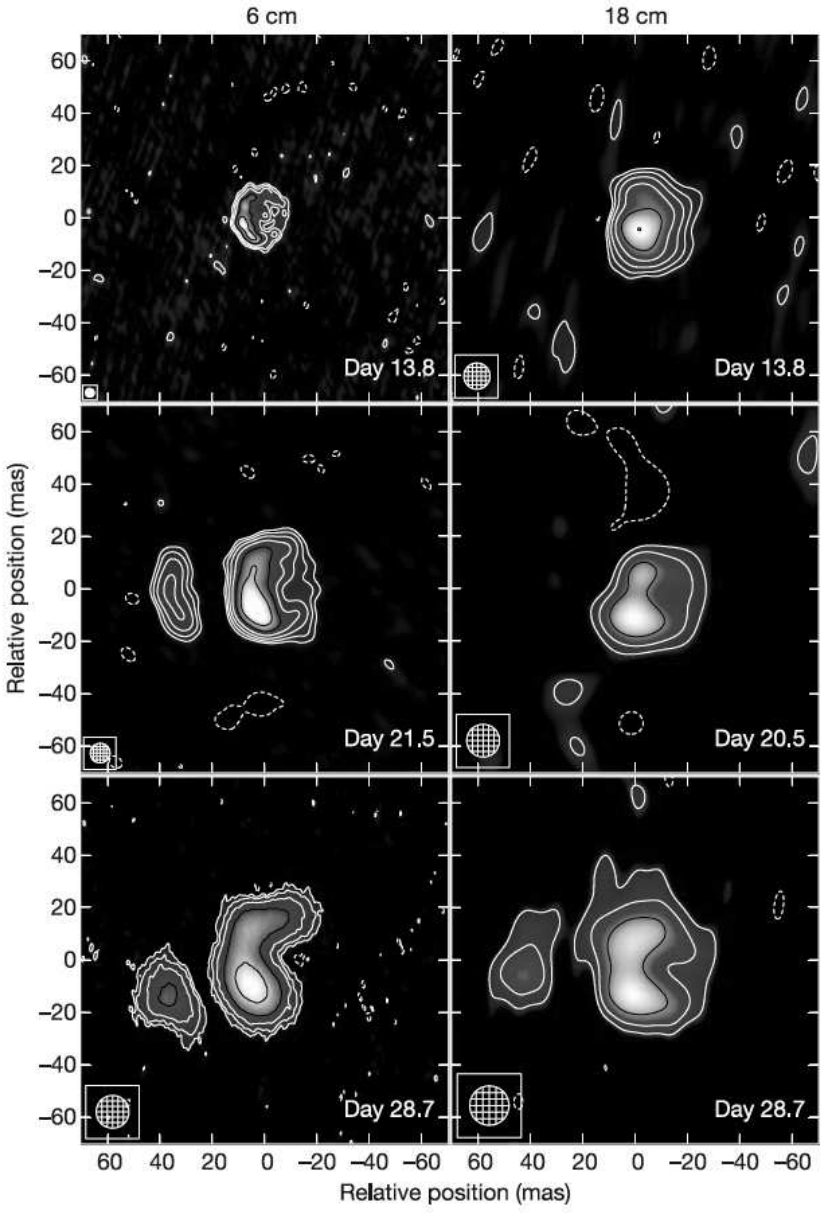

Figure 5.9 The very early expanding shock wave recorded at wavelengths of 6 cm and 18 cm (left and right column, resp.) using the VLBA observatory on day 13.8 and 28.7 post-outburst. Reproduced from O'Brien et al. (2006)

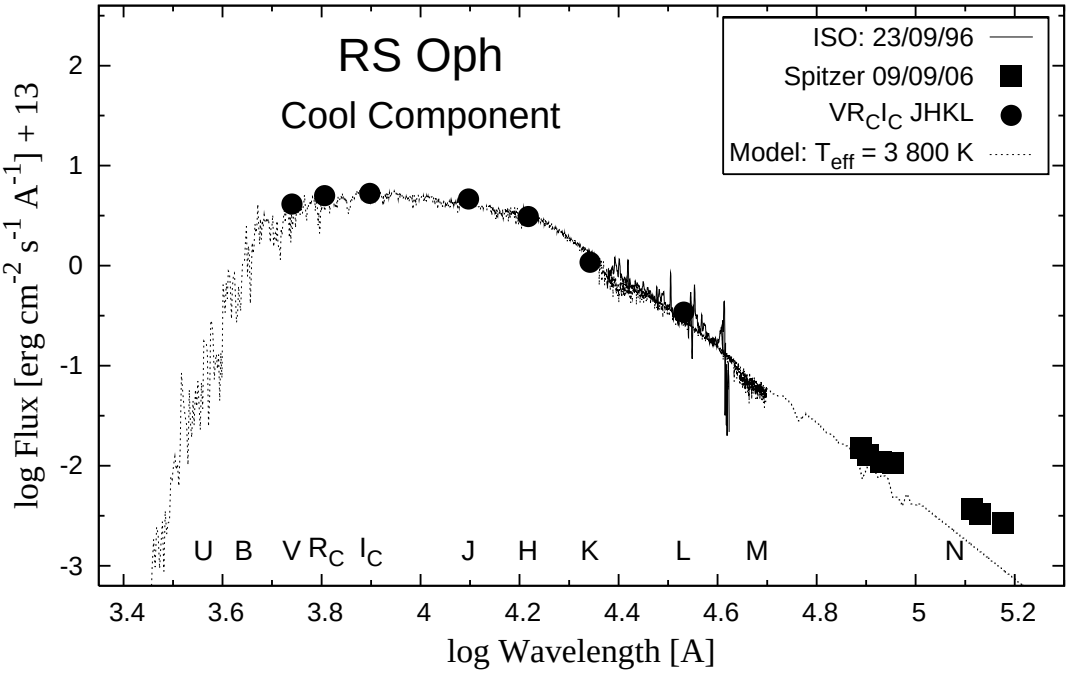

Figure 5.10 The multicolor spectrum of the nova RS Oph showing how the RG model alone does not fit the data well in the N-band at the far right. Also note that the RG model is well-fitted by data from the Infrared Space Observatory data when RS Oph is in quiescence (Mürset and Schmid 1999) and flux points from UV to IR bands.

5.3.2 On the Detection of Dust

The first evidence of dust in the spectra obtained during this outburst of RS Oph is in the *Spitzer* data on 2006 September 9 (day 209). At this point, the object was faint in V-band and its N-band luminosity was likely dominated by the spectrum of the RG. In quiescence the strongest sources of emission are the accretion disk, in the UV, and the RG in the IR (Zajczyk et al. 2007; Gehrz 1988). After identifying the correct Hauschildt RG model by fitting dereddened flux points in the ultraviolet through infrared, we completed the fit by adding the N-band portion of the *Spitzer* 2006 September 9 spectrum. In this model, shown in Figure 5.10, there is a clear

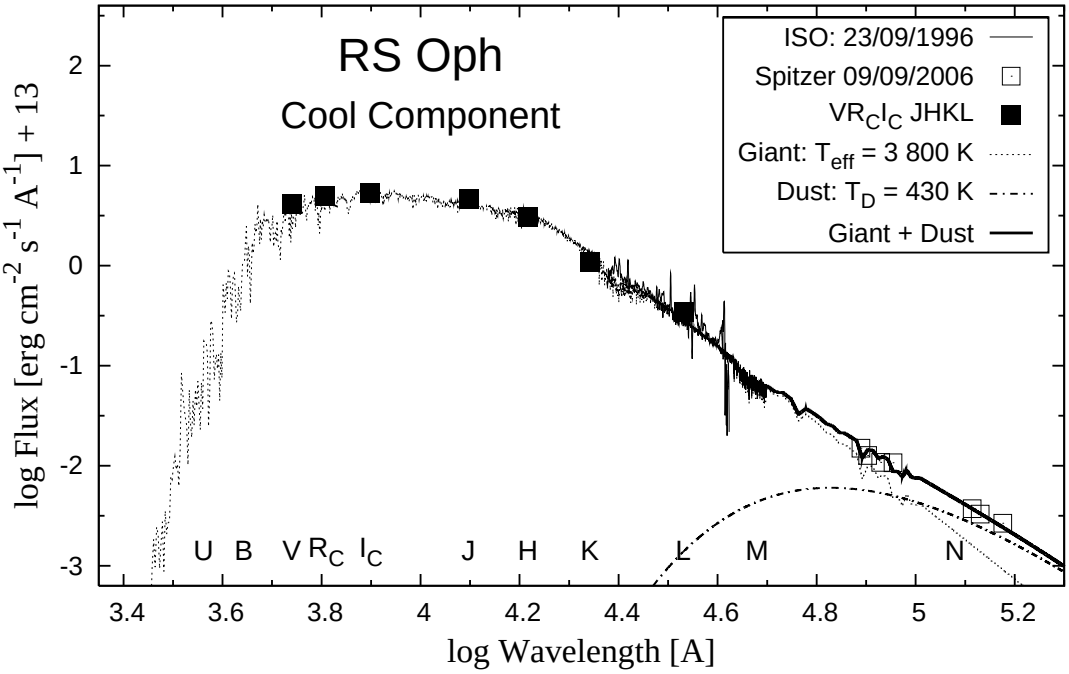

Figure 5.11 The multi-band spectrum of the nova RS Oph showing how the inclusion of a dust blackbody results in a model SED that fits the data more closely.

excess over the Hauschildt model which suggests reprocessing of the stellar light by intervening dust.

Including a dust continuum emission modeled as a simple blackbody curve, we constructed a model SED, shown in Figure 5.11. We also note that the *Spitzer* 2006 September 9 spectrum described in Chapter 4 shows classic molecular bands associated with the interaction of phonons in aggregates of molecules further supporting an indication of nucleated dust.

This model, which represents a composition of the light contributions from the giant and the dust (the nebular being negligible in quiescence), allows us to establish continuum dust emission independently of other mid-IR observations. The dust is modeled as black-body radiation at the temperature $T_D = 430 \pm 50$ K with an ef-

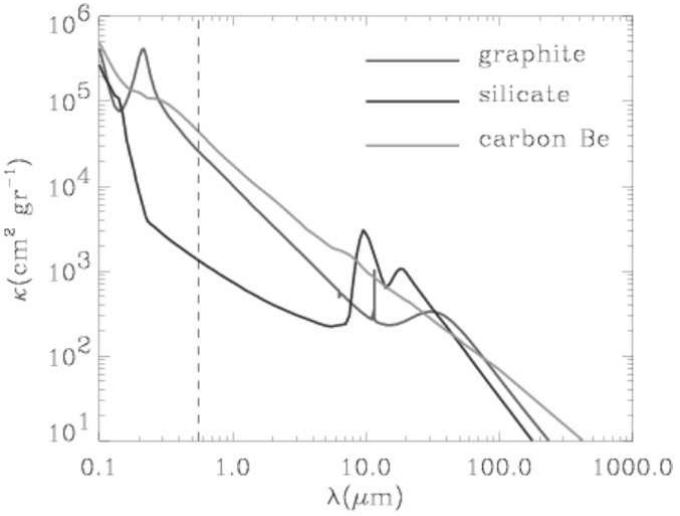

Figure 5.12 A plot of laboratory measurements of the absorption coefficient, κ, of three species of dust; silicate, carbon, and graphite. These loci are then convolved with blackbodies of various temperatures to obtain the emission from each species of dust. Adopted and modified from Dwek (2005)

fective emitting angular radius of $\theta_D = R_D^{eff}/d = 5.4 \pm 0.7$ mas. A distance d=1.4 kpc converts these parameters to the effective, spherical radius of the emitting dust medium of $R_D^{eff} = 380 + / - 50 R_\odot$ with a luminosity L_D between 2.1 and 8.9 $L_\odot$ on day 209 post-outburst. The limits of L_D correspond to the maximum range given by uncertainties in T_D and θ.

To further establish that the evident bands are dust, we conducted analysis of dust models and compared those to the *Spitzer* 2006 September 9 spectrum. Our analysis included modeling of three different kinds of dust; graphite, silicate and carbon dust. We first obtained laboratory data (Dwek 2005) on the absorption coefficient, κ, of dust of these species depicted in Figure 5.12. We then convolved these individual loci with blackbodies of various temperatures until we found one species and one

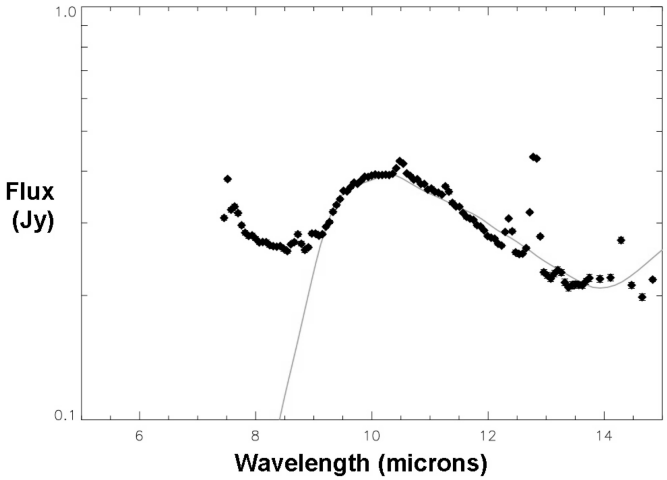

Figure 5.13 Model χ^2/dof = 1.7 fit to *Spitzer* 9 September 2006 spectrum. We attribute departure from fit at wavelengths in excess of 11.5 μm to be due, possibly, to reprocessing of dust by UV radiation.

temperature that approximately fit the data. We give the best fit, with a reduced χ^2_r= 1.7, to the *Spitzer* data in Figure 5.13. We note that the shape of the modeled curve is slightly different than that of the data at wavelengths longwards of $\lambda = 11.5$. We attribute this departure from fit to processing of the dust by UV radiation from the HSS.

The detection of dust in this late *Spitzer* 2006 September 9 spectrum motivated us to look for a similar signature in other data. In particular, we examined the KIN data and constructed a total model SED for day 3.8. We show the final model in Figure 5.14. This figure depicts the combined SED for the total KIN spectrum and the outer KIN spatial regime spectrum. We note that the KIN inner spatial regime spectrum and the KIN total spectrum are almost indistinguishable because the inner KIN spectrum has a much greater total flux than the outer.

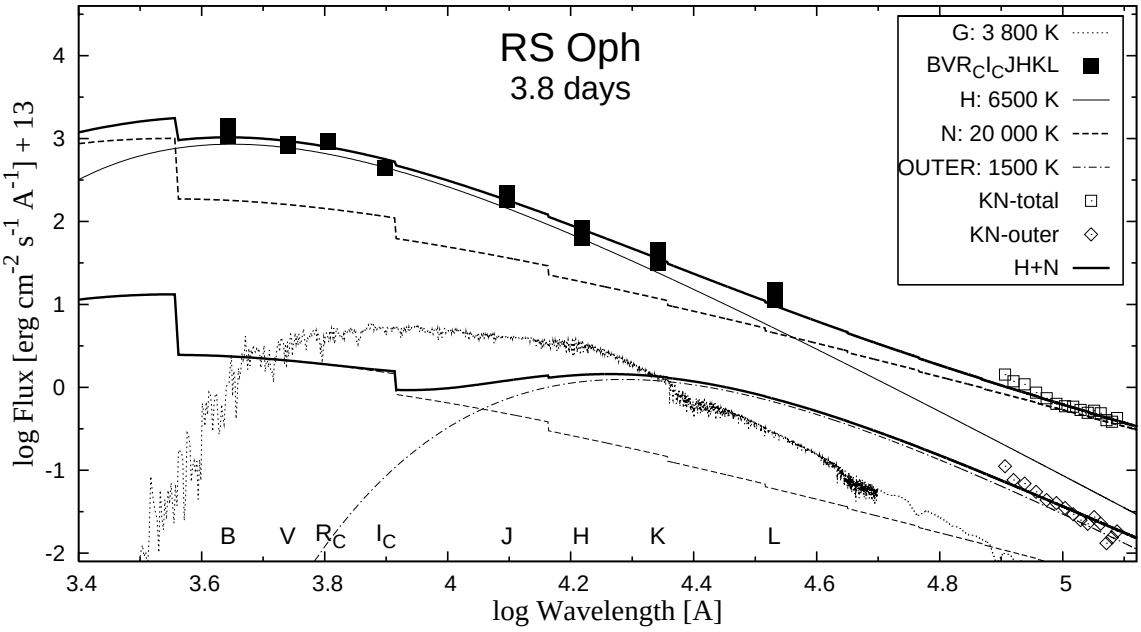

Figure 5.14 Final total SED fit to all data on day 3.8 post outburst - including the KIN total and outer spatial regime measurements. KIN total spectrum is strongly dominated by the KIN inner spatial regime spectrum.

Of particular interest in this figure is the model for the KIN outer spatial regime - the lower trace. These data are best fitted by the sum of emission from the nebular emission and a fairly strong continuum emission of hot dust. The nebular emission is from material with an electron temperature of $T_e = 20,000$ K but at a lower emission measure (scale factor) than for the inner KIN spectrum, as expected. The SED also includes the Hauschildt 3800K RG model but its flux, and that of the nebula, are dominated by the dust emission. The strong continuum emission in the outer KIN spatial regime is primarily from dust just at the sublimation temperature of crystalline silicate. We suggest that this dust may have been heated by the UV flash emitted by the WD in TNR but has not been sublimated by the blast wave at this distance

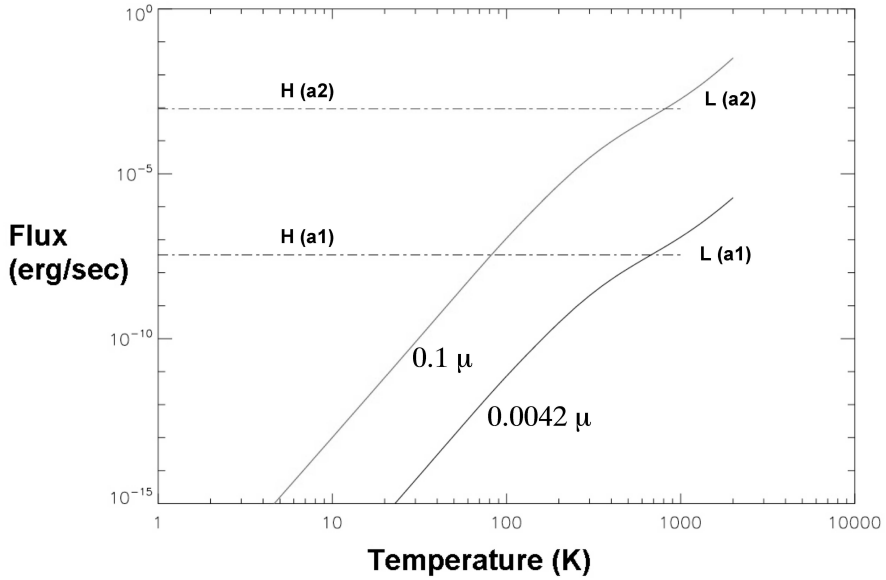

Figure 5.15 Dust temperatures for two sizes of silicate dust. We show two loci of the luminosity of silicate dust of two representative sizes, 0.1μm and 0.0042μm. The intersection of these loci with the heating rates as calculated using Equation 5.10 gives the temperature of the dust. These calculations admit the existence of silicate dust in the KIN outer spatial regime.

from the star which is approximately 13.4 AU at a distance to the object of 1.4 kpc.

To further test this hypothesis we conducted calculations of dust heating rates for differing sizes of silicate dust to determine if conditions admit its existence and to ascertain a range of possible temperatures for the dust. On day 3.8 the luminosity of the HSS was approximately 2×10^{37} erg/sec. The distance from the WD to the center of the KIN outer spatial regime first constructive fringe is approximately 15 AU. The heating rate is determined the expression

$$H = \frac{L}{(4\pi R^2)}(\pi a^2)Q \tag{5.10}$$

in which L is the luminosity of the the HSS, $L/4\pi R^2$ is the stellar flux at a distance, R, from the WD, πa^2 is the geometrical cross-section of the dust of radius, a, and Q is the radiative absorption efficiency (c.f. Figure 5.12). Figure 5.15 shows the dust temperatures for two sizes of silicate dust. The two loci running diagonally across the figure are the luminosity of silicate dust of two representative sizes, 0.1 μm and 0.0042 μm. The intersection of these loci with the heating rates as calculated using Equation 5.10 gives the equilibrium temperature of the dust - at this point the amount of energy absorbed by a particle of dust is equivalent to the amount it is emitting. Silicate dust has an approximate sublimation temperature of 1500K. We note that the KIN outer spatial regime first constructive fringe is centered at about 15 AU (N-band center) but is quite broad and so doubtlessly detects dust emitting at a broad range of temperatures. Also, determination of distance to the nova is quite problematical as noted by Barry et al. (2008). However, these calculations are consistent with the detection of hot dust in the spatial region observed by the KIN outer regime ($\sim$ 15 AU), just outside of the sublimation radius.

5.3.3 Implications for the KIN Outer Spatial Regime Data

Close examination of the lower trace in Figure 5.14 shows a slight departure in the slope of the fit between the KIN outer spatial regime data and the model SED

in the N-band. If the model SED is correct, there are implications for the calibration of data from the KIN. In particular, the stellar leakage in the KIN spectra have a wavelength dependence that may answer this departure from slope fit.

In this, the shortest 8 μm channel of the outer regime takes more radiation from the inner region because the sine corrugation profile of the interferometric acceptance pattern on the sky is relatively narrower than that of the longest N-band wavelength. Also, there may be a larger contribution from the nebula at this wavelength as nebular continuum luminosity varies inversely with wavelenth. Similarly, the longwards 12.5 μm channel has a broader sine profile acceptance pattern and takes smaller amount of radiation from the inner region. By the same mechanism, the longest wavelength channel of the outer regime has its greatest transmission at a greater distance from the source with the distance to the first constructive interferometric peak at an angular distance from the center of the source brightness distribution governed by the expression $\theta = \lambda/B$ where B is the projected baseline. Thus, the outer part of the N-band senses material further away from the WD.

These factors could make the slope of the fluxes obtained by the outer regime slightly steeper than the model SED and may explain this departure of the data and the model. It could, in principle, be possible to correct these fluxes, but we would need to incorporate additional technical details as, for example, the exact transmissivity of the instrument and the atmosphere for each of the 16 spectral channels in the spectrometer. If this *is* an instrumental effect then there is no additional source

physics associated with this slight departure from fit. This will be further explored in Barry et al. (2008a) as it may bear on future observations with this instrument.

5.3.4 Evolution of the Spectral Energy Distribution

In this section we present the evolution of the SED over several epochs following peak V-band brightness in the 2006 outburst using methods developed previously. Figure 5.16 displays data and model SED over the frequency range from the UV to the mid-IR. The left column shows the broad frequency-range fits and the right-hand panels present the detailed spectra in the mid-IR. As in the previous section we used the B, V, R, I magnitudes from the CCD photometric light curves summarized by VSOLJ members (Barry, private communication). We also used IUE spectra from the 1985 outburst of the nova to fit the Spitzer data from day 63, 73, and 209. No such broad-band UV data were available for the 2006 epoch. This is a valid approach because of the close similarity in the lightcurves of all recorded outbursts (Hachisu et al. 2006). Finally, we incorporated measurements in the mid-IR from an archival ISO spectrum from 1996 September 23 (during quiescence) for the region between 2.3 and 4.0 μm to establish the emission from the RG.

The top set of panels show the very early spectra including that of the KIN. The RG spectrum is shown fitted to quiescent data and the total day 3.8 spectrum is given as a continuous line. At this time, the SED is dominated by the HSS in wavelengths shortwards of the mid-IR and by the nebula in the mid-IR. Here we give the total

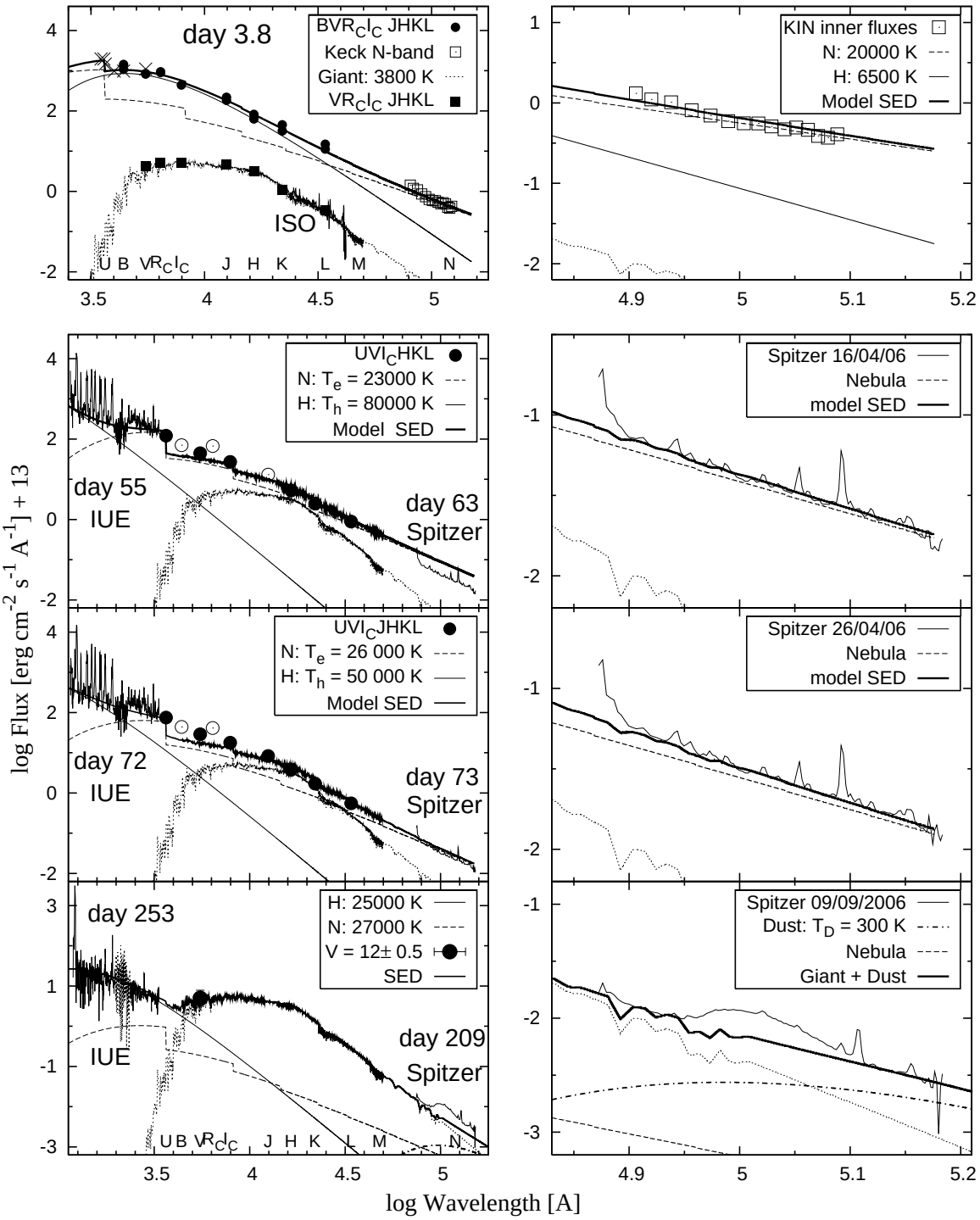

Figure 5.16 The continuum variation of the nova RS Oph. Empty circles on IUE spectra for days 55 and 72 are data we did not use for fitting as we were unable to correct these B and R photometric fluxes due to strong emission lines (Skopal 2007).

KIN spectrum (sum of inner and outer spatial channels). For the day-63 model SED in the second two panels from the top, the nearest IUE spectra in terms of the time elapsed from peak brightness are from 1985 March 23 - day 55 of that outburst. It is clear that the SED in this epoch are dominated by the nebular continuum emission. Day-73 *Spitzer* data in the third row of panels are similarly matched with day-72 IUE spectra from the 1985 outburst and are in excellent agreement with them. Again, the nebular continuum emission spectrum dominates.

Day-209 *Spitzer* data in the last row of panels shows a significant departure from the second two rows. The continuum shows the final-fit sum of the HSS, nebular, dust and RG contributions. In the right-hand bottom panel we show a detail of the N-band fit with the final dust temperature of about 300K when all components are accounted for. It is evident in the detail figure that modeling the dust as a black-body is insufficient at the very finest levels as it does not duplicate the silicate emission feature in the Day-209 *Spitzer* data. As noted above we have conducted further analyses using detailed models of dust emission to determine the composition of the dust detected. Now we discuss values of temperature, angular radius, effective radius, luminosity, and emission measure from the SED models in 5.16.

On day 3.8 the observed SED between 0.36 and 12.2 μm was determined by the optical B,V,Rc,Ic and infrared J,H,K,L photometry. The optical quantities at the day 3.8 were obtained by linear interpolation of the measured neighboring magnitudes in the light curve. Multicolor light curves were carried out by the VSOLJ observers,

Kiyota, Kubotera, Maehara and Nakajima (Hachisu et al. 2006). The measured flux through the R_C filter was corrected by +0.25 mag for a strong H-α emission to get the level of the real continuum (Skopal 2007). H-alpha flux at day 3.8 was interpolated from those measured at day 1.38 and 12.4 (Skopal et al. 2008). The JHKL magnitudes at day 3.8 were obtained by linear (assumed to represent a lower limit of the extrapolated brightness) and parabolic (upper limit) extrapolation of the measurements from 8.7 to 21.7 days as published by Evans et al. (1988). In addition, a few fluxes between 350 and 550 nm were taken from the optical spectrum carried out between the day 3 and 4 (Anupama 2008) and scaled to B and V fluxes. The cool giant's contribution at day 3.8 was negligible with respect to other emissions produced by the outburst.

The model SED throughout 0.36 - 12.2 μm is determined by two main components of radiation. The stellar one is characterized with rather low temperature of 6500 +/- 500 K with the luminosity of $L_h = 46400\ L_\odot \sim L_{Edd}$, which corresponds to the effective radius of $\sim 170\ R_\odot$. The stellar radiation dominates the spectrum in the optical/near-IR region (from B to L passband). Around the U band both the components, the stellar and the nebular, rival each other resulting in the presence of the Balmer discontinuity in emission. Supporting our finding we note that the Balmer jump due to recombination emission in the continuum was independently measured spectroscopically by Anupama (2008) at the same day (February 16) after the eruption. The nebular component of radiation dominates the continuum from

about M passband (5 μm) to longer wavelengths. It is characterized by a large $EM = 1.2 \times 10^{+62}$ cm^{-3} . However, it was not possible to accurately determine the electron temperature because of absence of the ultraviolet data. We adopted Te = 20,000 K in our model SED. The stellar component of radiation could be produced by the extended pseudo-photosphere simulated by the expanding optically thick equatorial ring that was measured directly by the interferometric observations with AMBER/VLTI at day 5.5 (Chesneau et al. 2007b).

Continuing with this process for 16 April 2006, the *Spitzer* data yield the result that no dust was detected by modeling the continuum SED. The region covered by the *Spitzer* data is dominated by the nebular radiation at the electron temperature, $T_e = 23000 \pm 5000$ K, where the uncertainty is given by the SED determined by the UV and optical fluxes. Note that the profile of the nebular continuum is most sensitive to T_e at the near-UV/optical wavelengths. The Spitzer continuum at day 73 corresponds to an $EM = 8.9 \times 10^{60}$cm^{-3}. The model SED for day 73 (26 April 2006) is quite similar to that of day 63 with the electron temperature rising to $T_e = 26,000 \pm 5000$ K and $EM = 6.9 \times 10^{60}$cm^{-3}.

The last observations modeled were from day 209 (2006 September 9) and the temperature of the dust was estimated to be $\sim T_D = 380 \pm 50$ K in a region that has an angular radius of 5.9 mas. At 1.4 kpc this results in $R_{dust} = 420 \pm 50 R_\odot$ The luminosity of the dust is $L_{dust} = 3.3\ L_\odot$ and the emission measure is $EM = 1.5 \times 10^{59}$cm^{-3}. Contribution of the nebular continuum to the N-band is negligible. We note that

dust region is thus relatively large, comparable or larger than the separation of the binary components.

5.3.5 Summary of the Continuum Analysis

In this chapter, we first outlined what the current literature tells us of symbiotic binary systems such as RS Oph and how this is manifested in the continuum emission from such systems. Next we elaborated a method of disentangling the observed SED — an approach based on earlier work in analysis of the composite spectra of symbiotic binaries (Kenyon and Webbink 1984; Muerset et al. 1991; Skopal 2005). We described how we extended this method to the mid-IR N-band for the purpose of ascertaining the contributions of various physical components in the system to the KIN data. We gave details on our analysis of the KIN outer spatial regime data, and on the tentative detection of dust. Lastly, we described the detection of dust in the *Spitzer* spectrum on 2006 September 9 and showed the temporal changes in the continuum emission from the object from day 3.8 until day 209 post outburst.

Chapter 6

Stellar Masses from Spectroscopy and Interferometry

In this chapter we discuss the importance precision measurement of masses and intrinsic luminosities of evolved giant and subgiant stars as well as low mass main-sequence stars and to test stellar evolution models. We first outline the problem in Section 6.1 and discuss the importance of high precision masses and luminosities and what has prevented us from obtaining them historically. Subsequently, in Section 6.2 we describe which classes of stars are of particular scientific interest in the current epoch and why. We then describe the observing campaign we conducted for this research in Section 6.3 and our method for combining radial velocity and interferometric astrometry in Section 6.4. We briefly review the mathematics of orbit determination by radial velocity measurements alone (Section 6.5). We also identify precisely where

new measurements are needed and describe the nature of those measurements.

Finally, in Section 6.7 we describe the process we used to determine the mass and luminosity of one of our observing campaign targets; the M-dwarf binary, Gliese 268. We report interferometric and radial velocity observations of the M-dwarf binary GL268 leading to masses of the constituent stars with uncertainties of 0.5%. The total mass of the GL268 system is $0.4182 \pm 0.0020 M_{\odot}$ (0.5%). The masses of the constituent stellar components are $0.2259 \pm 0.0011 M_{\odot}$ for component A and $0.1923 \pm 0.0009 M_{\odot}$ for component B. The system parallax is determined by these observations to be $0.1594 \pm .0039$ arcsec (2.4%) in agreement with Hipparcos. The absolute H-band magnitude of the component stars are 7.65 ± 0.08 and 8.19 ± 0.08 for GL268A and B, respectively. Note that throughout this chapter we follow the formalism of Bevington and Robinson (2003) in reporting of precision in our measurements.

6.1 The Importance of Stellar Mass and Luminosity

Historically, due to the intrinsic faintness of the sources or the rarity of low-mass binary targets with eclipsing and therefore unambiguous orbits, observations of members of these classes of objects have resulted in derived masses with insufficient precision to constrain stellar evolution models. We have used new observational methods in the course of this research to obtain high angular resolution astrometric

data using the IOTA interferometer (c.f. Chapter 2) for several low-mass binaries. These data, taken together with existing high-quality radial velocity and spectroscopic data, have allowed us to derive, for the M-dwarf binary GL268, orbital models using a simultaneous global best fit to all observables, an approach with few precedents. From this we have computed stellar masses with relative uncertainties of less than 1% - a significant improvement from almost all measurements obtained for these classes of objects.

Given the mass and metallicity of a star, stellar evolution models in principle can predict all its physical properties such as size, temperature, and luminosity at any given time in the past or the future. These models rely on a large number of physical assumptions, along with laboratory measurements of a variety of atomic and physical properties (nuclear reaction rates, radiative opacities, etc.). Subsequent to making our measurements and fitting the appropriate orbital models, we employed the masses and luminosities derived using this methodology to calibrate the appropriate astrophysical model Baraffe et al. (1998).

Historically, the measurement of velocities along the line of sight to a star (radial velocities) through the Doppler effect in multiple stellar systems has proven invaluable for obtaining information needed to challenge theoretical models. Specifically, the dynamical behavior of binary systems of stars are apt to a relatively simple physical central force model using opposite tangential velocities that can be measured spectroscopically. These particular systems of stars constitute astrophysical labora-

tories that allow the determination of critical stellar parameters such as the absolute mass of the components.

In some favorable cases stars in multiple systems may eclipse one another. This simple geometry allows us to derive precise information about the stellar radii of the components - a very sensitive diagnostic for evolution. Intrinsic luminosities may also be deduced, which, combined with the masses and radii, provide important constraints to test our knowledge of stellar evolution. When the orbits are not edge-on, the unknown projection factor prevents us from determining the absolute mass directly unless the inclination angle can be determined in some other way. This problem is called the $\sin i$ ambiguity because the masses are indeterminate to the sine of this projection angle cubed. (We show the derivation of this expression in Section 6.5.) Even so, masses are then sensitive to how accurately that angle is measured. Certain classes of stars for which few eclipsing cases are known therefore suffer a penalty in accuracy with errors that can sometimes exceed 10 or 20% in the mass. This means that models for such stars are more poorly constrained by observations.

Recent advances in stellar long-baseline interferometry allow the possibility of making extremely precise astrometric measurements of the motion of binaries in the tangent plane of the sky. In particular, the projection angle can be determined to high accuracy. When taken together with radial velocity observations, these orthogonal observables may be integrated into a global least-squares orbital solution that allows the determination of stellar characteristics with uncertainties small enough to be

useful for testing models (Andersen 1991). This comparison with theory is essential to improve our knowledge of the physics of stars.

6.2 Scientifically Interesting Binary Stars

Over half of all points of light on the night sky are actually multiple - most often binary - systems of stars (Duquennoy and Mayor 1991). Nearly all empirical determinations of stellar masses have been accomplished as a direct result of studies conducted on these systems. Of these, the best represented population is that of stars such as the Sun, located on the main sequence, defined as a locus of points of mass vs. luminosity for stars that are in their relatively stable, core hydrogen burning state. While not all of the currently available empirical data for this broad population of stars is as complete or accurate as we would like, a more precise determination of the mass of most of these objects will not substantially advance our scientific knowledge of them (Andersen 1997).

A broad category of stars for which very few precise masses have been determined are the Luminosity Class III and IV stars - giants and subgiants, respectively. These objects, which have left the main sequence as their core hydrogen fuel was exhausted, go through several distinct evolutionary phases, some of which are exceedingly brief on astronomical timescales depending on initial mass. Stellar evolution proceeds quite rapidly once a star begins to leave the main sequence but slows during several distinct phases. As a result models can be quite sensitive to the initial physical

constituents and assumptions. Obtaining accurate masses of giants or subgiants along with other properties such as the temperatures and luminosities, and radii (if the binary is eclipsing), enables us to put tight constraints on theory and test assumptions such as mass-loss mechanisms and certain aspects of the treatment of convection. Giants and subgiants have not been studied extensively primarily because massive stars, which will be the first to leave the main sequence due to their faster burn rate, are rarer to begin with. A second reason for this under-representation is that binaries that include giants or subgiants are often subject to significant mass loss over their lifetimes, and tidal mixing and mass exchange because of their extended envelopes. By definition, interacting binaries are ones in which the two stars do not pass through all of the stages of their evolution independently. If we wish to study the evolution of a particular giant or subgiant without its evolutionary path having been significantly altered by the presence of its companion, our target selection space is again limited.

At the very low-mass end of the main sequence are the M-dwarf stars. These are distinctly underrepresented in studies that have made precise determinations of stellar mass. This may be surprising given their numbers, as the stellar initial mass function gives the distribution of the number of stars of different masses as being proportional to $M^{-\gamma}$, where M is mass and $\gamma \simeq 1.5$ (Miller and Scalo 1979; Silk 1995). Only three well-detached eclipsing systems are known with significantly sub-solar masses of the component stars. These are CM Dra (Metcalfe et al. 1996), YYGem (Torres and Ribas 2002) and GJ 2069A (Delfosse et al. 1999). Detailed checks of evolutionary

models have relied heavily on these three measurements all of which are of stars that have been found to be chromospherically active. As a result, they may have colors that are atypical for their bolometric luminosities. So, although these objects are quite numerous, they are intrinsically faint with 0.01% solar luminosity being a typical value and therefore they are difficult to study. For example, Barnard's star, an M4 dwarf, has an intrinsic luminosity of $4 \times 10^{-4}\ L_{\odot}$ (Dawson and De Robertis 2004). Moreover, their small sizes relative to their separations in their orbits mean that M-dwarf binary systems will display eclipses only very rarely. One reason there is considerable scientific interest in this class of stars is that unlike other types of stars on the main sequence, mid to late M darfs are fully convective, a very complex phenomenon to model. Moreover, models for M stars are already known to show some serious discrepancies with the observations (Torres and Ribas 2002). As a result, it is important to find additional systems in this mass regime that are suitable for testing theory.

Other populations of stars with uncertain masses include pre-main sequence stars, hot and massive O stars, and metal-poor stars. Pre-main sequence stars that are still contracting toward the main sequence and are not yet burning hydrogen in their cores are, like M-stars, often exceedingly faint, and much less common. Although their binary frequency appears to be quite high (Leinert et al. 1997; Ghez et al. 1993), relatively few cases are known that have their orbits determined well enough to constrain models. Metal-poor stars, which, as their name implies, lack the metals

typically found in current-generation stars, are rare, faint and distant. They are of scientific interest because they probe a very different chemical regime than the overwhelming majority of stars in the solar neighborhood, and evolution models predict that they should be hotter, more luminous, and smaller in size than solar-composition stars of the same mass. Lastly, members at the massive O-star end of the main sequence are also underrepresented in definitive mass and luminosity determinations. This may be attributed to the fact that they are exceedingly rare (for the same reason that M-stars are numerous) and because the local solar neighborhood of the Galaxy is nearly devoid of examples of this type of star. Additionally, their radial velocities are difficult to measure due to their typically broad spectral features - a result of rapid rotation.

All of these categories of stars are of great scientific interest - there is clearly much to be learned about them. However, the sensitivity and spatial resolving power of available instruments limit our choices as does the availability and quality of extant spectroscopic velocity data. Of the classes of objects listed above, two that fall into this restricted search space are giant and subgiant stars, and low mass main-sequence stars. Mass determinations accurate to 1% should allow scientifically significant calibration of existing models for these groups of objects.

6.3 The Astrometric Observing Program

To partially fulfill the objectives of this research, we pursued an intensive campaign of astronomical observations at the IOTA facility at the F. L. Whipple Observatory in Arizona. We used observational methods as noted in Chapters 2 and 3 to obtain high angular resolution astrometric data using this experimental long-baseline near-infrared stellar interferometer. A summary of observations is outlined in Table 6.3. Importantly, IOTA was one of only three facilities worldwide that are capable of obtaining the closure phase of a source brightness distribution. This interferometric observable, which requires a minimum of three baselines and is mathematically independent of instrumental and atmospheric phase, is essential to obtain measurements of a caliber that can make this research possible. It is important to note that IOTA, being a PI-class experiment, did not have the support structure found at a typical astronomical facility. For example, in addition to observing program targets and assisting other researchers with productive Mira variable and Wolf-Rayet star observing programs, we wrote all of the observatory opening, optical alignment, observing and closing procedures. We also wrote a set of informal guidelines on how to obtain the best data from the observatory using techniques we developed for working with exceedingly dim targets, how to conduct instrument calibration, and how to optimize the facility to work with poor seeing conditions. On 2006 July 01 the IOTA facility ceased all operations and was dismantled due to funding constraints. We were fortunate to use this observatory and have conducted the last thesis research using

its particular capabilities.

During this 2.5 year campaign that comprised fifteen observing runs — some runs exceeding three weeks in duration — we have obtained a large number of high-quality observations of program objects. We have nearly complete phase coverage for several objects including Gliese 268, Gliese 815, ρ Tauri, and α Equulei among other multiple-star targets. We list campaign targets in Table 6.3.

6.4 An Approach to Determination of Mass

The general idea of combining astrometry (either from visibilities, or position angles and separations, or lunar occultation data, or Hipparcos data, or Hubble Fine Guidance Sensor data, etc.) with spectroscopy has been used before to establish the absolute masses of stars, by combining the elements of the spectroscopic and astrometric orbits solved independently of each other. The approach we took to obtain the masses of the component stars of GL268 are different in a significant way in that we did not simply take the extant spectroscopic orbital elements and use them to constrain the astrometric orbit (since several of the elements are in common). We instead combined all the measurements obtained from each astronomical technique directly into a simultaneous global least-squares orbital fit, from which we derived all of the elements of the three-dimensional orbit at once and infered the masses of the binary components (Torres 2004). It is important to note that this approach of combining both radial velocity data and astrometric data including closure phases

Table 6.1. Program stars

Object	Spectral Type	Coordinates[a]	B	V	H	Obs[b]	Note	Ref
GL487	M3 V	12 49 02.7537 +66 06 36.653	12.56	10.92	6.299	24	MDB[c], flare	Platais et al. (2003)
ρ Tau	A8 V	04 33:50.9177 +14 50 39.928	4.886	4.657	4.288	32	LMB[d], pms[e]	Blondel and Djie (2006)
η Boo	G0 IV	13 54 41.0787 +18 23 51.781	3.26	2.68	1.534	12	tidal mixing	van Belle et al. (2007)
ρ CrB	G0 V	16 01 02.6616 +33 18 12.634	6.01	5.40	···	12	substellar companion	Noyes et al. (1997)
α Equ	G0 III	21 15 49.4317 +05 14 52.241	4.449	3.949	2.442	53[f]	PsMS[g]	Baraffe (2005)
GL815	M1.5 V	21 00 05.3465 +40 04 13.002	11.6	10.1	···	32	MDB	Baraffe et al. (1998)
GL268	M4.5	07 10 01.8333 +38 31 46.058	13.19	11.47	6.152	60	MDB	Baraffe et al. (1998)
GL372	M2	09 53 11.7812 -03 41 24.400	12.08	10.55	6.409	28	MDB	Ramseyer et al. (1999)
HIP10535	F6 V	02 15 42.7773 +25 02 34.956	6.051	5.585	4.500	4	binary, metallically	Nordström et al. (2004)
RS Oph	KII - M2 RN	17 50 13.202 -06 42 28.48	5.30	4.3	6.858	87[h]	RN	Evans et al. (2007)
ϵEri	K2 V	03 32 55.8442 -09 27 29.744	4.61	3.73	1.880	4	substellar companions	Quillen and Thorndike (2002)
SS Lep	M III	06 04 59.1292 -16 29 03.965	5.148	4.974	2.105	4	Algol, RLO EmLS	Verhoelst et al. (2007)
ψ Leo	M2 III	09 43 43.9046 +14 01 18.091	6.997	5.384	1.105	4	PsMS	Baraffe (2005)
GL98	K5 V	02 27 45.8620 +04 25 55.749	10.15	8.72	5.332	4	MDB	Baraffe et al. (1998)
RR Crb	M3	15 41 26.2286 +38 33 26.599	9.04	7.74	1.394	8	semi-regular pulsating	Baraffe et al. (1998)
78 Leo	F4 IV	11 23 55.4523 +10 31 46.231	4.35	4.00	2.84	12	PsMS	Baraffe (2005)
GL423	F8.5 V K2 V	11 18 10.950 +31 31 45.74	5.383	4.729	···	64	MDB	Baraffe et al. (1998)
89 Her	F2 I	17 55 25.1889 +26 02 59.966	5.799	5.474	4.239	48[i]	PsMS contact binary	Baraffe (2005)

[a]ICRS epoch 2000 coordinates

[b]Visibility and CP measurements for a single night. The number of nightly observations and the corresponding number of degrees of freedom for χ^2 fitting is much larger. *Each* of these nightly observations consists of between 100 and 200 discrete measurements.

[c]M-dwarf binary (MDB)

[d]Low-mass binary (LMB)

[e]Pre-main sequence (PMS)

[f]Includes stellar size measurements of one component.

[g]Post main sequence (PsMS)

[h]Includes observations at PTI, IOTA, KIN and KI.

[i]Includes observations conducted by non-program observer, J.D. Monnier.

has only one known precedent, in the study of the binary star Omicron Leonis by Hummel et al. (2001). We provide details on how we accomplished this for the specific case of GL268 in Section 6.7.

The basic principle we followed to determine the masses of this target is as follows. First, we obtained archived radial velocity measurements from high-resolution spectroscopy for both components of each binary. We then integrated data, which by themselves will allowed a determination of the mass to within a factor of $\sin^3(i)$, as noted in Equation 6.15, with orthogonal astrometric data, obtained for this research using the IOTA instrument on Mt. Hopkins, into a global fit of the measurements. This yielded a three-dimensional orbital solution allowed deduction of the masses of the constituent stars. Here we note that speckle and adaptive optics data alone would be insufficient to properly define a visual orbit for most of these targets - GL268 in particular - because these techniques would never properly resolve the systems close to periastron were the minimum separation of binary components is small.

We were also able to determine the distance to GL268 very accurately using these techniques independently of any assumptions aside from Newtonian physics. Functionally, radial velocities allow us to determine the semi-major axis of the orbit in linear units, except for a trigonometric projection factor. Our astrometric measurements, on the other hand, allow us to determine the semi-major axis in angular units and also provided the orbital inclination angle. We then use the calculated inclination angle to de-project the linear semi-major axis obtained from spectroscopy. The

ratio of this term with the angular semi-major axis yields the stellar distance, or its reciprocal, the orbital parallax. We then used this measurement, which depends only on the dynamics of two-body central force interactions, to establish, with the measured apparent stellar flux and flux ratio determined spectroscopically, the intrinsic luminosity - the total energy emitted per unit time - of the constituent stars. We report the results of these calculations together with accurate component masses for GL268 in the final section of this thesis.

6.5 A Brief Review of Radial Velocity Orbits

We now give a brief review of how radial velocities are used to describe the orbit of binary stars. We will also show, explicitly, where this description results in a determination of the masses of the constituent stars that has large uncertainty. We will further describe how interferometry specifically breaks this degeneracy. We begin with a description, in barycentric coordinates, of the total angular momentum and energy of the binary stellar system based on the approach of Hilditch (2001).

The direction of the total angular momentum vector, **J**, and the total energy, C, of a binary system together with the magnitude of **J** completely describe the size, shape, and orientation of the relative orbit of the system. The total energy is given by the sum of the kinetic energy, K, and the potential energy, Q. The kinetic energy is

$$K = \tfrac{1}{2} m_1 V_1^2 + \tfrac{1}{2} m_2 V_2^2 = \tfrac{1}{2} \frac{m_1 m_2}{m_1 + m_2} V^2 \tag{6.1}$$

In which V_1 and V_2 are the speeds of the individual component stars of mass m_1 and m_2 and

$$V = (G(m_1 + m_2)\{(2/r) - 1/a\})^{1/2}. \tag{6.2}$$

In this expression, a is the length of the elliptical orbit semi-major axis. The term r is the length of the vector connecting the stars and is formed, in our barycentric coordinate space as

$$\vec{r} = \frac{(m_1 + m_2)}{m_2} \vec{R_1} = -\frac{(m_1 + m_2)}{m_2} \vec{R_2} \tag{6.3}$$

in which $\vec{R_1}$ and $\vec{R_2}$ are vectors from the center of mass to each of the stellar elements. The potential energy is

$$Q = -\int \frac{G m_1 m_2}{r^2} dr = -\frac{G m_1 m_2}{r}. \tag{6.4}$$

The total energy is then given by

$$C = K + Q = -\frac{G m_1 m_2}{2a} \tag{6.5}$$

which is a negative number as is appropriate for a bound orbit. The magnitude

of the total angular momentum is

$$J = m_1 L_1 + m_2 L_2 \tag{6.6}$$

In which L_1 and L_2, the specific angular momenta for each barycentric orbit are given by the expression

$$L_1 = \frac{m_2^2}{(m_1 + m_2)^2} L; \quad L_2 = \frac{m_1^2}{(m_1 + m_2)^2} L. \tag{6.7}$$

Here L is a constant for the ellipse given by

$$L = G(m_1 + m_2)a(1 - e^2). \tag{6.8}$$

By combining these formulae, the final expression for magnitude of total angular momentum for the binary system is

$$J = \frac{2\pi a^2 (1 - e^2)^{1/2} m_1 m_2}{P(m_1 + m_2)}. \tag{6.9}$$

From this we can see that the orbital eccentricity determines the magnitude of total angular momentum as we would expect. If the orbit is circular, eccentricity is 0, J is maximum. If the orbit is rectilinear, eccentricity = 1, the magnitude of total angular momentum is zero.

The total angular momentum vector, $\vec{J}$, for an isolated, two-body system, defines a

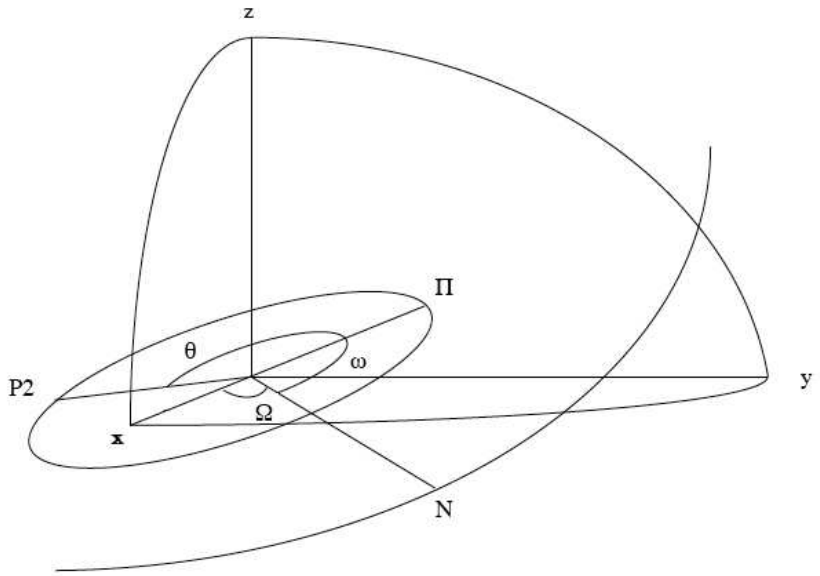

Figure 6.1 Depiction of the orbital elements of a binary stellar system. The relative orbit of the binary, located in the xyz coordinate system shown is defined by the *longitude of the ascending node*, Ω, the inclination of the orbit to the tangent plane of the sky, i, and the *longitude of pariastron*, ω. θ is the *true anomaly*, N is the location of the *ascending node*, and the orbit plane is denoted by the angle $O\Pi P_2$ where O is the origin of coordinates. Star m_1 is located at the origin and m_2 is at point P_2. The observer is on the $-Oz$ axis. See text for details.

plane which may be specified in terms of a practical, observational coordinate system. See Figure 6.1.

In this figure, the mass, m_1 is at the origin, O, of the cartesian coordinate system but is not labeled. The second stellar component, m_2 is located at P_2 at some particular time, t. The line of sight to the observer is along the Oz axis in the direction of $-z$ and the plane described by the axes, Oxy, is in the tangent plane

of the observer's sky. For binary work, the axis Ox is always taken to point to the celestial north pole. The orbital plane contains P_2, Π, and the origin. N is the intersection of the orbit plane with the tangent plane of the sky. This is the point in the orbit where the star is receding most rapidly and is termed the *ascending node*. There is another point, not depicted, on the opposite side of the orbit on a line from N through the origin for which the star is approaching most rapidly. This is the *descending node*, N'. The line NON' is termed the *line of nodes* and its orientation is defined by the angle, $\angle\, xON = \Omega$ termed the *longitude of the ascending node*. The inclination of the orbit to the tangent plane of the sky is given by the angle, i. The angle, $\angle\, \Pi OP_2 = \theta$ locates the mass, m_2, at time, t, and is given the curious name the *true anomaly*. Finally, the orientation of the orbit within its own plane is given by the angle, ω termed the *longitude of periastron*.

From Equation 6.9 we now find that the angular components of $\vec{J}$ with a direction defined by the orbital plane, are

$$J_x = J \sin i \sin \Omega; \quad J_y = -J \sin i \cos \Omega; and J_z = J \cos i. \tag{6.10}$$

The orbit is now completely defined in three-dimentional space by the five elements listed so far $(a, e, i, \omega, \Omega)$ together with a final element, T. This is the epoch of the orbit usually expressed as a Julian date.

The polar coordinates of the star at P_2 with the point O at the origin are $(r, \theta+\omega)$. Resolving these into two components in the orbital plane gives $r\cos(\theta+\omega)$ along the

line of nodes and the in-plane orthogonal $r\sin(\theta+\omega)$. Projecting $r\sin(\theta+\omega)$ onto the line of sight gives $z = r\sin(\theta+\omega)\sin i$. Using the polar equation of an ellipse, $r = a(1-e^2)/(1+e\cos\theta)$ and Kepler's second law, $r^2\dot{\theta} = 2\pi a^2(1-e^2)^{1/2}/P$, with P being the period of the orbit, the observed radial velocity is then given by

$$V_{rad} = \frac{2\pi a \sin i[\cos(\theta+\omega)+e\cos\omega]}{P(1-e^2)^{1/2}}. \tag{6.11}$$

This is usually given in terms of γ and K as

$$V_{rad} = K\{\cos(\theta+\omega)+e\cos\omega\}+\gamma \tag{6.12}$$

in which the component velocity semiamplitude is

$$K = \frac{2\pi a \sin i}{P(1-e^2)^{1/2}} \tag{6.13}$$

and γ is the radial velocity of the center of mass of the system. Here we note that the velocity semiamplitude, K, can only be known to within the sine of the inclination angle. For *double-lined* binary systems - ones for which we can determine the radial velocity of each component through assay of their emission lines - we can obtain a projected semimajor axis from the semiamplitudes, K_1 and K_2 as

$$a_{1,2}\sin i = \frac{(1-e^2)^{1/2}}{2\pi}K_{1,2}P. \tag{6.14}$$

These may then be used, after noting that $m_1 a_1 = m_2 a_2$ and $G(m_1 + m_2) = 4\pi^2 a^3/P^2$, to derive the expression

$$m_{1,2} \sin^3 i = \frac{(1-e^2)^{3/2}(K_1 + K_2)^2 K_{2,1} P}{2\pi G}. \tag{6.15}$$

This *particular* expression tells us why astrometry is critical for determination of stellar mass. The mass is uncertain by a factor of $\sin^3 i$. Without some means to determine the value of i all determination of mass and tests of models of stellar astrophysics that depend on calibration by measured masses are strictly limited to eclipsing systems.

6.6 Measurement Error and Derived Stellar Parameters

When reporting formal errors in calculated masses of astronomical sources that are below 1%, particularly for low mass stars, the dominant sources of measurement error will be systematic, although astrophysical effects must also be examined. In particular, cross-correlation line blending and the effects of stellar maculation bear on the final result and we are obliged to assure that each effect is fully understood before we may assert that we have obtained an accurate measurement. Because of the rarity of binary stars that are suitable for this type of measurement and extreme paucity of the types of astronomical data necessary for the required calculations, fundamental

properties of the successfully observed low-mass binaries are particularly important as a calibration for theoretical models. At the level of 1% uncertainty, as required for such calibration, the data must be examined with care for systematic errors that might bias the results, particularly the masses. In this section, we describe the effects due to line blending and starspots.

We carried out radial velocity and astrometric observations in such a manner that there are always multiple measurements of the same value. The central limit theorem tells us that any sum of many independent and identically distributed random variables will tend to dispersed according to a specific attractor distribution. For the particular case in which the sum of the variables has a finite variance then the attractor distribution is normal and is well-described by a Gaussian. Moreover, if the sample size is large, the sample distribution will have the same mean as the population of all possible samples. For example, if each measurement of the visibility we conducted consists of some number of individual scans, the resulting measurement is reported as the RMS of these scans with an error term that indicates the amount of scatter. To this, we add a conservative estimate of the systematic error obtained from previous observations and back check our result.

6.6.1 Line Blending

Emission line blending can effect our measurement of the velocities of the individual components of GL268 in the following way. Lines of one component may be

blended with those of the other emitted at a different rest wavelength when they are brought into alignment by their relative Doppler shifts. Blending with the same line or with unrelated lines at just the same wavelength also occurs, but this is at phases which carry very little weight in the orbital solution, so these have essentially no effect whatsoever. In our cross-correlation profile, which is an averaging over all lines in the observed spectrum, the blending described above manifests itself as variations radial velocity along the temporal baseline. In particular, we refer to systematic shifts in the velocities due to blending between the two main correlation peaks or between either peak and the sidelobes of the other peak. This effect, sometimes referred to as peak-pulling, is worse for velocimeters that have limited bandwidth because the effect on the error term averages out as $1/N^{1/2}$, with N the number of lines used in the correlation analysis.

6.6.2 Starspots

The subject of stellar maculation, starspots, is particularly topical to the current study. Starspots are relatively cool, dark regions, typically on the order of 500-2000 K cooler than the surrounding stellar photosphere, possibly due to the inhibition of convection by the strong magnetic fields in the spot region. Since starspots are cooler, their equivalent blackbody colors will be redder than the surrounding photosphere, and, If they have more absorption lines than the surrounding photosphere due to molecules, the additional absorption lines could make the spot colors even redder.

One of the principal ingredients for generating starspots is gradients in stellar angular rotation caused by angular momentum redistribution within the convective layers of cool stars resulting in large-scale magnetic fields. These fields, which are generated by magneto-hydrodynamical mechanisms - dynamo processes - operate in the outer envelopes of all stars but especially those of late-type such as GL268 because M-dwarfs are theorized to be fully convective. These effects can produce maculation that covers a sizable fraction of the stellar surface.

These surface inhomogeneities can produce irregularities or distortions in the light curves of the individual stellar components of binaries in the following way. The intrinsic luminosity of each component will be partly determined by its temperature while the total flux will depend on the percentage of the surface area emitting at that temperature. The presence of spots distorts the shapes of spectral lines and as a result, the cross-correlation peaks, a proxy for average line shape, will be asymmetrical. Consequently, the cross-correlation peaks will not be well-described by Gaussian functions and determination of the centroid, thus the measured radial velocities, may be affected. If one or both components are known to have starspots, the spots may be explicitly modeled and compared to LC data as was conducted by Torres and Ribas (2002).

6.7 The M-dwarf binary Gliese 268

We chose the M-dwarf binary, Gliese 268 (HIP34603, $\alpha = 7^h10^m01.83^s$, $\delta = 38°31'45.1'', J2000.0$), kinetically and photometrically a member of the young disk population, as a target for our scientific program for a number of compelling reasons. First, the object, while rather faint in Johnson V-band at $m_V = 11.47$ is reasonably bright in H-band at an approximate magnitude of $M_H = 6.152$. The object is an RS CVn-type binary consisting of late-type, cool stars with rotations that are tidally locked (or nearly tidally locked) with their system rotation rate. Previous radial velocity orbital analysis conducted by Tomkin and Pettersen (1986) give an orbital period of this system of about 10.4 days. The *Hipparcos* catalog (Perryman et al. 1997) gives the system at an approximate geometric parallax of 157 mas (6.38 pc) with component semi-major axes of about $a\sin(i) \simeq 0.29$ & 0.35AU. The radii of the individual spectroscopically categorized dwarfs is a negligible fraction of this distance making the binary a fully detached system.

The GL268 system has been observed using the ELODIE spectroscope by the Geneva Observatory (D. Segransan, private communication) and found to have narrow emission lines indicating that each of the elements of the binary are slowly rotating. Observations of late-type, short period, dwarf binary stars (Andersen 1991) indicate that most will become tidally locked. We infer from this that the average $V\sin(i)$ where $< 5\text{kms}^{-1}$ is an upper limit to the rotationally broadened line widths measured. From this, we further infer that because of the low rotational velocity of

the individual components of GL268 they are unlikely to be heavily maculated. As a result, this is unlikely to have a strong effect on final, derived results. The relative narrowness of emission lines in the spectrum of GL268 also has the effect of strongly reducing errors in the determination of velocity orbital components. These issues are further discussed in Section 6.7.

A high orbital inclination angle, that is, one that is nearly edge-on, is a desirable feature for a test system in that it makes the mass estimates less sensitive to errors in inclination angle. This is readily apparent by examination of Eqn. 6.15 in which the mass is proportional to $\sin^3(i)$. While we cannot know the orbital inclination angle a priori - without a fully solved physical orbit - we can make an estimate. We may do this through comparison of an approximate mass found by application of an empirical relation and a range of masses determined through radial velocity measurements alone. First, we interpolation along a roughly linear empirical function between mass and luminosity derived from evaluation of masses of binary stars from a very broad range of temperatures (Popper 1980). From this, we obtain a value of mass of approximately $0.2M_{\odot}$ for each component. Subsequently, we analyze extant radial velocity data found in Tomkin and Pettersen (1986). Applying Eqn. 6.15, we estimate a range of masses, $m_{1,2}\sin^3(i) = 0.18$. This suggests that the orbital inclination must be close to 90° - nearly edge-on - making GL268 ideal in this respect.

Radial Velocity measurements

We conducted extensive observations of the object at the Observatoire de Haute Provence, Saint Michel l'Observatoire, France using the ELODIE instrument. This fiber-fed echelle spectrograph, described by Baranne et al. (1996), can record, in a single exposure, a spectrum at a resolution of $R = 42,000$ ranging from $3906\mathring{A}$ to $6811\mathring{A}$ to a 1024×1024 CCD. The accuracy and efficiency of the instrument together with its long-term stability provides radial velocities with precision of ≤ 15 m s^{-1} for stars up to 9^{th} magnitude in V while it is also capable of measuring velocities to about 1 km s^{-1} for stars up to 16^{th} magnitude. Data we obtained using this facility are immediately post-processed with a system integrated with the spectrograph control software which produces optimally extracted and wavelength calibrated spectra.

We obtained spectral data for the object, using appropriate calibrator stars to remove telluric features, on 55 nights between 2000 April and 2004 June. We cross-correlated the spectra against a template derived by Delfosse et al. (1999) from a high S/N spectrum of GL699 (Barnard's star, M4.0 V). This processing is standard procedure for operations with the spectrograph ELODIE and are thoroughly reviewed by Queloz (1995). Subsequently, we fit a double Gaussian to the twin-peaked cross-correlation function and obtained the centroid of each feature to determine the orbit velocity of the component stars for the particular observation. Here we noted that the cross-correlation functions so obtained did not appear distorted and were well described by Gaussians indicating that the stars themselves are unlikely to be highly

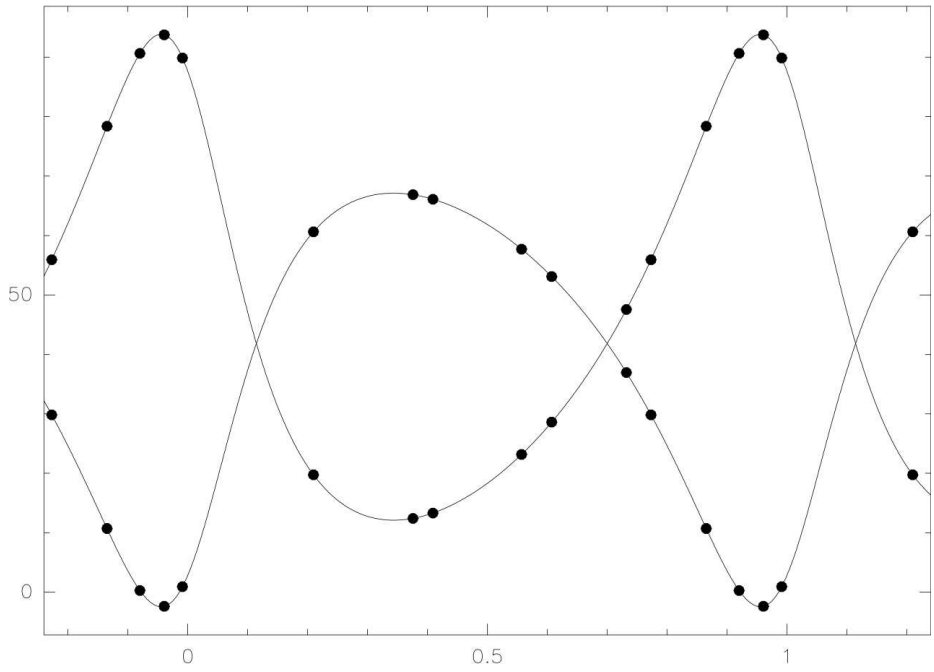

Figure 6.2 Depiction of the orbit of the M-dwarf binary GL268 as fitted to individual velocity data points measured at Observatoire de Haute Provence, Saint Michel l'Observatoire, France using the ELODIE instrument. Error bars are 0.5% and are buried in the data points themselves. The abscissa is orbital phase and the ordinate axis is velocity in km s^{-1}

spotted. We explore this issue further in Section 6.7. The velocity data for all measurements are plotted on a phase-wrapped velocity curve given in Figure 6.2.

From this figure we can ascertain some features of the binary immediately. The departure, in the main, of the shape of the curves from a rectified sinusoid — the curve of one component having a square-shouldered appearance — suggests that the orbit is not circular. The evident skewness of both of the curves connotes a departure of the argument of periapsis (ω) from the origin of longitude. We can also immediately see that the absolute velocity calibration of this data set is non-zero although this immaterial for these calculations.

Interferometric Measurements at IOTA

When the orbits are not perfectly edge-on, the absolute masses of the component stars may be calculated only by making a determination of the unknown projection factor, the inclination angle, i, in some way. Adaptive optics (AO), speckle interferometry, or secondary masking interferometry on a large, filled-aperture telescope, or long-baseline, sparse-aperture interferometry are observational technologies that could be exploited to enable such observations. Recent advances in stellar long-baseline interferometry allow the possibility of making extremely precise astrometric measurements of the motion of binaries in the tangent plane of the sky. We conducted such measurements using the Infrared and Optical Telescope Array (IOTA) at the F. L. Whipple Observatory (Arizona) over a period of six months from 2005 October to 2006 April. IOTA has baselines between 5 - 38 m and fiber-fed IONIC3 combiner optics (Berger et al. 2003) which we used to measure 3 visibilities (V^2) and 1 closure phase (CP) simultaneously in the broadband H band filter ($\lambda = 1.65\ \mu\mathrm{m}, \Delta\lambda = 0.3\ \mu\mathrm{m}$). Data analysis procedures have been documented in recent papers (Monnier et al. 2004).

For the astrometric data, each measurement consists of 200 discrete samples or scans. For the data here, we have adopted a calibration error of 3%.

While we observed GL268 during 11 epochs four of them were dropped because the SNR and piston were too bad. Out of the 7 remaining epochs, we dropped 2 additional nights because for one night a calibrator (GL251) is a suspected binary and for the second night the calibrator was measured 3 hours before the science

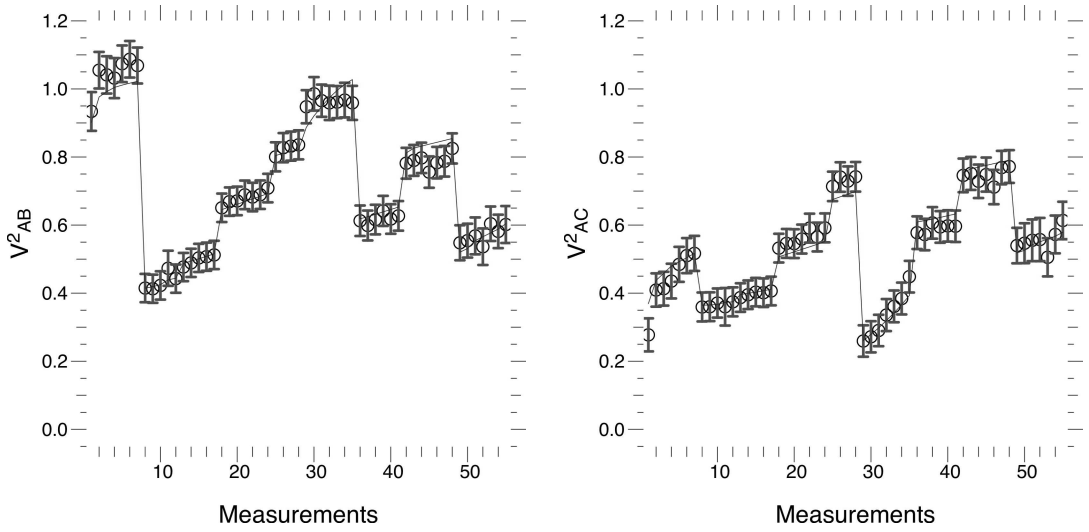

Figure 6.3 Depiction of the interferometric observations of the M-dwarf binary GL268 with IOTA for the two baselines we used; AB and AC. We used only the two longest baselines as the GL268 system has a small angular separation and the smallest baseline, BC, was very noisy.

target making the calibration unreliable. We conducted final orbit fitting with 5 epochs that are correctly phased. As indicated above, we did not use data from the shortest baseline because the instrumental transfer function is poor (too low with too much fluctuation). We kept data accumulated on the two longest baseline and constructed an orbit through simultaneous fitting of the radial velocities and the V^2. All parameters are fitted with at total of 88 V^2 measurements. The V^2 values of the AB and AC baselines of IOTA are depicted in Figure 6.3.

We note here that we used a very large number of discrete measurements of both interferometric and astrometric data and neither the interferometric nor the velocity data we used are available in a sensible form for compact publication that would add appreciably to the discussion. Consequently, we exclude explicit tables of them.

Measurement Errors

We do not anticipate that line blending will be a significant error term due to the very broad spectroscopic window granted us, by design, with the ELODIE instrument (Latham et al. 1996; Baranne et al. 1996). As noted in Section 6.4, the effect on the error term averages out as $1/N^{1/2}$, with N the number of lines used in the correlation analysis. However, we do directly address this using a profile correction process outlined by Forveille et al. (1999) in which systematic errors in the variation of the velocity curves due to line blending is reduced by a factor of approximately five.

As described by Delfosse et al. (1999) we analyzed the ELODIE echelle spectra by numerical cross correlation with an M4 V one-bit mask (Barnard's star). Simply determining the radial velocities by adjusting fitted double-Gaussians to the correlation profiles would have resulted in large systematic phase-dependent residuals. This is due to the fact that while the core of the correlation profiles are well-described by a Gaussian distribution, their baselines to not drop to zero as a Gaussian function would. The measured baselines instead drop to about one tenth of the depth of the secondary (fainter) star's correlation function dip. However, because of the good stability of the ELODIE spectrograph, the shape of the correlation profile for a given star is quite stable over time. This allows an estimate of the wings of the intrinsic correlation profile for each star by averaging all profiles obtained after aligning them at the measured velocity of the star. All pixels within two profile widths of the velocity of the companion star are subsequently blocked out and the residuals of the

Gaussian adjustment to the average profiles are then subtracted from all correlation profiles at the velocity of each star. Forveille et al. (1999) evolved this procedure, which we applied to our data to successfully reduce the fluctuation level of the profile baseline to a level of approximately $\pm 0.05\%$. The radial velocities measured by double-Gaussian fitting and the application of this procedure are, on average, ~ 18 ms^{-1} for the primary (brighter) and ~ 25 ms^{-1} for the secondary (fainter) component as reported below.

We account for measurement errors in our astrometric observations at IOTA as follows. Each measurement of the visibility we conducted is, in actuality, 100-200 individual measurements or scans. For statistical errors we report the RMS of these scans that quantifies the amount of scatter. To this, we add a conservative estimate of the systematic error obtained from previous observations. For IOTA, previous observations of the very bright target, Vega, were determined to have a systematic error of $\sim 1\%$ (E. DiFolco, private correspondence). For the particular case of GL268 a comparatively faint target, we conservatively estimate a systematic error of 3% then recheck our final results against the Baraffe models and the trigonometric parallax found by Hipparcos.

Unlike Torres and Ribas we do not have direct LC measurements of the GL268 with which we can definitively rule out maculation or to model them if detected but we do not anticipate that starspots, if they do exist on the components of GL268, will strongly effect our results for the following reasons.

The strength of dynamo processes in the outer envelopes of stars is strongly correlated with their rotational velocity. Line widths of the individual components of GL268 suggest that they are rotating at less than 5 km s^{-1}. Other evidence that suggests this slow rotational velocity is that the orbital period of GL268 is very long ($\sim$10.4 days) with an orbital separation of greater than 7 $R_{\odot}$. Calculations by Claret and Cunha (1997) show that tidal synchronization time varies directly with the major axis length to the sixth power. Claret and Cunha also argues that the time for co-alignment of the rotational axes of the component stars in a binary pair with the orbital axis is likewise very strong. This suggests that the components of GL268 are likely to be at least partially tidally locked and we may then infer a rotational rate of a little more than 10 days and component inclination equal to orbital inclination. From the relation

$$V_{Eq}\sin(i) = \frac{2\pi}{P}R\sin(i) \tag{6.16}$$

in which i is the rotational inclination of the component star, P is the rotational period, R is the radius of the component star, and V_{Eq} is the equatorial velocity, taken together with the well-known relation between mass and size of M-dwarf stars indicating that their radius is approximately numerically equal to their mass, we can calculate a rotational velocity, $V_{Eq}\sin(i) \simeq 0.95$ km s^{-1}. Because of this slow rotation rate, rotational sheer, and consequently, magneto-hydrodynamical generation of maculation, is expected to be negligible. Postulating a conservative upper limit of

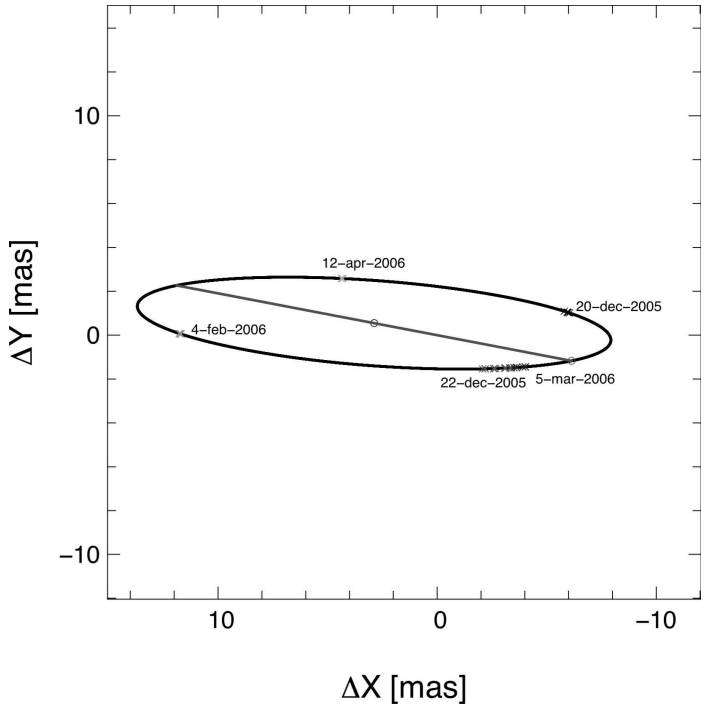

Figure 6.4 Depiction of the derived physical orbit of the M-dwarf binary GL268 in the binary's center-of-mass frame of reference. Superimposed on the orbit are the interferometric measurements conducted at IOTA. Error bars on the interferometric data are suppressed for clarity.

$V_{Eq}\sin(i) = 2$ km s^{-1} we calculate that we would require starspots covering 1% of the surface of each of the component stars of GL268 to induce shifts in the component velocity semi-amplitudes of 20 ms^{-1} and fully 5% coverage, assuming a worst-case spot configuration, to induce shifts that reach the level of current mass errors. These calculations suggest that significant stellar maculation is not at issue for GL268.

6.7.1 Orbital solution

Since the GL 268 system was not resolved on the smallest (BC) baseline, we decided at first to include only longest baseline (AB) V^2 measurements in the fit

for which the configuration remains the same over the run, this one including most of the information due to its higher spatial resolution. Unfortunately, the lack of spatial frequency coverage did not yield one solution in the parameter space. A χ^2 map revealed several minima with equivalent probabilities and fit results clearly showed a strong degeneracy between Ω and inclination. Although baseline BC V^2 measurements were useless in our case, AC baseline data inclusion allowed us to remove all but one orbital solution without changing the reduced χ^2. The resulting increased sampling of the (u, v) plane tightened orbital parameter precision.

We constructed the combined fit using a Levenberg-Marquardt (Press, 1992) procedure in which we parameterized a 2-body Keplerian orbit solution. Then, from it, we determined the coordinates of both stars in the orbital plane relative to the barycenter of the system. From the velocity vectors, as described previously, we obtained RV values which we then compared to our data. For the astrometry, from the parametric equation of an ellipse, we obtained the distance between the two components and the true anomaly. After having calculated the eccentric anomaly, we obtained coordinates on the sky - both separation and position angle. From V^2 data, we calculate position angle and use that to correct the model. Finally, we combine both data sources to our model by minimizing each χ^2 solution (RV reduced $\chi^2 = 1.39$, Astrometric reduced $\chi^2 = 0.83$). Subsequently, we exhibit the solution with fitted parameters. The final physical orbit of the binary pair is given in Figure 6.4. The corresponding reduced χ^2 for the fit is 1.18. We report the orbital elements

Table 6.2. Orbital and binary elements of GL268

Parameter	Unit	Value	Conf. Interval -	Conf. Interval +
V0	(km s^{-1})	41.831986	41.820132	41.842239
Epoch	(JD)[a]	51544.500000	51544.500000	51544.500000
P	(days)	10.426713	10.426710	10.426740
T0	(JD)	49993.494572	49993.491594	49993.496103
e		0.321515	0.321173	0.322076
a	(arcsec)	0.011132	0.010897	0.011365
Ω	(deg)	89.977400	89.673321	90.538451
ω	(deg)	211.971839	211.885353	212.054265
i	(deg)	100.574936	100.362933	100.594644
K1	(km s^{-1})[b]	34.792386	34.774201	34.807518
K2	(km s^{-1})	40.870589	40.844963	40.892787
W1[c]	(km s^{-1})	5.889880	5.658130	5.905093
W2	(km s^{-1})	5.864757	5.532533	5.889643
EW1	(km s^{-1})	0.431754	0.407069	0.433255
EW2	(km s^{-1})	0.295106	0.270494	0.296672
Flux frac (H) [d]		0.345921	0.347178	0.379495

Note. — A listing of the derived orbital and binary parameters of GL268. We give the corresponding confidence intervals for 0.684 confidence level.

[a]The Epoch is fixed. All other parameters are adjustable.

[b]The typical accuracy of ELODIE for SB1 G dwarfs is 6-10m/s and for SB2 M-dwarfs, the accuracy is of the order of 20-30m/s. The confidence interval noted is from Monte-Carlo analysis as noted in the text.

[c]$W_{1,2}$ and $EW_{1,2}$ are the width and equivalent width of the average Gaussian cross correlation profile.

[d]H-band flux fraction given as $\frac{flux\ 1}{flux\ 1\ +\ flux\ 2}$ derived from IOTA data.

and derived physical parameters in Tables 6.2 and 6.3, respectively.

We computed errors for the parameters derived by our process using the *full* covariance matrix of the linearized least-square adjustment rather than merely from the diagonal terms of that matrix which are the standard errors of the orbital elements. Additionally, we estimate confidence intervals for both derived parameters and orbital elements through Monte-Carlo analysis. These intervals, also reported in Tables 6.2 and 6.3, are consistent with analytic standard errors and Gaussian statistics thus providing a check against analytic gradients. The Monte-Carlo analysis is an

Table 6.3. Physical parameters of the GL268 system and individual components

Physical Parameter	Value	Unit
a1 $\sin i$	6.79	$R_\odot$
f1(M)	$0.386E-01$	$M_\odot$
a2 $\sin i$	7.97	$R_\odot$
f2(M)	$0.626E-01$	$M_\odot$
M1 $\sin^3 i$	0.2146 ± 0.0003	$M_\odot$
M2 $\sin^3 i$	0.1827 ± 0.0002	$M_\odot$
Total Mass	0.4182 ± 0.0020	$M_\odot$
Mass A	0.2259 ± 0.0011	$M_\odot$
Mass B	0.1923 ± 0.0009	$M_\odot$
Parallax[a]	159.4 ± 3.9	mas
M_H A	7.65 ± 0.08	mag
M_H B	8.19 ± 0.08	mag

Note. — Parameters of the system derived through χ^2 fitting of 55 cross-correlated velocity measurements and 88 individual single-baseline interferometric measurements.

[a]Hipparcos parallax: 157.2 ± 3.3 mas.

essential feature of Tables 6.2 and 6.3 because the GL 268 system is faint in H-band, consequently, our interferometric measurements are somewhat noisy. As a result, the vicinity of the minimum of the χ^2 surface departs somewhat from the quadratic ideal. This may cause the error statistics for the parameters to be asymmetric. Here we note, however, that the contributions to the overall χ^2 solution by the two different data types we included were approximately commensurate with their respective number of measurements. This shows that there are no large, unaccounted systematic errors in either type of data and that the adopted standard errors are approximately correct.

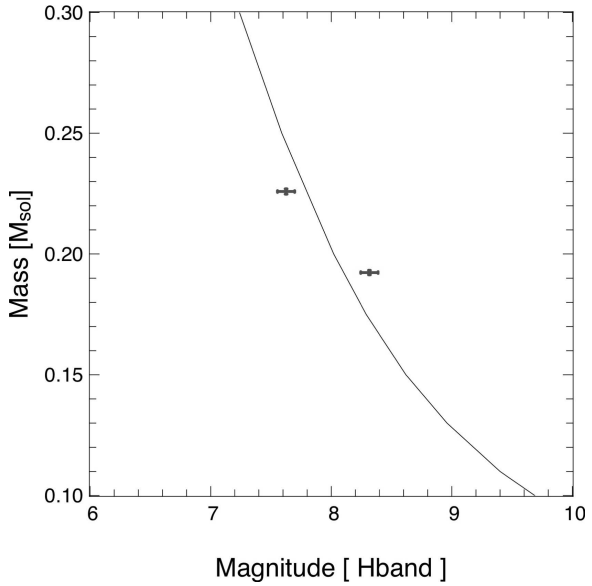

Figure 6.5 Depiction of the derived masses of the two components of the M-dwarf binary GL268 compared to the prediction (Baraffe et al. 1998) of a mid-M 10 Gy dwarf of solar metallically.

6.7.2 Model Testing

We tested these physical parameters against the predictions of models by Baraffe et al. (1998) who combined the stellar evolution models of Chabrier and Baraffe (1997) with the high fidelity, non-grey atmospheric models of Hauschildt et al. (1999) previously discussed in Chapter 5. Note that dust may become an issue for very low mass stars (Allard et al. 1998) but is not included in the model we exercised. The temperature of the component stars of GL 268 in combined light may be approximated by the color differential $I - J = 1.67$ which indicates a temperature of 2800 - 3000 K (Leggett 1992). The nucleation temperature of dust is $\sim$ 2000K (Carrez et al. 2002; Dwek 2005; Nuth and Hecht 1990). Thus, we do not anticipate that dust will have a strong effect on our result.

Stellar luminosities depend on chemical composition and mass as well as age. For the particular case of the age and mass range for GL 268 the age of the stellar components is not critical. Quantitative metallicity determination for low-mass stars is quite difficult (Viti et al. 1997) and so we rely on photometric metallicity estimators. Photometric measurements of combined light from the GL268 system have been made by a number of authors over a broad range of colors. We adopt the colors as compiled by Leggett (1992), which are: U = 14.38,V = 11.49, B = 13.29, R = 9.77, I = 8.44, J = 6.77, K = 5.87, and L = 5.5. Indeterminacy on the IJHK values of 3%, for UB, 5%, and for LM, 10%. Leggett indicates that these colors are consistent with those of stars with solar metallicity so we adopt this for first order model testing.

Note that the absolute magnitude, presented in Table 6.3, excludes the effects of interstellar reddening. Because of the proximity of the GL268 system (∼6.38 pc) this effect is expected to be negligible (i.e., within the 2MASS color error bars).

We present the modeled results in Figure 6.5 in which the locus of points flowing diagonally across the figure is a model isochrone - a line of constant time for varying mass and luminosity - for a 10 Gy M-dwarf star of solar metallicity. In this figure we directly compare the mass and absolute magnitude of each component against that predicted by the model. The level of agreement evident in this figure is immediately comforting but the discrepancies shown may point towards a low-level departure from fidelity in the model. We intend to conduct a more thorough investigation of this in the near future (Barry et al. 2008).

We note that the availability of an Hipparcos parallax (ESA 1997) represents an opportunity to independently verify the derived orbital parallax and, therefore, to globally check the orbital solution for systematic errors. Our derived orbital parallax, 159.4 ± 3.9 mas, is in agreement to within one—σ of that reported by Hipparcos (157.2 ± 3.3 mas). However, note that the value determined by Hipparcos has large error bars because the unaccounted orbital motion of the target couples into the parallax solution over the limited temporal baseline of the Hipparcos measurement. We intend to reanalyze the Hipparcos intermediate transit data and account for the orbital motion of GL 268 to reduce these error bars and back-check our orbital parallax with greater accuracy. We will report these findings in Barry et al. (2008).

6.7.3 Conclusion

As last comprehensively reviewed (Andersen 1997, 1998) the fundamental determination of stellar masses from binary orbits is a classical discipline of astrophysics. Accurate stellar masses in binary systems define and calibrate a mass-luminosity relation used throughout astronomy to convert observed stellar light to mass. They also provide what is the most demanding of tests of stellar evolution theory. Stellar masses, which are directly measured through processes as outlined in this research, are a fundamental input to such theoretical models, and these models must, in turn, reproduce the effective luminosities and temperatures of the component stars. All stellar parameters are strongly dependent on mass. This fundamental discriminator,

however, only shows its power as a diagnostic for masses with relative errors below $\sim$ 1-2% (Andersen 1991).

We have now provided a new measurement of two stellar masses and absolute magnitudes for the components of the GL268 system with which to calibrate these theoretical models. We here report interferometric and radial velocity observations of the system leading to masses of the constituent stars with uncertainties of 0.5%. The total mass of the GL268 system is $0.4182 \pm 0.0020 M_{\odot}$ (0.5%). The masses of the constituent stellar components are $0.2259 \pm 0.0011 M_{\odot}$ for component A and $0.1923 \pm 0.0009 M_{\odot}$ for component B. The system parallax is determined by these observations to be $0.1594 \pm .0039$ arcsec (2.4%) in agreement with Hipparcos (within $1 - \sigma$). The absolute H-band magnitude of the component stars are 7.65 ± 0.08 and 8.19 ± 0.08 for GL268A and B, respectively. These results are among the most precise masses ever measured for visual binaries of any luminosity class or spectral type.

How vast those Orbs must be, and how inconsiderable this Earth, the Theater upon which all of our mighty Designs, all of our Navigations, all of our Wars are transacted, when compared to them. A very fit consideration and matter for Reflection, for those Kings and Princes who sacrifice the lives of so many people, only to flatter their Ambition in being Masters of some pitiful corner of this small Spot.

— Christiaan Huygens, *New Conjectures Concerning the Planetary Worlds, Their Inhabitants and Productions*, c. 1690

Bibliography

Adams, W. S. and A. H. Joy (1933, December). Coronal Lines in the Spectrum of RS Ophiuchi. *PASP 45*, 301–+.

Allard, F., D. R. Alexander, and P. H. Hauschildt (1998). Model Atmospheres of Very Low Mass Stars and Brown Dwarfs. In R. A. Donahue and J. A. Bookbinder (Eds.), *Cool Stars, Stellar Systems, and the Sun*, Volume 154 of *Astronomical Society of the Pacific Conference Series*, pp. 63–+.

Allard, F., P. H. Hauschildt, I. Baraffe, and G. Chabrier (1996). Synthetic Spectra and Mass Determination of the Brown Dwarf GI 229B. *ApJ 465*, L123+.

Andersen, J. (1991). Accurate masses and radii of normal stars. *A&A Rev. 3*, 91–126.

Andersen, J. (1997). Precise stellar mass and mass-luminosity data. In T. R. Bedding, A. J. Booth, and J. Davis (Eds.), *IAU Symposium*, Volume 189 of *IAU Symposium*, pp. 99–108.

Andersen, J. (1998). Precise stellar mass and mass-luminosity data. In T. R. Bedding, A. J. Booth, and J. Davis (Eds.), *Fundamental Stellar Properties*, Volume 189 of *IAU Symposium*, pp. 99–+.

Anupama, G. C. (2008). Near infrared observations of the nova RS Oph. In A. Evans, M. F. Bode, and T. J. O'Brien (Eds.), *RS Ophiuchi (2006) and the recurrent nova phenomenon*.

Anupama, G. C. and N. G. Kantharia (2006, March). RS Ophiuchi. *IAU Circ. 8687*, 2.

Arp, H. C. (1956, February). Novae in the Andromeda nebula. *AJ 61*, 15–34.

Assendorp, R., T. R. Bontekoe, A. R. W. de Jonge, D. J. M. Kester, P. R. Roelfsema, and P. R. Wesselius (1995, April). The Groningen IRAS imaging software (IST). *A&AS 110*, 395–+.

Baraffe, I. (2005, January). Structure and Evolution of Giant Planets. *Space Science Reviews 116*, 67–76.

Baraffe, I., G. Chabrier, F. Allard, and P. H. Hauschildt (1998, September). Evolutionary models for solar metallicity low-mass stars: mass-magnitude relationships and color-magnitude diagrams. *A&A 337*, 403–412.

Baranne, A., D. Queloz, M. Mayor, G. Adrianzyk, G. Knispel, D. Kohler, D. Lacroix, J.-P. Meunier, G. Rimbaud, and A. Vin (1996, October). ELODIE: A spectrograph for accurate radial velocity measurements. *A&AS 119*, 373–390.

Barbon, R., A. Mammano, and L. Rosino (1969, January). Spectroscopic observations of the recurrent nova RS Ophiuchi from 1959 to 1968. *Commmunications of the Konkoly Observatory Hungary 65*, 257–260.

Baring, M. G. (2004, November). Diffusive Shock Acceleration of High Energy Cosmic Rays. *Nuclear Physics B Proceedings Supplements 136*, 198–207.

Barry, R. K., W. C. Danchi, J. L. Sokoloski, C. Koresko, J. P. Wisniewski, E. Serabyn, W. A. Traub, M. J. Kuchner, and M. A. Greenhouse (2008). High Spatial Resolution N-band Observations of the Nova RS Ophiuchi with the Keck Interferometer Nuller. Manuscript submitted.

Barry, R. K. and W. D. Danchi (2008). High-resolution interferometric observations of the nova RS Ophiuchi and a proposed unification model for persistent dust creation in repeater novae. In A. Evans, M. F. Bode, and T. J. O'Brien (Eds.), *RS Ophiuchi (2006) and the recurrent nova phenomenon*, Utrecht, Netherlands. VNU Science Press.

Barry, R. K., B. Demory, D. Segransan, T. Forveille, W. C. Danchi, E. Di Folco, D. Queloz, G. Torres, W. Traub, X. Delfosse, M. Mayor, C. Perrier, and S. Udry (2008). A Physical Orbit for the M Dwarf Binary Gliese 268. Manuscript in preparation.

Barry, R. K., K. Mukai, J. L. Sokoloski, W. C. Danchi, I. Hachisu, A. Evans, R. D. Gehrz, and M. Mikołajewski (2008). On the distance to the recurrent nova RS Ophiuchi. In A. Evans, M. F. Bode, and T. J. O'Brien (Eds.), *RS Ophiuchi (2006) and the recurrent nova phenomenon*, Utrecht, Netherlands. VNU Science Press.

Barry, R. K., A. Skopal, and W. C. Danchi (2008a). Calibration of the wavelength dependency of stellar leakage for the Keck Interferometer Nuller. Manuscript in preparation.

Barry, R. K., A. Skopal, and W. C. Danchi (2008b). Continuum Evidence for Non-spherical Expansion of Ejecta in the 2006 Outburst of RS Ophiuchi. Manuscript in preparation.

Berger, J.-P., P. Haguenauer, P. Y. Kern, K. Rousselet-Perraut, F. Malbet, S. Gluck, L. Lagny, I. Schanen-Duport, E. Laurent, A. Delboulbe, E. Tatulli, W. A. Traub, N. Carleton, R. Millan-Gabet, J. D. Monnier, E. Pedretti, and S. Ragland (2003, February). An integrated-optics 3-way beam combiner for IOTA. In W. A. Traub (Ed.), *Interferometry for Optical Astronomy II. Edited by Wesley A. Traub . Proceedings of the SPIE, Volume 4838, pp. 1099-1106 (2003).*, Volume 4838 of *Presented at the Society of Photo-Optical Instrumentation Engineers (SPIE) Conference*, pp. 1099–1106.

Bevington, P. R. and D. K. Robinson (2003). *Data reduction and error analysis for the physical sciences*. Data reduction and error analysis for the physical sciences, 3rd ed., by Philip R. Bevington, and Keith D. Robinson. Boston, MA: McGraw-Hill, ISBN 0-07-247227-8, 2003.

Blair, W. P., W. A. Feibelman, A. G. Michalitsianos, and R. E. Stencel (1983, November). Spectrophotometric observations of symbiotic stars and related objects. *ApJS 53*, 573–590.

Blondel, P. F. C. and H. R. E. T. A. Djie (2006, September). Modeling of PMS Ae/Fe stars using UV spectra. *A&A 456*, 1045–1068.

Bode, M. F., D. J. Harman, T. J. O'Brien, H. E. Bond, S. Starrfield, M. J. Darnley, A. Evans, and S. P. S. Eyres (2007). Hubble Space Telescope Imaging of the Expanding Nebular Remnant of the 2006 Outburst of the Recurrent Nova RS Ophiuchi. *ApJ 665*, L63–L66.

Bode, M. F. and F. D. Kahn (1985, November). A model for the outburst of nova RS Ophiuchi in 1985. *MNRAS 217*, 205–215.

Bode, M. F., T. J. O'Brien, J. P. Osborne, K. L. Page, F. Senziani, G. K. Skinner, S. Starrfield, J.-U. Ness, J. J. Drake, G. Schwarz, A. P. Beardmore, M. J. Darnley, S. P. S. Eyres, A. Evans, N. Gehrels, M. R. Goad, P. Jean, J. Krautter, and G. Novara (2006, November). Swift Observations of the 2006 Outburst of the Recurrent Nova RS Ophiuchi. I. Early X-Ray Emission from the Shocked Ejecta and Red Giant Wind. *ApJ 652*, 629–635.

Bohigas, J., J. Echevarria, F. Diego, and J. A. Sarmiento (1989, June). Spectrophotometry of RS OPH during the nebular phase. *MNRAS 238*, 1395–1405.

Bondi, H. and F. Hoyle (1944). On the mechanism of accretion by stars. *MNRAS 104*, 273–+.

Bordé, P., V. Coudé du Foresto, G. Chagnon, and G. Perrin (2002, October). A catalogue of calibrator stars for long baseline stellar interferometry. *A&A 393*, 183–193.

Born, M. and E. Wolf (Eds.) (1999). *Principles of optics : electromagnetic theory of propagation, interference and diffraction of light*.

Brandi, E. (2008). A Radial Velocity Orbit for RS Ophiuchi. In A. Evans, M. F. Bode, and T. J. O'Brien (Eds.), *RS Ophiuchi (2006) and the recurrent nova phenomenon*.

Cardelli, J. A., G. C. Clayton, and J. S. Mathis (1989, October). The relationship between infrared, optical, and ultraviolet extinction. *ApJ 345*, 245–256.

Carrez, P., K. Demyk, H. Leroux, P. Cordier, A. P. Jones, and L. D'Hendecourt (2002, November). Low-temperature crystallisation of MgSiO3 glasses under electron irradiation: Possible implications for silicate dust evolution in circumstellar environments. *Meteoritics and Planetary Science 37*, 1615–1622.

Cassatella, A., B. J. M. Hassall, A. Harris, and M. A. J. Snijders (1985). Ultraviolet Observations of the Recurrent Nova Rs-Ophiuchi in Outburst. In W. R. Burke (Ed.), *Recent Results on Cataclysmic Variables. The Importance of IUE and Exosat Results on Cataclysmic Variables and Low-Mass X-Ray Binaries*, Volume 236 of *ESA Special Publication*, pp. 281–+.

Chabrier, G. and I. Baraffe (1997, November). Structure and evolution of low-mass stars. *A&A 327*, 1039–1053.

Chesneau, O., N. Nardetto, F. Millour, C. Hummel, A. Domiciano de Souza, D. Bonneau, M. Vannier, F. Rantakyrö, A. Spang, F. Malbet, D. Mourard, M. F. Bode, T. J. O'Brien, G. Skinner, R. G. Petrov, P. Stee, E. Tatulli, and F. Vakili (2007a, March). AMBER/VLTI interferometric observations of the recurrent Nova RS Ophiuchii 5.5 days after outburst. *A&A 464*, 119–126.

Chesneau, O., N. Nardetto, F. Millour, C. Hummel, A. Domiciano de Souza, D. Bonneau, M. Vannier, F. Rantakyrö, A. Spang, F. Malbet, D. Mourard, M. F. Bode, T. J. O'Brien, G. Skinner, R. G. Petrov, P. Stee, E. Tatulli, and F. Vakili (2007b). AMBER/VLTI interferometric observations of the recurrent Nova RS Ophiuchii 5.5 days after outburst. *A&A 464*, 119–126.

Claret, A. and N. C. S. Cunha (1997, February). Circularization and synchronization times in Main-Sequence of detached eclipsing binaries II. Using the formalisms by Zahn. *A&A 318*, 187–197.

Cohen, J. G. (1985, May). Nova shells. II - Calibration of the distance scale using novae. *ApJ 292*, 90–103.

Colavita, M. M. (1999, January). Fringe Visibility Estimators for the Palomar Testbed Interferometer. *PASP 111*, 111–117.

Colavita, M. M., A. F. Boden, S. L. Crawford, A. B. Meinel, M. Shao, P. N. Swanson, G. T. van Belle, G. Vasisht, J. M. Walker, J. K. Wallace, and P. L. Wizinowich (1998, July). Keck Interferometer. In R. D. Reasenberg (Ed.), *Proc. SPIE Vol. 3350, p. 776-784, Astronomical Interferometry, Robert D. Reasenberg; Ed.*, Volume 3350 of *Presented at the Society of Photo-Optical Instrumentation Engineers (SPIE) Conference*, pp. 776–784.

Colavita, M. M., G. Serabyn, P. L. Wizinowich, and R. L. Akeson (2006, July). Nulling at the Keck interferometer. In *Advances in Stellar Interferometry. Edited by Monnier, John D.; Schöller, Markus; Danchi, William C.. Proceedings of the SPIE, Volume 6268, pp. 626803 (2006).*, Volume 6268 of *Presented at the Society of Photo-Optical Instrumentation Engineers (SPIE) Conference*.

Colavita, M. M., J. K. Wallace, B. E. Hines, Y. Gursel, F. Malbet, D. L. Palmer, X. P. Pan, M. Shao, J. W. Yu, A. F. Boden, P. J. Dumont, J. Gubler, C. D. Koresko, S. R. Kulkarni, B. F. Lane, D. W. Mobley, and G. T. van Belle (1999, January). The Palomar Testbed Interferometer. *ApJ 510*, 505–521.

Colavita, M. M. and P. L. Wizinowich (2000, July). Keck Interferometer: progress report. In P. J. Lena and A. Quirrenbach (Eds.), *Proc. SPIE Vol. 4006, p. 310-320, Interferometry in Optical Astronomy, Pierre J. Lena; Andreas Quirrenbach; Eds.*, Volume 4006 of *Presented at the Society of Photo-Optical Instrumentation Engineers (SPIE) Conference*, pp. 310–320.

Colavita, M. M. and P. L. Wizinowich (2003, February). Keck Interferometer update. In W. A. Traub (Ed.), *Interferometry for Optical Astronomy II. Edited by Wesley A. Traub. Proceedings of the SPIE, Volume 4838, pp. 79-88 (2003).*, Volume 4838 of *Presented at the Society of Photo-Optical Instrumentation Engineers (SPIE) Conference*, pp. 79–88.

Connelley, M. and A. Sandage (1958, December). Photoelectric Observations of RS Ophiuchi. *PASP 70*, 600–+.

Coude Du Foresto, V. (1998). Optical Fibers in Astronomical Interferometry. In S. Arribas, E. Mediavilla, and F. Watson (Eds.), *Fiber Optics in Astronomy III*, Volume 152 of *Astronomical Society of the Pacific Conference Series*, pp. 309–+.

Cowie, L. L. and A. Songaila (1986). High-resolution optical and ultraviolet absorption-line studies of interstellar gas. *ARA&A 24*, 499–535.

Das, R., D. P. K. Banerjee, and N. M. Ashok (2006, December). A Near-Infrared Shock Wave in the 2006 Outburst of Recurrent Nova RS Ophiuchi. *ApJ 653*, L141–L144.

Dawson, P. C. and M. M. De Robertis (2004, May). Barnard's Star and the M Dwarf Temperature Scale. *AJ 127*, 2909–2914.

Decourchelle, A., D. C. Ellison, and J. Ballet (2000, November). Thermal X-Ray Emission and Cosmic-Ray Production in Young Supernova Remnants. *ApJ 543*, L57–L60.

Delfosse, X., T. Forveille, J.-L. Beuzit, S. Udry, M. Mayor, and C. Perrier (1999, April). New neighbours. I. 13 new companions to nearby M dwarfs. *A&A 344*, 897–910.

Dickey, J. M., S. R. Kulkarni, C. E. Heiles, and J. H. van Gorkom (1983, November). A survey of H I absorption at low latitudes. *ApJS 53*, 591–621.

Dobrzycka, D. and S. J. Kenyon (1994, December). A new spectroscopic orbit for RS Ophiuchi. *AJ 108*, 2259–2266.

Downes, R. A. and H. W. Duerbeck (2000, October). Optical Imaging of Nova Shells and the Maximum Magnitude-Rate of Decline Relationship. *AJ 120*, 2007–2037.

Dumm, T., W. Schmutz, H. Schild, and H. Nussbaumer (1999). Circumstellar matter around M-giants in symbiotic binaries: SY MUSCAE and RW Hydrae. *A&A 349*, 169–176.

Duquennoy, A. and M. Mayor (1991, August). Multiplicity among solar-type stars in the solar neighbourhood. II - Distribution of the orbital elements in an unbiased sample. *A&A 248*, 485–524.

Dwek, E. (2005, November). Dust notes. Unpublished notes.

Eisner, J. A., B. F. Lane, R. L. Akeson, L. A. Hillenbrand, and A. I. Sargent (2003, May). Near-Infrared Interferometric Measurements of Herbig Ae/Be Stars. *ApJ 588*, 360–372.

Eskioglŭ, A. N. (1963, February). Courbes de lumière de RS Ophiuchi (1958) et de Wz Sagittae (1946). *Annales d'Astrophysique 26*, 331–+.

Evans, A. (1987). Infrared Observations of RS Ophiuchi. In M. F. Bode (Ed.), *RS Ophiuchi (1985) and the Recurrent Nova Phenomenon*, pp. 117–+.

Evans, A., C. M. Callus, J. S. Albinson, P. A. Whitelock, I. S. Glass, B. Carter, and G. Roberts (1988). Infrared observations of the 1985 outburst of RS Ophiuchi. *MNRAS 234*, 755–771.

Evans, A., T. Kerr, Y. Matsuoka, Y. Tsuzuki, T. R. Geballe, R. D. Gehrz, C. E. Woodward, M. F. Bode, T. J. O'Brien, R. J. Davis, J. P. Osborne, K. L. Page, G. Schwarz, S. Starrfield, J.-U. Ness, J. Krautter, J. Drake, and S. P. S. Eyres (2006). RS Ophiuchi. *IAU Circ. 8682*, 2–+.

Evans, A., T. Kerr, B. Yang, Y. Matsuoka, Y. Tsuzuki, M. F. Bode, S. P. S. Eyres, T. R. Geballe, C. E. Woodward, R. D. Gehrz, D. K. Lynch, R. J. Rudy, R. W. Russell, T. J. O'Brien, S. G. Starrfield, R. J. Davis, J.-U. Ness, J. Drake, J. P. Osborne, K. L. Page, A. Adamson, G. Schwarz, and J. Krautter (2007). Infrared observations of the 2006 outburst of the recurrent nova RS Ophiuchi: the early phase. *MNRAS 374*, L1–L5.

Evans, A., C. E. Woodward, L. A. Helton, R. D. Gehrz, D. K. Lynch, R. J. Rudy, R. W. Russell, T. Kerr, M. F. Bode, M. J. Darnley, S. P. S. Eyres, T. R. Geballe, T. J. O'Brien, R. J. Davis, S. Starrfield, J.-U. Ness, J. Drake, J. P. Osborne, K. L. Page, G. Schwarz, and J. Krautter (2007). Spitzer and Ground-based Infrared Observations of the 2006 Eruption of RS Ophiuchi. *ApJ 663*, L29–L32.

Evans, A., C. E. Woodward, L. A. Helton, J. T. van Loon, R. K. Barry, M. F. Bode, R. J. Davis, J. Drake, S. P. S. Eyres, T. R. Geballe, R. D. Gehrz, T. Kerr, J. Krautter, D. K. Lynch, T. J. O'Brien, J. P. Osborne, K. L. Page, R. J. Rudy, R. W. Russell, G. Schwarz, S. G. Starrfield, and V. H. Tyne (2008). Silicate dust in the environment of rs ophiuchi following the 2006 eruption. Manuscript accepted.

Eyres, S. P. S., A. Evans, A. Salama, P. Barr, J. Clavel, N. Jenkins, K. Leech, M. Kessler, T. Lim, L. Metcalfe, and B. Schulz (1998). ISO Observations of Symbiotic Stars. *Ap&SS 255*, 361–366.

Feast, M. W. and I. S. Glass (1990). M Stars in the Galaxy's Thick Disk. Unpublished notes.

Fekel, F. C., R. R. Joyce, K. H. Hinkle, and M. F. Skrutskie (2000, March). Infrared Spectroscopy of Symbiotic Stars. I. Orbits for Well-Known S-Type Systems. *AJ 119*, 1375–1388.

Fleming, W. and E. C. Pickering (1904, December). Stars Having Peculiar Spectra. *Harvard College Observatory Circular 92*, 1–3.

Forveille, T., J.-L. Beuzit, X. Delfosse, D. Segransan, F. Beck, M. Mayor, C. Perrier, A. Tokovinin, and S. Udry (1999, November). Accurate masses of very low mass stars. I. GL 570BC (0.6 M_sun+0.4 M_sun). *A&A 351*, 619–626.

Frogel, J. A. and A. E. Whitford (1987, September). M giants in Baade's window - Infrared colors, luminosities, and implications for the stellar content of E and S0 galaxies. *ApJ 320*, 199–237.

Garcia, M. R. (1986, June). Spectroscopic orbits of symbiotic stars - Preliminary results. *AJ 91*, 1400–1415.

Gehrz, R. D. (1988). The infrared temporal development of classical novae. *ARA&A 26*, 377–412.

Gehrz, R. D. (2008). *Classical Novae* (second ed.). Cambridge: University Press. in press.

Gehrz, R. D., N. Smith, B. Jones, R. Puetter, and A. Yahil (2001, September). Keck LWS Images of the Compact Nebula around RY Scuti in the Thermal Infrared. *ApJ 559*, 395–401.

Geisel, S. L., D. E. Kleinmann, and F. J. Low (1970, August). Infrared Emission of Novae. *ApJ 161*, L101+.

Ghez, A. M., G. Neugebauer, and K. Matthews (1993, November). The multiplicity of T Tauri stars in the star forming regions Taurus-Auriga and Ophiuchus-Scorpius: A 2.2 micron speckle imaging survey. *AJ 106*, 2005–2023.

Gorbatskii, V. G. (1972, August). Formation of Coronal Lines in the Spectra of Novae. I. *Soviet Astronomy 16*, 32–+.

Grevesse, N. (1984). Accurate atomic data and solar photospheric spectroscopy. *Phys. Scr 8*, 49–58.

Hachisu, I. and R. K. Barry (2008). A Wind Velocity Correction for RS Ophiuchi. Manuscript in preparation.

Hachisu, I. and M. Kato (2000, June). A Theoretical Light-Curve Model for the 1985 Outburst of RS Ophiuchi. *ApJ 536*, L93–L96.

Hachisu, I. and M. Kato (2001, September). Recurrent Novae as a Progenitor System of Type Ia Supernovae. I. RS Ophiuchi Subclass: Systems with a Red Giant Companion. *ApJ 558*, 323–350.

Hachisu, I., M. Kato, S. Kiyota, K. Kubotera, H. Maehara, K. Nakajima, Y. Ishii, M. Kamada, S. Mizoguchi, S. Nishiyama, N. Sumitomo, K. Tanaka, M. Yamanaka, and K. Sadakane (2006). The Hydrogen-Burning Turnoff of RS Ophiuchi (2006). *ApJ 651*, L141–L144.

Harrington, J. A. and A. Katzir (Eds.) (1989). *Infrared fiber optics; Proceedings of the Meeting, Los Angeles, CA, Jan. 16, 17, 1989*, Volume 1048 of *Presented at the Society of Photo-Optical Instrumentation Engineers (SPIE) Conference*.

Harrison, T. E., J. J. Johnson, and J. Spyromilio (1993, January). Infrared observations of the recurrent novae V745 SCO and V3890 SGR. *AJ 105*, 320–330.

Hartmann, L. (1998, June). *Accretion Processes in Star Formation*. Accretion processes in star formation / Lee Hartmann. Cambridge, UK ; New York : Cambridge University Press, 1998. (Cambridge astrophysics series ; 32) ISBN 0521435072.

Hauschildt, P. H., F. Allard, J. Ferguson, E. Baron, and D. R. Alexander (1999). The NEXTGEN Model Atmosphere Grid. II. Spherically Symmetric Model Atmospheres for Giant Stars with Effective Temperatures between 3000 and 6800 K. *ApJ 525*, 871–880.

Hilditch, R. W. (2001, March). *An Introduction to Close Binary Stars*. An Introduction to Close Binary Stars, by R. W. Hilditch, pp. 392. ISBN 0521241065. Cambridge, UK: Cambridge University Press, March 2001.

Hjellming, R. M., J. H. van Gorkom, E. R. Seaquist, A. R. Taylor, S. Padin, R. J. Davis, and M. F. Bode (1986, June). Radio observations of the 1985 outburst of RS Ophiuchi. *ApJ 305*, L71–L75.

Hodge, T. M., K. E. Kraemer, S. D. Price, and H. J. Walker (2004, April). Classification of Spectra from the Infrared Space Observatory PHT-S Database. *ApJS 151*, 299–312.

Houck, J. R., T. L. Roellig, J. van Cleve, W. J. Forrest, T. Herter, C. R. Lawrence, K. Matthews, H. J. Reitsema, B. T. Soifer, D. M. Watson, D. Weedman, M. Huisjen, J. Troeltzsch, D. J. Barry, J. Bernard-Salas, C. E. Blacken, B. R. Brandl, V. Charmandaris, D. Devost, G. E. Gull, P. Hall, C. P. Henderson, S. J. U. Higdon, B. E. Pirger, J. Schoenwald, G. C. Sloan, K. I. Uchida, P. N. Appleton, L. Armus, M. J. Burgdorf, S. B. Fajardo-Acosta, C. J. Grillmair, J. G. Ingalls, P. W. Morris, and H. I. Teplitz (2004, September). The Infrared Spectrograph (IRS) on the Spitzer Space Telescope. *ApJS 154*, 18–24.

Hummel, C. A., J.-M. Carquillat, N. Ginestet, R. F. Griffin, A. F. Boden, A. R. Hajian, D. Mozurkewich, and T. E. Nordgren (2001, March). Orbital and Stellar Parameters of Omicron Leonis from Spectroscopy and Interferometry. *AJ 121*, 1623–1635.

Iijima, T. (2008). The Stellar Wind from the RS Ophiuchi Red Giant. In A. Evans (Ed.), *RS Ophiuchi (2006) and the recurrent nova phenomenon*.

Itoh, H. and I. Hachisu (1990, August). X-ray decline and rejuvenation of a recurrent nova. *ApJ 358*, 551–560.

Ivezic, Z. and M. Elitzur (1997, June). Self-similarity and scaling behaviour of infrared emission from radiatively heated dust - I. Theory. *MNRAS 287*, 799–811.

Jackson, J. D. (1998, July). *Classical Electrodynamics, 3rd Edition*. Classical Electrodynamics, 3rd Edition, by John David Jackson, pp. 832. ISBN 0-471-30932-X. Wiley-VCH , July 1998.

Joy, A. H. (1939, April). Rotation Effects, Interstellar Absorption, and Certain Dynamical Constants of the Galaxy Determined from Cepheid Variables. *ApJ 89*, 356–+.

Kenyon, S. J. and T. Fernandez-Castro (1987, April). The cool components of symbiotic stars. I - Optical spectral types. *AJ 93*, 938–949.

Kenyon, S. J. and R. F. Webbink (1984). The nature of symbiotic stars. *ApJ 279*, 252–283.

Koresko, C., M. M. Colavita, E. Serabyn, A. Booth, and J. Garcia (2006, July). Measuring extended structure in stars using the Keck Interferometer Nuller. In *Advances in Stellar Interferometry. Edited by Monnier, John D.; Schöller, Markus; Danchi, William C.. Proceedings of the SPIE, Volume 6268, pp. 626816 (2006).*, Volume 6268 of *Presented at the Society of Photo-Optical Instrumentation Engineers (SPIE) Conference*.

Kuchner, M. and R. K. Barry (2008). A Mathematical Description of the Keck Interferometer Nuller. Manuscript in preparation.

Kurucz, R. L. (1992). Model Atmospheres for Population Synthesis. In B. Barbuy and A. Renzini (Eds.), *The Stellar Populations of Galaxies*, Volume 149, pp. 225–+.

Lane, B. F., A. Retter, J. A. Eisner, R. R. Thompson, and M. W. Muterspaugh (2005, December). Interferometric Observations of Nova Aql 2005. In *Bulletin of the American Astronomical Society*, Volume 37 of *Bulletin of the American Astronomical Society*, pp. 1335–+.

Lane, B. F., J. L. Sokoloski, R. K. Barry, W. A. Traub, A. Retter, M. W. Muterspaugh, R. R. Thompson, J. A. Eisner, E. Serabyn, and B. Mennesson (2007). Interferometric Observations of RS Ophiuchi and the Origin of the Near-Infrared Emission. *ApJ 658*, 520–524.

Latham, D. W., B. Nordstroem, J. Andersen, G. Torres, R. P. Stefanik, M. Thaller, and M. J. Bester (1996, October). Accurate mass determination for double-lined spectroscopic binaries by digital cross-correlation spectroscopy: DM Virginis revisited. *A&A 314*, 864–870.

Lawson, P. R. (1999, December). A History of Stellar Interferometry: from 1868 to the present. In *Bulletin of the American Astronomical Society*, Volume 31 of *Bulletin of the American Astronomical Society*, pp. 1406–+.

Lawson, P. R. (Ed.) (2000). *Principles of Long Baseline Stellar Interferometry*.

Leggett, S. K. (1992, September). Infrared colors of low-mass stars. *ApJS 82*, 351–394.

Leinert, C., T. Henry, A. Glindemann, and D. W. McCarthy, Jr. (1997, September). A search for companions to nearby southern M dwarfs with near-infrared speckle interferometry. *A&A 325*, 159–166.

Livio, M., J. W. Truran, and R. F. Webbink (1986). A model for the outbursts of the recurrent nova RS Ophiuchi. *ApJ 308*, 736–742.

Lucek, S. G. and A. R. Bell (2000, May). Non-linear amplification of a magnetic field driven by cosmic ray streaming. *MNRAS 314*, 65–74.

Lynch, D. K., C. E. Woodward, T. R. Geballe, R. W. Russell, R. J. Rudy, C. C. Venturini, G. J. Schwarz, R. D. Gehrz, N. Smith, J. E. Lyke, S. J. Bus, M. L. Sitko, T. E. Harrison, S. Fisher, S. P. Eyres, A. Evans, S. N. Shore, S. Starrfield, M. F. Bode, M. A. Greenhouse, P. H. Hauschildt, J. W. Truran, R. E. Williams, R. B. Perry, R. Zamanov, and T. J. O'Brien (2006, February). Early Infrared Spectral Development of V1187 Scorpii (Nova Scorpii 2004 No. 2). *ApJ 638*, 987–1003.

Lynden-Bell, D. and J. E. Pringle (1974, September). The evolution of viscous discs and the origin of the nebular variables. *MNRAS 168*, 603–637.

Mason, K. O., F. A. Córdova, M. F. Bode, and P. Barr (1987). Intense Soft X-rays from RS Ophiuchi during the 1985 Outburst. In M. F. Bode (Ed.), *RS Ophiuchi (1985) and the Recurrent Nova Phenomenon*, pp. 167–+.

Mastrodemos, N. and M. Morris (1999, September). Bipolar Pre-Planetary Nebulae: Hydrodynamics of Dusty Winds in Binary Systems. II. Morphology of the Circumstellar Envelopes. *ApJ 523*, 357–380.

Mathis, J. S. (1998, April). The Near-Infrared Interstellar Silicate Bands and Grain Theories. *ApJ 497*, 824–+.

Mauron, N. and P. J. Huggins (2006, June). Imaging the circumstellar envelopes of AGB stars. *A&A 452*, 257–268.

McLaughlin, D. B. (1960, January). The Spectra of Novae. In J. L. Greenstein (Ed.), *Stellar Atmospheres*, pp. 585–+.

Metcalfe, T. S., R. D. Mathieu, D. W. Latham, and G. Torres (1996, January). The Low-Mass Double-lined Eclipsing Binary CM Draconis: A Test of the Primordial Helium Abundance and the Mass-Radius Relation near the Bottom of the Main Sequence. *ApJ 456*, 356–+.

Mikami, T. and A. Heck (1982). Absolute Magnitudes of F-Type G-Type K-Type and M-Type Stars from Maximum Likelihood Statistical Parallaxes. *PASJ 34*, 529–+.

Miller, G. E. and J. M. Scalo (1979, November). The initial mass function and stellar birthrate in the solar neighborhood. *ApJS 41*, 513–547.

Monnier, J. D. (2003, May). Optical interferometry in astronomy. *Reports of Progress in Physics 66*, 789–857.

Monnier, J. D., R. K. Barry, W. A. Traub, B. F. Lane, R. L. Akeson, S. Ragland, P. A. Schuller, H. Le Coroller, J.-P. Berger, R. Millan-Gabet, E. Pedretti, F. P. Schloerb, C. Koresko, N. P. Carleton, M. G. Lacasse, P. Kern, F. Malbet, K. Perraut, M. J. Kuchner, and M. W. Muterspaugh (2006). No Expanding Fireball: Resolving the Recurrent Nova RS Ophiuchi with Infrared Interferometry. *ApJ 647*, L127–L130.

Monnier, J. D., J.-P. Berger, R. Millan-Gabet, W. A. Traub, F. P. Schloerb, E. Pedretti, M. Benisty, N. P. Carleton, P. Haguenauer, P. Kern, P. Labeye, M. G. Lacasse, F. Malbet, K. Perraut, M. Pearlman, and M. Zhao (2006, August). Few Skewed Disks Found in First Closure-Phase Survey of Herbig Ae/Be Stars. *ApJ 647*, 444–463.

Monnier, J. D., W. A. Traub, F. P. Schloerb, R. Millan-Gabet, J.-P. Berger, E. Pedretti, N. P. Carleton, S. Kraus, M. G. Lacasse, M. Brewer, S. Ragland, A. Ahearn, C. Coldwell, P. Haguenauer, P. Kern, P. Labeye, L. Lagny, F. Malbet, D. Malin, P. Maymounkov, S. Morel, C. Papaliolios, K. Perraut, M. Pearlman, I. L. Porro, I. Schanen, K. Souccar, G. Torres, and G. Wallace (2004, February). First Results with the IOTA3 Imaging Interferometer: The Spectroscopic Binaries λ Virginis and WR 140. *ApJ 602*, L57–L60.

Morris, M., R. Sahai, K. Matthews, J. Cheng, J. Lu, M. Claussen, and C. Sánchez-Contreras (2006). A Binary-Induced Pinwheel Outflow from the Extreme Carbon Star, AFGL 3068. In M. J. Barlow and R. H. Méndez (Eds.), *Planetary Nebulae in our Galaxy and Beyond*, Volume 234 of *IAU Symposium*, pp. 469–470.

Morrison, W. (1985, January). RS Ophiuchi. *IAU Circ. 4030*, 2–+.

Muerset, U., H. Nussbaumer, H. M. Schmid, and M. Vogel (1991). Temperature and luminosity of hot components in symbiotic stars. *A&A 248*, 458–474.

Mürset, U. and H. M. Schmid (1999, June). Spectral classification of the cool giants in symbiotic systems. *A&AS 137*, 473–493.

Narumi, H., K. Hirosawa, K. Kanai, W. Renz, A. Pereira, S. Nakano, Y. Nakamura, and G. Pojmanski (2006, February). RS Ophiuchi. *IAU Circ. 8671*, 2–+.

Ness, J.-U., S. Starrfield, A. P. Beardmore, M. F. Bode, J. J. Drake, A. Evans, R. D. Gehrz, M. R. Goad, R. Gonzalez-Riestra, P. Hauschildt, J. Krautter, T. J. O'Brien, J. P. Osborne, K. L. Page, R. A. Schönrich, and C. E. Woodward (2007, August). The SSS Phase of RS Ophiuchi Observed with Chandra and XMM-Newton. I. Data and Preliminary Modeling. *ApJ 665*, 1334–1348.

Ney, E. P. and B. F. Hatfield (1980, September). Are Novae Shells Optically Thick in the Infrared. *AJ 85*, 1292–+.

Nordström, B., M. Mayor, J. Andersen, J. Holmberg, F. Pont, B. R. Jørgensen, E. H. Olsen, S. Udry, and N. Mowlavi (2004, May). The Geneva-Copenhagen survey of the Solar neighbourhood. Ages, metallicities, and kinematic properties of 14 000 F and G dwarfs. *A&A 418*, 989–1019.

Noyes, R. W., S. Jha, S. G. Korzennik, M. Krockenberger, P. Nisenson, T. M. Brown, E. J. Kennelly, and S. D. Horner (1997, July). A Planet Orbiting the Star Rho Coronae Borealis. *ApJ 483*, L111+.

Nussbaumer, H. and M. Vogel (1987, August). A new approach to symbiotic stars. *A&A 182*, 51–62.

Nussbaumer, H. and M. Vogel (1989, April). Z Andromedae and the symbiotic phenomenon. *A&A 213*, 137–147.

Nuth, III, J. A. and J. H. Hecht (1990, January). Signatures of aging silicate dust. *Ap&SS 163*, 79–94.

O'Brien, T. J., M. F. Bode, and F. D. Kahn (1992, April). Models for the remnants of recurrent novae. III - Comparison with the X-ray observations of RS Ophiuchi (1985). *MNRAS 255*, 683–693.

O'Brien, T. J., M. F. Bode, R. W. Porcas, T. W. B. Muxlow, S. P. S. Eyres, R. J. Beswick, S. T. Garrington, R. J. Davis, and A. Evans (2006, July). An asymmetric shock wave in the 2006 outburst of the recurrent nova RS Ophiuchi. *Nature 442*, 279–281.

Oppenheimer, B. and J. A. Mattei (1993, December). An Analysis of Longterm AAVSO Observations of the Recurrent Nova RS Ophiuchi. In *Bulletin of the American Astronomical Society*, Volume 25 of *Bulletin of the American Astronomical Society*, pp. 1378–+.

Ossenkopf, V., T. Henning, and J. S. Mathis (1992, August). Constraints on cosmic silicates. *A&A 261*, 567–578.

Osterbrock, D. E. and G. J. Ferland (2006). *Astrophysics of gaseous nebulae and active galactic nuclei*. Astrophysics of gaseous nebulae and active galactic nuclei, 2nd. ed. by D.E. Osterbrock and G.J. Ferland. Sausalito, CA: University Science Books, 2006.

Pauls, T. A., J. S. Young, W. D. Cotton, and J. D. Monnier (2005, November). A Data Exchange Standard for Optical (Visible/IR) Interferometry. *PASP 117*, 1255–1262.

Payne-Gaposchkin, C. (1957). *The Galactic Novae*. Dover Publications.

Pedretti, E., N. D. Thureau, E. Wilson, W. A. Traub, J. D. Monnier, S. Ragland, N. P. Carleton, R. Millan-Gabet, F. P. Schloerb, M. K. Brewer, J.-P. Berger, and M. G. Lacasse (2004, October). Fringe tracking at the IOTA interferometer. In W. A. Traub (Ed.), *New Frontiers in Stellar Interferometry, Proceedings of SPIE Volume 5491. Edited by Wesley A. Traub. Bellingham, WA: The International Society for Optical Engineering, 2004., p.540*, Volume 5491 of *Presented at the Society of Photo-Optical Instrumentation Engineers (SPIE) Conference*, pp. 540–+.

Perryman, M. A. C., L. Lindegren, J. Kovalevsky, E. Hoeg, U. Bastian, P. L. Bernacca, M. Crézé, F. Donati, M. Grenon, F. van Leeuwen, H. van der Marel, F. Mignard, C. A. Murray, R. S. Le Poole, H. Schrijver, C. Turon, F. Arenou, M. Froeschlé, and C. S. Petersen (1997, July). The HIPPARCOS Catalogue. *A&A 323*, L49–L52.

Pickering, E. C. (1905, July). A probable new star, RS Ophuichi. *ApJ 22*, 90–92.

Platais, I., D. Pourbaix, A. Jorissen, V. V. Makarov, L. N. Berdnikov, N. N. Samus, T. Lloyd Evans, T. Lebzelter, and J. Sperauskas (2003, January). Hipparcos red stars in the HpV_T2 and V I_C systems. *A&A 397*, 997–1010.

Podsiadlowski, P. and S. Mohamed (2007). The Origin and Evolution of Symbiotic Binaries. *Baltic Astronomy 16*, 26–33.

Popper, D. M. (1980). Stellar masses. *ARA&A 18*, 115–164.

Pottasch, S. R. (1967, January). An interpretation of the spectrum of the recurrent nova RS Ophiuchi. *Bull. Astron. Inst. Netherlands 19*, 227–+.

Pringle, J. E. (1981). Accretion discs in astrophysics. *ARA&A 19*, 137–162.

Queloz, D. (1995, January). *On the Detection of a Planet in Orbit About the Star 51 Peg*. Ph. D. thesis, 2788, University of Geneva, (1995).

Quillen, A. C. and S. Thorndike (2002, October). Structure in the ϵ Eridani Dusty Disk Caused by Mean Motion Resonances with a 0.3 Eccentricity Planet at Periastron. *ApJ 578*, L149–L152.

Ramseyer, T. F., C. Lasley, C. Davis, C. Leonard, and A. Portoni (1999, December). Photometry of Gliese 372. *AJ 118*, 2988–2992.

Rupen, M. P., A. J. Mioduszewski, J. L. Sokoloski, C. R. Kaiser, and C. Brocksopp (2006, December). Radio Imaging of the Recurrent Nova RS Ophiuchus. In *Bulletin of the American Astronomical Society*, Volume 38 of *Bulletin of the American Astronomical Society*, pp. 1160–+.

Rupen, M. P. and J. L. Sokoloski (2008). Observations of Nova RS Ophiuchi During the 2006 Outburst. Manuscript in preparation.

Rybicki, G. B. and A. P. Lightman (1986). *Radiative Processes in Astrophysics*. Radiative Processes in Astrophysics, by George B. Rybicki, Alan P. Lightman, pp. 400. ISBN 0-471-82759-2. Wiley-VCH , June 1986.

Sacuto, S., O. Chesneau, M. Vannier, and P. Cruzalèbes (2007, April). A compact dust shell in the symbiotic system ¡ASTROBJ¿HM Sagittae¡/ASTROBJ¿. *A&A 465*, 469–480.

Savage, B. D. and J. S. Mathis (1979). Observed properties of interstellar dust. *ARA&A 17*, 73–111.

Schaefer, B. E. (2004, August). RS Ophiuchi. *IAU Circ. 8396*, 2–+.

Schild, H., S. P. S. Eyres, A. Salama, and A. Evans (2001, October). ISO observations of symbiotic stars. I. HM Sge. *A&A 378*, 146–152.

Scott, A. D., J. M. C. Rawlings, J. Krautter, and A. Evans (1994, June). Evidence for a Change of Composition in the Giant Component of Rs-Ophiuchi after the 1985 Outburst. *MNRAS 268*, 749–+.

Seaton, M. J. (1978, October). Calculated intensities of He II recombination lines in the ultraviolet. *MNRAS 185*, 5P–8P.

Seaton, M. J. (1979, June). Interstellar extinction in the UV. *MNRAS 187*, 73P–76P.

Sekiguchi, K., P. A. Whitelock, M. W. Feast, P. E. Barrett, J. A. R. Caldwell, B. S. Carter, R. M. Catchpole, J. D. Laing, C. D. Laney, F. Marang, and F. van Wyk (1990, September). The 1989 Outburst of the Recurrent Nova V745-SCORPII. *MNRAS 246*, 78–+.

Shore, S. N. and J. P. Aufdenberg (1993). On the Interpretation of the Ultraviolet Spectra of Symbiotic Stars and Recurrent Novae. I. *ApJ 416*, 355–+.

Silk, J. (1995, January). A theory for the initial mass function. *ApJ 438*, L41–L44.

Skopal, A. (2005). Disentangling the composite continuum of symbiotic binaries. I. S-type systems. *A&A 440*, 995–1031.

Skopal, A. (2007). On the effect of emission lines on UBVR photometry. *New Astronomy 12*, 597–604.

Skopal, A. and T. Pribulla (2006). The first detection of the bipolar jets from the symbiotic prototype Z And. *The Astronomer's Telegram 882*, 1–+.

Skopal, A., T. Pribulla, C. Buil, A. Vittone, and L. Errico (2008). A non-spherical mass outflow for RS Oph during its 2006 outburst. In A. Evans, M. F. Bode, and T. J. O'Brien (Eds.), *RS Ophiuchi (2006) and the recurrent nova phenomenon*, Volume 4013.

Skopal, A. and M. Wolf (2006). Continuous presence of bipolar jets from Z And during its 2006 outburst. *The Astronomer's Telegram 930*, 1–+.

Skrutskie, M. F., R. M. Cutri, R. Stiening, M. D. Weinberg, S. Schneider, J. M. Carpenter, C. Beichman, R. Capps, T. Chester, J. Elias, J. Huchra, J. Liebert, C. Lonsdale, D. G. Monet, S. Price, P. Seitzer, T. Jarrett, J. D. Kirkpatrick, J. E. Gizis, E. Howard, T. Evans, J. Fowler, L. Fullmer, R. Hurt, R. Light, E. L. Kopan, K. A. Marsh, H. L. McCallon, R. Tam, S. Van Dyk, and S. Wheelock (2006, February). The Two Micron All Sky Survey (2MASS). *AJ 131*, 1163–1183.

Snijders, M. A. J. (1987a). Multi-frequency observations of the 1985 outburst of RS Ophiuchi. *Ap&SS 130*, 243–254.

Snijders, M. A. J. (1987b). Ultraviolet Observations of the 1985 Outburst of RS Ophiuchi. In M. F. Bode (Ed.), *RS Ophiuchi (1985) and the Recurrent Nova Phenomenon*, pp. 51–+.

Snijders, M. A. J., A. Cassatella, B. J. M. Hassall, A. Harris, and D. W. E. Green (1985, May). RS Ophiuchi. *IAU Circ. 4067*, 2–+.

Sokoloski, J. L., G. J. M. Luna, K. Mukai, and S. J. Kenyon (2006). An X-ray-emitting blast wave from the recurrent nova RS Ophiuchi. *Nature 442*, 276–278.

Speck, A. K., M. J. Barlow, R. J. Sylvester, and A. M. Hofmeister (2000, November). Dust features in the 10-mu m infrared spectra of oxygen-rich evolved stars. *A&AS 146*, 437–464.

Spruit, H. C. and R. E. Taam (2001, February). Circumbinary Disks and Cataclysmic Variable Evolution. *ApJ 548*, 900–907.

Starrfield, S., W. M. Sparks, and J. W. Truran (1985, April). Recurrent novae as a consequence of the accretion of solar material onto a 1.38 solar mass white dwarf. *ApJ 291*, 136–146.

Stickland, D. J. (1988, June). IUE and stars with composite spectra. In E. J. Rolfe (Ed.), *A Decade of UV Astronomy with the IUE Satellite, Volume 2*, Volume 2, pp. 27–44.

Tatischeff, V. and M. Hernanz (2007, July). Evidence for Nonlinear Diffusive Shock Acceleration of Cosmic Rays in the 2006 Outburst of the Recurrent Nova RS Ophiuchi. *ApJ 663*, L101–L104.

Taylor, A. R., R. J. Davis, R. W. Porcas, and M. F. Bode (1989, March). VLBI observations of RS OPH - A recurrent nova with non-spherical ejection. *MNRAS 237*, 81–91.

Tielens, A. G. G. M., C. F. McKee, C. G. Seab, and D. J. Hollenbach (1994, August). The physics of grain-grain collisions and gas-grain sputtering in interstellar shocks. *ApJ 431*, 321–340.

Tomkin, J. and B. R. Pettersen (1986, December). The M dwarf double-lined spectroscopic binary Gliese 268. *AJ 92*, 1424–1427.

Torres, G. and I. Ribas (2002, March). Absolute Dimensions of the M-Type Eclipsing Binary YY Geminorum (Castor C): A Challenge to Evolutionary Models in the Lower Main Sequence. *ApJ 567*, 1140–1165.

Traub, W. A., A. Ahearn, N. P. Carleton, J.-P. Berger, M. K. Brewer, K.-H. Hofmann, P. Y. Kern, M. G. Lacasse, F. Malbet, R. Millan-Gabet, J. D. Monnier, K. Ohnaka, E. Pedretti, S. Ragland, F. P. Schloerb, K. Souccar, and G. Weigelt (2003, February). New Beam-Combination Techniques at IOTA. In W. A. Traub (Ed.), *Interferometry for Optical Astronomy II. Edited by Wesley A. Traub. Proceedings of the SPIE, Volume 4838, pp. 45-52 (2003).*, Volume 4838 of *Presented at the Society of Photo-Optical Instrumentation Engineers (SPIE) Conference*, pp. 45–52.

van Belle, G. T., D. R. Ciardi, and A. F. Boden (2007, March). Measurement of the Surface Gravity of η Bootis. *ApJ 657*, 1058–1063.

van Belle, G. T., B. F. Lane, R. R. Thompson, A. F. Boden, M. M. Colavita, P. J. Dumont, D. W. Mobley, D. Palmer, M. Shao, G. X. Vasisht, J. K. Wallace, M. J. Creech-Eakman, C. D. Koresko, S. R. Kulkarni, X. P. Pan, and J. Gubler (1999,

January). Radii and Effective Temperatures for G, K, and M Giants and Supergiants. *AJ 117*, 521–533.

van Loon, J. T., M.-R. L. Cioni, A. A. Zijlstra, and C. Loup (2005, July). An empirical formula for the mass-loss rates of dust-enshrouded red supergiants and oxygen-rich Asymptotic Giant Branch stars. *A&A 438*, 273–289.

Verhoelst, T., E. van Aarle, and B. Acke (2007, August). Direct diameter measurement of a star filling its Roche lobe. The semi-detached binary SS Leporis spatially resolved with VINCI/VLTI. *A&A 470*, L21–L24.

Viti, S., H. R. A. Jones, A. Schweitzer, F. Allard, P. H. Hauschildt, J. Tennyson, S. Miller, and A. J. Longmore (1997, November). The effective temperature and metallicity of CM Draconis. *MNRAS 291*, 780–+.

Wallerstein, G. (1958, December). Sharp Lines in the Spectrum of Nova RS Ophiuchi. *PASP 70*, 537–+.

Wallerstein, G. (1963, February). Observations of Nova RS Ophiuchi During 1960-62. *PASP 75*, 26–+.

Warner, B. (1976). Observations of Dwarf Novae. In P. Eggleton, S. Mitton, and J. Whelan (Eds.), *Structure and Evolution of Close Binary Systems*, Volume 73 of *IAU Symposium*, pp. 85–+.

Warner, B. (1995). *Cataclysmic variable stars*. Cambridge Astrophysics Series, Cambridge, New York: Cambridge University Press, —c1995.

Whittet, D. C. B. (Ed.) (2003). *Dust in the galactic environment*.

Yaron, O., D. Prialnik, M. M. Shara, and A. Kovetz (2005, April). An Extended Grid of Nova Models. II. The Parameter Space of Nova Outbursts. *ApJ 623*, 398–410.

Yoon, S.-C. and N. Langer (2004, May). Presupernova evolution of accreting white dwarfs with rotation. *A&A 419*, 623–644.

Young, T. (1803). *The bakerian lecture : Experiments and calculations relative to physical optics*. London : Philosophical transactionis of the Royal Astronomy; da p. 1 a p. 76; AQ 209.

Zajczyk, A., T. Tomov, M. Mikołajewski, M. Cikala, and G. Galazutdinov (2007). High-Resolution Spectroscopy of RS OPH during the Quiescence Before the 2006 Outburst. *Baltic Astronomy 16*, 62–64.

Zamanov, R. K., M. F. Bode, C. H. F. Melo, R. Bachev, A. Gomboc, I. K. Stateva, J. M. Porter, and J. Pritchard (2007, September). Rotational velocities of the giants in symbiotic stars - II. Are S-type symbiotics synchronized? *MNRAS 380*, 1053–1063.

Vita

Education

- 2008 - Ph.D. Physics and Astronomy, Johns Hopkins University, Baltimore, MD
- 2005 - MA Physics and Astronomy, Johns Hopkins University, Baltimore, MD
- 1996 - MS Electrical Engineering, Johns Hopkins University, Baltimore, MD
- 1989 - BS Electrical Engineering, University of Washington, Seattle, WA
- 1986 - AS Avionics Engineering, USAF Community College, Okinawa, Japan

Experience

NASA, Goddard Space Flight Center, Greenbelt, MD

- 2002-Present: Science Instrument Engineer / Graduate Student
  - Co-Investigator, Keck Interferometer Nuller; dusty debris disks
  - Co-Investigator, Keck Interferometer Nuller; debris disk variability
  - Co-Investigator, VLTI/Bright Novae, European Southern Observatory
  - Co-Investigator, Fourier-Kelvin Stellar Interferometer nulling testbed
  - Co-Investigator, Advanced Architectures,Terrestrial Planet Finder
  - Principal Investigator, Ditherless Quadrature Phase Detector, DDF
  - Proposal Team Co-Investigator: ROSES APRA and ADP
  - Proposal Team Co-Investigator: IRAD and DDF
  - Proposal Team Co-Investigator: Spitzer, HST, IOTA, Keck, KIN obs.
  - Observational astronomy; Keck Interferometer
  - Observational astronomy; Infrared Optical Telescope Array
  - Interactive Data Language (IDL) programming, astronomy algorithms
  - Member, People with Disabilities Advisory Committee

- 2002: Hubble Space Telescope (HST) Mission, WFPC-II Primary Shutter Anomaly, Tiger Team mechanism dynamics engineer

- 2001 - 2002: Airborne Earth Science Microwave Imaging Radiometer, controls engineer
  - Design, integration and test, aircraft gimbal control system
  - Derivation of control laws and equations of motion of system
  - Development of MATLAB Simulink mathematical model of system

- 2001 - 2002: Infrared Array Camera (IRAC) primary shutter anomaly, Tiger Team mechanism dynamics engineer

- 1999 - 2001: Demonstration Unit for Low-order Cryogenic Etalon (DULCE) for the James Web Space Telescope (JWST), lead controls engineer
  - Design, integration, and test of nanometer capacitive sensor system
  - Design and coding of labVIEW data acquisition system
  - Analysis, design, and coding of DSP-based multivariable controller
  - Calculations involving multilayer, semiconductor interference filters
  - Development and alignment of the optical testing system
  - Management of budget and schedule for design and test team

- 1998 - 1999: Submillimeter and Far infraRed Explorer (SAFIRE), electrical engineer
  - Development of a cryogenic capacitive positional sensing system
  - Design and analysis of cryo-mechanisms
  - Calculations of vibration modes of 20cm inductive-grid FP elements
  - Actuator trade studies comparing voice-coil to piezo-based actuators

- 1997 - 1998: Superconducting Voice Coil Actuators, DDF Principal Investigator
  - Investigate thermal effects due to flux pinning in super conductors
  - Design and analysis of cryogenic SC voice coil actuators
  - C-programming of test hardware interface
  - Actuator trade studies comparing voice-coil to piezo-based actuators

- 1997 - 1998: Zephyr, control system engineer, optical Fabry-Perot interferometer control system analysis

- 1995 - 1998: Lunar Advanced Technology Telescope, design engineer. Developed a graphite-fiber composite telescope with ultra-light composite mirrors produced by replication technology

- 1994 - 1996: Transition Region and Coronal Explorer (TRACE) and Wide-field Infra-Red Explorer (WIRE), power system lead engineer
  - Developed and launched a digitally controlled power system
  - Designed power-saving, partial array shunt, energy transfer system
- 1991 - 1994: X-Ray Timing Explorer (XTE), power system lead engineer Design, development and launch of a digitally controlled 1200 Watt spacecraft power subsystem

Johns Hopkins, Center for Talented Youth, Baltimore, MD

- 2001: Instructor, physics of flight and physical mechanics

Capital College, Laurel, MD

- 1999 - 2001: Adjunct Instructor, undergraduate calculus-based physics

NASA, Kennedy Space Center, Cape Canaveral, FL

- 1989 - 1991: Space Shuttle, power system engineer; Electrical power system engineering, launch console and launch pad operations

Nuclear Physics Laboratory, University of Washington, Seattle, WA

- 1986 - 1989: Engineering technician - development of RF circuitry for 18 MeV, superconducting linear particle accelerator facility

The United States Air Force, Kadena Air Base, Okinawa, Japan

- 1981 - 1986: Technician, F-16 Falcon
  - Troubleshoot and repair all aircraft systems
  - ATLAS computer language programming
  - Distinguished Graduate, NCO Preparatory School
  - Honorable Discharge

Publications

1. Barry, R. K., Mukai, K., Sokoloski, J. L., Danchi, W. C., Hachisu, I., Evans, A., Gehrz, R., Mikołajewska, J., "On the distance to the recurrent nova RS Ophiuchi". In *RS Ophiuchi (2006) and the recurrent nova phenomenon.*, A. Evans, M. F. Bode, and T. J. OBrien (Eds.), (Utrecht, Netherlands: VNU Science Press) (2008).

2. Barry, R. K. "Milliarcsecond Resolution Infrared Observations of the Recurrent Nova RS Ophiuchi and Low Mass Stellar Systems". Ph.D. thesis, The Johns Hopkins University, Baltimore, MD. (2007).

3. Barry, R. K., W. C. Danchi, V. J. Chambers, J. Rajagopal, L. J. Richardson, A. Martino, D. Deming, M. Kuchner, R. Linfield, R. Millan-Gabet, L. A. Lee, J. D. Monnier, L. G. Mundy, C. Noecker, S. Seager, D. J. Wallace, R. J. Allen, W. A. Traub, and H. C. Ford (2005, August). "The Fourier-Kelvin stellar interferometer (FKSI): a progress report and preliminary results from our nulling testbed". In *Techniques and Instrumentation for Detection of Exoplanets II.* Edited by Coulter, Daniel R. Proceedings of the SPIE, Volume 5905, pp. 311-321 (2005).

4. Barry, R. K., "The Infrared and Optical Telescope Array Observatory Opening and Closing Procedure". F. L. Whipple Astronomical Observatory, Tucson, AZ. (2005).

5. Barry, R. K., W. C. Danchi, L. D. Deming, L. J. Richardson, M. J. Kuchner, V. J. Chambers, B. J. Frey, A. J. Martino, J. Rajagopal, R. J. Allen, J. A. Harrington, T. T. Hyde, V. S. Johnson, R. Linfield, R. Millan-Gabet, J. D. Monnier, L. G. Mundy, C. Noecker, S. Seager, andW. A. Traub. "The Fourier-Kelvin Stellar Interferometer: an achievable, space-borne interferometer for the direct detection and study of extrasolar giant planets". In IAU Colloq. 200: *Direct Imaging of Exoplanets: Science & Techniques*, C. Aime and F. Vakili (Eds.), pp. 221- 226. (2006)

6. Barry, R. K., "The Infrared and Optical Telescope Array Observatory Optical Alignment Procedure". F. L. Whipple Astronomical Observatory, Tucson, AZ. (2005).

7. Barry, R. K., W. C. Danchi, L. D. Deming, L. J. Richardson, M. J. Kuchner, S. Seager, B. J. Frey, A. J. Martino, K. A. Lee, M. Zuray, J. Rajagopal, T. T. Hyde, R. Millan-Gabete, J. D. Monnier, R. J. Allen, and W. A. Traub (2006, July). "The Fourier-Kelvin stellar interferometer: a low-complexity low-cost

space mission for high-resolution astronomy and direct exoplanet detection". In *Space Telescopes and Instrumentation I: Optical, Infrared, and Millimeter*. Edited by Mather, John C.; MacEwen, Howard A.; de Graauw, Mattheus W. M.. Proceedings of the SPIE, Volume 6265, pp. 62651L (2006).

8. Barry, R. K., W. C. Danchi, J. K. Rajagopal, V. J. Chambers, L. J. Richardson, A. J. Martino, R. J. Allen, L. D. Deming, M. J. Kuchner, D. T. Leisawitz, R. Linfield, J. D. Monnier, L. G. Mundy, C. Noecker, S. Seager, and W. A. Traub. "The Fourier-Kelvin Stellar Interferometer: A Concept for an Interferometric Mission for Discovering and Investigating Extrasolar Giant Planets and a Progress Report". In *Proceedings of the European Southern Observatory*. (2005)

9. Barry, R. K., W. C. Danchi, J. L. Sokoloski, C. Koresko, J. P.Wisniewski, E. Serabyn, W. A. Traub, M. J. Kuchner, and M. A. Greenhouse. "High Spatial Resolution N-band Observations of the Nova RS Ophiuchi with the Keck Interferometer Nuller". *ApJ* Manuscript submitted.

10. Barry, R. K. and W. D. Danchi. "High-resolution interferometric observations of the nova RS Ophiuchi and a proposed unification model for persistent dust creation in repeater novae". In , *RS Ophiuchi (2006) and the recurrent nova phenomenon*. A. Evans, M. F. Bode, and T. J. OBrien (Eds.), (Utrecht, Netherlands: VNU Science Press) (2008)

11. Barry, R. K., B. Demory, D. Segransan, T. Forveille, W. C. Danchi, E. Di Folco, D. Queloz, G. Torres, W. Traub, X. Delfosse, M. Mayor, C. Perrier, and S. Udry. "A Physical Orbit for the M Dwarf Binary Gliese 268". *ApJ* Manuscript in preparation.

12. Barry, R. K. and K. Labelle. "Radiation Testing of Power Electronics for Space Flight". In *Proceedings of the Nuclear and Plasma Sciences Society*. (1993)

13. Barry, R. K., J. K. Rajagopal, W. C. Danchi, M. J. Kuchner, and L. J. Richardson (2004). "Simulating interferometric imaging with the Fourier-Kelvin Stellar Interferometer". Technical report, National Aeronautics and Space Administration/Goddard Space Flight Center. (2004)

14. Barry, R. K., S. Satyapal, M. A. Greenhouse, R. B. Barclay, D. D. Amato, B. Arritt, G. Brown, V. Harvey, C. Holt, J. L. Kuhn, L. Lesyna, N. J. Fonneland, and T. W. Hilgeman . "Near-IR Fabry-Perot interferometer for widefield low-resolution hyperspectral imaging on the Next Generation Space Telescope". In *UV, Optical, and IR Space Telescopes and Instruments*, J. B. Breckinridge and P. Jakobsen (Eds.), Proc. SPIE Vol. 4013, p. 861-871. (2000)

15. Barry, R. K., A. Skopal, and W. C. Danchi. "Calibration of the wavelength dependency of stellar leakage for the Keck Interferometer Nuller". Manuscript in preparation.

16. Barry, R. K. and A. Skopal. "Continuum Evidence for Non-spherical Expansion of Ejecta in the 2006 Outburst of RS Ophiuchi". Manuscript in preparation.

17. Barry, R. K., A. Skopal, and W. C. Danchi. "Disentangling the Continuum Emission from the Nova RS Ophiuchi". Manuscript in preparation.

18. Chen, P. C., R. J. Oliversen, R. K. Barry, R. Romeo, R. Pitts, and K. B. Ma. "New Technology Lunar Astronomy Mission". In *Bulletin of the American Astronomical Society*, Volume 27, pp. 1384. (1995)

19. Danchi, W. C., W. C. Allen, R. K. Barry, D. J. Benford, L. D. Deming, D. Y. Gezari, M. J. Kuchner, D. T. Leisawitz, R. Linfield, R. S. Millan-Gabet, J. D. Monnier, L. G. Mundy, C. Noecker, J. K. Rajagopal, L. J. Richardson, S. Rinehart, S. Seager, W. A. Traub, and D. J. Wallace. "The Fourier-Kelvin stellar interferometer (FKSI): a Pratical Interferometeric Mission for Discovering and Investigating Extrasolar Giant Planets". In *New Frontiers in Stellar Interferometry*, W. A. Traub (Ed.), Proc. SPIE Vol. 5491, pp. 236. (2004)

20. Danchi, W. C., R. K. Barry, D. Deming, M. Kuchner, J. D. Monnier, L. G. Mundy, J. Rajagopal, J. Richardson, S. Seager, and W. Traub. "Scientific rationale for exoplanet characterization from 3-8 microns: the FKSI mission". In *Advances in Stellar Interferometry*. Edited by J. D. Monnier, M. Scholler and W. C. Danchi. Proc. SPIE, Vol. 6268, pp. 626820. (2006)

21. Danchi, W. C., L. D. Deming, J. M. Carpenter, R. K. Barry, P. Hinz, K. J. Johnson, P. R. Lawson, O. Lay, J. D. Monnier, L. J. Richardson, S. Rinehart, and W. A. Traub. "Towards a Small Prototype Planet Finding Interferometer (SPPFI) - The next step in planet finding and characterization in the infrared". Technical report, National Aeronautics and Space Administration ExoPlanet Task Force. (2007)

22. Danchi, W. C., B. Lopez, J. Schneider, A. Belu, R. K. Barry, J. Rajagopal, and L. J. Richardson. "Evolution of the Habitable Zone and Search for Life Around Giant Stars Part II: Feasibility with Darwin/TPF". In IAU Colloq. 200: *Direct Imaging of Exoplanets: Science & Techniques*, C. Aime and F. Vakili (Eds.), pp. 6570. (2006)

23. Evans, A., C. E. Woodward, L. A. Helton, J. T. van Loon, R. K. Barry, M. F. Bode, R. J. Davis, J. Drake, S. P. S. Eyres, T. R. Geballe, R. D. Gehrz, T. Kerr, J. Krautter, D. K. Lynch, T. J. O'Brien, J. P. Osborne, K. L. Page, R. J. Rudy,

R. W. Russell, G. Schwarz, S. G. Starrfield, and V. H. Tyne. "Silicate dust in the environment of rs ophiuchi following the 2006 eruption". *ApJ* Manuscript accepted. (2008)

24. Frey, B. J., R. K. Barry, W. C. Danchi, T. T. Hyde, K. Y. Lee, A. J. Martino, and M. S. Zuray. "The Fourier-Kelvin Stellar Interferometer (FKSI) nulling testbed II: closed-loop path length metrology and control subsystem". In *Space Telescopes and Instrumentation I: Optical, Infrared, and Millimeter*. J. C. Mather, H. A. MacEwen, M. W. M. de Graauw (Eds.), Proc. SPIE, Vol. 6265, pp. 62651N (2006)

25. Hachisu, I. and R. K. Barry. "A Wind Velocity Correction for RS Ophiuchi". Manuscript in preparation.

26. Johnson, K. J., D. J. Hutter, J. A. Tycner, J. A. Benson, J. T. Zavala, S. R. Armstrong, R. T. A., T. A. Pauls, X. Hindsley, N. Zhang, R. L. Akeson, A. F. Boden, C. Beichman, M. M. Colavita, L. Prato, D. W. Koerner, B. F. Lane, W. R. Burke, H. M. Schmid, W. C. Danchi, R. K. Barry, S. Rinehart, and D. T. Leisawitz. "Architectures and environments of planet formation zones: New frontiers in exoplanet research with the Navy Prototype Optical Interferometer and the 1.8 meter Keck Outrigger Telescopes". Technical report, National Aeronautics and Space Administration ExoPlanet Task Force. (2007)

27. Kuchner, M. and R. K. Barry. "A Mathematical Description of the Keck Interferometer Nuller". Manuscript in preparation.

28. Lane, B. F., J. L. Sokoloski, R. K. Barry, W. A. Traub, A. Retter, M. W. Muterspaugh, R. R. Thompson, J. A. Eisner, E. Serabyn, and B. Mennesson. "Interferometric Observations of RS Ophiuchi and the Origin of the Near-Infrared Emission". *ApJ* 658, 520-524. (2007)

29. Lopez, B., W. C. Danchi, J.-L. Menut, J. Rajagopal, J. Schneider, A. Belu, and R. K. Barry. "Evolution of the Habitable Zone and Search for Life Around Red Giant Stars, Part I: Interest of the Study". In IAU Colloq. 200: *Direct Imaging of Exoplanets: Science & Techniques*, C. Aime and F. Vakili (Eds.), pp. 9398. (2006)

30. Monnier, J. D., R. K. Barry, W. A. Traub, B. F. Lane, R. L. Akeson, S. Ragland, P. A. Schuller, H. Le Coroller, J.-P. Berger, R. Millan-Gabet, E. Pedretti, F. P. Schloerb, C. Koresko, N. P. Carleton, M. G. Lacasse, P. Kern, F. Malbet, K. Perraut, M. J. Kuchner, and M. W. Muterspaugh. "No Expanding Fireball: Resolving the Recurrent Nova RS Ophiuchi with Infrared Interferometry". *ApJ* 647, L127-L130. (2006)

31. Rajagopal, J. K., R. K. Barry, B. Lopez, W. C. Danchi, J. D. Monnier, P. G. Tuthill, and C. H. Townes. "Adaptive optics and aperture masking: a comparison". In *New Frontiers in Stellar Interferometry*, W. A. Traub (Ed.). Proc. SPIE Vol. 5491, p.1120, (2004)

32. Rajagopal, J. K., D. J. Wallace, R. K. Barry, L. J. Richardson, W. A. Traub, and W. C. Danchi. "Near IR Keck Interferometer and IOTA Observations of Wolf-Rayet Stars". In Proceedings of the European Southern Observatory. (2005)

33. Richardson, L. J., L. D. Deming, S. Seager, R. K. Barry, J. K. Rajagopal, D. J. Wallace, and W. C. Danchi. "Infrared Light Curves and the Detectability of Extrasolar Giant Planets with FKSI". In Proceedings of the European Southern Observatory. (2005)

34. Richardson, L. J., S. Seager, D. Deming, J. Harrington, R. K. Barry, J. Rajagopal, and W. C. Danchi. "Infrared Light Curves and the Detectability of Close-In Extrasolar Giant Planets". In IAU Colloq. 200: *Direct Imaging of Exoplanets: Science & Techniques*, C. Aime and F. Vakili (Eds.), pp. 185188. (2006)

35. Satyapal, S., M. Greenhouse, R. Barry, R. Barclay, D. Amato, B. Arritt, V. Harvey, C. Holt, J. Kuhn, N. Fonneland, and L. Lesyna . "Tunable Filters for NGST". In Bulletin of the American Astronomical Society, Vol. 31, pp. 1501. (1999)

36. Satyapal, S., M. A. Greenhouse, R. Barclay, D. Amato, B. Arritt, R. Barry, C. Holt, S. Irish, J. Kuhn, A. Kutyrev, A. Morrel, T. Higelman, N. Fonneland, and L. Lesyna. "The Tunable Filter Program for NGST". In Bulletin of the American Astronomical Society, Vol. 31, pp. 984. (1999)

37. Satyapal, S., M. A. Greenhouse, R. Barclay, D. Amato, B. Arritt, R. Barry, C. Holt, J. Kuhn, T. Higeiman, N. Fonneland, and L. Lesnya. "The Tunable Filter Program for NGST". In *Imaging the Universe in Three Dimensions*, W. van Breugel and J. Bland-Hawthorn (Eds.), Astronomical Society of the Pacific Conference Series, Vol. 195, pp. 437. (2000)

38. Satyapal, S., M. A. Greenhouse, R. Barclay, D. Amato, B. Arritt, R. Barry, C. Holt, J. Kuhn, T. Higelman, N. Fonneland, and L. Lesyna. "Tunable Filters on NGST". In *Next Generation Space Telescope Science and Technology*, E. Smith and K. Long (Eds.), Astronomical Society of the Pacific Conference Series, Vol. 207, pp. 212. (2000)

39. Satyapal, S., M. A. Greenhouse, R. Barclay, D. Amato, B. Arritt, R. Barry, S. Irish, J. Kuhn, A. Kutyrev, A. Morell, T. Hilgeman, L. Lesyna, and N.

Fonneland. “Near-Infrared Tunable Bandpass Filters for the NGST ISIM”. In Bulletin of the American Astronomical Society, Vol. 30, pp. 1296. (1998)

40. Wallace, D. J., J. K. Rajagopal, R. K. Barry, L. J. Richardson, B. Lopez, O. Chesneau, and W. C. Danchi. “Mid-Infrared Spectrally-Dispersed Visibilities ofWC and WN Type Wolf-Rayet Stars”. In Proceedings of the European Southern Observatory. (2005)

41. Weiner, J., K. Tatebe, D. D. S. Hale, C. H. Townes, J. D. Monnier, M. Ireland, P. G. Tuthill, R. Cohen, R. K. Barry, J. Rajagopal, and W. C. Danchi. “The Asymmetric Dust Environment of IK Tauri”. *ApJ* 636, 10671077. (2006)

42. Wiseman, J., M. Clampin, W. C. Danchi, J. Mather, W. Oegerle, R. K. Barry, W. A. Traub, K. Stapelfeldt, J. Lissauer, W. Borucki, T. Green, D. Bennet, and K. J. Johnston. “Space-based probe class missons for exoplanet research”. Technical report, National Aeronautics and Space Administration ExoPlanet Task Force. (2007)